

Nonlinear Terahertz Phononics: A Novel Route to Controlling Matter

Dissertation

zur Erlangung des Grades eines
Doktors (Dr. rer. nat.)

am Fachbereich Physik
der Freien Universität Berlin



vorgelegt von

Sebastian F. Mährlein

Berlin, September 2016

This work was done between April 2012 and September 2016 in the Department of Physical Chemistry (Professor Martin Wolf) at the Fritz-Haber-Institute of the Max-Planck-Society.

Berlin, September 2016

Erstgutachter: Prof. Dr. Martin Wolf

Zweitgutachterin: Prof. Dr. Katharina Franke

Datum der Disputation: 12. Dezember 2016

Abstract

Periodically arranged atoms are the fundamental building blocks of solids, and determine the mechanical, thermal, and electric properties of a material. Thus, it is no surprise that lattice vibrations (phonons) govern a number of exciting phenomena such as spin transport in thermal gradients, phase transitions and superconductivity. In this thesis, we take advantage of phonons as a novel and specific pathway to drive ultrafast processes in solids. By direct excitation with intense, ultrashort THz electric-field transients, high frequency phonons in insulating solids are accessed on their intrinsic time- and energy-scales, while avoiding parasitic electronic processes. These studies were enabled by the design and implementation of a high-field THz source, which allows for phase-sensitive pump-probe experiments over multiple time scales: from femto- to microseconds.

This work provides new insights into the coupling between the lattice and magnetic ordering, which is of central relevance for rapid data processing and information storage in future technological applications. Furthermore, fundamental dynamic processes such as magnetization switching and transport of spin angular momentum require an understanding of the way spins interact with oscillations of the crystal lattice. In order to gain such fundamental insights we investigate pure spin-lattice coupling by resonant excitation of infrared-active phonon modes of the textbook ferrimagnetic insulator Yttrium Iron Garnet. Remarkably, two distinctive time scales for phonon-magnon equilibration are revealed. A surprisingly rapid change of magnetic order with a time constant of ~ 1 ps is found to be driven by phonon-induced fluctuations of the exchange coupling, which leads to a sublattice demagnetization under the constraint of conserved total spin angular momentum. The resulting metastable state persists for nanoseconds until the spin angular momentum is released to the lattice via weaker coupling mechanisms. The experimental observations can be reproduced by atomistic spin-dynamics simulations. These findings have important implications for contemporary research fields like the spin Seebeck effect, antiferromagnetic spintronics and ultrafast magnetization switching.

In contrast, phonon modes with vanishing electric dipole moments were so far excluded from such direct THz excitation. In this thesis, a novel type of light-matter interaction is presented that enables coherent-phonon excitation via non-resonant two-photon absorption of intense THz fields. This second-order nonlinear process is the so far neglected up-conversion counterpart of stimulated Raman scattering. Here, it is demonstrated by the coherent control of the 40 THz Raman-active optical phonon in diamond via the sum frequency of two intense terahertz field components. Remarkably, the CEP of the driving pulse is directly imprinted on the lattice vibration. This study opens up a novel pathway to the phase-sensitive coherent control of phonons that were previously inaccessible by THz radiation. Furthermore, new prospects in vibrational and magnon spectroscopy, lattice trajectory control and laser machining emerge from this work.

In conclusion, this thesis demonstrates that phonons are a key component for controlling ultrafast processes in solids.

Kurzfassung

Die Gitterstruktur kristalliner Festkörper bestimmt deren grundlegende Eigenschaften, wie z.B. das mechanische, thermische und elektrische Verhalten. Daher wird eine ganze Reihe außergewöhnlicher Phänomene wie Spintransport in Temperaturgradienten, Phasenübergänge und Supraleitung von Gitterschwingungen (Phononen) bestimmt. In der vorliegenden Arbeit werden daher Phononen-Anregungen aktiv dazu benutzt, ultraschnelle Prozesse in Festkörpern zu steuern. Hierfür werden in einem elektrischen Isolator hochfrequente Phononen auf ihren fundamentalen Zeit- und Energieskalen mittels ultrakurzer intensiver elektrischer Terahertz (THz)-Felder angeregt. Durch die geringe Photonenenergie werden keine parasitären elektronischen Prozesse induziert. Diese Studien wurden durch die Entwicklung einer Hochfeld-THz-Quelle ermöglicht, die phasensensitive Anrege-Abfrage-Experimente von Femto- bis Mikrosekunden erlaubt.

Die vorliegende Arbeit liefert neue Einsichten in die Kopplung von Kristallgitter und magnetischer Ordnung, die für schnellere Datenverarbeitung und zukünftige Informationsspeicher von zentraler Relevanz ist. Weitreichende Effekte wie Magnetisierungsrotation und Spin-Drehmomenttransport erfordern ein fundamentales Verständnis der Wechselwirkung zwischen Elektronenspins und Gitterschwingungen. Aus diesem Grund wird hier die Spin-Gitter-Kopplung anhand resonanter Anregung infrarotaktiver Phononenmoden des ferrimagnetischen Isolators Yttrium-Eisen-Granat gezielt und selektiv untersucht. Bemerkenswerterweise findet die Äquilibrierung von Phononen und Magnonen auf zwei äußerst unterschiedlichen Zeitskalen statt. Direkt nach Anregung der Probe beobachten wir eine extrem schnelle Reduktion der magnetischen Ordnung mit einer Zeitkonstanten von nur ~ 1 ps, die durch Phonon-induzierte Fluktuationen der Austauschwechselwirkungskonstanten verursacht wird. Dies führt zu einer Demagnetisierung der Spin-Untergitter, wobei jedoch der gesamte Spin-Drehimpuls erhalten bleibt. Der daraus resultierende metastabile Zustand besteht für viele Nanosekunden, bis schließlich mittels einer schwächeren Kopplung Spin-Drehimpuls an das Gitter abgegeben wird. Diese Interpretation unserer experimentellen Beobachtungen wird durch atomistische Spin-Dynamik-Simulationen bestätigt. Diese Resultate sind hochgradig relevant für andere aktuelle Forschungsfelder wie den Spin Seebeck-Effekt, antiferromagnetische Spin-Elektronik oder ultraschnelles Schalten der Magnetisierung von Festkörpern.

Phononen ohne elektrisches Dipolmoment sind andererseits von solchen direkten THz-Anregungen bisher ausgeschlossen. In dieser Arbeit wird eine neue Art von Licht-Materie-Wechselwirkung vorgestellt, die kohärente Phononenanregung mittels einer nicht-resonanten Zwei-Photonen-Absorption ermöglicht. Hierfür wird exemplarisch in Diamant die kohärente Kontrolle einer Raman-aktiven Gitterschwingung mittels der Summenfrequenzkomponente eines THz-Feldes demonstriert. Die CEP des Anregungsfeldes wird hierbei bemerkenswerterweise direkt auf die Schwingung übertragen. Dies eröffnet die Möglichkeit der phasenpräzisen Steuerung von Phononen, die bisher für THz-Strahlung unzugänglich waren. Damit ergeben sich neue Perspektiven für die Spektroskopie und Steuerung der Trajektorie von Phononen und Magnonen sowie für die Materialbearbeitung durch Laserstrahlung. Zusammenfassend zeigt die vorliegende Arbeit, dass Phononen zu den Schlüsselfiguren zur Steuerung von ultraschnellen Prozessen in Festkörpern gehören.

Contents

Abstract	V
Deutsche Kurzfassung	VII
Contents	IX
1. Introduction	1
2. Theoretical background	7
2.1. Subsystems of solids	7
2.2. Phonons	9
2.2.1. Harmonic approximation	9
2.2.2. Quantized lattice vibrations	12
2.2.3. Coherent phonons	13
2.3. Spins and magnetic order	14
2.3.1. Dirac equation	15
2.3.2. Additional angular momentum: spin	16
2.3.3. Spin-orbit coupling & Zeeman interaction	17
2.3.4. Exchange coupling & Heisenberg model	18
2.3.5. Molecular field approximation of the Heisenberg model	20
2.3.6. Spin waves (magnons)	22
3. Light-matter interaction	27
3.1. Non-resonant interaction with electrons	29
3.1.1. (Semi-)classical framework	29
3.1.2. Nonlinear polarization	29
3.1.3. Second order nonlinear processes (2-wave interaction)	30
3.2. Lattice control (coherent phonons)	31
3.2.1. Direct phonon driving (1-wave interaction)	32
3.2.2. Raman-coupling (2-wave interaction)	33
3.2.3. Summary and open questions	36
3.3. Spin control	37
3.3.1. Primary coupling (1-wave interaction)	38
3.3.2. Indirect coupling (2-wave interaction)	39
3.3.3. Properties of exchange coupling	42
3.3.4. Summary and open questions	42
4. Experimental methods	45
4.1. High power kHz-lasersystem	46
4.1.1. MHz oscillator	46
4.1.2. kHz amplifier	48
4.1.3. Dual optic parametric amplifier	50

4.2.	Table top high field THz generation	53
4.2.1.	Carrier envelope phase stability	53
4.2.2.	Optical rectification	54
4.2.3.	OPA based difference frequency generation	55
4.3.	Ultrafast optical probing mechanisms	56
4.3.1.	Electrooptic detection	57
4.3.2.	Magneto-optic detection	59
4.3.3.	Data acquisition from fs to ms time scales	61
5.	Ultrafast phonon driven magnetization dynamics	69
5.1.	Motivation	69
5.2.	Sample system: iron garnets	71
5.2.1.	Lattice structure	71
5.2.2.	Absorption spectrum	72
5.2.3.	Phonon properties	73
5.2.4.	Magnetic order and magnon dispersion	74
5.3.	Experimental details	75
5.3.1.	Experimental setup	75
5.3.2.	Sample details	77
5.3.3.	Signal Analysis	77
5.4.	Results: equilibrium measurements	78
5.4.1.	Static Hysteresis at room temperature	78
5.4.2.	Temperature dependence of the equilibrium Faraday rotation	79
5.5.	Results: phonon driven ultrafast magnetization dynamics	81
5.5.1.	External magnetic field dependence	81
5.5.2.	Magnetic versus nonmagnetic contributions	82
5.5.3.	Time scales: From femto- to microseconds	84
5.5.4.	Fluence dependence	85
5.5.5.	Phonon resonance behavior	86
5.5.6.	Comparison of BiGa:YIG and pure YIG	87
5.5.7.	Temperature dependence	89
5.6.	Interpretation and microscopic mechanisms	91
5.6.1.	Possible microscopic couplings	91
5.6.2.	Scenario: phonon-modulated exchange interaction	94
5.7.	Microscopic model: phonon induced modulation of exchange coupling	94
5.7.1.	Model assumptions	94
5.7.2.	Stochastic exchange via atomistic spin model simulations	96
5.7.3.	Simulation results	97
5.7.4.	Extraction of dJ_{ad}/du	99
5.7.5.	Temperature dependence	100
5.7.6.	Summary	101
5.7.7.	Elementary processes in exchange-induced reduction of magnetic order	102
5.8.	Conclusion and outlook	103

6. Terahertz two-photon absorption generates a coherent phonon	107
6.1. Motivation	107
6.1.1. New nonlinear excitation scheme	108
6.2. Diamond material properties	110
6.2.1. Unit cell and phonon band structure	111
6.2.2. Raman tensor	111
6.3. Experimental details	112
6.3.1. Experimental setup	112
6.3.2. Sample properties and experimental geometries	113
6.3.3. CEP-modulation technique	114
6.4. Experimental results	116
6.4.1. Excitation frequency dependence	116
6.4.2. Fluence dependence	120
6.4.3. Symmetry properties	121
6.5. Model	121
6.5.1. Equation of motion	121
6.5.2. Modelling of the pump-probe signal	123
6.5.3. Results	123
6.6. Coherent phonon phase control	126
6.6.1. Concept	126
6.6.2. Experimental confirmation	126
6.7. Conclusion and outlook	127
7. Summary	131
A. Appendix	135
A.1. Harmonic approximation for antiferromagnets	135
A.2. Electron-phonon coupling	136
A.3. Description of light propagation	137
A.3.1. Maxwell and material equations	137
A.3.2. Wave equation of optics	138
A.3.3. Phase matching	138
Bibliography	141
Publications	167
Acknowledgments	171

1 Introduction

Technological progress has always relied on the growing understanding of dynamical processes in nature. Nowadays, the gain of knowledge is especially important in terms of processes occurring on microscopic length scales and on fast time scales. Therefrom resulting examples of technological advances, like digital electronics and data storage technology are based on solids such as semiconductors and magnetic metals. For instance, bit memories in the form of field-effect transistors (FETs) in random-access memories (RAMs) [Sbi11] or magnetic islands, representing single bits in hard-disk drives, have reached very small, nanometer dimensions [Sto07]. At the same time, the demand for higher operation speed, increased data rates and lower power consumption has grown drastically. Consequently, future information technology will aim for data processing on the picosecond ($1 \text{ ps} = 10^{-12} \text{ s}$) time scale and likely has to rely on novel information carriers. First devices, such as wireless local area networks (WLAN) [Fed10], fiber telecommunication schemes [Hil11] and FETs [dA11] are gradually approaching bandwidths on the THz (10^{12} Hz) scale. Accordingly, one of the main goals of contemporary research is the exploration of material control on ultrafast time scales, that is, on the order of femto- (10^{-15}) and picoseconds.

Equally important, from a basic research point of view, most elementary excitations of solids occur on THz energy- and time scales. The photon energy of the THz radiation (4 meV at 1 THz) is resonant to lattice vibrations (phonons), collective spin waves (magnons), Cooper pairs in high-temperature superconductors and internal excitations of bound electron-hole pairs (excitons). The interaction of these excitations (quasiparticles) bears a large number of fundamental physical questions which are crucial for the basic understanding of fascinating phenomena in correlated systems: insulator-metal transitions [Wal13, May15], charge density wave order [Hub14] or high-temperature superconductivity [Pas10], to name a few. The oscillation period ($\sim 1 \text{ ps}$) of a THz wave is on equal timescale as e.g. charge carrier scattering, electron-phonon equilibration and structural transitions. Therefore, coupled phenomena in the THz spectral region are highly relevant for state-of-the-art condensed-matter science.

Since general characteristics of solids, such as mechanical, thermal and electric properties, are to a large extent determined by the lattice structure [Ash05], lattice vibrations provide a promising and fundamental way for observation and dynamical control of solid-state properties. Examples such as phase transitions [Sta71, Ash05] or superconductivity [Ega07, Ben12, Pas14] indicate that phonons might be the novel key players for steering ultrafast solid-state processes. Despite this widely known role of vibrational excitations [Sat15, Fra12], only few recent studies have begun to use the lattice degree of freedoms to actively pilot these dynamics [Rin07, Fau11, Kim12b, Liu12].

In this thesis, new methods to control and probe insulating solids by selectively exciting lattice vibrations are developed and investigated. These methods offer the central benefit

of avoiding unwanted parasitic excitation of other, electronic degrees of freedom and, therefore, provide more specific excitation channels. Accordingly, this approach reduces the complexity of subsequent relaxation processes in order to potentially enable better understanding of the underlying elementary mechanisms. In the first study, we use this methodology to gain new insights into the fundamental mechanisms of spin-lattice coupling by resonant excitation of infrared (IR)-active phonon modes. The resulting knowledge gain encourages future phonon-driven studies. However, such studies are only feasible if the phonon modes of interest exhibit a non-vanishing electric dipole moment. For the case of IR-inactive yet Raman-active phonons, in a second study, we look for a novel excitation scheme, which allows strong THz fields to couple nonlinearly to these vibrational modes. This new light-matter interaction mechanism should be also extendable to other Raman modes such as magnons or plasma oscillations (plasmons). In the following paragraphs, the high-field THz source is briefly reviewed. Then the scope of the two main studies will be introduced, followed by further developments and the structure of this thesis at hand.

Development of a table top high field THz source

The scientific achievements of this thesis require a unique THz source, that combines high intensity, short pulse durations and flexible tunability. Further, CEP-stability and a precisely synchronized fs probe laser are necessary in order to control and observe coherent effects. Even for contemporary free electron laser (FEL) THz sources these requisites are challenging [Gre16]. Therefore, within this thesis a table top THz sources was developed and implemented that meets all these crucial demands. It is based on a nonlinear difference frequency mixing scheme to provide ultrashort intense THz fields, which are tunable over several frequency octaves ranging from 10 THz up to the mid infrared (MIR) above 60 THz [Sel08a]. In this way, field strength of around 50 MV/cm are easily reached, which already start to compete with the atomic field gradient of $\sim 1 \text{ V/\AA}$ in solids and therefore offer the ability of nonlinear light matter interactions at THz frequencies [Sel08a].

Synchronized 8 fs probe pulses enable the phase resolved detection of transient sample properties in a pump-probe scheme. With extensive noise studies, even leading to a redesign of parts of the commercial laser amplifier, the timing jitter between THz-pump field and visible probe pulse could be pushed below 1 fs. The table top high-field THz source developed within this thesis, will also be a versatile and unique state of the art tool for a number of future studies.

Ultrafast phonon driven magnetization dynamics

Despite the aforementioned advances in data processing, the storing speed of data still lags behind, creating an ultrafast technology gap [Kir10]. To approach faster magnetic data storage devices, the change of magnetic order has to be understood and controlled on ultrafast time scales [Sta14]. Therefore, the leading scientific question in this study is: how does magnetic order couple to strongly driven optical phonons? What are the ultimate time scales and microscopic coupling mechanisms? Are there different speed limits for energy and angular momentum transfer? Answers to these questions may help iden-

tify the highly debated role of the lattice during laser induced ultrafast demagnetization [Bea96, Koo10, Kir10]. Novel excitation channels of spin degrees of freedom, especially spin transport and spin waves (magnons), provide also the basis for potential spintronic [Bad10] and magnonic devices [Chu15, Ser10].

To address these questions, we make use of our direct lattice-pump/spin-probe technique to investigate spin-lattice coupling of magnetic insulators over multiple time scales, from ultrafast (femtoseconds) to slow (milliseconds). As model system, we choose the textbook ferrimagnetic insulator Yttrium Iron Garnet (YIG) [Che93a] which is a highly relevant material in the fields of magnonics [Ser10] and spin caloritronics [Bau12] owing to the very long lifetime of its long-wavelength magnons [Spe62, Hun10].

The results of this study demonstrate the manipulation of magnetic order via high-frequency optical phonons, even on ultrafast time scales. Further, we reveal that the model ferrimagnet YIG exhibits two extremely different time scales of phonon-magnon coupling: The initial energy transfer, found to be mediated by lattice-induced fluctuations of exchange coupling, occurs on a picosecond timescale. The angular-momentum equilibration between lattice and spins is 5 orders of magnitude slower and takes place on 100 ns time scales. In between these two time scales, we observe a novel long-lived quasi-equilibrium state of the magnetic order, in which the spin system is rearranged under the constraint of constant total spin.

Terahertz two-photon absorption generates a coherent phonon

The first study of this thesis demonstrates the potential of intense phonon excitation in order to trigger and understand ultrafast phenomena. In previous studies, even phase transitions were successfully initiated by phonon stimuli [Kim12b, Rin07]. However, in all these studies, the primarily excited phonons were strongly infrared-active, a prerequisite that is only fulfilled for a subset of lattice vibrations [Ash05]. But what if key phonon modes are not directly accessible by light excitation, due to a lack of electric dipole moment? How can we excite infrared-forbidden yet Raman-active phonons while keeping the advantages of THz excitation? Is it at all possible to launch coherent lattice excitations with photon energies below the fundamental phonon resonance?

In this study, we look for a novel non-linear excitation mechanism for Raman active modes using intense phase-stable THz pump pulses [Sel08a]. Exemplarily, we employ the archetypical reference system of many Raman studies, the F_{2g} -mode of diamond [Ram56, Sol70, Ish06]. We find a so far overlooked mechanism for driving coherent lattice vibrations via non-resonant two-photon THz absorption, which can be conveniently described in the framework of stimulated Raman excitation (SRS) [Mer97, Gri08]. Additionally, the phase of the phonon motion can be directly controlled by the carrier-envelope phase (CEP) of the pump pulse. This universal approach enables THz coherent control of Raman-active modes including phonons [Dek00], magnons [Kal08] and plasmons [Arm04], without parasitic electronic excitations [Cho90, Rif07].

Further developments

For the aforementioned results, a number of new tools, methods and models were developed and will be presented within this thesis. For example, a novel data-acquisition scheme for time-resolved pump-probe studies spanning 12 orders of magnitude in time (from femtoseconds to microseconds) was developed. This large range allows for the observation of very different time scales of spin-lattice coupling. Further, the demonstration of phonon phase control requires the design of a unique, drift-free THz CEP-modulation technique, which is clocked to the laser repetition rate.

For a microscopic understanding of ultrafast lattice-spin coupling, a theoretical model was elaborated in cooperation with leading theoreticians in the field, namely J. Baker, P. Maldonado and P. M. Oppeneer. In contrast, the phenomenological model of sum-frequency stimulated Raman excitation will be presented on the basis of a simple damped harmonic oscillator and classical light-matter interaction.

The work of this thesis also included the design and implementation of free-electron-laser (FEL) experiments at the large scale facilities FHI FEL, FELBE and FLASH which was done in close collaboration with A. Paarmann, M. Gensch and I. Radu, respectively.

Thesis structure

This thesis is organized as follows. First, in chapter 2, a brief introduction to the theoretical treatment of a solid is given, by starting with the division into three subsystems: lattice, spins and electron orbital degree of freedoms. The description of the ground state and collective excitations (phonons and magnons) also includes interactions with the other degrees of freedom and an incident ultrashort laser pulse (section 3). For electrons, interaction with a strong laser pulse far away from resonances (i.e. transparent media) is discussed phenomenologically, leading to the field of nonlinear optics. For the lattice degrees of freedom, we distinguish between direct driving (1-wave interaction) of coherent phonons (IR-active phonons) and excitations by non-resonant 2-wave interaction, namely stimulated Raman effects. In the case of spins, a number of different direct and indirect coupling mechanisms in transparent and opaque media are discussed. In chapter 4, the experimental methods including the high-field THz source are reviewed in detail. The two main studies of this thesis are presented in chapter 5 (*Ultrafast phonon driven magnetization dynamics*) and in chapter 6 (*Terahertz two-photon absorption generates a coherent phonon*). Finally, chapter 7 concludes this thesis.

In summary, this thesis unveils a novel light-phonon coupling mechanism that enables the coherent control of Raman active phonons via nonlinear excitation with intense THz fields. Further, in insulating model ferrimagnets, we find an ultrafast phonon-spin coupling mechanism that quenches the magnetic order on ultrafast time scales and leads to a metastable magnetically ordered state that persists over hundreds of nanoseconds. This allows for a temporal disentanglement of the energy and angular momentum transfer between phonons and spins. Therefore, this work demonstrates novel routes to controlling matter via THz-field driven phonons.

2 Theoretical background

2.1 Subsystems of solids

The scope of this chapter is the introduction and summary of concepts that describe the fundamental excitations of condensed matter and their interaction (mainly chapter 3). The theoretical background of these concepts is useful for the understanding of the novel results presented in chapter 5 and 6. It is also a helpful background to understand the experimental techniques (chapter 4) developed for obtaining these results.

Contemporary physics describes the world that we are living in as interacting many body systems. Even force fields are mostly described in terms of exchange particles. This holds true since the dawn of quantum physics in the early 20th century [Ein05, Hei25, Dir81], ranging from fundamental quantum field theory [Fey49] to the most recent discovery of the Higgs-boson[Cha12], which completes the standard model of particle physics.

In this work, the general interest focuses mostly on phenomena in the solid state. In terms of applications, solid state matter systems are the most promising systems, because they surround us in our everyday life and ensure feasibility and durability. To predict and exactly describe the behavior and temporal evolution of a solid, it is necessary to solve the corresponding many body *Schrödinger equation*:

$$i\hbar\frac{\partial}{\partial t}|\psi_N\rangle = \hat{H}_N|\psi_N\rangle, \quad (2.1)$$

where $|\psi_N\rangle$ is a state in a N -body Hilbert Space. The N -body Hilbert Space is a product space of all single particle states basis vectors:

$$\mathcal{H}_N = \mathcal{H}_1^{(1)} \otimes \mathcal{H}_1^{(2)} \otimes \dots \otimes \mathcal{H}_1^{(N)} \quad (2.2)$$

with $\mathcal{H}_1^{(i)}$ being single particle Hilbert space of the i th particle. For identical particles in quantum mechanics (e.g. electrons), numbering of particles makes only sense, if permutation symmetry or anti-symmetry is fulfilled [Nol05]. This is an obvious requirement as a physically measured quantity (= expectation value of an observable) must not change upon permutation of indistinguishable particles.

In general it is unfeasible to find solutions to the full many body Schroedinger's equation. Therefore the real challenge is to find physical reasonable approximations and models to solve such many problems¹.

To model a solid state material, the following assumptions in order to get a reasonable approximation are common:

The solid state system is decoupled into subsystems and the interaction of those subsystems is introduced afterwards a perturbation. The first subsystem are lattice ions, which consist of a positively charged atom nucleus and core electrons. The core electrons mostly

¹Quote attributed to Albert Einstein: "Everything should be made as simple as possible, but not simpler."

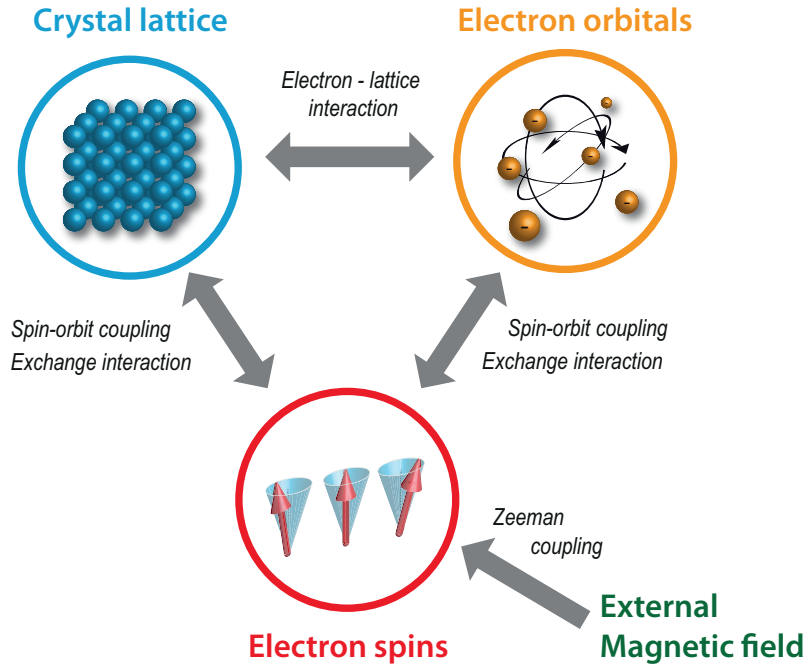


Figure 2.1.: Subsystems of condensed matter. Within this thesis, condensed matter is assumed to be divisible into three subsystems: Crystal lattice, electron orbitals and electron spins. All three systems are first described separately by their unperturbed many body Hamiltonian. The interactions and coupling phenomena indicated by grey arrows can be introduced (e.g. by perturbation theory) subsequently.

occupy fully filled shells and therefore have no big influence on material properties [Ash05]. The second subsystem consists of valence electrons, which mostly occupy partially filled "outer" shells. Hence, they are dominantly responsible for electric and magnetic properties of the solid.

The Hilbert Space of all states of a solid state material can be consequently expressed by a product space of the two sub spaces for lattice ions $\mathcal{H}_{\text{lat}}^N$ (including core electrons) and valence electrons \mathcal{H}_e . In the subchapter Spins & Magnetism (section 2.3), it will be shown, that it is reasonable to subdivide the electronic degrees of freedom in orbital degrees and spin degrees of freedom. Therefore, the main framework of this thesis is based on the many particle product space

$$\mathcal{H}_N = \mathcal{H}_{\text{orbit}}^N \otimes \mathcal{H}_{\text{spin}}^N \otimes \mathcal{H}_{\text{lat}}^N, \quad (2.3)$$

which is depicted in the most important schematic of this work in figure 2.1. Thus the following ansatz for the N -body Hamiltonian $H^{(N)}$ is justified:

$$H^{(N)} = H_{\text{lat}}^{(N)} + H_e^{(N)} + H_{e-\text{lat}}^{(N)}. \quad (2.4)$$

Here the $H_e^{(N)}$ contains both valence electron orbital and spin degrees of freedom. The interaction between the ion lattice and valence electrons is summarized by $H_{e-\text{lat}}^{(N)}$.

This chapter is subdivided as follows:

For the ionic part of the Hamiltonian H_{lat} , the assumption is made that the ions move in

a homogenous sea of electrons (section Phonons 2.2) [Ash05]. The valence electron part of the Hamiltonian H_e , is separated with the assumption that the ions are stationary, corresponding to a stiff lattice [Ash05]. Further, nuclear spin contributions are assumed to be negligible. This leads to the description of spin order and fundamental magnetic models in section 2.3.

The question leading to the main topic of this work is: How does the interaction between the lattice and the spin subsystem evolve? How can we study their interaction dynamics separately? And can their excitations couple on fundamental time scales? Accordingly, the perturbation of both system by an external light field has to be understood. The principles of these light-matter interactions and state of the art studies are summarized in the next chapter 3

2.2 Phonons

Starting from the previous assumption, that it is possible to describe the dynamics of the ion cores and valence electrons separately, the goal of this subchapter is to find the Hamiltonian H_{lat} of equation 2.4 describing the core ions that move in a time averaged adiabatic potential of the valence electrons. This often called Born-Oppenheimer or adiabatic approximation therefore assumes that the valence electrons follow the ionic motion adiabatically [Ash05, Yu05, Nol05]. Afterwards, the electron-phonon interaction can be reintroduced as a perturbation by means of $H_{e-\text{lat}}$ as shown in appendix A.2.

The most general ansatz for the energy of the lattice is a simple sum over the kinetic energy $H_{\text{lat,kin}}$ and potential energy of all N_{ion} ions. Due to the adiabatic following of the valence electrons, the potential energy Hamiltonian consists only of the ion-ion interaction $H_{\text{ion-ion}}$ [Nol05]:

$$H_{\text{lat}} = \underbrace{\sum_i^{N_{\text{ion}}} \frac{p_i^2}{2M_i}}_{H_{\text{lat,kin}}} + \underbrace{\frac{1}{2} \sum_{i,j}^{i \neq j} V_i(\mathbf{R}_i - \mathbf{R}_j)}_{H_{\text{ion-ion}} = H_{\text{ion-ion}}^{(0)} + H_{\text{ph}}} . \quad (2.5)$$

Here \mathbf{R}_i and \mathbf{R}_j is the actual position of the i th and j th ion and M_i is the mass of the corresponding ion. $H_{\text{ion-ion}}^{(0)}$ corresponds to the static interaction responsible for the equilibrium lattice bonds, whereas H_{ph} determines the lattice dynamics [Nol05].

2.2.1 Harmonic approximation

The binding forces that determine the equilibrium positions of the ions in the lattice can be caused by several physical mechanisms (mostly coulomb forces). On the other hand, the interaction between two ions can be mostly described by a pair potential $V_i(|\mathbf{R} - \mathbf{R}'|)$ as qualitatively depicted in figure 2.2 a. Nevertheless, a pair potential is not required for the harmonic approximation. For small elongations around the equilibrium distance $R_i^{(0)}$, the potential V_i can be approximated as parabolic and thus is similar to an harmonic oscillator. Usually, this is justified as motions of the ions normally do not exceed 5% of

the lattice distance [Nol05].

To describe the motion around the equilibrium lattice site $R_i^{(0)}$, we make use of a generalized index i , counting over N Bravais lattice sites [Ash05, Kit66] with p atoms in 3 independent directions (x, y, z) each [Nol05]. Accordingly, all ion positions are defined by

$$x_i(t) = R_i^{(0)} + u_i(t) \quad \text{with } i = (\{N\}, \{p\}, [x, y, z]). \quad (2.6)$$

The Taylor expansion for small elongations $u_i(t)$ around the equilibrium position $R_i^{(0)}$ ($\Leftrightarrow u_i = 0$) leads to

$$V(x_i) = V_0 + \sum_i \varphi_i^{(1)} u_i + \frac{1}{2} \sum_{i,j} \varphi_{i,j}^{(2)} u_i u_j + \mathcal{O}(u^3). \quad (2.7)$$

Here the harmonic approximation means that all terms of the order $\mathcal{O}(u^3)$ or higher will be neglected. $V_0 = V(\{R_i^{(0)}\})$ corresponds to static lattice bonds ($H_{\text{ion-ion}}^{(0)}$) and $\varphi_i^{(1)} = \frac{\partial V}{\partial x_i}$ is required to be zero, because of the local minimum of V at $u_i = 0$. The Matrix

$$\varphi_{ij}^{(2)} = \left. \frac{\partial^2 V}{\partial x_i \partial x_j} \right|_{u_i=0} \quad (2.8)$$

can be seen as atomic force constant. Consequently $\varphi_{ij}^{(2)} u_j$ is the force on ion i , when ion j moves along a certain direction. The direction of the force and the direction of the

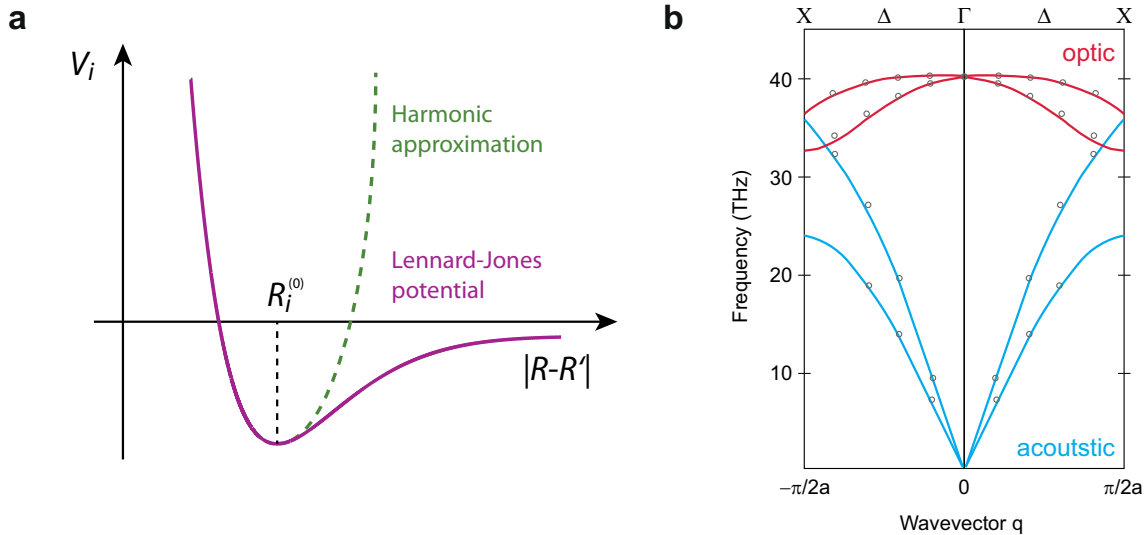


Figure 2.2.: Pair interaction potential and phonon dispersion. **a**, Coulomb pair interaction potential V_i for the i th ion with equilibrium distance $R_i^{(0)}$. For small distances $|R-R'|$ the Lennard-Jones potential can be approximated as a harmonic potential. This is the origin of the commonly justified harmonic approximation. **b**, Prototypical phonon dispersion of Diamond along the Δ -direction. The circles are experimental data measured by inelastic neutron scattering [War67], whereas the solid lines for optic (red) and acoustic phonons (blue) are calculated by an adiabatic bond charge model [Web77].

elongation is included in the indices i and j , respectively. With this force, the equation of motion represents a set of $3pN$ coupled harmonic oscillators, describing a collective motion [Nol05]. In order to lower the complexity, advantage of the discrete translational symmetry of the lattice is taken. In this way the number of eigenvalues reduces to $3p$, which are then characterized by a wavevector \mathbf{q} and a band index r . Therefore, the corresponding eigenfunctions $u_i(t)$ can be written as [Nol05]:

$$u_i(t) = \frac{\hat{u}_i}{\sqrt{M_i}} e^{i(\mathbf{q} \cdot \mathbf{R}_i^{(0)} - \omega_r(\mathbf{q})t)}. \quad (2.9)$$

This eigenfunction is a discrete Bloch wave [Ash05, Nol05] and corresponds to a Fourier transformation from real space (\mathbf{x}, t) to reciprocal space (\mathbf{q}, ω) . Therefore the $3p$ eigenvalues are wavevector \mathbf{q} dependent and can be seen as dispersion curves $\omega_r(|\mathbf{q}|)$ in the first Brillouin zone with $r = 1, 2, 3 \dots 3p$ branches. This very general result leads to 3 acoustic branches ($\omega(q=0) = 0$) and $3(p-1)$ optical branches ($\omega(q=0) \neq 0$) [Ash05]. A prototypical phonon dispersion, in this case for diamond, is shown in figure 2.2 b.

In the final step, a new set of orthonormal eigenfunction $Q_r(\mathbf{q}, t)$ can be found from linear superpositions of the eigenfunctions $u_i(t)$, which diagonalizes the force matrix $\varphi_{ij}^{(2)}$ [Nol05]. These new motion coordinates are called normal coordinates $Q_r(\mathbf{q}, t)$. Apparently, every oscillation along such a normal coordinate is decoupled from other coordinates and thus can be described with the equation of motion for an (undamped) harmonic oscillator:

$$\ddot{Q}_r(\mathbf{q}, t) + \omega_r^2(\mathbf{q}) Q_r(\mathbf{q}, t) = 0. \quad (2.10)$$

The picture of classical harmonic oscillators along the normal coordinates (phonon modes) is most of the time sufficient to even describe novel nonlinear coupling phenomena like presented in chapter 6.

The particular difference between optic and acoustic modes can be depicted very understandable for the case of a linear two-atomic chain model ($p = 2$). In the long wavelength limit ($\mathbf{q} \rightarrow 0$), it can be shown that for optic phonons the two types of atoms vibrate out of phase (figure 2.3 a), whereas in the case of acoustic phonons they oscillate nearly in phase (figure 2.3 b). This is also where their name stems from: As the wavelength of visible light is much larger than the lattice spacing, the previous limiting case for $\mathbf{q} \rightarrow 0$ has to be considered. The optic modes may exhibit electric dipoles in polar lattices, whereas the electrical dipole moment nearly vanishes for acoustic phonons. Therefore, light can only couple directly to specific optical phonons.

Taking the description of vibrational modes back to 3 dimensions, longitudinal and transverse oscillation directions have to be distinguished. The longitudinal modes usually exhibit higher frequencies, because their planes of charges vibrating against each other can be pictorially seen as distance modulated parallel plane capacitors.

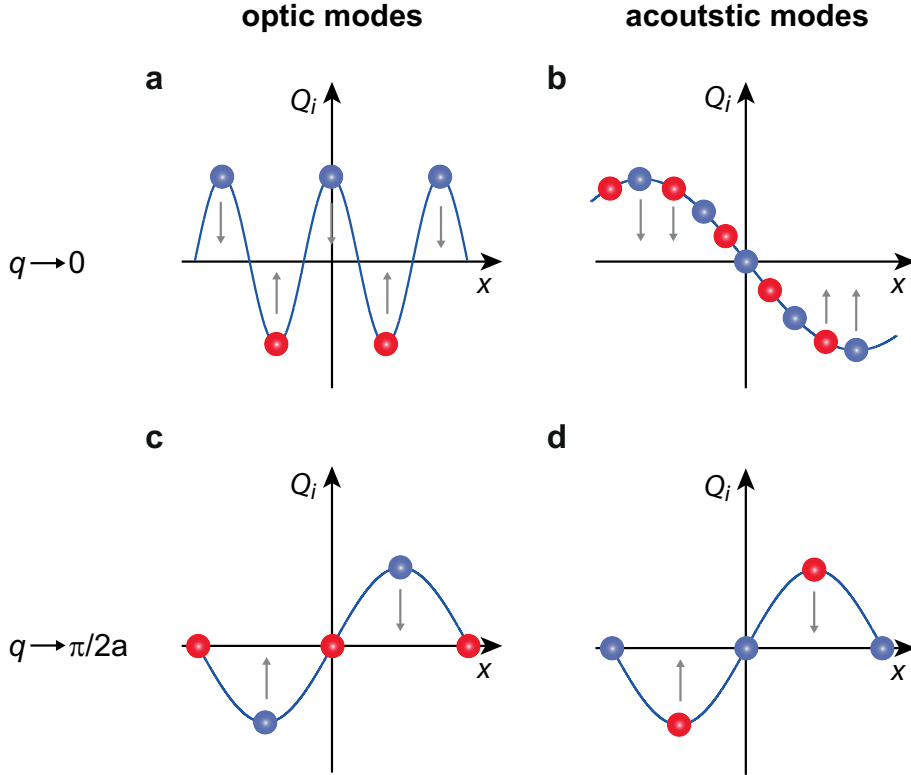


Figure 2.3.: Linear two-atomic chain model. Long wavelength limit: **a**, for optic phonons ($q \rightarrow \pi/2a$), two species of atoms vibrate out of phase, whereas **b**, for acoustic phonons they move nearly in phase. **c**, **d**, In the short wavelength limit ($q \rightarrow \pi/2a$), optic and acoustic modes only differ by the mass difference of the two different types of atoms [Ash05].

2.2.2 Quantized lattice vibrations

In order to make the transformation from a classical harmonic oscillator to a quantum-mechanical oscillator, a many body Hamiltonian in second quantization is required. The second quantization describes a many body system by creation and annihilation of quasi-particles, whose energy correspond to the quantized excitations of the system [Ash05, Nol05]. This is also derived for the second quantization of spin waves in section 2.3.6, which leads analogously to the quasi particle magnon.

As it was shown in the previous section 2.2.1, lattice vibrations can be described in the harmonic approximation as uncoupled harmonic oscillators after transformation to normal coordinates $Q_r(\mathbf{q})$. Therefore it is possible to define for each oscillator $Q_r(\mathbf{q})$ a canonical momentum $\Pi_r(\mathbf{q})$. Both classical variables $Q_r(\mathbf{q})$ and $\Pi_r(\mathbf{q})$ can be quantized as operators. It can be further shown (see e.g. the textbook by W. Nolting [Nol05]), that this approach leads to the following annihilation operator $b_{\mathbf{q}r}$ and creation $b_{\mathbf{q}r}^\dagger$ operator for

lattice excitations of the r th mode with wavevector \mathbf{q} [Nol05]:

$$b_{\mathbf{q}r} = \frac{1}{\sqrt{2\hbar\omega_r(\mathbf{q})}} \left(\omega_r(\mathbf{q}) Q_r(\mathbf{q}) + i\Pi_r^\dagger(\mathbf{q}) \right) \quad (2.11)$$

$$b_{\mathbf{q}r}^\dagger = \frac{1}{\sqrt{2\hbar\omega_r(\mathbf{q})}} \left(\omega_r(\mathbf{q}) Q_r^\dagger(\mathbf{q}) - i\Pi_r(\mathbf{q}) \right). \quad (2.12)$$

Here obviously, the expectation value of $\langle b_{\mathbf{q}r} + b_{-\mathbf{q}r}^\dagger \rangle$ corresponds to the classical amplitude $Q_r(\mathbf{q})$ ². These operators fulfill the characteristic Bose operator commutation relations:

$$\left[b_{\mathbf{q}r}, b_{\mathbf{q}'r'}^\dagger \right]_- = \delta_{\mathbf{q}\mathbf{q}'} \delta_{rr'} \quad (2.13)$$

$$\left[b_{\mathbf{q}r}, b_{\mathbf{q}'r'} \right]_- = \left[b_{\mathbf{q}r}^\dagger, b_{\mathbf{q}'r'}^\dagger \right]_- = 0. \quad (2.14)$$

With these commutation relations the Hamiltonian for quantized oscillations of the ion lattice can be expressed by creation and annihilation operators [Nol05]:

$$H_{\text{ph}} = \sum_{\mathbf{q}r} \hbar\omega_r(\mathbf{q}) \left(b_{\mathbf{q}r}^\dagger b_{\mathbf{q}r} + \frac{1}{2} \right). \quad (2.15)$$

Obviously, the energy of the ion lattice consists of the sum of excitations of $3pN$ uncoupled oscillators, but the ground state energy of each mode is $\hbar\omega_r(\mathbf{q})/2$ and not zero. The energy of each oscillator is accordingly given by its occupation number $\langle \hat{n}_{\mathbf{q},r} \rangle = \langle b_{\mathbf{q}r}^\dagger b_{\mathbf{q}r} \rangle$ and the energy quantum $\hbar\omega_r(\mathbf{q})$.

In conclusion, the energy of the excited lattice H_{ph} is given by $\{\langle \hat{n}_{\mathbf{q},r} \rangle\}$ quasi particles, which represent the lattice vibrations along the normal coordinates $Q(\{r\}, \{\mathbf{q}\})$. These quasi particles with energies $\hbar\omega_r(\mathbf{q})$ are called phonons. Every change in lattice energy is equivalent to creation or annihilation of phonons.

The bosonic nature of the excitations allows every oscillation state to be occupied by an arbitrary occupation number. This of course only holds true, if the amplitude $\langle b_{\mathbf{q}r} + b_{-\mathbf{q}r}^\dagger \rangle$ does not exceed the harmonic approximation limit. Otherwise anharmonic coupling phenomena have to be included [Mil87, Has02, Foe11a].

2.2.3 Coherent phonons

In the previous section 2.2.2 it has been derived that phonons are bosons and therefore obey Bose-Einstein-statistics. Accordingly, a finite number of phonon states are already occupied at finite temperatures. These phonons are usually called thermal phonons as their distribution is dictated by the Bose-function [Nol05]:

$$\langle \hat{n}_{\mathbf{q},r} \rangle (T) = \frac{1}{\exp\left(\frac{\hbar\omega_r(\mathbf{q})}{k_B T}\right) - 1}, \quad (2.16)$$

²Please note: $Q_r^\dagger(-\mathbf{q}) = Q_r(\mathbf{q})$ and $\Pi_r^\dagger(-\mathbf{q}) = \Pi_r(\mathbf{q})$

where k_B is the Boltzmann factor.

The thermal phonon occupation is not necessarily a coherent state, meaning that there is only an occupation of states $\langle \hat{n}_{\mathbf{q},r} \rangle$, but no correlation between these states of harmonic oscillators [Muk99]. This leads to a vanishing of the classical amplitude $Q_r(\mathbf{q}) \propto \langle b_{\mathbf{q}r} + b_{-\mathbf{q}r}^\dagger \rangle = 0$.

In contrast, a coherent phonon is a distinctively different non-equilibrium state of the structure of the ion lattice. It is a transient state and therefore it cannot be described by a Bose-distribution [Nol05]. In this case of coherent phonons, ions oscillate in-phase along a certain direction of the crystal and keep their special coherence on a macroscopic length scale (larger than a unit cell). This in-phase collective motion therefore quantum-mechanically exhibits correlations between phonon states, leading to a non-vanishing classical amplitude $Q_r(\mathbf{q}) \propto \langle b_{\mathbf{q}r} + b_{-\mathbf{q}r}^\dagger \rangle \neq 0$ [Muk99] (in the following the wavevector \mathbf{q} and branch r indices will be suppressed).

Accordingly, the amplitude Q fulfills the classical equation of motion and therefore can still be adequately described in the framework of a damped harmonic oscillator with an external driving force $F(t)$ (see section 6.5). Hence, the isolated motion along a normal coordinate $Q(t)$ is conveniently described by the fundamental equation of motion [Kuz94, Mer97]:

$$\frac{\partial^2 Q(t)}{\partial t^2} + 2\gamma \frac{\partial Q(t)}{\partial t} + \omega_r^2 Q(t) = \frac{F(t)}{m^*} \quad (2.17)$$

with the phenomenological damping constant γ , reduced mass m^* and eigenfrequency ω_r .

In chapter 3 the interaction of a solid state material with a light field will be introduced. There, different kind of driving forces $F(t)$ will be discussed. In principle one has to distinguish between direct forces like a resonant electric field $E(\omega_0)$ coupling to IR-active optical phonons, and indirect forces like in the case of impulsive or dispersive Raman excitations, which are mediated by electron-phonon coupling H_{e-ph} .

In the case of anharmonic coupling, the driving force $F(t)$ can also stem from other excited phonons, for example from the rectified electric field of a polar (IR-active) phonon. This would correspond to a driving force proportional to Q_{IR}^2 , where Q_{IR} is the amplitude of the initial IR-active phonon [Sub14]. In this case, there is obviously a phonon-phonon coupling, so the harmonic approximation of non-interacting phonons is not justified anymore. Therefore this processes have to be described by anharmonic potentials. Thus this effect is called anharmonic Raman scattering and could be recently experimentally observed by making use of the advent of strong table top THz sources [Foe11a].

2.3 Spins and magnetic order

After the last section, where mainly the decoupled lattice subsystem was described, we come back to fundamental the N -Body-Hamiltonian $H^{(N)}$ of equation 2.4. In this section, it will be shown that a further separation of the valence electron Hamiltonian $H_e^{(N)}$ into a spin degree and electron orbit degree of freedom, as shown in the central figure 2.1, is reasonable. Here, the focus lies on the spin part to establish the theoretical background for the novel results concerning spin manipulation and ultrafast coupling of the magnetic

order in chapter 5.

The background of magnetism is approached as follows: In the first section 2.3.1, the relativistic treatment of a single free electron (Dirac equation) already results in an additional degree of freedom, the spin, which also exhibits a magnetic moment. Afterwards a central potential is introduced, e.g. stemming from an ion core in a solid state compound (section 2.3.2). This directly leads to the finding that the electron orbital momentum l and the spin degree of freedom s are directly coupled (section 2.3.3).

In the following section 2.3.4, the transition from a single particle to collective effects is performed. In the quantum mechanical description this leads to the exchange interaction and thus to a Heisenberg model of the spin lattice. This model is the basis for the description of magnetic order, e.g. ferro-, ferri- oder antiferro-magnetic order. Finally in section 2.3.6, we make the transition from the unperturbed spin ordered ground state to excited states, which corresponds to spin wave (magnon) excitations.

2.3.1 Dirac equation

The relativistic treatment of a free electron leads to a magnetic moment of a spin, spin orbit coupling and further relativistic effects. Thus, the starting point for the theoretical background of spins is the energy of a free relativistic classic particle with mass m :

$$E^2 = c^2 \mathbf{p}^2 + m^2 c^4, \quad (2.18)$$

where $\mathbf{p} = \gamma \mathbf{v}$ is the relativistic mechanical momentum with $\gamma = (1 - v^2/c^2)^{-1/2}$ and light velocity c . Applying Schrödinger's correspondence rule [Nol13, Nol15] to the co-variant four momentum operator yields

$$p_\mu = \begin{pmatrix} E/c \\ \gamma m \mathbf{v} \end{pmatrix} \longrightarrow i\hbar \partial^\mu = i\hbar \begin{pmatrix} \frac{1}{c} \frac{\partial}{\partial t} \\ -\nabla \end{pmatrix}. \quad (2.19)$$

Plugging p_μ into equation 2.18 leads to the relativistic generalization of the Schrödinger equation:

$$\left(\Delta - \frac{1}{c^2} \frac{\partial^2}{\partial t^2} - \frac{m^2 c^2}{\hbar^2} \right) \psi = 0. \quad (2.20)$$

This so called *Klein-Gordon equation* is a differential equation of second order in time t , whereas the initial non-relativistic Schrödinger equation contains only first order derivatives. A factorization of equation 2.20 leads to solely first order derivatives in every factor and finally yields the *Dirac equation* for a free particle [Nol09]:

$$\left(i\hbar \frac{\partial}{\partial t} - c \boldsymbol{\alpha} \cdot \mathbf{p} - \beta m c^2 \right) \psi = 0. \quad (2.21)$$

Accordingly, the Dirac Hamiltonian of a free particle can be written in simplified notation:

$$H_D^{(0)} = c \hat{\alpha} \cdot \mathbf{p} + \hat{\beta} m c^2 \quad (2.22)$$

with the 4x4-matrices $\hat{\alpha}$ and $\hat{\beta}$ that are defined by Pauli's spin matrices $\sigma = (\sigma_x, \sigma_y, \sigma_z)$ and the 2x2-unity matrix \mathbb{I}_2 :

$$\hat{\alpha} = \begin{pmatrix} 0 & \sigma \\ \sigma & 0 \end{pmatrix} ; \quad \hat{\beta} = \begin{pmatrix} \mathbb{I}_2 & 0 \\ 0 & -\mathbb{I}_2 \end{pmatrix}. \quad (2.23)$$

The solutions for $H_D^{(0)}$ are determined by the energy eigenvalues $\pm E_p$ and by a new quantum number, called spin: $\pm\hbar/2$. In the following section it will be concluded that the spin operator \hat{s} fulfills the properties of an angular momentum operator and thus leads to a spin magnetic moment.

2.3.2 Additional angular momentum: spin

For the next step towards more realistic conditions, an additional charged nucleus is considered. The presence of an external electro-magnetic field manifests itself in an additional contribution to the four momentum

$$p_\mu \longrightarrow p_\mu + eA_\mu \quad \text{with} \quad A_\mu = \left(\mathbf{A}, \frac{1}{c}\phi \right) \quad (2.24)$$

Where A_μ is the electromagnetic four potential. Thus the Hamiltonian for a Dirac particle in an electromagnetic field can be directly derived from equation 2.22:

$$H_D = c\hat{\alpha} \cdot (\mathbf{p} + e\mathbf{A}) + \hat{\beta}mc^2 - e\phi. \quad (2.25)$$

In a central potential $V(r)$ the total angular momentum has to be conserved. In quantum mechanics that means that the operator $\mathbf{l} = \mathbf{r} \times \mathbf{p}$ has to commute with the Hamiltonian. Simplifying the Hamiltonian above (equation 2.25) by assuming only a central potential $V(r)$, results in:

$$H_D^{(V)} = c\hat{\alpha} \cdot \mathbf{p} + \hat{\beta}mc^2 - V(r). \quad (2.26)$$

From this it can be remarkably seen that the commutator $[\mathbf{l}, H_D^{(V)}]_- \neq 0$ and thus the orbital momentum is not conserved anymore in a field of a central force. This violates classical mechanics conservation laws. Thus Dirac proposed an additional intrinsic angular momentum (spin) according to the following spin operator [Dir81, Nol09]

$$\hat{\mathbf{s}} := \frac{\hbar}{2}\hat{\sigma} = \frac{\hbar}{2} \begin{pmatrix} \sigma & 0 \\ 0 & \sigma \end{pmatrix} \quad (2.27)$$

Calculating the commutation of the spin operator with $H_D^{(V)}$, directs to the intriguing result:

$$[\mathbf{l}, H_D^{(V)}]_- = -[\hat{\mathbf{s}}, H_D^{(V)}]_- \neq 0 \quad (2.28)$$

In conclusion, neither $\hat{\mathbf{s}}$ nor \mathbf{l} commutes with $H_D^{(V)}$. Likewise, the spin operator acts similar to an angular momentum operator. It can be shown that the observable spin obeys

the algebraic properties of a quantum-mechanical angular momentum [Nol15]. From the commutator relations 2.28, it can be directly seen that total angular momentum $\mathbf{j} = \mathbf{l} + \mathbf{s}$ is a conserved quantity in a central field. This finding already suggests the coupling of the spin degree of freedom with the orbital momentum of valence electrons.

2.3.3 Spin-orbit coupling & Zeeman interaction

In order to identify further contributions in the Dirac Hamiltonian and to define a concrete spin-orbit-coupling Hamiltonian, a simplification by a reasonable approximation has to be considered. Therefore, the central potential ϕ is kept, but terms second order in v/c are neglected to approach the non-relativistic limit. Thereupon, the four dimensional state vector (or double spinor)

$$\psi = \begin{pmatrix} \psi_1 \\ \psi_2 \\ \psi_3 \\ \psi_4 \end{pmatrix} = \begin{pmatrix} \psi_+ \\ 0 \end{pmatrix} + \begin{pmatrix} 0 \\ \psi_- \end{pmatrix} \quad (2.29)$$

of Dirac's equation is reduced to a two dimensional state vector (spinor), where every dimension represents a certain spin direction. The expansion in v/c leads to a suppression of the ψ^- component and while accounting for the right normalization of the single spinor state ψ^+ , finally the known *Pauli-Hamiltonian with relativistic corrections* can be derived [Nol09]:

$$H_p = \underbrace{\frac{p^2}{2m}}_T - \underbrace{\frac{p^4}{8m^3c^2}}_{T_{\text{rel}}} - \underbrace{e\phi}_{H_C} + \underbrace{\frac{i\hbar e}{4m^2c^2} (\nabla\phi \cdot \mathbf{p})}_{H_{\text{Darwin}}} + H_{\text{SO}} + H_Z, \quad (2.30)$$

where T is the non-relativistic kinetic energy, T_{rel} is the first relativistic correction to the kinetic energy, H_C is just the coulomb central potential and H_{Darwin} is the so called Darwin term, which is a purely relativistic correction to the electronic motion (also known as zitterbewegung[Hes90]).

The additional H_{SO} term is a contribution that can be identified as spin-orbit coupling Hamiltonian [Nol09]

$$H_{\text{SO}} = \frac{-e}{2m^2c^2} \left[\underbrace{(\nabla\phi \times \mathbf{p})}_{\propto \mathbf{r} \times \mathbf{p}} \cdot \mathbf{s} \right] := \lambda (\mathbf{l} \cdot \mathbf{s}). \quad (2.31)$$

The cross product $\nabla\phi \times \mathbf{p}$ clearly has the structure of an orbital momentum $\mathbf{r} \times \mathbf{p}$. Thus the spin orbit Hamiltonian can be expressed as a direct $\mathbf{l} \cdot \mathbf{s}$ coupling with an effective spin orbit coupling parameter λ . For a single nucleus with Z^* protons λ is simply given by [Nol09]:

$$\lambda = \frac{1}{8\pi\epsilon_0 m^2 c^2} \frac{Z^* e^2}{r^3}. \quad (2.32)$$

The same correct result for H_{SO} can be equivalently obtained by a pictorial view of the effective field \mathbf{B}_{eff} caused by the moving ion in the rest frame of the electron (see figure 2.4 a). Accordingly, this effective field experienced by the electron can be written as

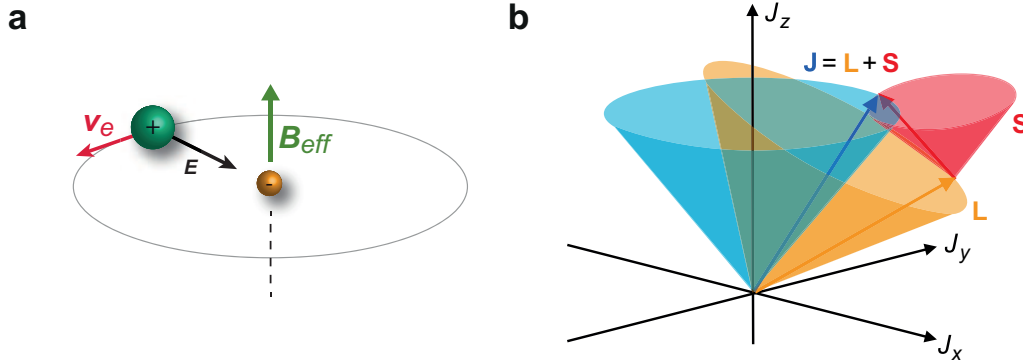


Figure 2.4.: Spin-orbit coupling. **a**, Pictorial classical view of SOC. In the restframe of the orbiting electron, the positively charged nucleus induces an effective magnetic field $\mathbf{B}_{\text{eff}} \propto \mathbf{v} \times \mathbf{E}$ due to Faraday’s law of induction, which then interacts with the electron spin. **b**, In the presence of strong SOC the total angular momentum $\mathbf{J} = \mathbf{L} + \mathbf{S}$ is a conserved observable and m_l and m_s are no good quantum numbers anymore.

$\mathbf{B}_{\text{eff}} = -\frac{1}{c^2} \mathbf{v} \times \mathbf{E}$, if $v \ll c$. By accounting for the quantum mechanically correct correspondence principle this leads to the expression 2.31 [Nol09].

Further, because orbital momentum \mathbf{l} and spin \mathbf{s} do no longer commute with the Hamiltonian in presence of SOC, m_l and m_s are no good quantum numbers anymore. On the other hand, the total angular momentum $\mathbf{j} = \mathbf{l} + \mathbf{s}$ (depicted in figure 2.4 b) is a conserved observable [Nol09] and therefore a new set of quantum numbers is necessary in order to describe a single particle system in the presence of SOC:

$$|l, s, m_l, m_s\rangle \longrightarrow |j, m_j, l, s\rangle. \quad (2.33)$$

Coming back to the Pauli-Hamiltonian (equation 2.30), if an external magnetic field \mathbf{B}_0 is applied, a further contribution proportional to the magnetic field appears. For weak external fields $\mu_B B_0 \ll \lambda_{\text{SOC}}$, that means SOC is not lifted by the external field \mathbf{B}_0 , Zeeman term H_Z can be easily added to the Pauli Hamiltonian:

$$H_Z = -\frac{\mu_B}{\hbar} (\mathbf{l} + 2\mathbf{s}) \cdot \mathbf{B}_0 \quad (2.34)$$

Further corrections stemming from nuclear effects, e.g. like the nuclear quadrupolefield can be added as well. Taking into account the nuclear spin, leads to three more hyperfine interactions: orbital-, dipolar- and contact- hyperfine interaction [Nol09].

2.3.4 Exchange coupling & Heisenberg model

In order to describe magnetic order of condensed matter adequately, the description of many particle effects including the quantum mechanical character of their wavefunctions is required. Therefore the starting point of this section is the transition from the single particle Hamiltonian of the previous sections to the direct interaction of two spin- $\frac{1}{2}$ particles (electrons).

As a reminder of Pauli's principle: A wave function of a spin- $\frac{1}{2}$ particle is always anti-symmetric with respect to particle exchange. Accordingly, a many body wavefunction of spin- $\frac{1}{2}$ particles has to be also constructed by fully antisymmetric wavefunctions.

First, a two electron system is considered neglecting their spin-spin magnetic dipole interaction. Thus the two particle wavefunction for a spin independent Hamiltonian can be written as a product state between a two-particle space part $|q\rangle$ and two-particle spin part $|S, m_s\rangle$:

$$|\psi\rangle^{(-)} = |q\rangle^{(\pm)} |S; m_s\rangle^{(\mp)} \quad (2.35)$$

Here the final wavefunction $|\psi^{(-)}\rangle$ has to be antisymmetric, which is indicated by the superscript "(-)". Obviously, the symmetry of the spin part determines the symmetry of the corresponding space part and vice versa. Consequently, the two possible wavefunctions build up a singlet $|\psi_1\rangle$ and triplet $|\psi_2\rangle$ state, respectively:

$$|\psi_1\rangle = |q\rangle^{(+)} (|\uparrow\downarrow\rangle - |\downarrow\uparrow\rangle) / \sqrt{2} \quad (2.36)$$

$$|\psi_2\rangle = |q\rangle^{(-)} \begin{cases} |\downarrow\downarrow\rangle \\ (|\uparrow\downarrow\rangle + |\downarrow\uparrow\rangle) / \sqrt{2} \\ |\uparrow\uparrow\rangle \end{cases} \quad (2.37)$$

Here the arrows depict the configurations for the spin part of $|\psi_1\rangle$ and $|\psi_2\rangle$ being $|0; 0\rangle$ and $|1; m_S\rangle$ with $m_S = (-1, 0, 1)$, respectively. So overall, the wavefunctions exhibit 4 eigensolutions, with two energy eigenvalues E_{\pm} of the spin independent Hamiltonian

$$H |q\rangle^{\pm} = E_{\pm} |q\rangle^{\pm} \quad (2.38)$$

If $E_+ \neq E_-$, it means that the degeneracy of the singlet and triplet state is lifted. Thus a certain spin ordering is energetically preferred, which reduces the electron-electron Coulomb interaction. That is equivalent to a spontaneous magnetic order.

Moreover, it should be possible to create an equivalent Hamiltonian \tilde{H} that only acts on the spin part of the wave function and that has the same energy eigenvalues E_{\pm} as H :

$$\tilde{H} |0; 0\rangle = E_+ |0; 0\rangle \quad (2.39)$$

$$\tilde{H} |1; m_S\rangle = E_- |1; m_S\rangle \quad (2.40)$$

It can be easily seen that these eigenequations are satisfied by the so called *molecular Heisenberg model* Hamiltonian [Nol09]:

$$\tilde{H} = J_0 - J_{12} \mathbf{S}_1 \cdot \mathbf{S}_2 \quad \text{with} \quad J_{12} = \frac{1}{\hbar^2} (E_+ - E_-), \quad (2.41)$$

leading to the important result: Even for spin independent Hamiltonians, Coulomb interaction and Pauli's principle lead to spin interactions and thus magnetic effects. This interaction between the spins stems from the symmetry of the wavefunction under particle exchange and is therefore called *exchange interaction*. The strength and sign of the exchange interaction is given by the exchange constant J_{12} . If $J_{12} > 0$, parallel spin alignment is energetically favored and thus leads to ferromagnetism. If $J_{12} < 0$, the antiparallel

spin ordering in the ground state is called antiferromagnetism.

It can be shown that this model Hamiltonian is even justified for two ions with one electron each [Nol09]. In this so called *Heitler-London Model* [Hei27] all Coulomb interactions between all four particles (2 cores, 2 electrons) are considered. It is assumed that the electrons are close enough so that the wavefunctions overlap, but not too close to avoid polar states (meaning that "every electron sticks to its dedicated core ion"). This model is therefore justified for insulators and leads also to an effective exchange Hamiltonian identical to equation 2.41.

Therefrom, it is postulated, that the Heitler-Lodon Hamiltonian for two single valence electron atoms can be generalized to N multi-electron atoms (*Heisenberg Model*):

$$H = - \sum_{i,j} J_{ij} \mathbf{S}_i \cdot \mathbf{S}_j \quad (2.42)$$

It is important to keep in mind that the coupling constant J_{ij} is only a parameter of the model and is thus strongly dependent on the assumptions (see assumptions above for the Heitler-London-Model) and boundary conditions (e.g. which wavefunctions are considered). Quantitatively, J_{ij} needs to be determined by ab-initio calculations or by experiments. Further the coupling can be also mediated by other diamagnetic ions (e.g. oxygen) like in MnO (Mn-O-Mn) or Yttrium Iron Garnet (Fe-O-Fe, see figure 5.2) [Nol09]. This indirect exchange coupling is called *super exchange*. The interpretation of the coupling constant J_{ij} is in this case obviously completely different, but still results in a Heisenberg-type Hamiltonian.

Complementary, the Heisenberg Hamiltonian can be also derived in first order perturbation theory of the electron-electron Coulomb interaction ($H = H_0 + H_1$) [Nol09]. With this approach J_{ij} can be calculated with the exchange matrix element $\langle \psi | H_1 P^{ij} | \psi \rangle$, where P^{ij} permutes the i th and j th electron.

In this work, the spin excitations of a ferrimagnet are investigated, which can be described as two separate magnetic sublattices coupled via super exchange. Therefore the most general Heisenberg Hamiltonian for a 2-sublattice magnetically ordered system has to account for intra-sublattice exchange (J_{ij} and $J_{\alpha\beta}$) and inter-sublattice exchange $J_{i\alpha}$

$$H = - \sum_n \left(\sum_{ij} J_{ij} \mathbf{S}_i \cdot \mathbf{S}_j + 2 \sum_{i\alpha} J_{i\alpha} \mathbf{S}_i \cdot \mathbf{S}_\alpha + \sum_{\alpha\beta} J_{\alpha\beta} \mathbf{S}_\alpha \cdot \mathbf{S}_\beta \right) \quad (2.43)$$

Here i, j and α, β only account for the spins within one unit cell and \sum_n sums over all unit cells.

2.3.5 Molecular field approximation of the Heisenberg model

One of the most important properties of an ordered spin system, is its temperature dependence, which can be found by a molecular field approximation (MFA) of the Heisenberg

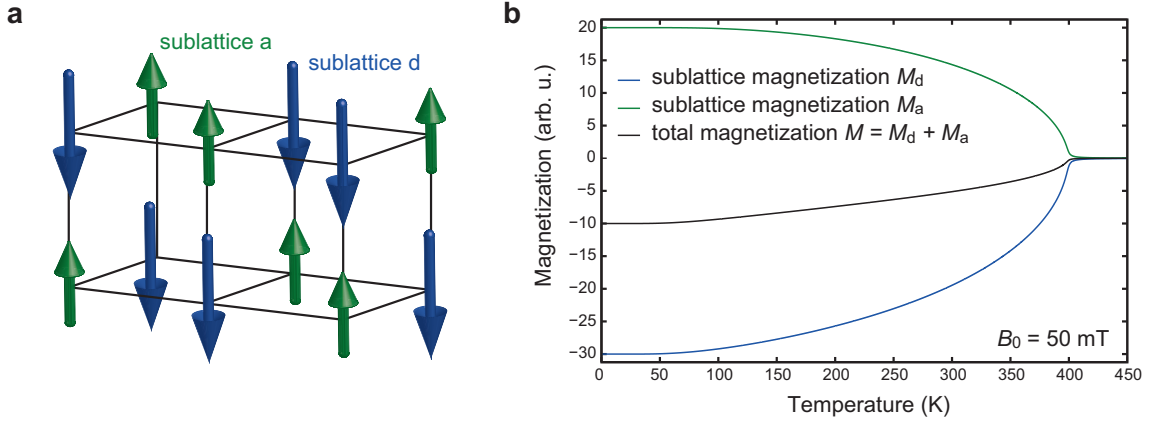


Figure 2.5.: Two sublattice ferrimagnet. **a**, Spin lattice model for two arbitrary spin species a and d , which are coupled antiferromagnetically. **b**, Numerical MFA calculations of temperature dependence of the 2-sublattice ferrimagnet Yttrium Iron Garnet with known coupling ratios [Dio09] and adjusted to experimentally observed $T_C \approx 398$ K.

Hamiltonian including Zeemann term [Nol09]. MFA means that the fluctuation of the mean values are neglected³. Therefore the impact of all other spins on one single spin can be described by an effective exchange field \mathbf{B}_e . Here, the model will be directly generalized to different spin species (e.g. stemming from different atoms or different lattice sites), which can be described by separate spin sublattices that couple to each other (see figure 2.5 a). In case of N coupled spin lattices, this finally leads to N coupled transcendental equations for the magnetizations $M_i(T, B_0)$ of the spin sublattices [Nol09]:

$$M_i(T, B_0) = M_0^{(i)} B_{S_i} \left(\beta S_i g_{J_i} \mu_B \left(B_0 + B_e^{(i)} \right) \right) \quad (i = 1, 2, \dots, N) \quad (2.44)$$

Here S_i , g_{J_i} and $M_0^{(i)}$ are spin per lattice site, electron spin g-factor and initial magnetization $M_i(T = 0 \text{ K})$ of the i th sublattice, respectively. The temperature is hidden in $\beta = 1/(k_B T)$ and B_0 is the external magnetic field. B_{S_i} is the Brillouin function with respect to S_i [Dar67]. All spins couplings are introduced by the exchange fields:

$$B_e^{(i)} = \mu_0 \sum_j \lambda_{ij} M_j, \quad (2.45)$$

where λ_{ij} is the $N \times N$ molecular field coupling matrix, which defines the intra- (diagonal elements) and inter- (off-diagonal elements) sublattice coupling strengths. The total magnetization is simply given by $M = \sum_i M_i$. For the work of this thesis, equilibrium solutions of equation 2.45, where found numerically⁴ for the prototype 2-sublattice ferrimagnet Yttrium Iron Garnet (YIG). The results based on realistic coupling constants λ_{ij} [Dio09] are shown in figure 2.5 b.

In the easiest case for $i = 1$, equation 2.45 yields a single spin lattice, equivalent to the phenomenological Weiss model [Kit66, Nol09], which shows a critical temperature T_C with

³molecular field approximation: $A \cdot B \approx A \langle B \rangle + \langle A \rangle B - \langle A \rangle \langle B \rangle$

⁴Numerically solved with MATLAB's `fsolve` algorithm.

ferromagnetic order for $T < T_C$ and paramagnetism for $T > T_C$ (see small tail in figure 2.5 b). The critical temperature (called Curie temperature for ferromagnets and Néel temperature for anti-ferromagnets) is defined such that $M(T > T_C, B_0 = 0) \equiv 0$ holds true. The critical temperature T_C is in general determined by the molecular field coupling constants λ_{ij} and can be derived in the $T \rightarrow T_C$ limit. For a two-sublattice ferrimagnet (like investigated in chapter 5) this leads to the critical temperature [Nol09, Dio09]

$$T_C = \frac{1}{2} (C_1 \lambda_{11} + C_2 \lambda_{22}) + \frac{1}{2} \sqrt{(C_1 \lambda_{11} - C_2 \lambda_{22})^2 + 4C_1 C_2 \lambda_{12}^2} \quad (2.46)$$

with

$$C_i = n_i \mu_0 g J_i \frac{S_i (S_i + 1)}{3k_B} \mu_B^2 \quad (i = 1, 2), \quad (2.47)$$

where n_i is the spin density of spin sublattice i .

2.3.6 Spin waves (magnons)

So far, only ground state properties of magnetically ordered materials without any excitations were considered. Now, the excitations of the Heisenberg ground state $|0\rangle$ shall be described. As shown in the previous sections, the Heisenberg model describes the magnetically ordered system as a periodic lattice of spins. Consequently, the concepts from lattice excitations (phonons) in section 2.2 can be borrowed here. Along these lines a Hamiltonian for spin excitations (magnons) will be derived by making use of an analogous harmonic approximation (section 2.2.1).

The ground state at temperature $T = 0$ K corresponds to the total alignment of all electron spins. In order to look at its perturbation, once again we make use of the lattice periodicity and thus transform all spin operators in reciprocal \mathbf{k} -space [Nol09]:

$$S^\alpha(\mathbf{k}) = \sum_i S_i^\alpha e^{-i\mathbf{k} \cdot \mathbf{R}_i} \quad (\text{with } \alpha = x, y, z, +, -) \quad (2.48)$$

The smallest perturbation of the collective spin order is the flip of one single spin. This corresponds to $S^-(\mathbf{k})|0\rangle$, which is again an eigenstate of the Heisenberg Hamiltonian H . The new state means a reduction of the total magnetic moment of the whole system by $gJ\mu_B$. Therefore the smallest excitation of the Heisenberg ground state can be seen as a spin deflection of angular momentum $1\hbar$, which is distributed collectively among all spins. This excitation is called a magnon and can be described as a quasiparticle with integer spin in the framework of second quantization.

The normalized one-magnon state can be written as:

$$|\mathbf{k}\rangle = \frac{1}{\hbar\sqrt{2SN}} S^-(\mathbf{k})|0\rangle, \quad (2.49)$$

which leads to eigenenergies of the one-magnon state in an external magnetic field B_0 [Nol09]:

$$E(\mathbf{k}) = E_0(B_0) + \underbrace{g_J\mu_B B_0 + 2S\hbar^2(J_0 - J(\mathbf{k}))}_{:=\hbar\omega(\mathbf{k})}, \quad (2.50)$$

with the ground state energy of the Heisenberg ferromagnet

$$E_0(B_0) = -N\hbar^2 J_0 S^2 - N g_J \mu_B B_0 S \quad (2.51)$$

where the last part is due to the external magnetic field B_0 .

In a general multi magnon state the excitations can be described by creation operators a_i^\dagger and annihilation operators a_i of magnons analogous to the quantization of phonons (see section 2.2.2). The therefore necessary transformations of the spin operators S^α are given by the Holstein-Primakoff transformation for $S \geq 1/2$ [Hol40, Nol09]:

$$\frac{1}{\hbar} S_i^z = S - \hat{n}_i \quad (2.52)$$

$$\frac{1}{\hbar} S_i^+ = \sqrt{2S} \phi(\hat{n}_i) a_i \quad (2.53)$$

$$\frac{1}{\hbar} S_i^- = \sqrt{2S} a_i^\dagger \phi(\hat{n}_i) \quad (2.54)$$

$$(2.55)$$

with the usual occupation number operator $\hat{n}_i = a_i^\dagger a_i$ and the Taylor expansion of $\phi(\hat{n}_i)$ for small magnon numbers \hat{n}_i :

$$\phi(\hat{n}_i) = \sqrt{1 - \frac{\hat{n}_i}{2S}} = 1 - \frac{\hat{n}_i}{4S} - \frac{\hat{n}_i^2}{32S^2} - \frac{\hat{n}_i^3}{128S^3} - \dots \quad (2.56)$$

In the following, this expansion shall be considered only up to the linear term in \hat{n}_i . Therefore, this corresponds to the *harmonic approximation* or so called *linear spin wave approximation*. The annihilation and creation operators in the reciprocal space [Nol05, Nol09]

$$a_{\mathbf{q}} = \frac{1}{\sqrt{N}} \sum_i e^{-i\mathbf{q}\cdot\mathbf{R}_i} a_i \quad (2.57)$$

$$a_{\mathbf{q}}^\dagger = \frac{1}{\sqrt{N}} \sum_i e^{i\mathbf{q}\cdot\mathbf{R}_i} a_i^\dagger \quad (2.58)$$

fulfill the fundamental commutation relations for Bose operators⁵. Accordingly, the spin dependent Hamiltonian for a Heisenberg ferromagnet can be written in the linear spin wave approximation as a sum over all magnon occupation numbers:

$$H_{\text{SW}} = E_0(B_0) + \sum_{\mathbf{q}} \hbar\omega_{\mathbf{q}} \underbrace{a_{\mathbf{q}}^\dagger a_{\mathbf{q}}}_{\hat{n}_{\mathbf{q}}}. \quad (2.59)$$

⁵ $[a_{\mathbf{q}}, a_{\mathbf{q}'}^\dagger]_- = \delta_{\mathbf{q}\mathbf{q}'} ; [a_{\mathbf{q}}, a_{\mathbf{q}'}]_- = [a_{\mathbf{q}}^\dagger, a_{\mathbf{q}'}^\dagger]_- = 0$

Here the spin wave dispersion relation is given by

$$\hbar\omega_{\mathbf{q}} = 2S\hbar^2 (J_0 - J(\mathbf{q})) \quad \text{with} \quad J(\mathbf{q}) = \frac{1}{N} \sum_{i,j} J_{ij} e^{i\mathbf{q}\cdot(\mathbf{R}_i - \mathbf{R}_j)} \quad (2.60)$$

Noticeably, this corresponds to only one branch of the magnon dispersion. As soon as there are N distinct spins per spin lattice cell, this will lead to N branches $\hbar\omega_r(\mathbf{q})$ with branch index r .

In full analogy to the description of phonons, H_{SW} is obviously a sum of uncoupled harmonic oscillators and therefore the eigenstates of the spin ordered system can be therefore built up by a product of one-magnon-states:

$$|\psi\rangle = \prod_{\mathbf{q}} \left(a_{\mathbf{q}}^\dagger \right)^{n_{\mathbf{q}}} |0\rangle, \quad (2.61)$$

with $n_{\mathbf{q}}$ being the eigenvalues of $\hat{n}_{\mathbf{q}} = a_{\mathbf{q}}^\dagger a_{\mathbf{q}}$.

By using the grand canonical partition function (chemical potential $\mu = 0$ for magnons), it can be confirmed that magnons also obey the Bose-Einstein-statistic and the magnetization of the excited spin system can be calculated [Nol09]:

$$M(T, B_0) = g_J \mu_B S \frac{N}{V} \left(1 - \frac{1}{NS} \sum_{\mathbf{q}} \langle \hat{n}_{\mathbf{q}} \rangle \right). \quad (2.62)$$

This confirms that the saturation magnetization $M_0 = g_J \mu_B SN/V$ is decreased with every magnon by $g_J \mu_B/V$. So in conclusion a reduction of the magnetization ΔM in an ordered spin system corresponds to the emission of magnons.

The magnon formalism becomes more sophisticated once there is more than one spin sublattice involved. See for example appendix A.1 for the harmonic approximation of an antiferromagnet. Note also that in the general case of a ferrimagnet, where two opposite sublattice magnetizations have different magnitudes, two distinctive species of magnons exist. The magnons of the dominating sublattice, called *ferromagnons*, reduce the total magnetization. Whereas the magnons of the opposite sublattice (with smaller magnetization) increase the total magnetization and are thus called *antiferromagnons*. Nevertheless, the main formalism of this section is still applicable, even in the case of 20 magnon branches in a two-sublattice ferrimagnet, as it is the case for Yttrium iron garnet investigated in chapter 5.

3 Light-matter interaction

So far, the unperturbed Hamiltonian H_0 of an arbitrary solid state material system has been discussed by separating its three subsystems and their interactions: the lattice system (section 2.2), spin system (section 2.3) and the electron orbital degrees of freedom (see figure 2.1). Here, in order to investigate or even control the state of matter on ultrafast time scales, the interaction with short laser pulses will be introduced. Therefore, it is necessary to add light-matter interaction to the previous model considerations.

The most important assumption in this case is that the light matter interaction is only a weak perturbation by the light field. Thus perturbation theory delivers the appropriate ansatz:

$$H = H_0 + \lambda \hat{V}(t). \quad (3.1)$$

Here $\hat{V}(t)$ can be any interaction Hamiltonian and λ is the perturbation parameter, which characterizes the strength of interaction. If $\lambda \hat{V}(t)$ is sufficiently small, the eigenstates of the perturbed system can be expanded with respect to λ :

$$|\psi\rangle = |\psi\rangle^{(0)} + \lambda |\psi\rangle^{(1)} + \lambda^2 |\psi\rangle^{(2)} + \dots + \lambda^N |\psi\rangle^{(N)} + \dots \quad (3.2)$$

Here, every $|\psi\rangle^{(N)}$ has to be part of a solution of Schrödinger's equation with interaction energy \hat{V} on the order of N . Plugging this ansatz into the Schrödinger equation leads to a set of Schrödinger equations, which can be solved iteratively [Boy08]:

$$i\hbar \frac{\partial}{\partial t} |\psi\rangle^{(0)} = H_0 |\psi\rangle^{(0)} \quad (3.3)$$

$$i\hbar \frac{\partial}{\partial t} |\psi\rangle^{(N)} = H_0 |\psi\rangle^{(N)} + \hat{V} |\psi\rangle^{(N-1)}. \quad (3.4)$$

In the following, we specify the interaction Hamiltonians $\hat{V}(t)$ which describe the primary coupling between the subsystems and the electric and magnetic light field component.

In the case of the interaction of an electromagnetic wave with electrons or polar ions, the interaction Hamiltonian $\hat{V}(t)$ is commonly approximated by an electric-dipole interaction term:

$$\hat{V}(t) = - \sum_j \hat{\boldsymbol{\mu}}_j \cdot \mathbf{E}(t). \quad (3.5)$$

Here, $\hat{\boldsymbol{\mu}}_j$ is the electric dipole operator, neglecting magnetic dipoles or electric multipoles [Boy08, Ash05]. The summation over j takes all electric dipole moments into account, e.g. ionic dipole moments or the electron dipole moments.

On the other hand, in the case of interaction of a light field with the spin degrees of freedom, direct coupling is only possible via a torque of the magnetic-field component of

the electromagnetic wave (Zeeman coupling) [Sto07, Kam11]:

$$\hat{V}(t) = - \sum_j \mathbf{m}_j \cdot \mathbf{B}(t) = -\gamma \sum_j \mathbf{S}_j \cdot \mathbf{B}(t) \quad (3.6)$$

Here, the summation runs over all spins j . By neglecting nuclear spins and orbital momentum contributions, the electron-spin magnetic moments can be directly expressed by the product of the gyromagnetic ratio γ and electron spin \mathbf{S}_j .

The two independent cases of equation 3.5 and 3.6 suggest that light can be used to directly and possibly selectively drive certain degrees of freedom (electron orbit, lattice and spins). In addition to this primary interaction, other degrees of freedom become excited through subsequent (secondary) interaction processes between the subsystems. These indirect couplings make use of the internal interactions of the equilibrium Hamiltonian H_0 , i.e. spin-lattice coupling, electron-lattice coupling or electron-spin coupling (recall figure 2.1). A further assumption that is made, originates from the focus of this thesis on driving matter by lattice degree of freedoms: The theoretic description in the following sections is mostly restricted to insulators or large band gap semiconductors (i.e. "transparent" media) to exclude resonant effects of the electronic system.

These considerations lead to three sorts of light-matter interactions relevant for the scope of this thesis:

- **Non-resonant interaction with electrons (section 3.1)**

When using ultrashort strong laser pulses, non-resonant interaction with electronic degrees of freedom can still lead to a response, e.g. effects of nonlinear optics. A sufficient theoretical background for basic non-linear optics will be therefore introduced in section 3.1. This introduction is also helpful for the understanding of the main experimental methods within this thesis (chapter 4).

- **Interaction with phonons (section 3.2)**

The interaction of short laser pulses with phonons can be either resonant, meaning that the spectrum of the excitation pulse contains the eigenfrequencies of IR-active phonon modes, or non-resonant. The resonant excitation is directly coupled by the dipole moments of polar lattice modes. The non-resonant excitation of coherent phonons can be performed (indirectly) by Raman-excitation. This involves the electronic degrees of freedom by means of second order nonlinear optics and therefore the interaction of two electromagnetic waves. Here we mainly focus on the excitation mechanisms of coherent phonons.

- **Interaction with electron spins (section 3.3)**

The coupling mechanism for gaining control of the spin degrees of freedom can be either direct or indirect via orbital or lattice degrees of freedom. Like shown in figure 2.1, the three dominating coupling mechanism are Zeeman coupling (direct), Spin-orbit coupling (indirect) and exchange coupling (indirect).

For the description of the interaction with phonons and spins, we will ascend in complexity starting from a one-wave interaction going to a two-wave interaction of the light field.

3.1 Non-resonant interaction with electrons

3.1.1 (Semi-)classical framework

Despite the diversity of the interactions of light with matter summarized in the beginning of chapter 3, a semi-classical description of light-matter interaction is sufficient [GG10, Lou00] to interpret the results of this work. That means that light is treated as a classical electromagnetic wave with quantized energy $\hbar\omega$ in the photon picture. Whereas, the second quantization of the light field [Nol05, Lou00] is not necessary. Further, for the description of matter a relativistic and quantum mechanical description is required in order to include spin effects in general, such as e.g. exchange interaction or spin-orbit coupling (like explained in section 2.3). In this picture, the interaction of light with matter is fully described by the macroscopic Maxwell equations and the corresponding material equations (see appendix A.3.1). For the work of this thesis, it is sufficient to restrict the following 2 sections to light-electron interactions that do not require transitions between electronic states. These non-resonant interactions mostly lead to nonlinear optics.

3.1.2 Nonlinear polarization

The macroscopic effect of the electric field $\mathbf{E}(t)$ of an electromagnetic wave on a solid state material, can be expressed by a response function. The dielectric polarization $\mathbf{P}(t)$ describes the macroscopic response of the electric dipole moment per unit volume to an applied electric field $\mathbf{E}(t)$. Since the first demonstration of the laser [Mai60] in the year 1960 and the only one year later demonstrated second harmonic generation (SHG) in quartz [Fra61], it is known that the polarization $\mathbf{P}(t)$ can depend nonlinearly on the incident electric field $\mathbf{E}(t)$ for high intensities $I(t) = n\epsilon_0 c |\mathbf{E}(t)|^2 / 2$.

Therefore, within the perturbative regime, it is common to describe the induced polarization as an expansion in the electric field $\mathbf{E}(t)$:

$$\mathbf{P}(t) = \epsilon_0 \sum_{i=1}^{\infty} \chi^{(i)} \mathbf{E}^i(t) \quad (3.7)$$

The proportionality constants $\chi^{(i)}$ are called electric susceptibilities and are tensors of rank $(i + 1)$. The tensor elements of the susceptibilities are given by the structural symmetry properties of the specific material. For example, for inversion symmetric crystals all susceptibilities with even order (i.e. even i) are vanishing, because under space inversion ($\mathbf{E} \rightarrow -\mathbf{E}$) the polarization \mathbf{P} has to transform likewise to $-\mathbf{P}$. A good introduction to group theory and its influence on the nonlinear properties is given in [Yu05] and [Boy08], respectively.

All nonlinear effects of visible, NIR and THz pulses utilized and explored within this work can be conveniently described by nonlinear processes up to third order. Thus, the

following expansion of the nonlinear polarization is sufficient:

$$P_j = \epsilon_0 \left(\sum_{k=1}^3 \chi_{jk}^{(1)} E_k + \sum_{k,l=1}^3 \chi_{jkl}^{(2)} E_k E_l + \sum_{k,l,m=1}^3 \chi_{jklm}^{(3)} E_k E_l E_m \right). \quad (3.8)$$

These components of the nonlinear polarization act as a source term for light waves with additional frequency components according to the wave equation of optics, given in appendix A.3.2.

3.1.3 Second order nonlinear processes (2-wave interaction)

In the following, parametric processes that stem from interaction of electronic degrees of freedom with a non-resonant short laser pulse are considered. The incident electric field of a light pulse, containing field contributions with angular frequencies ω_j , is given by:

$$\mathbf{E}(t) = \sum_j \mathbf{A}_j e^{-i\omega_j t} + \mathbf{A}_j^* e^{i\omega_j t} \quad (3.9)$$

These electric field components have to be plugged into the second order nonlinear polarization $\mathbf{P}^{(2)}$, given in frequency domain by [Boy08]:

$$P_i^{(2)}(\omega) = \sum_{j,k=1}^3 \int_{-\infty}^{\infty} d\omega_1 \int_{-\infty}^{\infty} d\omega_2 \chi_{ijk}^{(2)}(\omega, \omega_1, \omega_2) E_j(\omega_1) E_k(\omega_2) \quad (3.10)$$

Here, the integrations has to be performed to include all components (ω_1, ω_2) in a broadband laser pulse. Also negative frequencies are introduced, such that $E_i(-\omega) = E_i^*(\omega)$. It can be directly seen, that the product of two electric fields oscillating with ω_1 and ω_2 (according to equation 3.9) produce polarizations $\mathbf{P}(\omega)$ with the following frequencies:

$$\begin{array}{ll} \omega = \omega_1 - \omega_2 & \text{difference frequency generation (DFG)} \\ \omega = \omega_1 + \omega_2 & \text{sum frequency generation (SFG)} \\ \omega = 2\omega_{1,2} & \text{second harmonic generation (SHG)} \\ \omega = \omega_{1,2} - \omega_{1,2} = 0 & \text{optical rectification (OR)} \end{array}$$

In the photon picture (see figure 3.1), these components can be seen as 3 photon mixing processes, where the initial and final electronic state is the same state (parametric process). The intermediate state is a virtual state, but could be also close to a real state in the resonant case [Boy08]. Which one of the processes dominates the nonlinear frequency conversion is given by the tensor elements and their frequency dependence of the $\chi^{(2)}$ tensor. An efficient energy conversion can only be obtained by the right phase matching conditions for the respective process. A description of light propagation and phase matching is given in the appendix A.3.

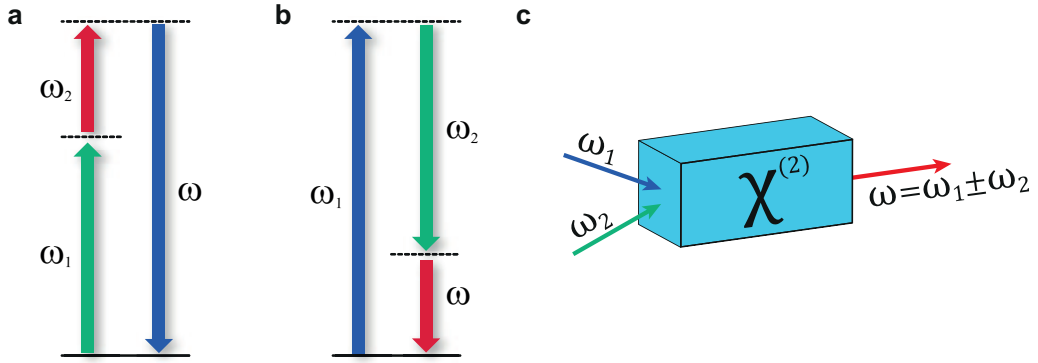


Figure 3.1.: Second order nonlinear processes. **a**, Sum frequency generation ($\omega = \omega_1 + \omega_2$) and **b**, difference frequency generation ($\omega = \omega_1 - \omega_2$). In this energy schemes photon energies are depicted as arrows and virtual electronic states indicated by broken lines. **c**, In a photonic medium with non-vanishing second order susceptibility $\chi^{(2)}$, the type of nonlinear interaction is selected by by adjusting the phase matching conditions that account for wavevector conservation (see appendix A.3.3).

3.2 Lattice control (coherent phonons)

In contrast to the non-resonant interaction with electronic degrees of freedom in nonlinear optics, in this section, the coupling of light to phonon resonances is introduced. This coupling can be either direct via the electric dipole moment of certain phonon modes or indirect via nonlinear optics (non-parametric processes). This discussion is restricted to the interaction with coherent phonons in order to give the theory background for non-equilibrium effects driven by phonons (see results in chapter 6 and 5).

For the sake of simplicity and in order to model the results of chapter 6, a phenomenological model is developed to describe the essential interactions of light with coherent phonons. Therefore, the normal coordinate of a phonon mode is treated as a classical amplitude $Q(t)$ (see section 2.2.3). In the following, light-matter interaction is introduced in the electric dipole approximation (equation 3.1).

The classical Lagrangian for a single normal coordinate Q is given by the difference of kinetic Energy T and generalized potential energy U [Nol10a]. The additional potential energy V , originating from light matter coupling, is given by the electric dipole moments μ_j in the electric field $E(t)$ (equation 3.5). In the electric dipole approximation (neglecting magnetic dipoles and electric multipoles), the summation over all microscopic dipole moments μ_j equals the macroscopic polarization $P(Q, E)$ [She84]. Here, the macroscopic polarization $P(Q, E)$ is also depended on the phonon normal coordinate Q , because the ionic dipole moment μ_{ion} changes when the lattice distances are modulated by coherent phonons. Accordingly these considerations lead to the scalar Lagrangian:

$$L = T - U = \frac{1}{2}m\dot{Q}^2 - (V_{\text{eq}}(Q) - P(Q, E) \cdot E(t)). \quad (3.11)$$

Here V_{eq} can be any equilibrium potential. For the further discussion of the results within this thesis, it is sufficient to consider a potential of a (damped) harmonic oscillator. As the external electric field E is assumed to be only a small perturbation, the Polarization $P(Q, E)$ can be approximated by a Taylor expansion in E around $E = 0$:

$$P(Q, E) = P(Q, 0) + \frac{\partial P(Q, 0)}{\partial E} E + O(E^2) = P(Q, 0) + \epsilon_0 \chi(Q) E. \quad (3.12)$$

In the last step, the definition of the linear susceptibility $\chi = \chi^{(1)}$ from equation 3.7 has been used. Further, the Euler-Lagrange equation [Nol10a]

$$\frac{d}{dt} \left(\frac{\partial L}{\partial \dot{Q}} \right) = \frac{\partial L}{\partial Q} \quad (3.13)$$

delivers directly the equation of motion:

$$m\ddot{Q} = -\frac{\partial V_{\text{eq}}}{\partial Q} + \frac{\partial P(Q, 0)}{\partial Q} E + \epsilon_0 \frac{\partial \chi(Q)}{\partial Q} E^2. \quad (3.14)$$

Here, both Q and E are functions of time t . The first term $-\frac{\partial V_{\text{eq}}}{\partial Q}$ is nothing else but the restoring force of the harmonic oscillator, whereas the two other terms depending on E are obviously the external driving forces of the oscillator. Thereupon, the equation of motion 2.17 is reproduced and can be extended under the assumptions of weak perturbation, while neglecting nonlinear effects higher than second order in field E :

$$\frac{\partial^2 Q(t)}{\partial t^2} + 2\gamma \frac{\partial Q(t)}{\partial t} + \omega_r^2 Q(t) = \frac{1}{m^*} \left(\frac{\partial P(Q, 0)}{\partial Q} E(t) + \epsilon_0 \frac{\partial \chi^{(1)}(Q)}{\partial Q} (E(t))^2 \right). \quad (3.15)$$

This simple equation already contains the two principal interactions of an electric field with a specific phonon mode. The first term on the right hand side corresponds to the direct coupling to IR-active modes. The second term describes the nonlinear coupling of the electric field via a Raman-process. In inversion-symmetric materials, the mutual exclusion principle holds true, meaning that the coupling can be either by one or the other type, but not both at the same time (see chapter 2.2). Therefore, these two mechanisms will be discussed separately in the following two sections.

3.2.1 Direct phonon driving (1-wave interaction)

The first term on the right hand side of the equation of motion 3.15 is proportional to the gradient of the polarization \mathbf{P} along the normal coordinate direction Q (corresponding to an effective charge density). For a single ion elongated along the normal coordinate $R = R_0 + Q$, this reproduces the Coulomb force:

$$F(t) = \frac{\partial \mu_{\text{ion}}(Q, 0)}{\partial Q} E(t) = \frac{q_c \partial (R_0 + Q)}{\partial Q} E(t) = q_c E(t). \quad (3.16)$$

This force is nonzero only if the unit cell exhibits a change of the macroscopic polarization P upon ion movements "along" ¹ the normal coordinate Q , meaning $\partial P/\partial Q \neq 0$.

This direct coupling by strong resonant fields, only recently became possible due to advanced high field THz sources [Rei03, Heb08, Sel08a, Jun10, Hub15, Car02], like the one developed within the work of this thesis (see chapter 4). The high field CEP-stable THz pulses allow for a phase resolved detection of coherent dynamics caused by the light field (magnetic or electric field). Thus, it is possible to directly observe excited coherent phonons by standard time-domain methods (see schematic in figure 3.3 a).

The advantage of direct excitation, is that the strong THz fields can resonantly excite large amplitudes of IR-active phonons without the excitation of further parasitic effects caused by excess energy that is dumped into the electronic system. Thereupon, the direct excitation of IR-active phonons enables the systematic study of non-equilibrium lattice states and their effect on other degrees of freedom, such as electron spins.

3.2.2 Raman-coupling (2-wave interaction)

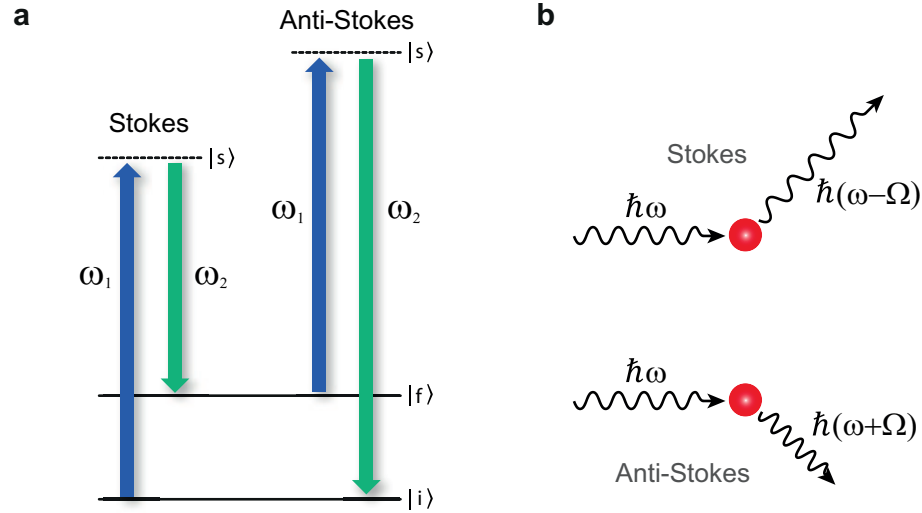


Figure 3.2.: Raman scattering. **a**, Stokes and anti-Stokes Raman scattering in the photon picture. The resonance (e.g. phonon, magnon, etc.) is described by a ground state $|i\rangle$ and an excited state $|f\rangle$ (solid lines). Virtual intermediate states $|s\rangle$ are indicated by broken lines. If light of both frequencies ω_1 and ω_2 are incident, the Raman scattering process is stimulated and thus occurs with higher probability. **b**, Classical picture of spontaneous Raman scattering. The light wave $\hbar\omega$ either loses or gains energy upon scattering while absorbing or emitting a excitations respectively.

Coming back to the equation of motion 3.15, the second term on the right hand side describes a driving force that is proportional to the product of two electric fields $\mathbf{E}_i(\omega_i)$ (depicted as blue and green arrow in figure 3.2 a). The tensor $\frac{\partial \chi_{jk}}{\partial Q}$ is a Raman-tensor,

¹Reminder: Q is a collective motion of ions that diagonalizes the force matrix of the coupled harmonic oscillators (see section 2.2.1)

which gives the strength of this so called Raman interaction when applying a field $E_j E_k^*$ [Mer97]. Depending on the absorption and lifetime of the excited states, different excitation forces $\mathbf{F}(t)$ have to be distinguished (see figure 3.2 a, b). In the model equation 3.15, where no electronic excitation was assumed, the temporal response function of the material is immediate ($\delta(t)$ -function). This corresponds to the limiting case of *impulsive stimulated Raman scattering* (ISRS), which is adequate for transparent media.

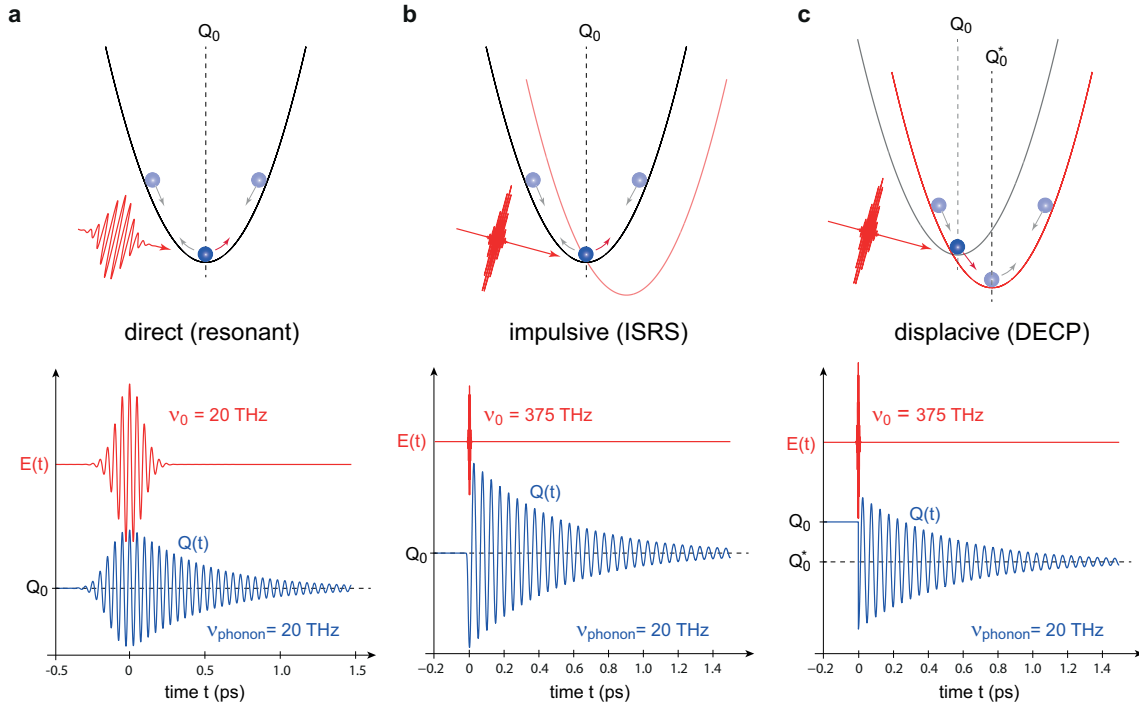


Figure 3.3.: Excitation mechanisms for coherent phonons. **a**, Direct (resonant) excitation. The coherent phonon excitation can be described as a resonantly driven harmonic oscillator. Here, the electric field $E(t)$ directly couples to the dipole moment $\partial P/\partial Q(t)$ along the phonon coordinate Q . The lower panel shows a simulation of a damped harmonic oscillator with resonance frequency $\nu_{\text{phonon}} = 20$ THz (blue line) driven by an electric field $E(t)$ (red line) similar to the experimental conditions. **b**, Impulsive stimulated Raman scattering. If a non-resonant light pulse is shorter than an oscillation period it disturbs the phonon potential for a very short time leading to an impulsive start of a coherent phonon oscillation. Lower panel: Simulation with parameters identical to **a**, except for the visible driving field (red line) **c**, Displacive excitation. The excitation of real electronic states can lead to a shift in the potential energy surface. Thereby the equilibrium position Q_0 shifts to Q_0^* , which is revealed in a baseline shift in the coherent phonon signal (broken line) in the lower panel. All other simulation parameters are identical to **b**.

Impulsive stimulated Raman scattering (ISRS)

Like assumed from the beginning of this chapter, when there is no electronic resonance, the intermediate state for stimulated Raman excitation can only be a very short-lived virtual electronic state (broken lines in figure 3.2 a). If additionally both photons $\hbar\omega_1$ and $\hbar\omega_2$ are contained in the same short laser pulse, the force

$$F(t) \propto |E(t)|^2 \quad (3.17)$$

acts instantaneously [Gar96, Mer97]. In this case it is called impulsive force and leads to an oscillation $Q(t) \propto \sin(\omega_r t)$ [Mer97]. The classic analog corresponds to a pendulum that is pushed out of its equilibrium by an infinitesimal short but strong force (see figure 3.3 b).

As a model system, the F_{2g} -mode ($\hbar\omega_r(q=0) = 165$ meV) in diamond has been the work horse for many Raman-studies since several decades [Ram56, Lou64, Sol70, Ish06].

In the case of pump-absorbing media (e.g. close to or above-band-gap excitations), the dielectric tensor $\chi(Q)$ is not frequency independent anymore. That leads to a more complex temporal response of $\frac{\partial\chi^{(1)}(Q)}{\partial Q}$. If temporal response can be considered as a step function, this corresponds to the other limiting case called displacive excitation of coherent phonons (DECP).

Displacive excitation of coherent phonons (DECP)

If the spectrum of the pump pulse permits electronic transitions (in "opaque materials"), the efficiency of the coherent phonon generation by ISRS can be even enhanced [Zei92, Zij06]. Additionally, a further coherent phonon excitation mechanism can play a role. For materials with strong electron-phonon coupling (see section A.2), the equilibrium position Q_0 of a normal mode can change upon the excitation of a long-lived electronic state. With the abrupt change of the equilibrium position ($Q_0 \rightarrow Q'_0$), a coherent phonon is launched. This mechanism was first introduced by Zeiger et. al [Che91, Zei92] and is known as *displacive excitation of coherent phonons* (DECP). Its classic analog is a pendulum which's mounting point is moved abruptly (see figure 3.3 c).

Accordingly, the characteristic signal of a coherent phonon excited by DECP exhibits a steps function after the electronic excitation (see figure 3.3 c). The force for DECP can be also semiclassically derived as [Ste02]:

$$F(t) \propto \int_{-\infty}^t (E(\tau))^2 d\tau. \quad (3.18)$$

This leads to a phonon motion $Q \propto [1 - \cos(\omega_r t)]$ [Mer97]. A typical example for DECP is the A_{1g} -mode of bismuth [Zij06]. Other mechanisms that involve the generation of electron-hole pairs can also generate coherent phonons for example by transient screening fields in the depletion layer close to a surface in gallium arsenide [Kuz94, Kuz95] or non-equilibrium Dember fields in tellurium [Dek95].

Generalization: quantum mechanical description

Quantum mechanically the Raman tensor is related to the transition matrix element M_R of the electron dipole operator $\hat{V} = -e\mathbf{r} \cdot \mathbf{E}$, where \mathbf{E} is the sum of complex electric fields $\mathbf{E}_i(\omega_i)$. The Raman excitation probability (per unit time per unit volume and per unit energy) is the given by [She84]:

$$\frac{8\pi^3 N \omega_1 \omega_2}{E_1 E_2} |\langle f | M | i \rangle|^2 \left| \langle \alpha_f | a_2^\dagger a_1 | \alpha_i \rangle \right|^2 g(\hbar\Delta\omega) \quad (3.19)$$

with

$$M_R = \sum_s \left[\frac{\mathbf{e}\mathbf{r} \cdot \hat{\mathbf{e}}_2 |s\rangle \langle s| \mathbf{e}\mathbf{r} \cdot \hat{\mathbf{e}}_1}{\hbar(\omega_1 - \omega_{si})} - \frac{\mathbf{e}\mathbf{r} \cdot \hat{\mathbf{e}}_1 |s\rangle \langle s| \mathbf{e}\mathbf{r} \cdot \hat{\mathbf{e}}_2}{\hbar(\omega_2 + \omega_{si})} \right]. \quad (3.20)$$

This probability factor contains all important processes of the lowest order Raman interaction (see figure 3.2):

The first term in M_R corresponds to the dipole transition from the unexcited state $|i\rangle$ to a virtual intermediate state $|s\rangle$ by absorption of a photon with energy $\hbar\omega_1$, followed by a dipole transition from $|s\rangle$ to the excited state $|f\rangle$ by emitting of a photon with energy $\hbar\omega_2$. This process requires $\omega_2 < \omega_1$ and is called Stokes transition. The second term in M_R describes the dipole transition from the excited state $|f\rangle$ to $|s\rangle$ and then the transition to $|i\rangle$. Here again the $\hbar\omega_1$ photon is absorbed and an $\hbar\omega_2$ photon is emitted, which requires $\omega_2 > \omega_1$. This second process is called anti-Stokes transition. $\hat{\mathbf{e}}_{1,2}$ is the unit vector of the electric field and thus corresponds to the two field polarizations of $\mathbf{E}(\omega_{1,2})$.

The second probability amplitude $|\langle \alpha_f | a_2^\dagger a_1 | \alpha_i \rangle|^2$ in equation 3.20 denotes the transition from light state $|\alpha_i\rangle$ to $|\alpha_f\rangle$ by annihilation of a $\hbar\omega_1$ photon and creation of a $\hbar\omega_2$ photon. This already requires the description of the field states by photon numbers $n_{1,2}$ (second quantization). Therefore we can write the transition probability:

$$|\langle \alpha_f | a_2^\dagger a_1 | \alpha_i \rangle|^2 = |\langle n_1 - 1, n_2 + 1 | a_2^\dagger a_1 | n_1, n_2 \rangle|^2 = n_1 (n_2 + 1). \quad (3.21)$$

This equation explains the higher probability for stimulated Raman emission ($n_2 \neq 0$) compared to spontaneous Raman scattering ($n_2 = 0$). The term Raman "scattering" stems from the classical description of the inelastic scattering of one photon with one phonon that accurately describes the spontaneous Raman emission (see figure 3.2 b).

The last factor in equation 3.20 $g(\hbar\Delta\omega)$ accounts for the lineshape of the joint density of states of the $|i\rangle \rightarrow |f\rangle$ transition.

3.2.3 Summary and open questions

In conclusion, in the last decades, the control of coherent phonons became feasible due to the broad availability of ultrashort pulsed visible and NIR lasers (Raman excitation schemes) [Che91, Zei92, Kuz95, Gar96, Dek00, Ish06]. Since very recently, the advent of high-field THz sources [Car02, Rei03, Heb08, Sel08a, Jun10, Hir11, Hub15, Gre16] provides access to direct phonon excitation. This excitation with strong THz fields offers the significant advantage of avoiding excess photon energy and thus prevents parasitic electronic excitations. Hence, the control of solid state phenomena via coherent phonons (such as phase transitions and phonon coupled properties) is state of the art of contemporary research [Foe11b, Rin07, Sub14, Gra16].

But, so far this promising THz excitation approaches are limited only to IR-active phonons. What happens if solely Raman-active phonons have to be controlled? Is it possible to also directly drive them with strong THz fields?

Furthermore, is it in general possible to excite phonons by a nonlinear process from below their fundamental resonance? If yes, what are the coherence and phase properties of such

a novel mechanism? These questions will be answered with the results of this work in chapter 6.

3.3 Spin control

In chapter 2.3, concepts for describing a magnetically ordered state and its excited states were introduced. Now, the question is addressed, how the spin state can be controlled or manipulated, especially on ultrafast time scales. This is a very important question not only for fundamental science but also for potential technological applications, such as ultrafast data storage devices, spin-transistors or quantum computing devices [Sch08, Ser10, Sta14, Vog14, Chu15].

Therefore, in this section, the focus lies on the parts of the Hamiltonian that can actually change the state of the spin order by means of specific coupling mechanisms to external perturbations. It is still assumed that magnetic dipole-dipole interaction and nuclear effects only play a negligible role. With these assumptions and the description of section 2.3, all spin couplings are summarized by the following Hamiltonian:

$$H = \underbrace{\sum_{i,j} J_{ij} \mathbf{S}_i \cdot \mathbf{S}_j}_{H_{\text{XC}}: \text{Exchange coupling}} + \lambda \underbrace{\sum_i \left(\frac{\mathbf{v}_i}{c^2} \times \mathbf{E}_i \right) \cdot \mathbf{S}_j}_{H_{\text{SOC}}: \text{Spin-orbit coupling}} - g_J \frac{\mu_B}{\hbar} \underbrace{\sum_i \mathbf{B}_0 \cdot \mathbf{S}_i}_{H_z: \text{Zeeman coupling}}. \quad (3.22)$$

This Hamiltonian arises from the Heisenberg Hamiltonian (section 2.3.4) by including relativistic effects from an electro-static potential (Spin-orbit coupling, eq. 2.31) and an external magnetic field \mathbf{B}_0 (Zeeman coupling). Here, the more pictorial expression for SOC is used, where the electric field \mathbf{E}_i of the ion belonging to the i th electron and the electron velocity \mathbf{v}_i explicitly shows up due to the effective magnetic field $\mathbf{B}_{\text{SOC}} = -\frac{1}{c^2} \mathbf{v}_i \times \mathbf{E}_i$ in the rest frame of the electron.

The three microscopic coupling mechanisms of equation 3.22 can be modulated by a variety of perturbations. In this work, we want to restrict ourselves to effects that can lead to an ultrafast response of the spin system. Thus ultrashort laser pulses are the adequate tools for such kind of perturbations.

In analogy to the phonon control in section 3.2, the most important and state of the art mechanisms for ultrafast spin control will be introduced in the following section. Therefore, it will be distinguished between direct (1-wave) and non-linear (2-wave) interaction scenarios. For each case, the contributions by the different types of coupling will be discussed and linked to excitations in the three subsets of condensed matter (Spin, lattice and electron orbital degrees of freedom) like shown in figure 2.1.

3.3.1 Primary coupling (1-wave interaction)

Magnetic field (Zeeman) coupling

The Zeeman term H_Z is the only interaction, that couples an external field \mathbf{B}_0 directly to the orientation of the spins without involving electron orbital degrees of freedom or transport phenomena (see equation 3.22). In general, a magnetic field exerts a torque on any magnetic moment \mathbf{m} in the material. Therefore, the precession of the macroscopic magnetic moment is usually phenomenologically described by the Landau-Lifshitz-Gilbert (LLG) equation [Sto07]:

$$\frac{\partial \mathbf{m}}{\partial t} = \gamma_g \mathbf{m} \times \mathbf{B}_j + \frac{\alpha}{|\mathbf{m}|} \mathbf{m} \times \frac{\partial \mathbf{m}}{\partial t} \quad (3.23)$$

Here γ_g is the gyromagnetic ratio [Sto07], α is a damping parameter and \mathbf{B}_j is an external magnetic field \mathbf{B}_0 or a phenomenological effective field \mathbf{B}_{eff} that can arise from inverse magneto-optic effects (see section 3.3.2). For most scientific cases, a linearization of this differential equation is sufficient and therefore the 1-wave interaction picture is justified.

Zeeman coupling is traditionally used in ferromagnetic resonance (FMR) experiments [Blo30, Pel03, Sto07]. In that case usually a strong static magnetic field \mathbf{B}_0 is applied together with an weaker AC microwave field $\mathbf{B}(\omega) \perp \mathbf{B}_0$. The static field \mathbf{B}_0 causes a macroscopic spin precession around the direction of \mathbf{B}_0 (see figure 3.4 a). The frequency of this precession is the Larmor frequency $\omega_L = \gamma_g B_0$ and thus proportional to the gyromagnetic ratio γ_g and static magnetic field. If the microwave field $\mathbf{B}(\omega)$ is in resonance with this spin precession, its absorption increases significantly. This method can be applied to investigate coherent magnons and their dephasing times [Bha74, Coc91, Urb01, Hum10, Kur11].

Recently it has been observed that the Zeeman torque is also applicable at THz frequen-

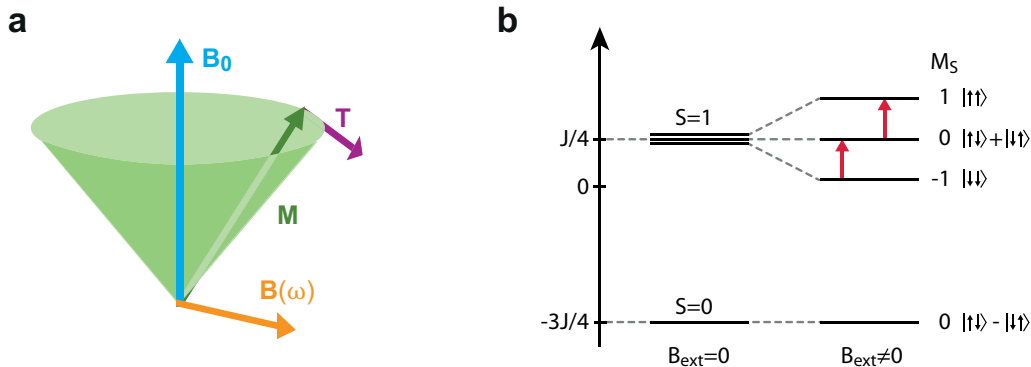


Figure 3.4.: Spin control. **a**, Typical precession of a magnetic moment \mathbf{M} in a static field \mathbf{B}_0 . Here $\mathbf{B}(\omega)$ can be any applied AC-field that applies a torque $\mathbf{T} = \mathbf{M} \times \mathbf{B}(\omega)$ on \mathbf{M} . The precession dynamics and their damping (α) are described by the phenomenological Landau-Lifshitz-Gilbert (LLG) equation. **b**, Change of the spin state via electronic transitions between exchange split states. In the example shown here, the degeneracy of the electronic p -state (total spin quantum number $S = 1$) is lifted by an external magnetic field.

cies: A strong THz pulse, that covers a magnon resonance frequency, can couple resonantly to this magnon with its magnetic field \mathbf{B}_{THz} . This coherent control of this spin wave was demonstrated by switching the precession of a zone center magnon ($\mathbf{q} = 0$) coherently on and off [Kam11].

Magnetoelectric coupling

In multiferroic materials an electric field \mathbf{E} can lead to a magnetization $M_i = \sum \alpha_{ij} E_j$ or vice versa, a magnetic field \mathbf{B} can lead to an electric polarization $P_i = \sum \alpha_{ij} B_j$ [Che07, VA07]. For the lowest order 1-wave interaction process (linear coupling), this requires broken inversion symmetry as \mathbf{P} and \mathbf{E} are odd functions of the space inversion operator, whereas \mathbf{M} and \mathbf{B} behave even under space inversion [Sto07, Che07].

For example spin-cycloid multiferroics, such as TbMnO_3 , fulfill this requirement and exhibit a strong magnetoelectric coupling. This leads to phenomena like the electromagnon, which corresponds to a spin excitation driven linearly by an THz electric field via magnetoelectric coupling [Kub14]. Here, spin interactions between canted spins on neighboring sites induce the ferroelectric polarization. Hence, the microscopic coupling can be either mediated by spin orbit torque or by modulations of the ferromagnetic exchange constant [Kub14].

3.3.2 Indirect coupling (2-wave interaction)

The description of light-spin coupling phenomena that scale with higher orders of the magnetic or electric field, becomes significantly more complex. Accordingly, mostly only phenomenological models are commonly applied to describe these interactions. Here, we will distinguish between transparent media, in which the excitation takes places far away from electronic resonances, and opaque media, where also electronic absorption effects produce further difficulties.

Transparent media

Equation 3.22 shows that spin-orbit coupling (SOC) can affect the spin state, when the electron orbit ($\rightarrow \mathbf{v}_i$) or the microscopic electric field (\mathbf{E}_i) is modified, e.g. by lattice motion. Therefore, SOC can mediate electron orbit-spin coupling as well as spin-lattice coupling, as depicted in figure 2.1, without necessarily exciting of electronic resonances.

Analogous to phonons (section 3.2.2), collective spin wave (magnons) can also be excited by a Raman process. For example, Kalashnikova and co-workers demonstrated the Raman excitation of coherent magnons in the weak ferromagnet FeBO_3 [Kal07, Kal08]. Also here one has to distinguish the limiting cases of excitation in transparent (far away from electron resonances) and absorbing media (close to electron resonances), which leads analogously to an impulsive (ISRS) and displacive (DECM, displacive excitation of coherent magnons) phenomenological description, respectively. The complex normal coordinate Q describes the precessional spin motion in this case [Gri08, Kal08].

Most importantly, the electric-dipole transition matrix elements, describing the Raman process are not able to directly act on the spin state (see section 3.2.2). Therefore, the microscopic mechanism to create coherent magnons in this way has to involve spin-orbit interactions in the excited state [Kal08].

By using the simple magnon Hamiltonian $H_{\text{mag}} = \Omega_0 Q(t)Q^*(t)$ (with FMR frequency Ω_0) and Raman interaction Hamiltonian $H_{\text{int}} \propto \chi_{ij} E_i(t)E_j^*(t)$ the general equation of motion can be found [Kal08]:

$$\frac{dQ}{dt} + i\Omega_0 Q = -i \frac{\partial H_{\text{int}}}{\partial Q^*} \quad (3.24)$$

Where the right hand side of the equation corresponds to the driving force $iF(t)$, which is either a delta function or a Heaviside step function in the limiting cases of ISRS or DECM, respectively [Gri08].

Phenomenologically, the action of the magnetic properties of a solid onto a light field are described as magneto-optic effects (see details in section 4.3.2). The most prominent example is the Faraday effect (see also section 4.3.2). Many works have demonstrated that the Raman excitations above can be also described as inverse magneto-optic effect [Per66, vdZ65], in the last 10 years even on ultrafast time scales [Kim05, Kim07, Han06b]. The electric field of circular polarized light \mathbf{E} acting on the magnetization, can be seen as an effective magnetic field \mathbf{B}_{eff} pointing along the wavevector of the light [Kir10]:

$$\frac{\partial H_{\text{int}}}{\partial Q} \propto \underbrace{\frac{\partial \chi_{ij}}{\partial Q} (\mathbf{E}(\omega) \times \mathbf{E}^*(\omega))}_{\mathbf{B}_{\text{eff}}} \times \mathbf{S}. \quad (3.25)$$

Thus, the effective field \mathbf{B}_{eff} scales with the magneto-optic constants and therefore the term "inverse magneto-optic effect" arises. A non-vanishing $\frac{\partial \chi_{ij}}{\partial Q}$ mainly originates from SOC, confirmed by the increased magneto-optic effects in materials containing heavy elements [Ebe96, Sug00]. As can be seen from equation 3.25, the direction of the effective magnetic field \mathbf{B}_{eff} can be conveniently switched by changing from right- to left-handed circularly polarized light [Pit61, vdZ65, Per66].

Non-linear Zeeman interaction is a further mechanism that does not rely on electronic absorption, but it requires strong magnetic field pulses. This can be already seen by the inherent nonlinearity of equation 3.23. For example, very recently nonlinear Zeeman coupling could be demonstrated in the THz-frequency range by making use of a novel 2D magnetic resonance spectroscopy scheme [Lu16]. Here, the underlying physics are likewise described based on the phenomenological LLG.

Coherent spin dynamics in absorbing media

In an absorbing medium, where secondary or indirect excitations can be related to SOC or exchange split states, the situation becomes more complex. Apparently SOC and exchange interaction can change, when laser induced electronic transitions play a role. Especially if the transition takes place within split states (transitions within the fine structure), the final

state will obviously have a different exchange or SOC energy. This can also lead to a change of magnetic anisotropy. The result is a precessional behavior of the magnetic moments [Kab91, Kir10]. Moreover, these coherent effects can be performed on an instantaneous time scale only limited by the rise time of the exciting laser pulse. Coherent dynamics in absorbing media also include the previously mentioned displacive Raman excitation of magnons (DECM) [Kal08].

Incoherent spin dynamics in absorbing media

The underlying microscopic mechanism of incoherent dynamics are even more complex, because they result from a real loss or even switching of magnetic order [Vat92, Koo00, Koo03, Kir10, Rad11, Fri15]. Since the pioneering work of Beaurepaire and co-workers [Bea96], the ultrafast demagnetization caused by absorption of a short laser pulse still rises a number of open research questions. For example, the extremely fast change of magnetic order in a single-magnetic lattice ferromagnet such as nickel, cannot be mediated by solely exchange interaction (see next section 3.3.3). A complex cascade of processes has to be considered, when the excess energy of an absorbed light pulse leads to hot charge carriers. The thermalization of such laser induced hot charge carriers via electron-lattice scattering, may also lead to modulations of the SOC or exchange interaction due to lattice excitations (phonons). In this thermalization case, the incoherent change of total magnetization $\Delta\mathbf{M}$ can be phenomenologically described by a change of temperature of the spin system ΔT_S (e.g. in the MFA of the Heisenberg model, equation 2.44):

$$\Delta\mathbf{M} = \mathbf{M}(T_0 + \Delta T_S) - \mathbf{M}(T_0), \quad (3.26)$$

with equilibrium temperature T_0 . To calculate the new spin temperature $T_0 + \Delta T_S$, at least a three temperature model has to be applied, that also includes electron-electron scattering (see next section 3.3.3 about exchange coupling). This three temperature model (3TM, e.g. by Koopmanns et al [Koo05, Bea96]) is only a phenomenological description. Nevertheless, the microscopic 3TM, where spin-flip scattering of electrons with phonons or impurities is due to SOC, is able to explain the variety of demagnetization time scales from $3d$ transition metals (e.g. Ni or Co) to $4f$ rare-earth Gd [Koo10]. But still, the microscopic mechanism and angular momentum transfer is yet not completely understood and under debate [Car08, Bat10, Car11b, Esc13, Esc14]. The timescales of these processes are given by the specific electron-electron, electron-phonon and electron-spin equilibration times. They can range from 50 fs in metals (e.g. in nickel thin films [Bea96, Koo05, Koo00, Hoh97]) up to nanoseconds in dielectrics [Kir10, Han06b].

The microscopic description becomes even more challenging, when more than one magnetic sublattice is involved, such as in antiferromagnets or ferrimagnets. In this case, exchange coupling can play an important role, because the angular momentum transfer between antiparallel sublattices is allowed [Kir13] (see next section 3.3.3). Within this thesis, an experimental approach was developed to simplify the complex cascade of processes. In the experiments in chapter 5, the role of the lattice-spin coupling is investigated isolatedly in a two-sublattice ferrimagnet, while keeping electronic orbital degrees of freedom frozen

out.

3.3.3 Properties of exchange coupling

Most obviously exchange coupling is governing exchange split electron bands and thus can require spin flips for certain transitions (see figure 3.4 b). Additionally, as exchange interactions arises from the bare coulomb interaction of electrons, it is also contributing to the spin properties of electron scattering processes. Accordingly, exchange interaction is accountable for a number of spin transport phenomena [Sti02, Ral08, Bat10, Mel11].

On the other hand, it is very important to realize that the pure exchange Hamiltonian H_{ex} (equation 3.22) commutes with the total spin operator $\sum_i \mathbf{S}_i$. Therefore the Ehrenfest theorem [Nol13] predicts that the temporal change of the total magnetization in a pure spin magnet $\mathbf{M} \propto \langle \sum_i \mathbf{S}_i \rangle$ vanishes:

$$\frac{d}{dt} \left\langle \sum_i \mathbf{S}_i \right\rangle = \frac{1}{i\hbar} \left\langle \left[H_{\text{XC}}, \sum_i \mathbf{S}_i \right]_- \right\rangle + \left\langle \frac{\partial \sum_i \mathbf{S}_i}{\partial t} \right\rangle = 0, \quad (3.27)$$

because $[H_{\text{XC}}, \sum_i \mathbf{S}_i]_- = 0$. This is a very fundamental finding, as it forbids exchange mediated demagnetization in pure spin magnets. Nevertheless, angular momenta can be exchanged between different sub-lattices as long as the total spin $\mathbf{S}_{\text{tot}} = \sum_i \mathbf{S}_i$ over all spins \mathbf{S}_i in all sub-lattices is conserved [Kir13].

Thereupon, an appealing scenario is the direct modulation of the exchange constant J_{ij} in equation 3.22. This can be achieved by a change of the overlap of the electron wavefunctions in the unit cell. Thus, in a magnetically ordered solid (e.g. ferromagnet, ferrimagnet or antiferromagnet), the exchange integral can be obviously modulated by phonons² [Nol09]. Nevertheless, this scenario allows for spin angular momentum transfer between different magnetic sublattices. This phonon induced modulation of the exchange coupling will be investigated experimentally and modeled numerically in chapter 5.

3.3.4 Summary and open questions

In conclusion, there are several candidates for microscopic processes that can lead to spin-lattice coupling: Exchange interaction, Spin-orbit coupling or even the weaker and thus here neglected spin dipole coupling. Nevertheless, the role of the spin-lattice coupling and flow of angular momentum is still disguised. Therefore in this work, the interaction of lattice excitations with the spin system will be investigated isolatedly.

In fact, the energy transfer from the spins to the phonons has already been studied intensively by FMR measurements. The dephasing and energy relaxation of a spin wave (excited by FMR) can be due to magnon-magnon scattering but also due to spin-lattice coupling [Kas61, Rue14]. In this way, spin-lattice coupling times even up to some hundreds of nanoseconds were observed in some magnetically ordered insulators [Vit85, Hun10].

²This can be already seen from the perturbation Hamiltonian $H_1 = \frac{e^2}{4\pi\epsilon_0} \left(\frac{1}{r_{ab}} + \frac{1}{r_{12}} + \frac{1}{r_{1b}} + \frac{1}{r_{2a}} \right)$ of the Heitler-London Model, where r_{ij} are the distances between ion a & b and electrons 1 & 2 [Nol09]

In contrast, the opposite direction of the energy transfer, how excited phonons couple directly to spins has never been studied up to now. This leads to one of the main open research question of this thesis: Can excited phonons solely change the magnetic properties of magnetically ordered material? If yes, what are the time scales? And what are the microscopic mechanisms behind it?

These questions will be tackled and novel answers are found by the research within this thesis in chapter 5.

4 Experimental methods

To access fundamental solid state excitations, such as phonons, magnons, excitons or cooper pairs, resonantly in their unperturbed ground state, intense and stable THz-sources are crucially required. Further, in order to obtain deeper insights into the time evolution of these excitations on ultrafast non-equilibrium time scales, various experiments based on a pump-probe scheme are employed. The principles of a general pump-probe technique is sketched in figure 4.1, which shows the basic ingredients: laser pump pulses, synchronized probe pulses and a detector unit.

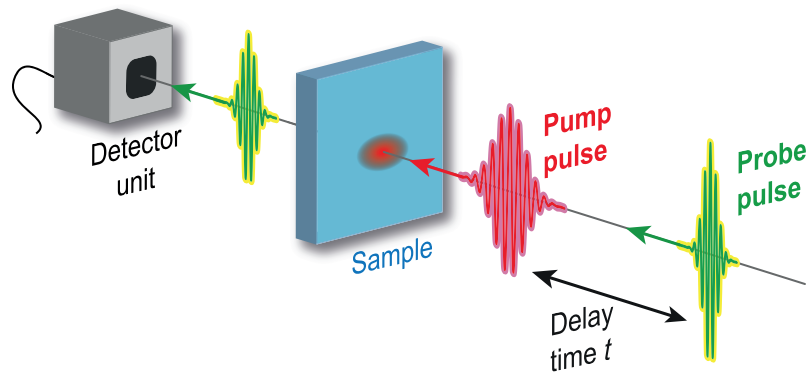


Figure 4.1.: Basic pump-probe scheme. After the excitation of the sample by a pump pulse, a synchronized probe pulse (not necessarily co-propagating) experiences the instantaneous properties of the sample. After the transmission through the sample, the modified pump pulse (e.g. intensity, polarization, spectrum) is monitored by a detection unit. Repeating this experiment with different pump-probe delays t , the dynamics of the excitation can be observed.

To push the boundaries of fundamental research beyond the pure observation towards the control of fundamental excitations, maybe even to the nonlinear regime, a table top intense and phase stable THz source was developed. Phase stability and fs-time precision combined with high intensities, ensure a reliable THz source tailored to the resonant and non-resonant driving of high frequency phonon modes. The high field THz source, developed within this thesis, is able to bridge several frequency octaves ranging from 10 THz up to the mid infrared (MIR) above 60 THz.

In order to reach these intense THz electric fields, a commercial kHz regenerative laser amplifier is used (section 4.1.2) that feeds two NIR-optical parametric amplifier (OPA) systems (section 4.1.3), which provide the necessary high pulse energies and relative phase stability for the difference frequency generation (DFG) (section 4.2.3).

For the time resolved pump probe studies with sub-femtosecond precision, a synchronized seed-oscillator is used (section 4.1.1). Its ultrashort 8 fs pulses interrogate the transient state of a physical quantity at a precise time delay in relation to the pump pulse arrival. For the observation of magnetization properties, the linear magneto-optic effect in transmission (Faraday effect) or magneto-optical Kerr effect (MOKE) in reflection (section

4.3.2) is utilized. Also the oscillatory motions of coherent phonons are probed by anisotropic transmission measurements. Further, transient non-equilibrium material properties such as the refractive index or complex conductivity can be extracted by means of transient THz transmittance or reflectance (section 4.3.1).

In this chapter, the experimental techniques and physical approaches that were used in the course of this work are introduced and discussed.

4.1 High power kHz-lasersystem

4.1.1 MHz oscillator

In order to explore new coupling phenomena between principal excitations of a solid on their fundamental time scales, ultrashort laser pulses are crucially required. Consequently, the beating heart (master clock) of the high field THz-source is an ultrashort pulse laser oscillator (Venteon Pulse One PE) with a repetition rate of 78.77 MHz and a pulse duration of 8 fs. This mode locked oscillator is an archetypical solid state laser that consists of the characteristic laser components: gain medium, cavity and pump energy source (see figure 4.2a).

The gain medium is a Titanium-doped Sapphire crystal $\text{Ti:Al}_2\text{O}_3$ (short Ti:Sapphire). The energy scheme of the Ti^{3+} -ions, depicted in figure 4.2 b, offers a typical 4 level system (energy levels L_i in the figure) with an absorption band between 370 - 670 nm (corresponding to $L_1 \rightarrow L_4$ transitions) and a homogeneous broadened fluorescence band between 670 - 1070 nm ($L_3 \rightarrow L_2$ transitions), which corresponds to the very broad gain profile that is required for ultrashort pulses [Fer02]. The absorption maximum around 500 nm, can be conveniently matched by a diode-pumped solid-state laser (Coherent Verdi-V6, 532 nm, 6 W). The rapid electron-lattice relaxation [Dem13, Fer02] causes the excited L_4 -level to decay into the L_3 -level within about 5 fs and creates the occupation inversion essentially required for stimulated emission [Mil10, Dem13].

Even though the amplification profile of a Ti:Sapphire crystal is extremely broad, the emission bandwidth also depends on the laser cavity design, which favors only certain modes. Here, the cavity is a linear optical resonator with a defined length l . This allows for a buildup of a frequency comb of longitudinal modes with an equidistant frequency spacing $\delta\nu = c/2l$ ¹.

In order to favor pulsed operation, the phases of these modes have to be locked. Such mode-locking is achieved by modulating a cavity parameter with frequency $\delta\nu$. As active periodic loss control (active Q-switching) [Mil10] is not fast enough for generating such ultrashort laser pulses, here the mode locking scheme relies on an inherent passive mechanism of the Ti:Sapphire gain medium: Ti:Sapphire exhibits non-negligible elements in the

¹The frequency offset ν_{CEO} of the whole comb is given by the relative carrier envelope offset (CEO) in between adjacent pulses (a detailed discussion of carrier envelope phase is given in section 4.2.1).

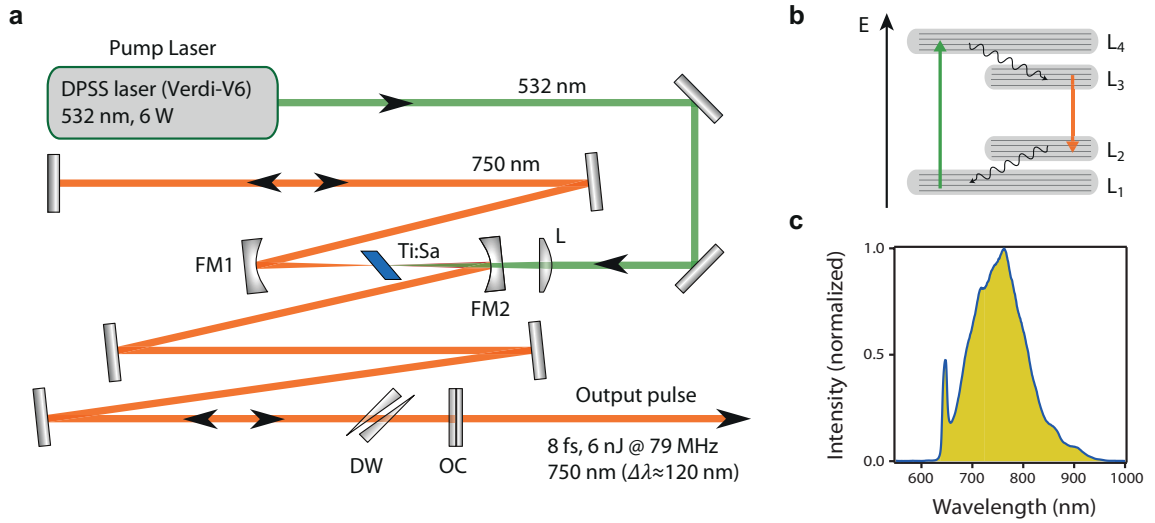


Figure 4.2.: Ultrashort pulse MHz oscillator. **a**, Beam path of the oscillator including lens (L), focusing mirrors (FM1 & FM2), Ti:Sapphire crystal (Ti:Sa) as gain and passive Q-switch medium, double wedge (DW) for dispersion compensation and outcoupling mirror (OC). **b**, Schematic 4-level energy scheme of Ti^{3+} -ions indicating absorption line (green), emission line (red) and non-radiative decay channels (black). **c**, Typical output spectrum used for all experiments within this thesis.

3rd order nonlinear electric susceptibility $\chi^{(3)}$ (see section 3.1.2). Therefore high intensities can lead to a nonlinear refractive index $n(I) = n_0 + n_2 I$, growing linearly with the intensity I and Kerr coefficient $n_2 = \frac{1}{\epsilon_0 n_0^2} \chi^{(3)}$. Consequently, an intense Gaussian beam profile leads to a laterally varying refracting index, acting like a transient lens [Fer02, Mil10]. This so called Kerr lens favors the propagation of the high intensity part of the modes (saturated absorption) also due to self-focusing ($n_2 > 0$), while modes with lower intensities comparatively experience more loss. Accordingly, this leads to a steady state distribution of the cavity modes and their phases. This manifests itself in the ultrashort pulsed operation of the laser oscillator.

In order to shorten the pulse duration as much as possible, a glass wedge pair (DW in figure 4.2a) is inserted into the cavity to fine tune its dispersive properties. Outside the cavity a prism pair and a pair of chirped mirrors pre-compensates for further dispersive losses in the following beam path. In this way pulse durations of about 8 fs are achieved at the sample position. A typical spectrum centered at 750nm wavelength can be seen in figure 4.2 c.

About 25% of the total output power (6 nJ) are used as an ultrashort probe pulse in all experiments within this thesis. The rest is needed to seed a regenerative kHz-amplifier (section 4.1.2) to ensure that the amplifiers, OPAs (section 4.1.3) and finally the resulting THz-pulses (section 4.2.3) are clocked to the MHz oscillator.

A good overview over the generation and application of ultrashort laser pulses is give in [Die06], [Fer02], [Mil10] and [Dem08].

4.1.2 kHz amplifier

To provide the high pulse energies in the NIR that are needed to generate intense THz fields, the oscillator pulse energies have to be amplified by more than a million times (10^6) and therefore the repetition rate has to be reduced to 1 kHz. This massive amplification is achieved by a kHz regenerative amplifier (Coherent Legend Elite Duo USP), followed by a single pass amplifier (SPA) and cryogenic amplifier (Cryo-PA).

After the seed pulses from the oscillator have propagated through two Faraday isolators [Chi89], which prevent back reflections into the oscillator, the pulses are stretched in time. This is done by a grating stretcher, which induces a large group velocity dispersion (GVD) $\partial^2 k / \partial \omega^2$ and therefore is able to stretch the formerly femtosecond pulses to the order of

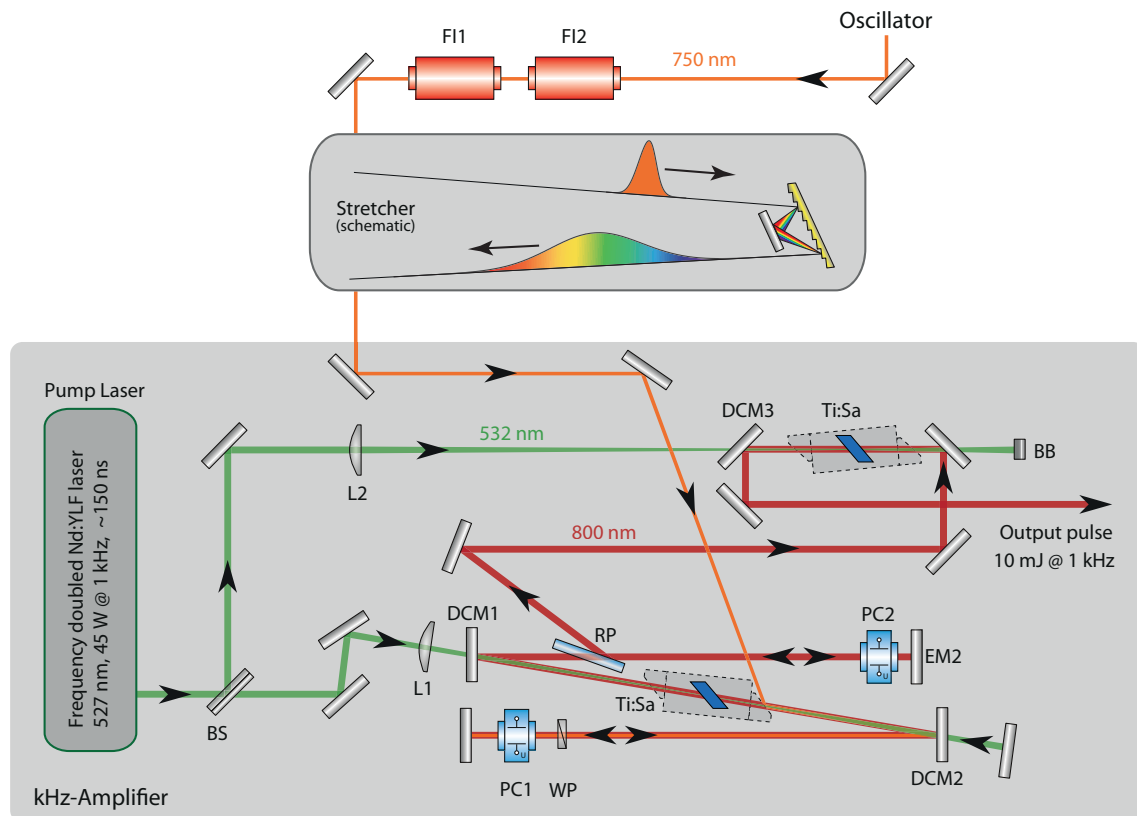


Figure 4.3.: Regenerative amplifier followed by single pass amplifier (SPA). Two Faraday isolators (FI1 & FI2) prevent back reflections into the oscillator. The seed pulses (orange) from the oscillator are stretched by a grating stretcher before they enter the regenerative amplifier via reflection on the window of the crystal housing. A waveplate (WP) and the switching of the Pockels cell PC1 allows the propagation through the windows and Ti:Sapphire crystal (Ti:Sa). The Ti:Sapphire crystal is pumped (green) through a dichroic mirror (DCM1). The remaining pump pulse is recycled after the second dichroic mirror (DCM2) and sent back into the Ti:Sapphire crystal. The switching of the second Pockels cell PC2 rotates the polarization again, enabling the out coupling via reflection at the thin film polarizer (RP). In the following SPA, the 800 nm pulses (red) are further amplified by a counter propagating 527 nm pump beam, which has been split off before at the beamsplitter (BS). Overall, output energies up to 10 mJ at a repetition rate of 1 kHz are reached.

hundreds of picoseconds (typical stretcher designs can be found in [Tre69, Che10, Bac98]). The long pulse duration prevents peak intensities to exceed the damage threshold of the optical components and deters parasitic nonlinear effects in the amplification process.

The regenerative amplifier works similar to the oscillator described in the previous section 4.1.1. In this case again a Ti:Sapphire crystal which's stimulated emission is seeded by an oscillator pulse (called *seed pulse* from here on) is used. Therefore, the seed pulse is coupled into a laser cavity with the Ti:Sapphire amplification medium. Subsequently, the pulses are amplified over several roundtrips through the cavity and then actively coupled out. In detail this scheme works like this:

The seed pulse is picked from the oscillator pulse train by a first Pockels cell (PC1) [Mil10], which rotates the polarization to be horizontal (p-polarized), such that a polarizing element (e.g. window or thin film polarizer) allows the seed pulse to enter the cavity. During each roundtrip through the cavity, the pulse is amplified as it propagates through the excited Ti:Sapphire crystal at Brewster angle incidence. The Ti:Sapphire crystal is pumped by an intra-cavity frequency doubled Nd:YLF laser [Rul05] (Coherent Evolution-HE, 527 nm, 45 mJ at 1 kHz repetition rate, ~ 150 ns pulse duration), which is actively Q-switched in synchronization with the Pockels cells. After the first pass through the crystal, the transmitted pump beam is recycled and used for pumping the crystal from the opposite side (see figure 4.3). Recycling the pump pulse increases the regenerative amplifier output power by about 30 %.

A second Pockels cell (PC2) inside the cavity determines the number of roundtrips of the amplified pulse, before it is allowed to leave the cavity. As soon as the PC2 switches, the polarization is rotated by 90° to be vertical (s-polarized) again and therefore a thin film polarizer (RP in figure 4.3) reflects the amplified pulse out of the cavity. The timing of PC2 is optimized to an out coupling right after the specific roundtrip, in which the amplification process enters the saturation regime. Typical output pulse energies around 5.7 mJ are reached. A detailed description of the Pockels effect (or linear electrooptic effect) is given in the section 4.3.1 about electrooptic sampling.

After the regenerative amplifier, the pulse is further amplified by propagating only once through another Ti:Sapphire crystal. This single-pass amplifier (SPA) is pumped by the same Nd:YLF laser in a counter propagating geometry. The two step amplification process leads to uncompressed output pulses with maximum pulse energies of 10 mJ at a repetition rate of 1 kHz and a central wavelength of 800 nm.

The immense power required for multiple nonlinear frequency conversion steps to finally reach high powers in the THz spectral range, is provided by a further SPA. Even though the active medium for amplification is again a Ti:Sapphire crystal, the pulse energies at this stage are very high and therefore the second SPA has to be operated under cryogenic conditions (see figure 4.4). Meaning that the whole amplification process takes place in a closed-cycle helium cryostat (Coherent Cryo-PA) operating at 62 K under a pressure of 10^{-8} mbar. This avoids thermal lensing in the crystal [Bac97] and takes advantage of the temperature dependent gain profile [Dan07]. The cryogenic SPA increases the pulse energy to about 18 mJ, which corresponds nearly to a doubling of the pulse energy. The pump energy is provided by a second identical Evolution-HE Nd:YLF laser.

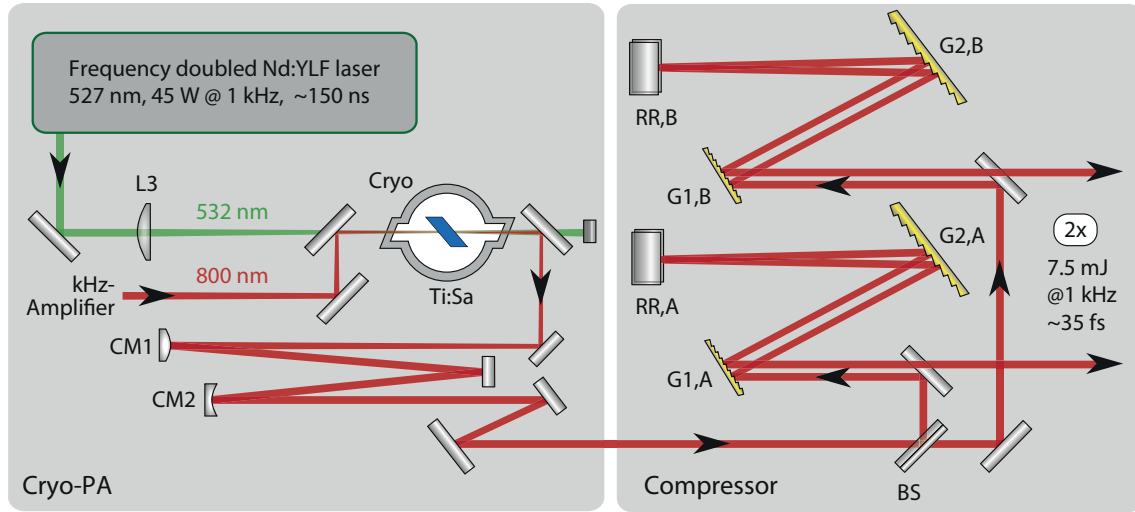


Figure 4.4.: Cryo-amplifier and twin compressor. The single pass amplification takes place in a Ti:Sapphire crystal (Ti:Sa), which is mounted in a closed loop helium cryostat (Cryo). The 527 nm pump beam (green) is provided by a separate frequency doubled Nd:YLF laser. The amplified 800 nm beam (red) is re-collimated by a telescope (CM1 & CM2) and afterwards split by a beamsplitter (BS) in ratio 50:50. The two independent Traey compressors are identical, each consisting of a grating pair (G1 & G2) and a vertical retroreflector (RR). Each output reaches 7.5 mJ pulse energy at 1 kHz with a pulse duration of about 35 fs.

After re-collimation by a periscope, a 50:50-beamsplitter divides the amplified pulse train equally into two parts (see figure 4.4), which are directed into two independent grating compressors in Traey configuration [Tre69]. The two compressors, consisting of a pair of parallel gold reflection gratings (1500 grooves per mm) each, recompress the pulses to about 35 fs in order to gain peak powers on the order of 200 GW in each of the two paths. The reason for the splitting and the two independent compressors is the following: as the amplified kHz pulses have to feed two coupled, but not identical OPAs (see section 4.1.3), it is necessary to adjust the pulse duration and dispersion properties independently according to the needs of each OPA. Additionally, this approach minimizes the risk of high intensity damages on the gold gratings. Overall, the kHz amplifier system produces two output beams with more than 7 mJ pulse energy each and a pulse duration of about 35 fs at a central wavelength of 800 nm.

4.1.3 Dual optic parametric amplifier

The generation of high field THz radiation by difference frequency generation (DFG) requires two high intensity laser beams with slightly offset spectra. Ideally, the offset in central frequency $\delta\nu = \nu_{0,A} - \nu_{0,B}$ corresponds to the desired THz central frequency ν_{THz} (see difference frequency THz generation in section 4.2.3). Consequently, it is important to keep the central wavelengths $\nu_{0,A}$ and $\nu_{0,B}$ independently tunable in order to keep the DFG based THz source flexible in frequency space. A NIR optic parametric amplifier (OPA) satisfies these requirements conveniently together with the additional benefit of lo-

wer linear and two photon absorption losses in THz-generation crystals like ZnTe or GaSe when pumped with NIR light instead of 800 nm radiation [Vid11, Ku13].

The principle of parametric amplification and a typical OPA stage are shown in figure 4.5 a and 4.5 b, respectively. Optical parametric amplification is an $\chi^{(2)}$ -effect and can therefore be described as a stimulated 3-wave mixing process (see section 3.1.3). A pump photon with frequency ω_p and a signal photon with lower frequency ω_s mix in a nonlinear medium ($\chi^{(2)} \neq 0$). Thereby, an additional signal photon with energy $\hbar\omega_s$ and a so called idler photon are emitted [Boy08]. The idler photon with energy $\hbar\omega_i = \hbar\omega_p - \hbar\omega_s$ accounts for energy conservation (see figure 4.5a). Wave vector conservation must be fulfilled as well.

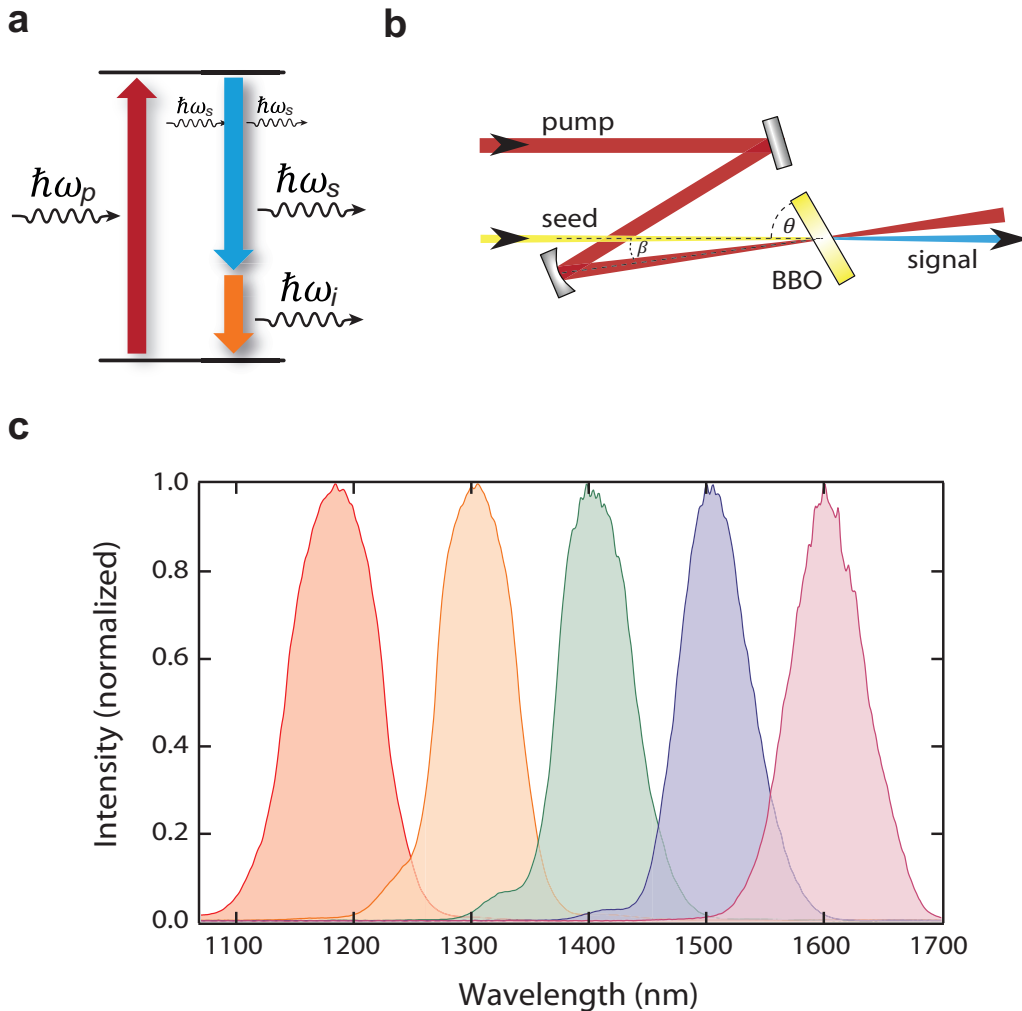


Figure 4.5.: Optic parametric amplification. **a**, Parametric amplification in a two level system: A pump photon with energy $\hbar\omega_p$ excites the system out of the ground state. Afterwards a weak signal beam with photon energy $\hbar\omega_s$ stimulates the emission of an additional $\hbar\omega_s$ photon. Simultaneously, an idler photon $\hbar\omega_i$ is emitted to fulfill energy and momentum conservation. **b**, Schematic OPA-stage: The desired amplified frequency ω_s is selected by the angle β between pump (red) and seed (yellow) beam and phase matching angle θ of the nonlinear crystal (BBO). **c**, Typical signal spectra used within this thesis.

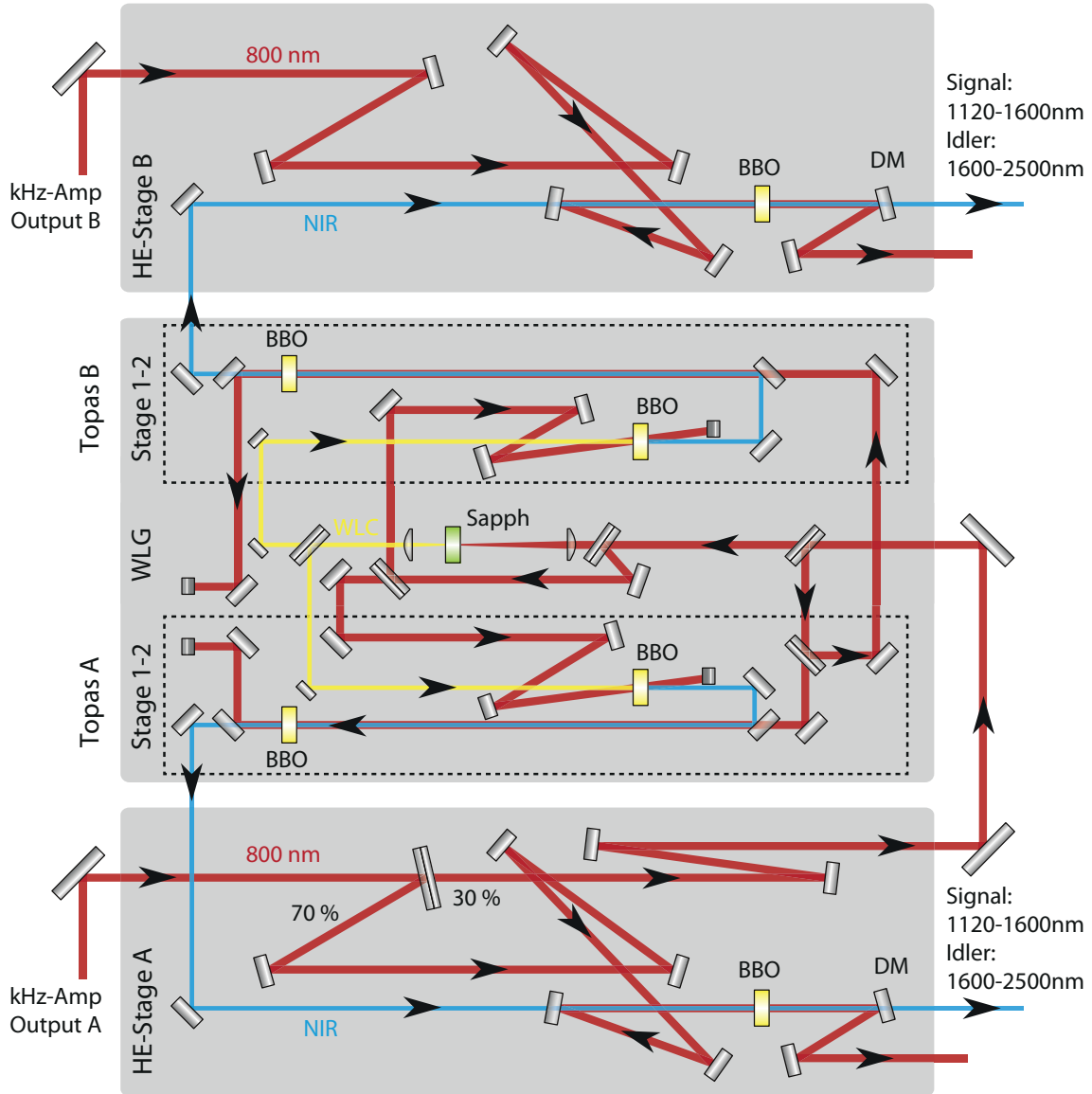


Figure 4.6.: High power dual OPA beam path. Each of the two OPAs (Topas A & Topas B) consists of a first OPA stage, seeded by the same white light continuum (WLC) that is generated in a thin sapphire plate (Sapph), followed by the second OPA stage (Stage 1-2 each). Afterwards each signal beam is used to seed a high power OPA (HE-Stage A & HE-Stage B). In all OPA stages β -BaB₂O₄ (BBO) crystals are used for the nonlinear frequency conversion. This simplified sketch does not account for the actual optical delays or focus conditions.

Therefore wave vector mismatch $\Delta k = k_p - k_s - k_i$ has to be minimized (meaning phase matching optimized) in order to maximize the signal gain in the desired direction. This is usually achieved by optimizing the angle β between signal beam and pump beam (non collinear OPA) and the phase matching angle θ for the birefringent nonlinear crystal (see figure 4.5b).

For the THz source developed in the course of this thesis, a commercial high power dual OPA (Light Conversion Topas Twins) plus two additional high energy (HE)-stages (Light

Conversion Topas HE) are used. The main part of the dual OPA, as schematically sketched in Figure 4.6, consists of two OPAs with two parametric amplification stages each (Topas A1,2 and Topas B1,2) and a shared white light continuum generation (WLG). Each of the two OPAs is followed by a third high power OPA-stage (HE-stage A and HE-stage B). As most of the pump power is used for the amplification in the 3rd high power stage, HE-stage B is pumped separately by the second amplifier output (Output B).

The common white light continuum [Cou07] is generated by focusing less than 1% of the input power into a sapphire window and is then divided in equal parts for the two OPAs. Its ultra-broadband spectra are then used as a seed for the parametric amplification in the first OPA stage respectively.

The 6 nonlinear amplification media in the Topas system are β -BaB₂O₄ (BBO) crystals, which are generally negative uniaxial birefringent. For the right choice of the angle β , it is possible to select the amplified signal wavelength with setting of the phase matching angle θ (at the second and third OPA stages, even a collinear $\beta \equiv 0$ configuration is used). In the Topas system this is done by software driven motorized rotation stages and additional motorized delay stages to account for the time delay between pump and signal pulses. Once all 6 crystal angles and 6 delay positions for several specific wavelengths are recorded to a tuning curve file, it is possible to select arbitrary output wavelengths between 1130 nm - 1600 nm (signal) and 1600 nm - 2500 nm (idler) remotely by software interface.

Most amplification is obtained in the (3rd) high energy (HE) OPA stage, where 70% of the initial input energy is used as a pump beam. A dichroic mirror after the HE OPA stage filters out most of the remaining 800 nm pump beam. Signal and idler beams can be easily separated because of the chosen type-II phase matching [Boy08]. In this case signal and idler waves are polarized perpendicular to each other and therefore can be discriminated efficiently by polarizing elements. Typical measured signal spectra are shown in figure 4.5 c.

4.2 Table top high field THz generation

4.2.1 Carrier envelope phase stability

In order to control and observe fundamental modes (like phonons, magnons, etc.) via laser pump probe spectroscopy, it is not only crucial to have intense light fields in the right frequency range available. Further these fields have to be carrier envelope phase (CEP) stable to resolve field driven effects or even perform coherent control as demonstrated in chapter 6. Usually pulsed laser sources like the oscillator and amplifier introduced in the previous section 4.1 are not CEP stable per se. The physical reason is the difference in phase velocity $v_{ph} = \omega/k$ and group velocity $v_g = \partial\omega(k)/\partial k$ within the laser resonator. The phase velocity $v_{ph}(\omega_0)$ determines the velocity of a single carrier wave with frequency ω_0 , whereas v_g describes the actual velocity of the envelope of the propagating laser pulse. Consequently the CEP changes from shot to shot in the usual case of $v_g \neq v_{ph}(\omega_0)$ in the cavity (see figure 4.7 a).

The Fourier transform of such a pulse train with constant repetition rate ν_{rep} is a comb structure in frequency space. The frequency comb's equidistant spacing is identical to the repetition rate. The constant CEP shift between two adjacent pulses $\Delta\phi$ is found in the frequency domain as an offset $\nu_0 = -\nu_{\text{rep}} \cdot \Delta\phi/2\pi$ of the whole frequency comb (see figure 4.7 b). Therefore the frequency comb can be described by only 2 frequencies and a natural number m :

$$\nu_m = \nu_0 + m\nu_{\text{rep}}. \quad (4.1)$$

Such frequency combs gained a lot of attention in the last decade [Hae06] for example due to important applications in high precision metrology [Hol00, Cun03, Ye05].

The pump-probe scheme used in this work requires phase stability ($\Delta\phi = 0$) of the THz pump pulses, because every pump probe delay requires a separate pump pulse (no single shot experiments). If CEP stability is not given, coherent field effects average out from shot to shot.

Fortunately, the table top THz generation methods that are used in this present work and introduced in the next sections 4.2.2 and 4.2.3 exhibit inherent CEP stability.

4.2.2 Optical rectification

Most modern standard techniques to generate very broadband THz pulses are based on optical rectification (OR) [Ric94]. The source of OR is a second order nonlinear polarization $P_{\text{NL}}^{(2)}$ as described in section 3.1. There, equation 3.9 exhibits non-oscillatory components in the nonlinear polarization $P_{\text{NL}}^{(2)}$, which are thereupon historically referred to as "rectified" components. On the other hand, if short pulses are used instead of two monochromatic waves, graphically spoken the OR component is broadened in frequency space around the former spectral line $\omega = 0$. Thus for short enough pulses the OR contribution expands to cover part of the THz spectral region [Hub00, Kue05]. In frequency space, this corresponds to multiple DFG (see section 3.1.3) processes between pairs of comb lines as schematically sketched by the lower red dots and black spectrum in figure 4.7.

As all pairs of mixing photons originate from the same frequency comb, the difference of their phase is always constant. Therefore OR produces inherently phase stable THz pulses.

There are several nonlinear crystals that are commonly used for OR based sources, e.g. semiconductors like ZnTe, GaP or GaSe. Also organic crystals like DAST², OH1³ and DSTMS⁴ show high conversion efficiencies, especially when they are pumped by a NIR pulse [Hau11, Ruc12, Sha15, Vic15]. On the other hand, These organic crystals suffer strongly from heat management problems though, especially when pumped by high power, high repetition rate laser systems.

The material with one of the highest conversion efficiencies is LbNbO₃ (Lithium niobate), which requires a sophisticated type of phase matching (tilted pulse front phase matching) [Heb02, Heb08, FÜ11]. The requirement of phase matching is discussed in the appendix

²4-N,N-dimethylamino-4'-N'-methyl-stilbazolium tosylate

³2-(3-(4-Hydroxystyryl)-5,5-dimethylcyclohex-2-enylidene)malononitrile

⁴4-N,N-dimethylamino-4'-N'-methyl-stilbazolium 2,4,6-trimethylbenzenesulfonate

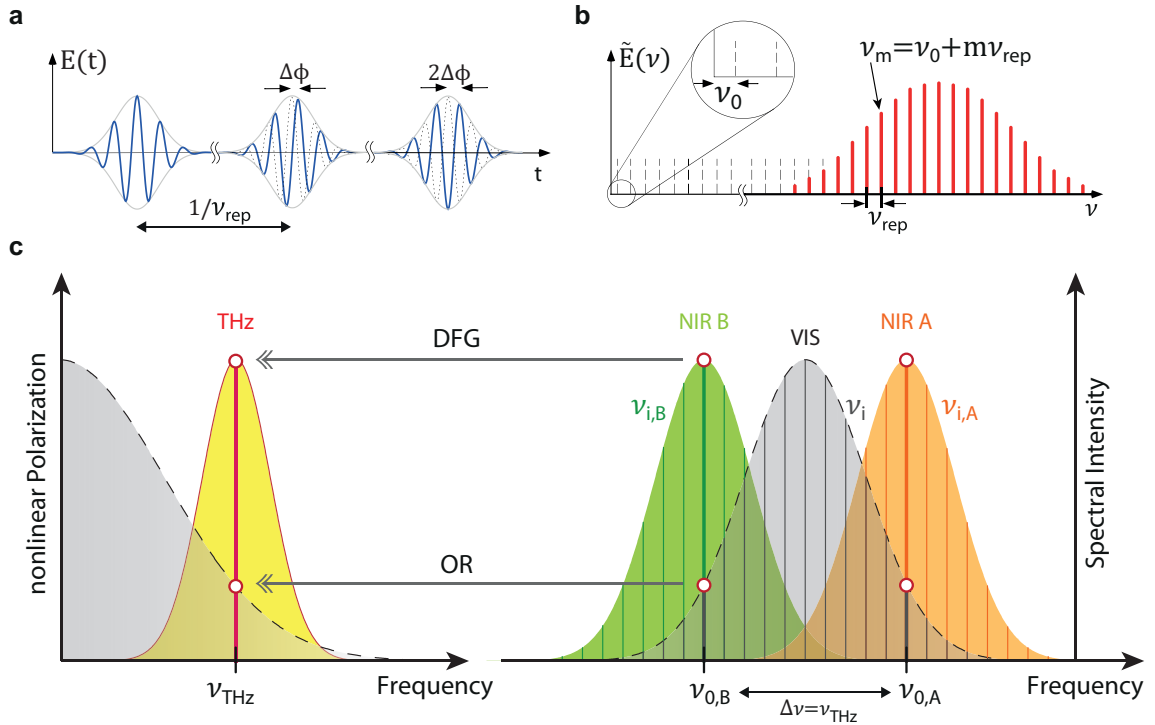


Figure 4.7.: CEP and optical rectification versus difference frequency THz generation. **a**, For a general laser pulse train with repetition rate ν_{rep} , the phase between the carrier wave (blue line) and pulse envelope function (grey line) shifts by an arbitrary carrier envelope offset $\Delta\phi$ from shot to shot. **b**, The Fourier transform of such a pulse train exhibits a simple comb structure with frequency lines $\nu_m = \nu_0 + m\nu_{\text{rep}}$, where $\nu_0 = -\nu_{\text{rep}} \cdot \Delta\phi/2\pi$ is the offset frequency caused by the carrier envelope offset $\Delta\phi$ (figure a, b adapted from [Hae06]). **c**, Schematic comparison of two THz generation methods: Optical rectification (OR) and difference frequency generation (DFG). OR mixes two photons from the same pulse (grey spectrum), whereas DFG mixes two photons from two slightly frequency shifted pulses (green and orange spectrum). For higher THz frequencies ν_{THz} less frequency pairs (ν_i, ν_j) can contribute to the mixing in the OR case. In the DFG process, in contrast, the spectra can be tuned such that all photon pairs $(\nu_{i,A}, \nu_{i,B})$ can contribute to the mixing such that $\nu_{i,A} - \nu_{i,B} = \nu_{\text{THz}}$.

A.3.3. THz emitters which are based on charge acceleration by the steep envelope of a pump pulse can also be described in terms of OR. Among these are for example photoconductive switches (also called Auston switches) [Smi89, Bec10, Dre05, Win09] or novel spintronic emitters [Sei16]. The latter are based on charge separation in magnetic fields due to the (inverse) Spin-Hall-Effect (ISHE).

Unfortunately, there is one inherent drawback of optical rectification: The higher the desired frequency ν_{THz} the less comb line pairs (ν_i, ν_j) exist, which can mix to $\nu_{\text{THz}} = \nu_i - \nu_j$. Thus, the THz conversion efficiency drops rapidly for higher THz frequencies and is therefore limited by the bandwidth⁵ of the generation pulse $\Delta\nu$. To overcome this issue, instead of mixing two photons with frequencies (ν_i, ν_j) within the same pulse, the two

⁵time bandwidth product for a Fourier transform-limited Gaussian pulse: $\Delta\tau \cdot \Delta\nu = 0.441$, with pulse duration $\Delta\tau$ and bandwidth $\Delta\nu$ both FWHM

initial photons are provided by two separate NIR pulses with slightly offset spectra (see figure 4.7).

4.2.3 OPA based difference frequency generation

As already mentioned in the previous section the efficiency of OR drops dramatically when aiming for higher THz frequencies. Hence, in order to obtain both, high THz fields at high THz frequencies, difference frequency mixing between two photons from two different NIR pulses is performed.

The conversion efficiency for a desired THz central frequency ν_{THz} rises by 3 orders of magnitude [Sel08a] when, instead of a visible pump pulse, two NIR pulses with a central frequency difference of $\nu_{0,A} - \nu_{0,B} = \nu_{\text{THz}}$ are mixed. This can be descriptively seen in figure 4.7 c: For OR only frequency pairs (ν_i, ν_j) at the low intensity wings of the spectrum can mix to the frequency ν_{THz} (black spectrum in figure 4.7 c). Whereas for two offset NIR spectra $(\nu_{i,A}$ and $\nu_{i,B})$, all frequencies $\nu_{i,B}$ in the pulse with the slightly lower central frequency have a mixing counterpart in the other pulse with frequency $\nu_{j,A} = \nu_{\text{THz}} + \nu_{i,B}$. Therefore in principle all photons are able to contribute to the THz generation process⁶. This leads to a photon conversion efficiency up to 14% [Sel08a].

Difference frequency mixing does not produce CEP-stable pulses per se. It requires further that the two mixing pulses are phase correlated. This means that the CEP may fluctuate from shot to shot, but the relative CEP shift between the two mixing NIR pulses has to be constant, inferring

$$\Delta\phi_A^{(m)} - \Delta\phi_B^{(m)} = \Delta\phi_A^{(n)} - \Delta\phi_B^{(n)} \quad (4.2)$$

for every arbitrary shot m and n . The use of the same 800 nm pump pulse for both OPAs and the seeding by the same white light continuum (which is the main source of phase fluctuations) ensures the previous requirement. Therefore the THz pulses generated via dual OPA based DFG can be regarded as inherently CEP stable as well. In the high field THz generation setup that was developed within this thesis (shown in figure 4.8 a) the THz CEP can be fixed to any arbitrary value and even modulated with an arbitrary frequency locked to the repetition rate of the kHz amplifier (for details see section 6.3.3). This is done by setting the absolute phase between the two OPA pulses via a piezo controlled optical delay (delay stage in figure 4.8 a).

Like for all frequency conversion processes, the efficiency of the DFG based THz generation crucially depends on the phase matching conditions. As discussed in more detail in appendix A.3.3, the resulting THz field scales with the phase matching factor:

$$\frac{\exp(i\Delta kd) - 1}{\Delta k} \quad \text{with} \quad \Delta k = k(\omega_1) - k(\omega_2) - k(\omega_{\text{THz}}) \quad (4.3)$$

and d being the effective crystal thickness. To minimize the wave vector mismatch Δk the birefringence of the generation crystal GaSe is used. GaSe is a negative uniax-

⁶In reality parasitic effects such as two photon absorptions and saturation effects determined by the Manley-Rowe limit [Boy08] have to be considered

ial crystal, exhibiting a larger refractive index $n_o(\omega)$ and therefore a larger wavevector $k_o(\omega_2) = n_o(\omega_2) \cdot \frac{\omega_2}{c}$ for the ordinary polarized lower frequency NIR beam (NIR B in figure 4.8 a). By rotating the polarization of the higher frequency NIR beam (NIR A) by 90° to an extraordinary polarization, it experiences a lower refractive index $n_e(\omega_1) < n_o(\omega_2)$. This type II phase matching scheme with polarizations (e, o, e) is valid for the frequencies $(\nu_1 > \nu_2 > \nu_{\text{THz}})$ respectively.

Experimentally, a major benefit arises from a collinear phase matching geometry: if the azimuthal angle φ is adjusted such that the optical axis is in the plane of incidence, the projection of the extraordinary beam onto the optical axis, and thus $n(\omega_1)$, can be controlled by the tilting angle θ (see figure 4.8 b). Consequently, the optimized THz emission frequency can be tuned merely by tilting the GaSe crystal in the plane of incidence ($\hat{=}$

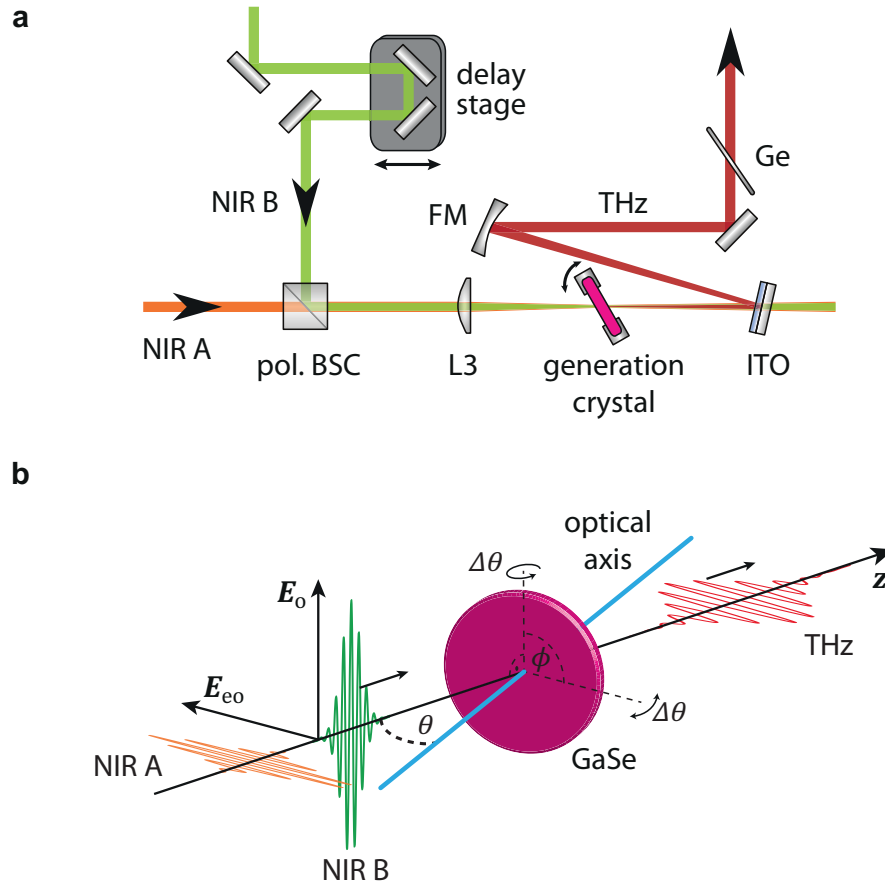


Figure 4.8.: THz Difference frequency generation setup. **a**, Two orthogonal NIR beams are combined in a polarizing beam splitter cube (pol. BSC) and then collinearly focused in the generation crystal. The temporal overlap is adjusted by delaying NIR B with respect to NIR A (delay stage). A focusing gold mirror (FM) collimates the THz beam. The remaining NIR beams are filtered out by a thin indium tin oxide (ITO) mirror, which is reflective for wavelengths longer than about $5 \mu\text{m}$ and by a germanium wafer (Ge), which is transparent for wavelengths longer than 1850nm . **b**, Type-II phase matching geometry for gallium selenide (GaSe): If the azimuthal angle ϕ is adjusted such that the optical axis is in the plane of incidence, the phase matched difference frequency ν_{THz} can be tuned by the tilting angle θ .

rotation around the ordinary polarization). This allows for tuning the THz central frequency without changing the beam path and therefore "on screen" control of the generated transient waveform via EOS (see section 4.3.1).

The frequency range of GaSe, the principal nonlinear crystal of this thesis, expands from 10 THz up to 60 THz. With Silver Gallium selenide (AgGaSe_2) even frequencies above 80 THz can be reached in the same way [Sel08a].

4.3 Ultrafast optical probing mechanisms

The generation of high intensity THz pulses to create specific excitations in a solid (e.g. phonons, magnons, excitons, cooper pairs, etc ...) was introduced in the previous section 4.2. In order to learn about the temporal evolution of such likely non-equilibrium states of matter, probing mechanisms to trace the dynamics of specific physical quantities like magnetization \mathbf{M} and electric field \mathbf{E} inside the sample are required. Changes in the electric field and magnetic field can both lead macroscopically to perturbations in the electric polarization \mathbf{P} , which can be detected as modulation of the (anisotropic) refractive index n . As explained in section 3.1.2, the perturbative response of the instantaneous polarization \mathbf{P} is described by the electric susceptibility χ , which can be also magnetic field dependent due to spin-orbit coupling [Opp01].

Because these dynamics occur on ultrafast time scales, observing them relies on synchronized short pulses from the oscillator (section 4.1.1). In this section the main probing schemes of this thesis and their physical background are introduced.

4.3.1 Electrooptic detection

One of the main advantages of THz-spectroscopy is the ability to detect both amplitude and phase of the electric field within the light pulse, whereas conventional VIS or NIR spectroscopy is commonly restricted to intensity envelopes. Knowledge of amplitude and phase allow the extraction of the complex dielectric function without the use of Kramers-Kronig-relations [Tay11, Zak90, Rub12]. Moreover, electrooptic detection is also applicable for small intensities, because it scales linearly with the electric field. It covers a broad frequency range from sub 100 GHz up to 120 THz (GaSe [Kue04] or even 130 THz (ZnTe [Sel08b])), depending on the choice of the detection crystal type and its thickness.⁷

The linear electrooptic effect, also called Pockels effect, describes the change of refractive index n linearly dependent on the electric field E . Accordingly it can be understood as a $\chi^{(2)}$ -process with the material dependent electrooptic tensor $r_{ijk} = \chi_{ijk}^{(2)}/n_0^3$ [Yar85] :

$$\left(\frac{1}{n^2}\right)_{ij} = \left(\frac{1}{n_0^2}\right)_{ij} + \sum_{k=1}^3 r_{ijk} E_k, \quad (4.4)$$

with unperturbed refractive index n_0 . The indices i and j can be simplified in a contracted notation depending on the crystal symmetry [Dmi96].

⁷This section is partly based on a description of electrooptic sampling in my Diplom thesis [Mae11].

Such a variation of the refractive index can be interpreted as a temporary modulation of the detection crystal birefringence, induced by the THz electric field. An ultrashort visible laser pulse co-propagating through the detection crystal therefore experiences a change in polarization depending on the instantaneous strength of the THz field. The retardation between the two orthogonal polarization components of the probe pulse is maximized for a 45° linear polarization with respect to the refractive index ellipsoid axes (see sketch 4.9 a). In this case, the induced anisotropic refractive index is directly proportional to the applied THz field E_{THz} :

$$\Delta n = E_{\text{THz}} n_0^3 r_{ijk} \quad (4.5)$$

A Fourier transform delivers the temporal evolution of the refractive index:

$$\Delta n(z, t) = \int d\omega E_{\text{THz}}(\omega) n_0^3(\omega) r_{ijk}(\omega_{\text{pr}}; \omega, \omega_{\text{pr}} - \omega) \exp[i(k(\omega)z - \omega t)]. \quad (4.6)$$

However, for short broadband THz pulses the electrooptic modulation of the refractive index is not exactly proportional to the instantaneous electric field, since $r_{ijk}(\omega)$ weights spectral components of the THz pulse differently. Therefore an additional detector response function has to be considered, which also includes propagation effects from the sample to the detection, in order to calculate the true THz electric field. The convolution of the THz field E_{THz} with this response function f turns into a simple product in the frequency domain. This justifies the simple relation: $\Delta n(\omega) \propto f(\omega)E_{\text{THz}}$. A detailed calculation of the material specific and thickness dependent response functions $f(\omega)$ is given in [Kam07].

For the experimental work within this thesis, a simple strategy yields an accurate representation of the pump pulse at the sample position: the THz-field incident onto the sample is measured via EOS at the very same position where later the sample is positioned. Accordingly frequency dependent propagation and focusing effects can be neglected. Further in most cases, central frequencies around 20 THz to 40 THz are detected with a very thin GaSe flake. The highest frequency phonon resonances in GaSe are located at 9 THz [Mad04]. Therefore $\chi^{(2)}$ and thus r_{ijk} can be considered nearly frequency independent above 9 THz [Fer94]. Hence $\Delta n(z, t)$ is proportional to $E_{\text{THz}}(z, t)$.

Experimentally, we do not access directly Δn , but rather the relative phase shift $\Gamma = \omega_{\text{pr}} \Delta n d / c$ of the electric field of the probe pulse (central frequency ω_{pr}) between slow and fast polarization axis after the detection crystal thickness d . Therefore EOS provides [Bak98]:

$$\Gamma(\Delta t) = \frac{2\pi n_0^3 r_{ijk}}{\lambda_{\text{pr}}} \int_{-\infty}^{\infty} dt \int_0^d dz E_{\text{THz}}(z, t + \Delta t) I_{\text{pr}}(z, t) \quad (4.7)$$

with normalized probe pulse intensity envelope $I_{\text{pr}}(z, t)$ and crystal thickness d . Equation 4.7 demonstrates that different propagation velocities between the THz phase velocity v_{ph} and the probe pulse group velocity v_{g} have to be considered in terms of wavevector mismatch Δk . For a detection crystals thickness d comparable to the coherence length $L_c = \pi / \Delta k$ of the crystal, the electrooptic tensor is reduced to an effective r_{eff} . Only for detection crystals with $d \ll L_c$ phase matching can be neglected. By including the spatial integration in equation 4.7 in r_{eff} , $\Gamma(\Delta t)$ is proportional to a cross correlation between the THz field and the intensity envelope of the probe pulse. Consequently the ratio in

between the oscillation period of THz electric field and probe pulse duration determines the frequency resolution.

Balanced detection

The polarization state of the probe pulse is interrogated with a balanced detection scheme, a standard technique to detect small changes in the ellipticity or linear polarization of light, which is sketched in figure 4.9 a. After the probe pulse leaves the electrooptic detection crystal, where it experienced a pump induced birefringence, it propagates through a waveplate followed by a Wollaston prism (WLP). The Wollaston prism spatially separates two orthogonal polarization components of the probe light. Depending on the waveplate, these two components measure either the linear polarization rotation or the ellipticity of the polarization. For a half-wave plate (HWP), the projections of the electric field onto two orthogonal axes are measured on separate photodiodes. For the purpose of electrooptic sampling, the two main axes of the polarization ellipticity are measured by replacing the half-wave plate by a quarter-wave plate (QWP). In order to detect only pump induced changes of the polarization state, the waveplate is oriented such that an unperturbed polarization leads to equal intensities on both diodes. As shown in figure 4.9 a, for example for an initially linear polarized probe beam the fast axis of the QWP has to be rotated by 45° with respect to the initial polarization direction. Consequently, the difference between the two intensities on the photodiodes is zero in the unperturbed case. Ideally, this leads to a cancellation of any intensity fluctuation of the probe beam.

Therefore the difference signal of the photodiodes directly measures the change of polari-

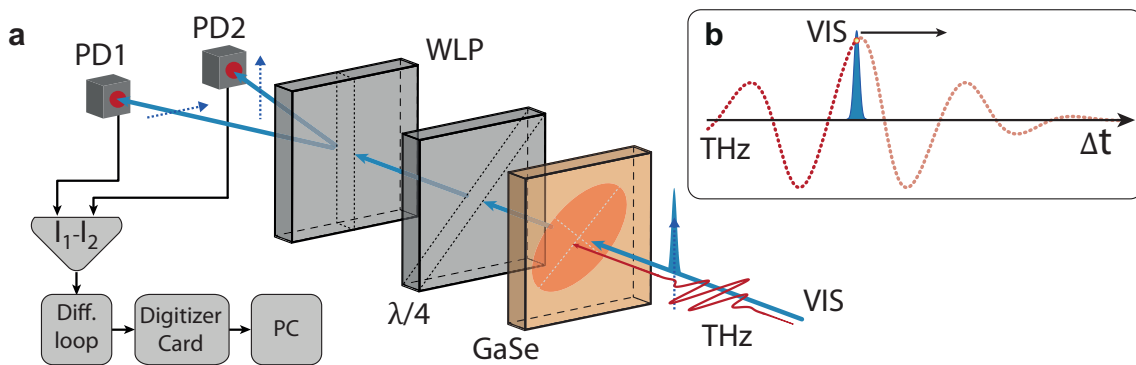


Figure 4.9.: Electrooptic sampling and balanced detection. **a**, The electric field of the THz pulse (red) induces a change of birefringence in the electrooptic sampling crystal (orange refractive index ellipsoid). Therefore a short sampling pulse (blue) experiences a change of polarization while co-propagation with the THz pulse, proportional to the instantaneous THz field $E_{\text{THz}}(\Delta t)$. The two components of the elliptic polarization are decomposed by a quarter wave plate (QWP) and a Wollaston Prism (WP). The photodiodes (PD1 & PD2) detect the two polarization components separately. Their current difference ΔI is then further processed in the data acquisition (see section 4.3.3). **b**, The variation of the time delay Δt between THz pulse and sampling pulse (blue) enables the phase resolved detection of the THz field (red dots).

zation Γ :

$$\Delta I = \frac{1}{2} \epsilon_0 c (|E_1|^2 - |E_2|^2) = I_0 \sin(\Gamma). \quad (4.8)$$

When using a QWP, Γ corresponds to the relative phase retardation in equation 4.7 and thus leads to the measured quantity of electrooptic sampling:

$$\frac{\Delta I(\Delta t)}{I_0} = \arcsin \left(\frac{2\pi d n_0^3 r_{\text{eff}}}{\lambda_{\text{pr}}} \int_{-\infty}^{\infty} dt E_{\text{THz}}(t + \Delta t) I_{\text{pr}}(t) \right) \quad (4.9)$$

For small signals the sine function can be linearized, leading to the simple relation: $\Delta I/I_0 \approx \Gamma$.

By changing the temporal delay between pump and probe pulse Δt from shot to shot, the electric field of the THz pulse is mapped in amplitude and phase directly in the time domain (see figure 4.9 b).

The electrooptic effect can be also described as a sum frequency - and difference frequency process between the THz-pulse and the broadband probe pulse [Kam06]. In the present work, mainly very thin ZnTe crystals (5 – 15 μm) or GaSe flakes were used in order to prevent non-linear effects in the detection crystals [Sel08a]. A comprehensive list of EOS detection crystals, their nonlinear coefficients and their phase matching conditions can be found in [Wu96] and [Dex07, Wil07].

4.3.2 Magneto-optic detection

Analogous to the previous section, where the electric field within the sample was measured by a linear electrooptic effect (Pockels effect), the magnetization inside magnetically ordered solids (ferromagnets, ferrimagnets, etc.) can be investigated via linear magneto-optic effects. The discovery of the linear magneto-optic effect in transmission, called Faraday effect⁸, was the first observation of direct interaction of magnetism and light. The corresponding effect in reflection is called magneto-optical Kerr effect (MOKE) and has been discovered 30 years later⁹. The advent of short pulse laser sources, led to a revival of these methods as common probes for ultrafast magnetization dynamics [Bea96, Kim02, Big09, Koo05, Koo10, Kir10].

Both effects change the polarization state of the transmitted (Faraday effect) or reflected (MOKE) light, which can be described as the complex Kerr-angle $\Phi(\mathbf{M}, t)$:

$$\Phi(\mathbf{M}, t) = \theta(\mathbf{M}, t) + i\eta(\mathbf{M}, t) \quad (4.10)$$

with linear polarization rotation θ and ellipticity defined as $\eta = \arctan \left(\sqrt{I_+/I_-} \right)$. Here I_+ and I_- denotes right handed and left handed circular polarized part of the intensity, respectively. Linear polarization θ and ellipticity η can be expressed by the dielectric tensor $\epsilon_{ij}(\mathbf{M}, \omega)$. Therefore they are determined, as in the electrooptic effect, by the electric susceptibility ($\epsilon_{ij} = 1 + \chi_{ij}$).

⁸discovered by the English scientist MICHAEL FARADAY in 1845

⁹named after the Scottish physicist JOHN KERR after the discovery in 1875

In this work, primarily transparent thin film samples are electro-magnetically investigated. Therefore the more reliable (due to easier alignment) Faraday effect in transmission is the better probe. It is also more trustworthy to switch between EOS and Faraday measurements, because of the common probe beam path.

Most samples under research in chapter 5 exhibit an easy magnetization axis which is parallel to the surface normal (also called: out of plane magnetization). Accordingly, the dielectric function determining the Faraday effect can be described analogously to the polar magneto-optical Kerr effect (PMOKE) [Ant04]. In PMOKE geometry the magnetization vector \mathbf{M} is perpendicular to the sample surface and in the plane of incidence. In this case and by assuming $\mathbf{M} \parallel \hat{\mathbf{z}}$, the dielectric tensor can be simplified to:

$$\epsilon(\mathbf{M}, \omega) = \begin{pmatrix} \epsilon_{xx} & i\epsilon_{xy} & 0 \\ -i\epsilon_{xy} & \epsilon_{xx} & 0 \\ 0 & 0 & \epsilon_{zz} \end{pmatrix} \quad \text{with} \quad \epsilon_{ij} = \epsilon'_{ij} + i\epsilon''_{ij}. \quad (4.11)$$

All tensor elements in equation 4.11 may be complex valued and depend on the magnetization, fulfilling the Onsager relations [Bos62, Kle66, Sug00]:

$$\epsilon_{ij}(-\mathbf{M}, \omega) = \epsilon_{ji}(\mathbf{M}, \omega). \quad (4.12)$$

Therefore the diagonal components of the dielectric tensor are even functions of \mathbf{M} , while the off diagonal components are odd in \mathbf{M} . From this relation it can already be seen that the magnetization \mathbf{M} induces an optical anisotropy in magnetically ordered solids.

The real and imaginary parts of the diagonal tensor element ϵ_{xx} are given by $\epsilon'_{xx} = n^2 - K^2$ and $\epsilon''_{xx} = 2nK$, respectively, with real valued refractive index n and extinction coefficient K .

The different material properties for right (+) and left (-) circular polarized light determine the off diagonal components of the dielectric tensor:

$$\epsilon_{xy} = \sqrt{\epsilon_0} [(n_+ - n_-) + i(K_+ - K_-)]. \quad (4.13)$$

Accordingly, right and left circular polarized components of a light wave travel with different velocities and absorption losses through the magnetically ordered material. This leads to a rotation of the linear polarization axis and change of the ellipticity, respectively, given by

$$\theta(\omega) = \frac{\omega}{2c} \cdot \text{Re} \left(\frac{\epsilon_{xy}(\omega)}{\sqrt{\epsilon_0(\omega)}} \right) = \frac{\omega}{2c} (n_+(\omega) - n_-(\omega)), \quad (4.14)$$

$$\eta(\omega) = \frac{\omega}{2c} \cdot \text{Im} \left(\frac{\epsilon_{xy}(\omega)}{\sqrt{\epsilon_0(\omega)}} \right) = \frac{\omega}{2c} (K_+(\omega) - K_-(\omega)), \quad (4.15)$$

per unit length.

The Faraday ellipticity $\eta(\omega)$ is better known as magnetic circular dichroism (MCD), which is defined by the different absorption coefficients $\alpha_{\pm}(\omega)$:

$$\Delta\alpha(\omega) = \alpha_+(\omega) - \alpha_-(\omega) = -\frac{4\eta(\omega)}{d}, \quad (4.16)$$

where d is the probed thickness. It is commonly used for element specific magnetization studies in the x-ray absorption regime [Bar07, Rad11].

As both Faraday rotation and Faraday ellipticity are proportional to the magnetization in the lowest order of \mathbf{M} , the phenomenological Verdet constant is usually introduced to simplify the relation. With Verdet constants V_{FR} and V_{FE} for rotation and ellipticity, respectively, equation 4.14 and 4.15 are condensed to:

$$\theta(\omega, t) = d \cdot V_{\text{FR}}(\omega) \hat{\mathbf{k}} \cdot \mathbf{M}(t), \quad (4.17)$$

$$\eta(\omega, t) = d \cdot V_{\text{FE}}(\omega) \hat{\mathbf{k}} \cdot \mathbf{M}(t), \quad (4.18)$$

with the unit wavevector $\hat{\mathbf{k}}$ of the propagating light wave and sample thickness d . The Verdet constants or linear magneto-optic coupling constants can be determined experimentally [Sug00, And76, Han84] or classically modeled (e.g. by the first model of Becquerel [Bec97, Ped90]). Quantum mechanically the Verdet constant depends on various sources, which makes the theoretical treatment much more complex [Hau04]. Multiple reflections, e.g. in a thin film sample, are neglected in the formulas above [Don63, Nie89].

The ultrafast pump induced Faraday signals are detected with the very same balanced detection setup that was introduced in the previous section 4.3.1 for electrooptic sampling. The EOS crystal is replaced by the magnetic sample (see figure 4.9).

Furthermore it was precisely taken care to separate magnetic from non-magnetic pump induced effects. Therefore the most general probe signal contains a time dependent Magnetization $\mathbf{M}(t)$, a time dependent magneto-optic coupling constant $a(t)$ and a time dependent non-magnetic contribution $b(t)$:

$$S(M, t) = a(t)M(t) + b(t) \quad (4.19)$$

The non-magnetic component $b(t)$ is very important because in a realistic experimental setup, the photo diodes can never be balanced completely below the noise floor due to slightly differing temporal response characteristics. A double differential detection scheme was developed to trace the ultrafast time evolution of the real magnetization. Details of the magneto-optic signal analysis for the specific material system are given in section 5.3.3, where equation 4.19 will be used as a starting point.

4.3.3 Data acquisition from fs to ms time scales

In order to measure dynamic effects spanning over more than 12 orders of magnitude in the time domain, two different low noise data acquisition procedures were developed. The goal of both methods is the detection of a pump induced modulation of the difference current of the two photodiodes $\Delta I = I_1 - I_2$ due to polarization changes (see figure 4.9). Signals arising from parasitic effects such as intensity fluctuation of the probe pulses or pointing instabilities have to be suppressed as good as possible in order to gain high sensitivity. In the following two subsections both data acquisition methods are introduced briefly.

Ultrashort time scales (sub fs to 100s ps)

For the ultrafast time scales, ranging from 0.1 fs up to 500 ps the time delay between the pump pulse and a single probe pulse is controlled by a high precision motorized delay stage (Newport linear stage GTS 150 + XPS motion controller) that runs in fast scan mode. The stage position is read out synchronized to the kHz-amplifier system for every THz-shot with a precision of 50 nm.

The data acquisition from the balanced photo diode signal ΔI makes use of the different repetition rates of the THz-pump pulse (1 kHz) and the oscillator probe pulse train (80 MHz). Since only one MHz-probe pulses carries the pump induced signal ΔI_j (see figure 4.10 a) the low frequency noise floor (< 80 MHz) and remaining unbalanced static signals can be suppressed by subtraction of the previous ΔI_{j-1} or succeeding ΔI_{j+1} probe pulse. This is performed by a passive electronic difference loop, which produces a pulse train of differences between adjacent pulses $\delta_j = \Delta I_j - \Delta I_{j+1}$. The resulting two cleaned up signal pulses $\delta_1 = -\delta_2$ are amplified and then converted separately by a broadband (100 MHz) digitizer Card (NI PXI-5122). Now the signal to noise ratio can be even more improved by a further subtraction of the two digital signals W_1 and W_2 from one another as depicted in figure 4.10 a ($W_2 \approx -W_1$).

With this data acquisition procedure usual signal to noise ratios of $1:10^{-4}$ can be achieved in the setup used for this work.

Long time scales (12.5 ns to 1 ms)

For pump-probe delay times reaching from ns up to 1 ms, it is unfeasible to use modulations of the optical path length. Thereupon a slightly different approach is used. Instead of using every THz shot and a passive difference loop, a chopper running at 500 Hz blocks every second THz-pump pulse (see figure 4.10 b). The optical delay between the 500 Hz pump pulse and the 80 MHz probe pulse train stays fixed, but every single probe pulse signal ΔI_j is sampled and digitized to A_j separately. That means, for every pump pulse the succeeding 80.000 probe pulses are recorded, leading to a time resolution of 12.5 ns given by the oscillator repetition rate. Additionally, the same record array is recorded for the next blocked THz pump pulse (B_j in figure 4.10 b) and subtracted from the pump modulated pulse train to get a significant noise reduction. Thousands of full traces can be averaged in a minute easily with this method, because no mechanical delays are used. The acquisition speed is only limited by the onboard memory of the digitizer card (32 MB) and its sampling rate (100 MS/s).

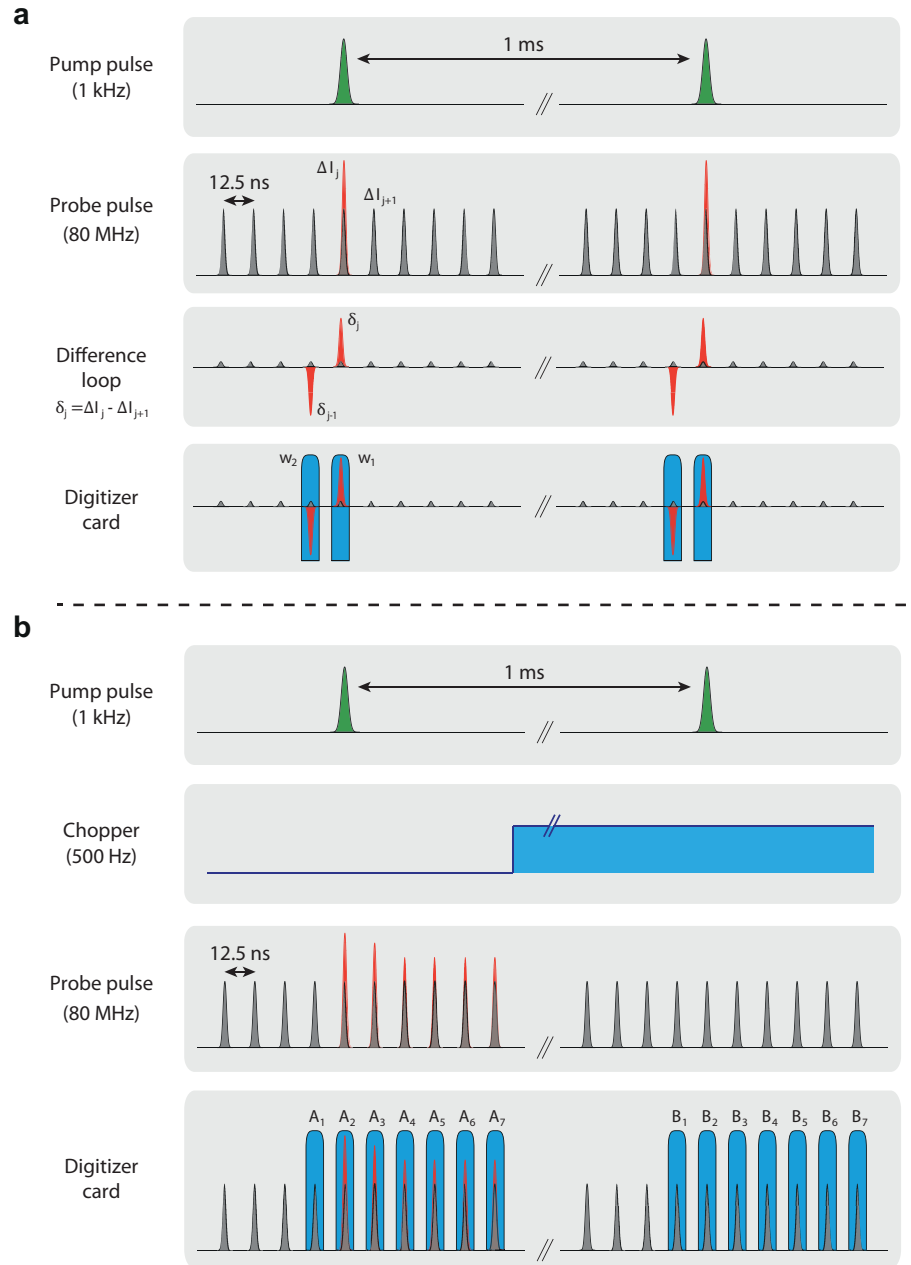


Figure 4.10.: Data acquisition schemes. **a**, Short time scales: Only one probe pulse ΔI_j carries the pump induced modulation. The signal propagation through an electronic difference loop with length corresponding to the repetition rate ($\nu_\varphi/\nu_{\text{rep}}$) results in a pulse train of differences δ_j between adjacent pulses. δ_j and δ_{j-1} are integrated independently and digitized by a broadband digitizer. **b**, Long time scale: The pump pulses are chopped with 500 Hz. After the fixed arrival of the pump pulse, all 80,000 probe shots are integrated separately (A_1, A_2, \dots, A_N). The same array is recorded at the next kHz-trigger signal, when the pump pulse is blocked (B_1, B_2, \dots, B_N). The difference between the chopped **B** and unchopped **A** arrays ideally yields the background free pump induced signal.

5 Ultrafast phonon driven magnetization dynamics

The control of elementary excitations in condensed matter on their natural time- and length scales is one of the major goals in contemporary science. Not only charge carriers or lattice dynamics but also spin degrees of freedom are of great interest (see figure 5.1). For instance, electron spins in spintronic materials are an environmental friendly and promising alternative to conventional electronics and will serve as key players in future information processing [Bad10, Sta14, Chu15]. Central dynamic effects such as magnetization switching [Kir10, Kub14, Fri15, Atx14] and transport of spin angular momentum [Uch08, Ada13, Ser10] require a fundamental understanding of the way spins interact with oscillations of the crystal lattice. However, despite its paramount importance, spin-phonon coupling in magnetically ordered solids is mostly discussed in phenomenological terms [Gur96] while leaving the precise microscopic processes unaddressed.

Within this thesis, an extensive study focusing on ultrafast pure spin-lattice coupling has been conducted together with the development of a novel experimental scheme based on resonant phonon excitation. A purely phonon driven ultrafast change of the magnetic order is found in the textbook ferrimagnetic insulator Yttrium Iron Garnet (YIG). These dynamics proceed on the timescale of 1 ps, several orders of magnitude faster than previously known spin lattice coupling times in the same material [Spe62, Vit85, Hun10]. The coupling mechanism is microscopically modeled by phonon-modulated super-exchange interaction between the two magnetic sublattices, thereby providing a scheme for ultrafast energy transfer from the lattice to the spin system under the constraint of conserved spin angular momentum. We find a much slower additional decay of magnetic order with a time constant of 100 ns, assigned to angular momentum transfer from the spin system to the lattice.

This chapter is based on the publication **Ultrafast phonon driven magnetization dynamics** in preparation by Mährlein et al. (2016) [Mae16b].

5.1 Motivation

The crystal lattice of a solid has a massive impact on the orbital dynamics of the electrons. Lattice vibrations strongly modify properties such as electrical conductivity and can even cause insulator-to-metal transitions [Rin07]. The subtle interplay of phonons and electron spins (see figure 5.1) can lead to similarly important phenomena as illustrated by three examples. First, the colossal magnetoresistance is found in oxides that show a huge change of electrical resistivity upon applying a static magnetic field. Lattice distortions are thought to play a central role for this effect [Tok00].

Second, another current hot topic in fundamental research towards spin-based information processing (spintronics) is the spin Seebeck effect. In analogy to the Seebeck effect [Geb55], the spin Seebeck effect describes how a spin current is generated in a magnetic

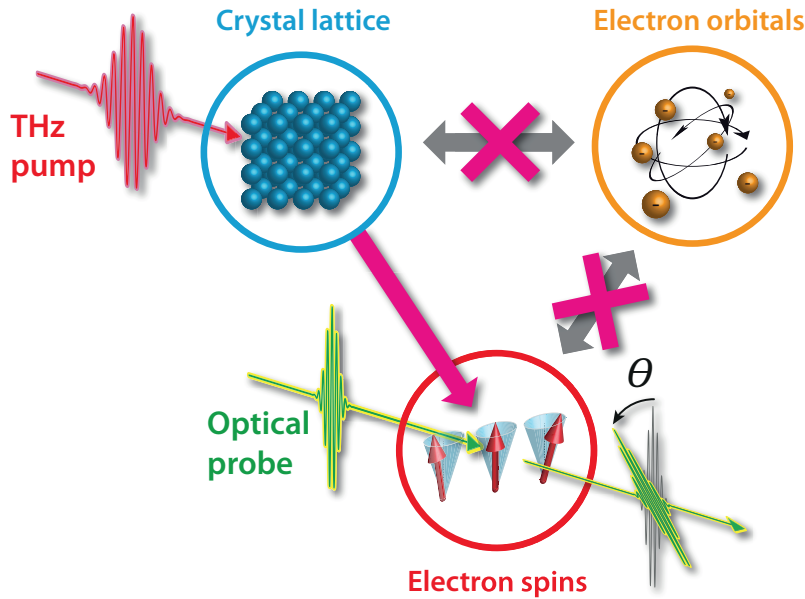


Figure 5.1.: Experimental principle. A THz pump pulse (red pulse) resonantly and exclusively excites optical phonons of a ferrimagnet. The resulting impact on the sample magnetization is monitored by the Faraday rotation $\theta(t)$ of a subsequently arriving femtosecond probe pulse (green pulse). By using a ferrimagnetic electric insulator, the electron orbital degrees of freedom are frozen out (indicated by red crosses).

material in response to a temperature gradient. [Uch08, Uch14, Ada13, Ros14]. Notably, this effect occurs in magnetic insulators where it produces a pure spin current without any transport of charges. The applications of the spin Seebeck effect could lead to the production of spin-voltage sources, which are crucial for the development of spintronic devices [Wol01, Cha07]. Here, the role of temperature dependent lattice properties and the applicability at THz-frequencies are still open research questions.

Third, one of the most advancing fields in magnetism in the last two decades is ultrafast magnetization switching [Kir10, Kub14, Fri15, Atx14]. Since the pioneering work by Beaurepaire and co-workers [Bea96], ultrafast spin dynamics has been observed in metals and insulators by using ultrashort visible or NIR pump pulses [Hue98, Big09, Kim02, Gui02, Kir10, Rad11]. However, the roles of orbital, spin and lattice degree of freedom, as sketched in figure 5.1, could not be fully disentangled and are still under debate.

In general, phenomenological models have provided deeper insights into macroscopic interactions of magnetization and lattice [Koo10], but the microscopic origin of spin-phonon coupling in the processes mentioned above remains an intriguing problem.

The novel approach of this thesis makes use of the latest advances in THz photonics (see chapter 4). The presented generic scheme directly probes spin-lattice coupling on the time scale of elementary scattering processes. As shown by figure 5.1, an incident intense ultrashort THz pump pulse selectively excites the crystal lattice by resonantly driving infrared-active transverse-optical (TO) phonons. The complexity of the subsequent process is significantly reduced by investigating electronic insulators in which the electron

orbital degrees of freedom are frozen out (see figure 5.3).

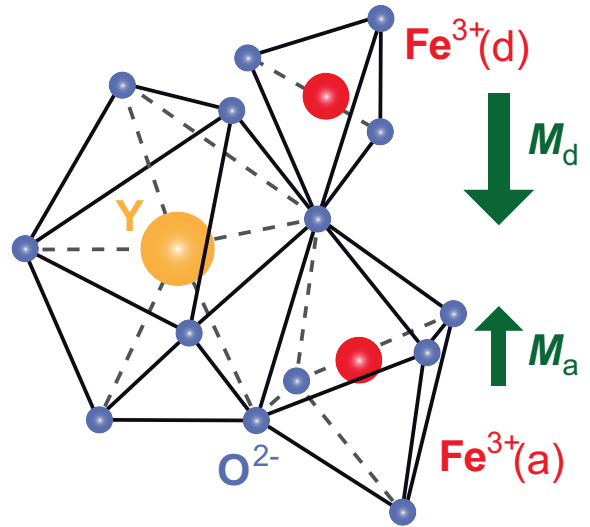
In the following, properties of the sample system Yttrium Iron Garnet (YIG) are introduced (section 5.2), followed by the experimental details (5.3), before the results are presented and discussed in section 5.4 and 5.5.

5.2 Sample system: iron garnets

Magnetically ordered garnets are ideal material systems for a variety of magnetic phenomena in theory and experiments [Che93b, And64, Sol62, Agr13, Kum67, Ser10]. Here, the ferrimagnetic insulators yttrium iron garnet $\text{Y}_3\text{Fe}_5\text{O}_{12}$ (YIG) and bismuth/gallium-substituted YIG (BiGa:YIG)¹ are chosen. YIG is a model magnetic system for spin dynamics and transport in insulators in numerous studies [Uch14, Ros14, Ser10, Gur96, Kur11, Deb15] Its electronic band gap (2.85 eV) exceeds the THz pump photon energy (20 THz $\hat{=}$ 85 meV) by more than one order of magnitude. Furthermore, magnetic Fe^{3+} ions at a- and d-sites in the unit cell (see figure 5.2) comprise two inequivalent, ferromagnetic sublattices that couple antiferromagnetically, resulting in nonzero net magnetization below the Curie temperature T_C . YIG and doped YIG accordingly fulfills the requirements of a spin ordered large bandgap insulator at room temperature.

5.2.1 Lattice structure

Figure 5.2: Part of the unit cell of ferrimagnetic YIG. Magnetic Fe^{3+} ions at tetrahedral d-sites and octahedral a-sites comprise the spin sublattices of the ferrimagnet. The Y ion is located in a dodecahedral oxygen surrounding and does not contribute to the magnetic properties. The two magnetic sublattices (indicated by green arrows) are established by 12 d-site Fe^{3+} atomic spins ($S_d = 5/2$) and the 8 a-site Fe^{3+} atomic spins ($S_a = 5/2$) per unit cell.



The most common natural garnet contains calcium instead of yttrium and aluminum and silicon instead of iron ($\text{Ca}_3\text{Al}_2\text{Si}_3\text{O}_{12}$) [Che93a]. Garnets grow in a typical bcc structure with a space group of O_h^{12} and a lattice constant of 12.4 Å. YIG cannot be found in nature and therefore has to be grown with special techniques such as liquid-phase epitaxy or chemical transport reaction [Che93a]. Generally, the garnet unit cell is centrosymmetric,

¹The substitution with Bismuth ions increases the magneto-optic coupling constants and therefore vastly improves the signal to noise ratio of magneto-optic probing techniques. Gallium substitution dilutes the d-iron sites and therefore reduces the Curie temperature.

but the inversion symmetry can be broken during epitaxial growth process [Han06a]. The typical garnet structure contains two inequivalent iron sites, which are defined by the coordination of the surrounding oxygen atoms. Summing up over the whole unit cell this leads to eight octahedral sites (a-sites) and twelve tetrahedral sites (d-sites) both occupied by Fe^{3+} ions. The unit cell can be subdivided into fundamental formula units; part of it shown in figure 5.2. The large unit cell enables the substitution of ions by a wide variety of cations. For instance, the dodecahedral Yttrium sites can be partly occupied or even completely substituted by nearly all rare earth ions. In this work, a substitution with Bi^+ ions is exploited, which increases the magneto-optic activity (see sample properties in section 5.3.2).

5.2.2 Absorption spectrum

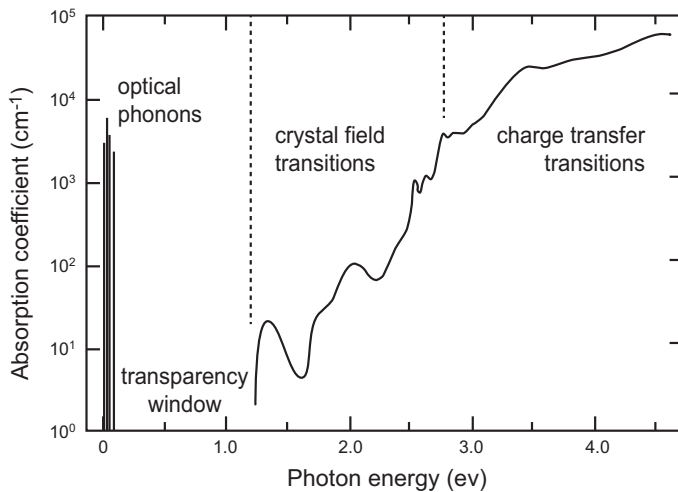


Figure 5.3: Absorption spectrum of YIG. Above the electronic bandgap ($E_g = 2.85$ eV), charge transfer transitions lead to an increased absorption. Crystal field transitions can still absorb electromagnetic radiation even below the electronic band gap down to a photon energy of about 1 eV. From roughly 100 meV to 1 eV, in the so called transparency window, no measurable absorption can be found. For photon energies below 100 meV, the absorption increases abruptly due to the onset of IR-active phonon resonances (figure taken from [Han06a]).

The schematic absorption spectrum of Yttrium iron garnet is shown in figure 5.3. The optical properties are mostly governed by the large electronic Bandgap of 2.85 eV, that provides the dominant contribution to the absorption at the high frequency end of the visible spectrum, spreading to UV-frequencies. However, even below the band gap, so called crystal-field transitions lead to minor but non-negligible absorption. These transitions are caused by the lifting of the degeneracy of the iron d -orbitals due to the octahedral and tetrahedral oxygen ligand field [Pap62, Vie75].

Below $1.5 \mu\text{m}$ down to approximately $10 \mu\text{m}$ (≈ 30 THz) there is no absorption ($\alpha \ll 0.03 \text{ cm}^{-1}$) [Win81, Hof92]. This frequency range is usually called transparency window. At the low frequency end of the transparency window (< 30 THz), absorption increases suddenly due to IR-active phonons. It is important to note that in the THz range linear absorption solely arises from phonon absorption.

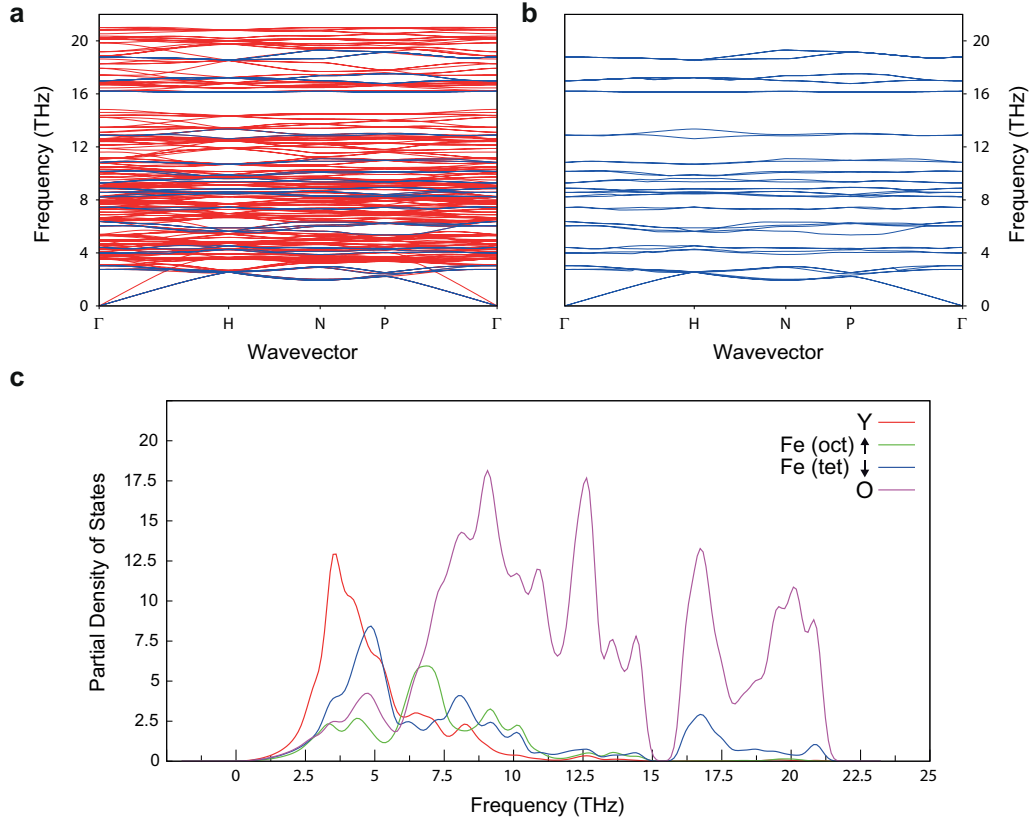


Figure 5.4.: Phonon dispersion of YIG (ab-initio calculation). [Mal16]. **a**, Phonon dispersion branches along high-symmetry lines calculated with DFT methods (IR-active modes in blue). **b**, IR-active phonon modes only. **c**, Element resolved phonon density of states (DOS) of the IR-active phonon branches. All calculations for temperature $T = 0$ K.

5.2.3 Phonon properties

Due to the vast number of 80 atoms in the unit cell, the phonon bandstructure is up to now too complicated to be fully resolved by means of experimental methods. Therefore, for this work, P. Maldonado² and P.M. Oppeneer² calculated the full phonon bandstructure and its element-resolved phonon density of states (DOS) by using an ab-initio approach [Mal16]. They first calculated the electronic structure within the density-functional theory (DFT) framework in order to obtain the electronic ground state properties [Kre96]. Afterwards they obtained the ground state lattice geometry by a finite-displacement method [Tog09] while a DFT method was employed to calculate the interatomic force constants. These calculations were performed using supercells with $2 \times 2 \times 2$ primitive cells (640 atoms). For a detailed description of these ab-initio studies please refer to the supplementary material of our common paper [Mae16b].

The ab-initio results for the 240 phonon dispersion branches along the high-symmetry lines are shown in figure 5.4 a. The blue lines indicate infrared (IR)-active phonon modes, which have been identified by symmetry considerations. They are accompanied by

²Department of Physics and Astronomy, Uppsala University, Box 516, 75120 Uppsala, Sweden

a nonzero electric dipole moment and can be resonantly excited by IR light near the Γ -point. The IR-active TO modes in the range from 16 to 20 THz are of particular interest for understanding the nature of the resonant THz excitation. Below 16 THz, a phononic bandgap is clearly visible. For better visibility, in figure 5.4 b, only the IR-active phonon modes are shown. The density of states for all phonon modes is displayed in figure 5.4 c. A closer analysis of the phonon DOS shows that the 3 double degenerate IR-active phonon modes above the phonon bandgap correspond to dipolar Fe-O stretch vibrations at the tetrahedral Fe-site [Hof92]. These are the coherent lattice modes that are mainly excited by intense THz pump fields with central frequencies around 20 THz.

5.2.4 Magnetic order and magnon dispersion

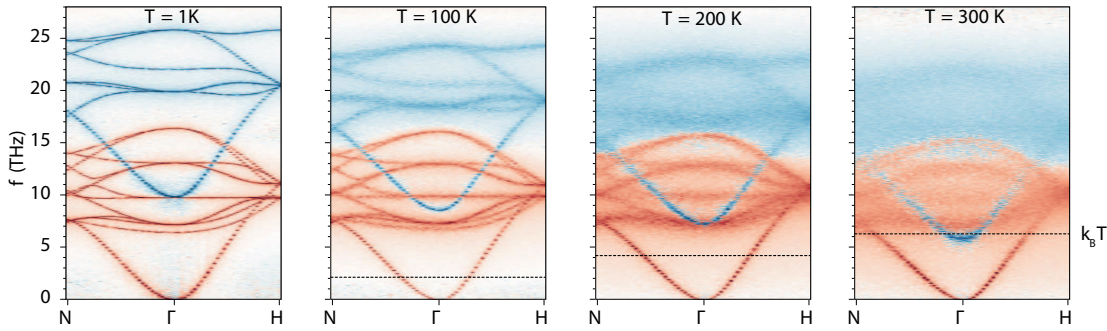


Figure 5.5.: Magnon dispersion of YIG. Atomistic spin dynamics simulation (see section 5.7.2) by J. Barker et. al yields all 12 ferromagnetic (red lines) and all 8 antiferromagnetic magnon branches (blue lines) for several equilibrium temperatures T_0 . The dashed lines mark the energy $k_B T$. Figure taken from [Bar16].

The fundamental magnetic properties of YIG are determined by the Fe^{3+} ions and the surrounding oxygen ions. The coordination of the oxygen ions at the two distinct iron sites (octahedral a -sites and tetrahedral d -sites) influence the electronic configuration and mediate the superexchange interaction between the iron ions at both sites. Each of the Fe^{3+} ions is in a $3d^5$ electronic configuration and carries a magnetic moment of $5 \mu_B$. Due to the antiferromagnetic coupling via superexchange, each of the two lattice sites builds up a magnetic sublattice with opposite magnetic orientation. Due to the 3:2 number ratio of d - and a -iron ions, the two sublattices cannot compensate each other and thus cause a ferrimagnetic order below the Curie temperature T_C [Che93a]. The Curie temperature for pure YIG is usually found around 560 K [Che93a]. Substituting the tetrahedral (d -site) with nonmagnetic Ga^{3+} leads to a lowering of the Curie temperature T_C and a reduction of the net magnetization.

The strong exchange interaction between the nearest neighbor a -site Fe^{3+} -ions and d -site Fe^{3+} -ions is determined by the exchange constant $J_{ad} = -3.45$ meV. All other exchange contributions are much weaker (e.g. $J_{dd} = -1.15$ meV and $J_{aa} = -0.33$ meV) [Che93a]. The total magnetic moment of a unit cell is $10 \mu_B$.

The calculated magnon spectrum of YIG is shown in figure 5.5. In principle, the zero temperature magnon dispersion $\omega_r(q)$ can be calculated by diagonalizing the Hamiltonian of the non-interacting magnon system [Che93a]. The resulting number of 20 branches arises due to the 20 magnetic iron sites in the YIG magnetic primitive unit cell. While 8 branches describe antiferromagnetic modes, the other 12 branches have ferromagnetic character. Excitation of an antiferromagnetic/ferromagnetic magnon increases/decreases the YIG magnetization by one Bohr magneton, respectively [Rub12]. Figure 5.5 shows the ferromagnetic (red) and antiferromagnetic (blue) magnon branches for different temperatures calculated via atomistic spin dynamics by J. Barker³ and G. Bauer³ [Bar16]. At room temperature the magnon branches are broadened so much, that they nearly offer a full overlap with the phonon bandstructure (see figure 5.4) and therefore generally enable magnon phonon coupling.

5.3 Experimental details

5.3.1 Experimental setup

The schematic of the pump-probe experiment is shown in figure 5.6 a. An intense THz pump pulse (center frequency ~ 21 THz, pulse energy $3 - 10 \mu\text{J}$, pulse duration ~ 200 fs), generated by the table top high field source (introduced in section 4.2), resonantly excites the Brillouin center TO-phonons above the phonon bandgap (> 16 THz). Thereupon, the instantaneous magnetic state of the sample is determined by a subsequent synchronized 8 fs optical probe pulse (repetition rate 80 MHz, center wavelength 750 nm, pulse energy 1 nJ) measuring the magneto-optical Faraday effect (see section 4.3.2). The actual physical quantities probed by the magneto-optical signal $S(t)$ are discussed in section 5.3.3. In order to distinguish non-magnetic and magnetic contributions, Faraday ellipticity $\eta(t)$, Faraday rotation $\theta(t)$ and isotropic transmission change ΔT_r is measured. By changing the pump-probe delay t with a high precision motorized stage, the magnetization dynamics are monitored over a large range of pump-probe delays up to 500 ps. The pump-probe range up to milliseconds is covered by the advanced long time-scale data acquisition method (see section 4.3.3). Additionally, after every 5th full delay cycle the sign of the external magnetic field \mathbf{B}_0 is switched.

The detailed experimental setup is shown in figure 5.6 b. The THz-pump pulse and the ultrashort probe pulse are always collinearly incident onto the sample. The sample orientation is adjusted such that the external magnetic field has sufficient projection on the easy magnetization axis to saturate the magnetization \mathbf{M} . Simultaneously, the projection of the magnetization \mathbf{M} along the propagation direction of the probe pulse $\hat{\mathbf{k}}$ should be optimized in order to get most the Faraday signal $\theta \propto \mathbf{M} \cdot \hat{\mathbf{k}}$ (see section 4.3.2). This leads to an angle of incidence (AOI) of 0° and about 45° for BiGa:YIG (easy axis out-of-plane) and pure YIG (easy axis in-plane) respectively. Faraday rotation (FR) and Faraday ellipticity (FE) are measured using a balanced detection scheme with a half-waveplate (HWP)

³Institute for Materials Research, Tohoku University, Sendai 980-8577, Japan

or quarter-waveplate (QWP) respectively. Further details of the beam path are described in section 6.3.2.

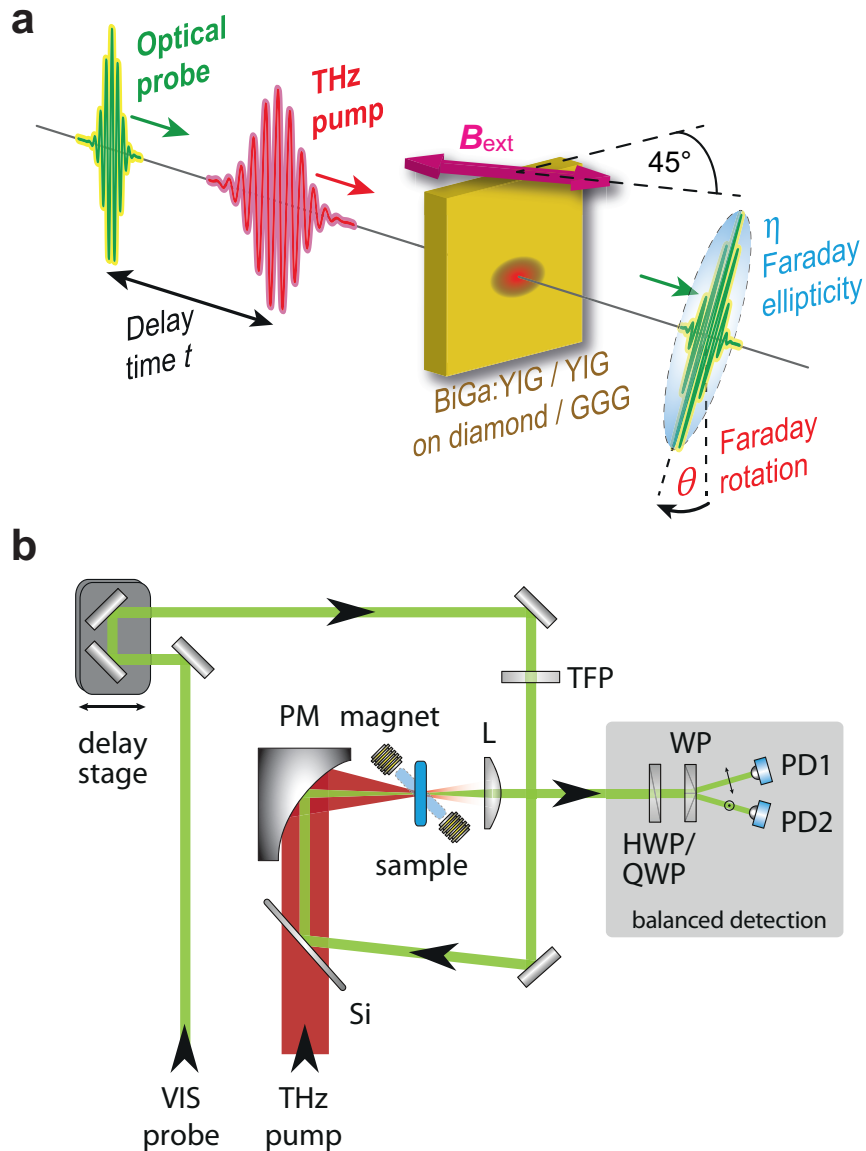


Figure 5.6.: Experimental details. **a**, Experimental scheme of THz pump/magneto-optical probe spectroscopy. The sample's out of plane magnetization is saturated by an external static magnetic field B_{ext} . The magnetization dynamics induced by the THz pump pulse are monitored by the Faraday ellipticity $\eta\theta(t)$ and Faraday rotation $\theta(t)$ of the transmitted pump pulse, which is delayed by a time t . **b**, Experimental setup. Pump and probe beam copropagate, focused by the same off-axis parabolic mirror, with an angle of incidence of 0° or 45° for out-of-plane or in-plane easy axis, respectively. The resulting probe beam polarization is resolved by a balanced detection scheme.

5.3.2 Sample details

The iron garnet films were grown by liquid-phase epitaxy on gadolinium gallium garnet $\text{Gd}_3\text{Ga}_5\text{O}_{12}$ (GGG) substrates by the group of R.V. Pisarev⁴. To prevent pump absorption by the substrate, several iron-garnet films are transferred on diamond windows after mechanically removing the GGG substrate. Test measurements confirm that GGG pump absorption is irrelevant to the ultrafast dynamics. Mostly two types of garnet samples were studied: pure yttrium iron garnet $\text{Y}_3\text{Fe}_5\text{O}_{12}$ (YIG) and bismuth/gallium-substituted iron garnet $\text{Bi}_x\text{Y}_{3-x}\text{Ga}_y\text{Fe}_{5-y}\text{O}_{60}$ ($x = 1.53$, $y = 1.33$, BiGa:YIG) with, respectively, a Curie temperature of 545 K and 398 K, and in-plane and out-of-plane magnetic anisotropy. Film thicknesses cover a range from 7 to 20 μm . Chemical composition of the garnet films was determined by X-ray fluorescence measurements by A. Kalashnikova⁴. Substitution of Y by Bi in the BiGa:YIG sample enhances the magneto-optical Faraday effect by one order of magnitude [Han81, Han84] in the visible frequency range. Typical hysteresis loops obtained by measuring the static Faraday rotation of the probe beam are shown in figure 5.7.

THz absorption spectra (such as that of BiGa:YIG later shown in figure 5.9 a) are obtained by combined reflection and transmission measurements with a broadband THz time-domain spectrometer [Rub12]. The maximum absorption occurs at 21 THz (see figure 5.9 a), which is 2 THz above the highest-frequency TO(Γ)-phonon resonance [Hof92] because absorption strength and low reflectance have optimum values at this frequency (restrahlen band effect). As mentioned before, absorption in this frequency range solely arises from TO phonons [Hof92], because Fe^{3+} crystal-field excitations and electronic charge transfer transitions appear at much higher frequencies (see figure 5.3).

5.3.3 Signal Analysis

All investigated pump-probe signals, such as transmission $\Delta T_{\pm}(t)$, Faraday ellipticity $\Delta\eta_{\pm}(t)$ and Faraday rotation $\Delta\theta_{\pm}(t)$ are traced for opposite external magnetic fields $\pm B_0$ in every measurement. To analyze these signals, we recall that magnetization and magneto-optical coupling induce an optical anisotropy in the sample which results in an elliptical polarization of the initially linearly polarized probe pulse (Faraday effect). Up to the linear order in magnetization, the Faraday rotation θ (and likewise the ellipticity η) of the probe's outgoing polarization is a weighted average [Han84] of the magnetization of the two sublattices $m = a, d$, that is,

$$\theta = \sum \langle a_m M_m \rangle d + b. \quad (5.1)$$

Here, a_m are the local magneto-optic coupling constants of YIG, $M_m = \hat{\mathbf{k}}_{\text{pr}} \cdot \mathbf{M}_m$ is the magnetization of sublattice m projected on the propagation-direction unit vector $\hat{\mathbf{k}}_{\text{pr}}$ of the probe beam, d is the sample thickness, and b is an offset arising from any magnetization-independent optical anisotropy. The angular brackets $\langle \cdot \rangle$ denote averaging over the probed

⁴Ioffe Physical Technical Institute, *Russian Academy of Sciences*, St. Petersburg

sample volume.

5.4 Results: equilibrium measurements

5.4.1 Static Hysteresis at room temperature

In order to understand complex phonon-induced magnetization dynamics, the unperturbed equilibrium state of the magnetically ordered system has to be investigated first. Therefore magneto-optic measurements as described in section 5.3 are applied.

Figure 5.7 shows the static magnetization M of both YIG and BiGa:YIG samples dependent on the external static magnetic field B_0 . This total static magnetization M is measured via the linear Faraday rotation θ as a function of the external magnetic field B_0 (see equation 5.1). $M(B_0)$ shows a typical hysteresis behavior [Han06b] (see figure 5.7). Saturation along the easy magnetization axis is already achieved by applying a static magnetic field $|B_0| > 5$ mT. By using an electromagnetic coil, these field strengths can be reached easily and remotely controlled by variation of the coil current.

The spatial homogeneity of the magnetic saturation was verified by polarization micro-

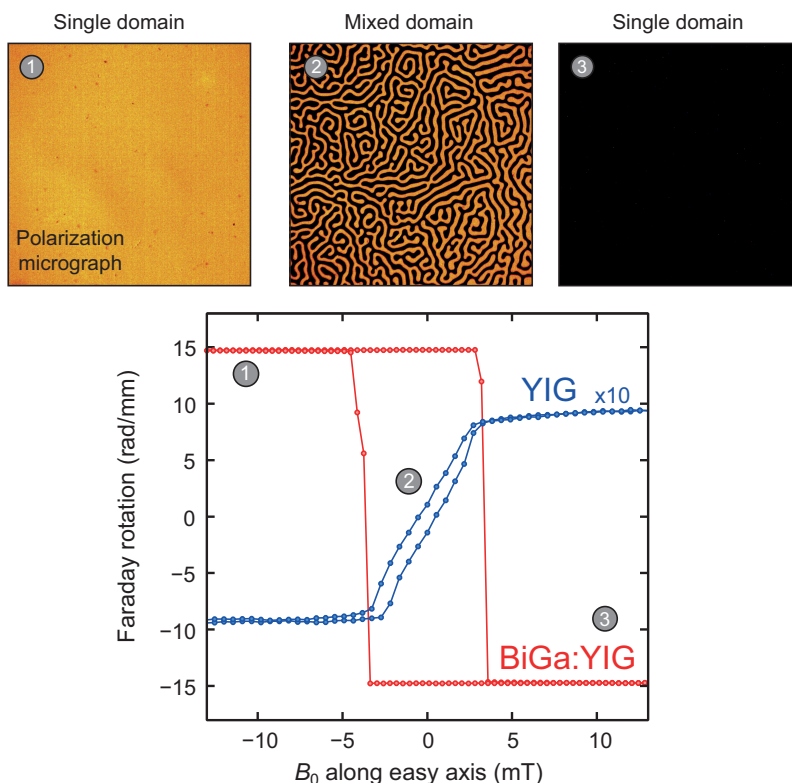


Figure 5.7.: Measurement of the static magnetization. **Lower panel**, Hysteresis loops of YIG and BiGa:YIG samples measured by the Faraday effect. The magneto-optic signals show clearly opposite sign and magnetic saturation for static fields $|B_0| \geq 5$ mT. **Upper panels**, Faraday rotation micrographs of the BiGa:YIG sample taken at three points of the loop. The sample exhibits a single domain state in magnetic saturation (state 1 and 3).

graphs (figure 5.7, upper panels). The micrographs were taken in a crossed polarizer-analyzer geometry [Car11a, Dil58]. For magnetic saturation ($|B_0| > 5$ mT), a homogeneous single-domain state is confirmed, indicated by the polarization micrograph in state 1 and 3 in figure 5.7. For the unsaturated case (state 2), a typical mixed domain state is observed [Wan16, Dil58, Eno75].

As mentioned before (section 5.3.2), the Bismuth substituted sample exhibits an increased magneto-optic effect, which manifests in an enhanced Faraday rotation of nearly ± 15 rad ($\approx \pm 859^\circ$) per mm sample thickness. This is in agreement with similarly Bi-substituted YIG samples [Han06b]. Pure YIG shows one order of less signal magnitude, which makes the observation of small transient magnetization changes challenging (section 5.5.6). Additionally the sign of the static signal is flipped in pure YIG compared to BiGa:YIG.

In equilibrium, the magneto-optic factors a_m are constant throughout the probed magnetic volume, resulting in $\theta = \sum a_m \langle M_m \rangle$ according to equation 5.1. The different sign of the Faraday rotation for YIG and BiGa:YIG arises from their different magneto-optic constants at the probing wavelength around 800 nm due to the Bi-doping [Han84]. While M_d approximately equals $-1.5M_a$ for both materials in magnetic saturation, $a_d M_d \approx -0.9a_a M_a$ in YIG differs from $a_d M_d \approx -2.3a_a M_a$ in BiGa:YIG [Han84]. Therefore, in YIG, the Faraday signal is dominated by a-sublattice contributions, whereas in BiGa:YIG the signal stems mostly from the magnetic d-sublattice.

For all following experimental series, full static hysteresis loops were measured in order to calibrate the static Faraday signals $\theta_0 = \theta(B_0 < -10 \text{ mT}) - \theta(B_0 > 10 \text{ mT})$.

5.4.2 Temperature dependence of the equilibrium Faraday rotation

One of the most important properties of a magnetization state is its temperature dependence because magnetic phenomena are directly related to spin order effects and their phase transitions. To vary the equilibrium temperature T_0 , the sample was glued onto a copper ring with a high thermal conductivity glue⁵. Afterwards, the copper ring was mounted on a home built temperature controlled sample holder.

Importantly, as the magneto-optic coupling constants a_d and a_m can be considered temperature independent [Han84], the static Faraday rotation θ_0 is proportional to the equilibrium total magnetization $M_0(T_0)$ and can be therefore directly determined from temperature dependent hysteresis. Hence, for every temperature T_0 a full hysteresis loop is measured, leading to the result shown in figure 5.8. Here, the inset of figure 5.8 a shows the difference in temperature dependence $\theta_0(T_0)$ of pure YIG and the BiGa:YIG sample. The two curves show a similar shape, but the critical temperature T_C is reduced in the BiGa:YIG sample due to the substitution of tetrahedral iron ions with Gallium ions [Che93a, Han06a].

The BiGa:YIG $\theta_0(T_0)$ curve was measured in more detail, shown by the blue and red circles in figure 5.8 a. The two different colors belong to two sets of measurement and therefore demonstrate the small error bar of these static measurements. Accordingly, the

⁵EPO-TEK 301-2

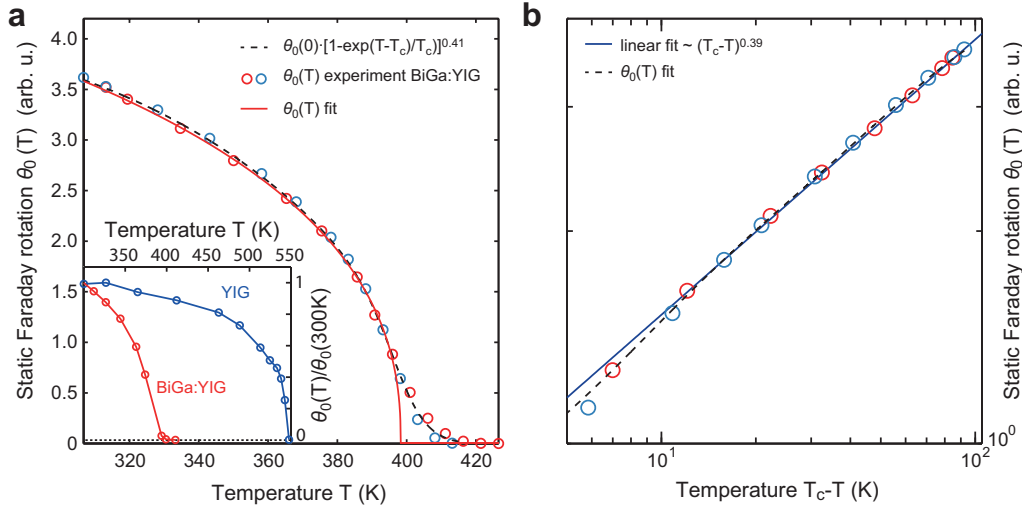


Figure 5.8.: Temperature dependent static magnetization. **a**, Temperature dependence of static Faraday rotation θ_0 (blue and red circles) of BiGa:YIG. The inset shows the difference in critical temperature between YIG and BiGa:YIG, mainly caused by the Ga doping. **b**, The double logarithmic plot reveals a good agreement with the expected ferrimagnetic behavior with fitted critical exponent $\beta = 0.39$. Small deviations close to T_C are caused by the onset of the paramagnetic phase (in agreement with simulation in figure 2.5).

$\theta_0(T_0)$ curve exhibits a typical ferrimagnetic behavior [Nol05] that is reproduced by MFA simulations in figure 2.5.

Moreover, the critical exponent β of this second order phase transition and the critical temperature T_C can be fit with the function:

$$\theta_0(T) = \theta_0(T = 0) \cdot \left[1 - \exp\left(\frac{T - T_C}{T_C}\right) \right]^\beta. \quad (5.2)$$

The fit procedure leads to $T_C = 398$ K and $\beta = 0.41$. Both values are in perfect agreement with previous studies of similar doped YIG samples [Han06b, Win81]. Complementary, the critical exponent can also be obtained from a linear fit, when θ_0 is plotted double logarithmically versus $T - T_C$. This nearly leads to the same critical exponent $\beta = 0.39$ (see blue line in figure 5.8 b).

On the other hand, both fitting procedures fail on the tail of the $\theta_0(T)$ -curve close to and slightly above T_C . This tail is caused by a paramagnetic contribution, induced by the external static field B_0 [Nol05]. A more accurate match of this paramagnetic tail is captured by a MFA simulation such as shown in figure 2.5.

Nevertheless, a better fit function is required in order to determine the expected $\partial\theta_0(T)/\partial T$ behavior that is need for comparison to the phonon induced magnetization dynamic in section 5.5.7. Thereupon, the phenomenological fit function

$$f(T) = A \frac{1 - (T/T_C)^E}{\exp\left(\frac{T-B}{D}\right)} \quad (5.3)$$

was developed with fit parameters A, B, D and E . Here the nominator accounts for the general trend below T_C and the denominator for the tail close and above T_C . The fit results in figure 5.8 a and b (broken lines) proof that $f(T)$ gives an adequate analytical function for $\theta_0(T)$, which can be used for further derivations.

5.5 Results: phonon driven ultrafast magnetization dynamics

In the following sections, the most important results stemming from the exclusive phonon excitation by intense THz fields are presented. Their implications will be discussed directly, while a microscopic model of the interaction will be developed in section 5.6 and 5.7.

5.5.1 External magnetic field dependence

To study the phonon dependence of the magnetization dynamics, we first focus on the evolution of the transient Faraday rotation $\Delta\theta$ upon excitation on the high frequency Γ -phonon resonances and off any phonon resonance (in the transparency window). The corresponding spectra, measured via EOS, are given in figure 5.9 a by the red line and the blue line respectively. Additionally, the phonon absorptance measured by a broadband THz time-domain spectrometer [Rub12] is indicated by the grey area. A typical THz pump pulse (on resonance) is shown in panel 5.9 b.

Figure 5.9 c displays the pump-induced change $\Delta\theta_{\pm}$ in the Faraday rotation as a function of the delay time t since excitation and dependent on the external field direction $\pm B_0$. For pumping off the phonon resonances (blue pump spectrum in figure 5.9 a), a relatively small long-lived signal is found (blue curve in figure 5.9 c). In striking contrast, a more than one order of magnitude stronger response is witnessed for resonant Γ -phonon excitation (red curve in figure 5.9 c). The pump-probe signal exhibits an ultrafast single-exponential change in the transient Faraday rotation.

In order to remove nonmagnetic signal contributions (d term in equation 5.1), the difference signal (or sometimes called *double differential signal*) normalized to static signals $\theta_{0,\pm}$ is calculated:

$$\frac{\Delta\theta}{\theta_0} = \frac{\Delta\theta_+ - \Delta\theta_-}{\theta_{0,+} - \theta_{0,-}} \quad (5.4)$$

From this difference signal, shown in figure 5.9 d, it is obvious that the long-lived, magnetic field dependent pump-probe signal shows resonance behavior with respect to the phonon absorption (compare red vs. blue curve). In contrast, the instantaneous signal during the pump-probe overlap ($-200 \text{ fs} \lesssim t \lesssim 200 \text{ fs}$) is also present off the resonance. In the difference signal (figure 5.9 d), remainders of this contribution in form of sharp peaks are found, which are due to a small total temporal drift between single delay cycles with opposite field direction.

In summary, the data of figure 5.9 are the first demonstration of a magnetic field de-

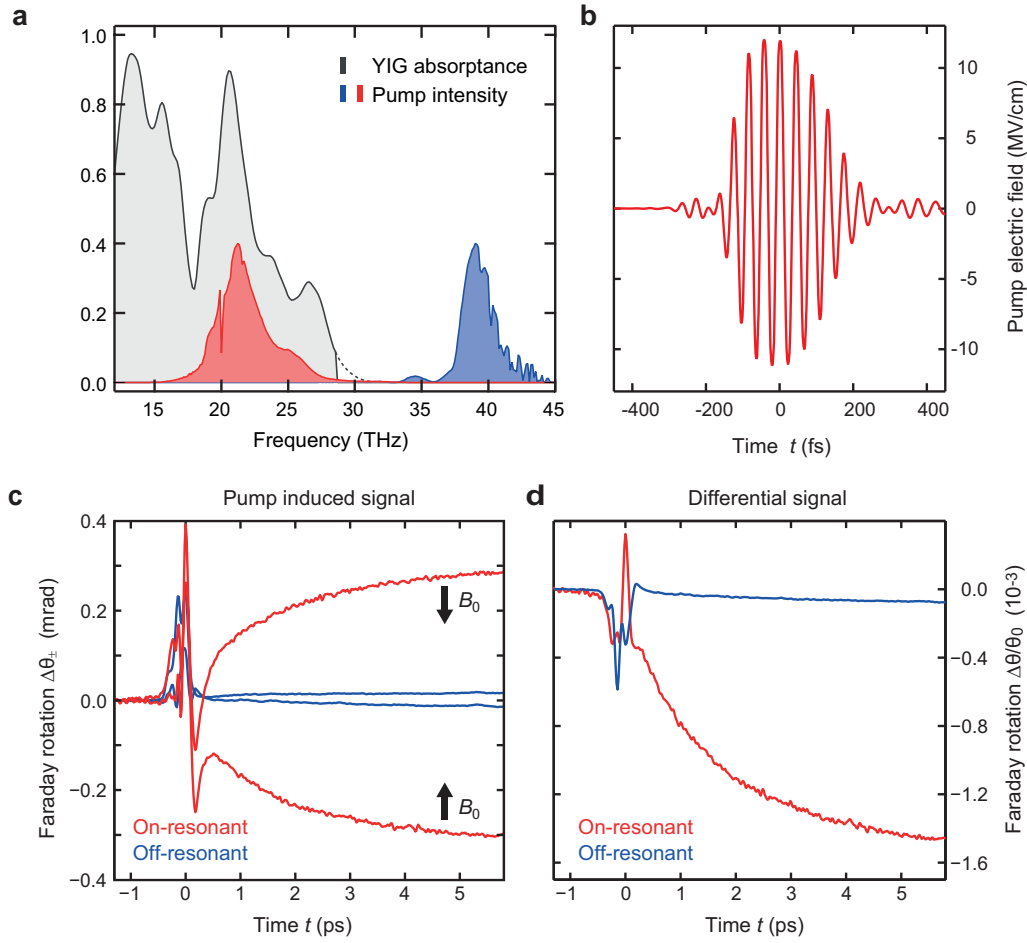


Figure 5.9.: Ultrafast phonon-driven dynamics. **a**, Infrared absorbance of the BiGa:YIG film (grey solid line) as well as pump intensity spectra resonant (red) and non-resonant (blue) with the TO(Γ) phonon absorption band. **b**, Transient electric field of a typical THz pump pulse measured by electrooptic sampling **c**, Transient Faraday rotation $\Delta\theta_{\pm}(t)$ of resonantly and off-resonantly excited BiGa:YIG for external saturating magnetic fields of ± 15 mT. **d**, Difference signal $\Delta\theta/\theta_0$ indicating the magnetic field dependent contribution. Clearly, the long lived signal is dominating, when pumping on the phonon resonance, whereas it is negligible for pumping off resonantly.

pendent ultrafast pump-probe signal with a clear resonance behavior upon excitation of the high frequency TO Γ -phonons. Moreover, the magneto-optical signal shows surprisingly fast dynamics on the order of 1 ps, and the resulting state survives for more than 500 ps.

5.5.2 Magnetic versus nonmagnetic contributions

To interpret the measured dynamics, we start with a general reminder: One has to be very careful with a measured anisotropic signals change, because it may also contain variations of nonmagnetic contributions [Koo00]. In the experimental study of this section, the magnetic contribution will be ascertained.

As mentioned in the section before, the change of the constant b can be discriminated by taking the difference signal for two opposite saturation magnetizations $\Delta\theta(t)$. Nevertheless,

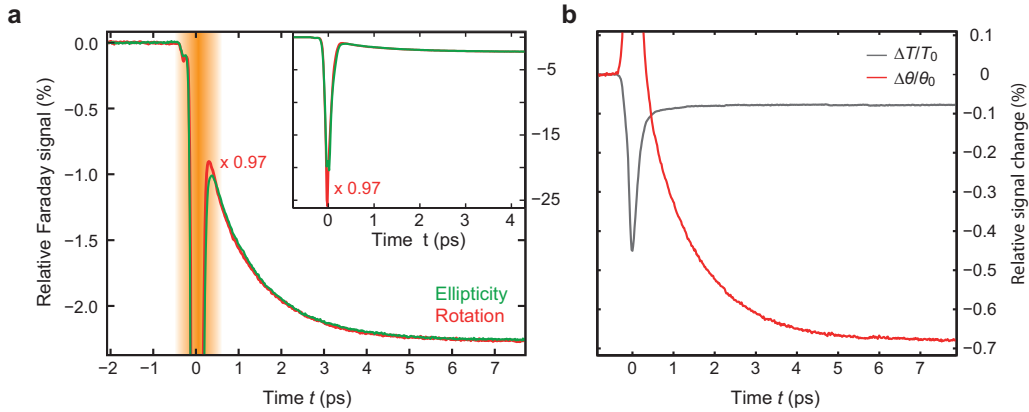


Figure 5.10.: Dynamics of Faraday signals and transmission change. **a**, Relative transient Faraday rotation $\Delta\theta/\theta_0$ and ellipticity $\Delta\eta/\eta_0$ of BiGa:YIG upon phonon pumping. Equal dynamics for $t > 200$ fs indicate magnetic origin, whereas the inset reveals non-magnetic contributions during the temporal pump-probe overlap. **b**, The isotropic transmission change $\Delta T_r/T_{r,0}$ is one order of magnitude weaker and shows a step like temporal behavior. Thus it no little influence on the magneto-optical signals $\Delta\theta/\theta_0$ and ellipticity $\Delta\eta/\eta_0$.

the impact of the pump pulse makes all quantities in equation 5.1 time-dependent [Kam02], resulting in relatively small changes $\theta(t) - \theta_0$ of the signal $\theta_0 = \theta(-2 \text{ ps})$, which can be also measured 2 ps before arrival of the pump pulse. As seen in figure 5.9 c, the transient Faraday rotation $\Delta\theta_{\pm}(t)$ reverses almost completely with the external saturating magnetic fields of ± 15 mT, apart from the region around $t = 0$. To analyze the content of the difference Faraday signal $\Delta\theta$, equation 5.1 is linearized to [Kam02]

$$\Delta\theta(t) = \frac{\Delta\theta_+ - \Delta\theta_-}{2} = \sum [a_{m,0} \langle \Delta M_m \rangle + M_{m,0} \langle \Delta a_m \rangle]. \quad (5.5)$$

The first term on the right-hand side scales with a weighted average of the sublattice magnetizations along the probe propagation $\hat{\mathbf{k}}_{pr}$, which is the quantity we are interested in. The second term, however, makes a contribution independent of the ΔM_m and arises from a possible pump-induced modulation Δa_m of the Verdet constants. The following arguments show that the second term is negligible and $\Delta\theta$ reflects the true magnetization dynamics.

Figure 5.10 a shows measurements of both relative transient Faraday rotation $\Delta\theta/\theta_0$ and ellipticity $\Delta\eta/\eta_0$ versus time t . The sharp feature around $t = 0$ is different for Faraday rotation and ellipticity signals. Its temporal extent coincides with the duration of the pump pulse (roughly indicated by the orange shaded area), and its magnitude and shape are found to depend sensitively on experimental geometry. Therefore, this feature cannot be dominated by true magnetization dynamics [Koo00, Koo03] and is, instead, assigned to the instantaneous optical birefringence induced by the presence of the pump pulse [Hof09]. Once t is large enough such that pump and probe pulses do not overlap any more, Faraday rotation and ellipticity signals take an identical course (see figure 5.10 a), thereby suggesting that both $\Delta\theta$ and $\Delta\eta$ reflect pure magnetization dynamics [Koo00].

Another source of non-magnetic signal contributions are isotropic transmission changes. These could produce additional contributions in the case of imperfect balancing of the differential photodiodes. In order to rule out this source of errors, the pump-induced transmission change was measured $\Delta T_r/T_{r,0}$ separately. The result is shown in figure 5.10 b, which displays a smaller signal and step-like temporal behavior of the isotropic transmission change (grey line). Accordingly, this cannot produce any exponentially decaying signal.

5.5.3 Time scales: From femto- to microseconds

To take a closer look at the timescales of the magnetization dynamics $\Delta\theta/\theta_0$, the pump induced signal is fitted with a mono-exponential function. This leads to a decay time as short as 1.6 ps (see broken line in figure 5.11 left part). To prove that magnetization dynamics are only governed by *one* time constant, a half-logarithmic plot of the transient Faraday rotation is shown in the inset of figure 5.11. Apparently, for times $t > 400$ fs, $\Delta\theta$ is excellently described by just one single-exponential component $f(t) = 1 - \exp(-t/\tau)$ with time constant $\tau = 1.6$ ps. Since no other temporal components are observed, equation 5.5 implies that $\langle\Delta M_m\rangle = \langle\Delta M_{m,\infty}\rangle f(t)$ and $\langle\Delta a_m\rangle = \langle\Delta a_{m,\infty}\rangle f(t)$ where ∞ indicates signals at times much larger than τ .

The fact that the Verdet constants of iron garnets are independent of the sample temperature [Han84], implies that $\langle\Delta a_{m,\infty}\rangle = 0$, because at times $t \gg 1$ ps, the lattice has thermalized and can be characterized by a temperature [Gal83]. Therefore, together with the previous results (section 5.5.2), once the pump pulse has left the sample, the Faraday signal reflects true magnetization dynamics,

$$\Delta\theta = \sum a_{m,0} \langle\Delta M_m\rangle. \quad (5.6)$$

Strikingly, the pump induced magnetization state is very long lived and thus requires the long-time-scale data acquisition scheme (section 4.3.3) in order to observe the fate of this state. Very surprisingly, after some nanoseconds not a signal relaxation, but instead a further decrease of the signal is found. This secondary minor signal can be fit with a time constant of about 90 ns (see broken line in figure 5.11 right part). After this second step the signal stays again constant and then slowly relaxes with a time constant on the order of 100s of μs depending on the substrate (see section 5.5.6).

In conclusion, the here observed ultrafast dynamics of the magnetic order is rather typical of laser-excited ferromagnetic metals [Kir10] where the electron orbital degrees of freedom provide many more spin-changing scattering channels [Koo10] than in the insulator YIG. The ultrashort time scale ($\propto 1$ ps) comes as a big surprise since YIG is famous for having the longest lifetime (> 0.1 μs) of coherent long-wavelength gigahertz spin waves [Che93a, Ser10], which coincides with the second long-time decay constant.

5.5.4 Fluence dependence

To understand the nature of the excitation process, the fluence dependence of the ultrafast pump-probe signal $\Delta\theta/\theta_0$ is investigated. For that purpose, two free-standing Gold wire grid-polarizers [Cos77] were inserted in the pump beam path in order to continuously change the incident pump fluence without any spectral or temporal distortions of the pump pulse. The result can be seen in figure 5.12: For an increasing pump fluence, the amount of pump-induced Faraday rotation grows linearly with the pump fluence (figure 5.12 b), whereas the single time constant remains unchanged. For all fluences, a (meta-

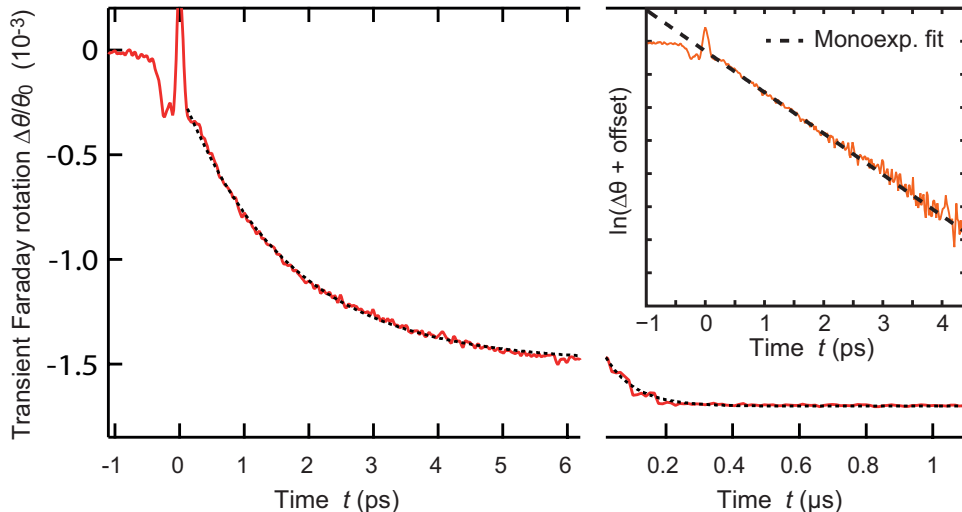


Figure 5.11.: Pump-induced dynamics from femto- to micro-second. Both short and long time scale dynamics of the transient Faraday rotation $\Delta\theta/\theta_0$ can be fitted with mono-exponential time constants of 1.6 ps and 90 ns, respectively. The inset shows a half-logarithmic plot of the vertically offset $\Delta\theta$ vs t as obtained from the left hand trace, confirming once again the single exponential behavior.

)stable state of the magnetization properties is reached after about 7 ps.

Since the pump-probe signal grows linearly with the pump fluence, the excitation is dominated by one-photon absorption, whereas strong-field effects such as field or impact ionization are negligible [Liu12, Gra16]. The latter is a very important result, because THz strong-field effects are known to produce free charge carriers, e.g. in semiconductors [Sch14]. These effects usually exhibit a very nonlinear pump fluence dependence [May15]. Therefore, the observed linear fluence dependence rules out the last possibility that electronic excitations could be involved in the THz induced ultrafast spin dynamics.

5.5.5 Phonon resonance behavior

So far, it was demonstrated qualitatively that the observed dynamics of the magnetic order show a resonance behavior on the highest frequency TO Γ -phonon. Additionally, it has been proved that the pump induced magnetic signal scales linearly with the incident fluence (figure 5.12). Therefore, the pump induced ultrafast change in Faraday signal should directly be related to the absorptance spectrum of the sample, which is solely due to IR-active Γ -phonons in this spectral region [Hof92].

Here, the tunability of our tabletop highfield THz-source is exploited: Figure 5.13 a shows the pump-induced Faraday signal $\Delta\theta$ after 10 ps for different incident pump spectra. As the pump-spectra are relatively broadband (recall figure 5.9 a), the red dots indicate the central frequency, while the horizontal error bar represents the spectral intensity FWHM. Despite the broadband nature of the excitation, a clear trend is visible: The ultrafast change in magnetic order follows, as expected, the sample's absorptance. This proves once more that linear phonon absorption is responsible for the surprisingly fast magnetization dynamics.

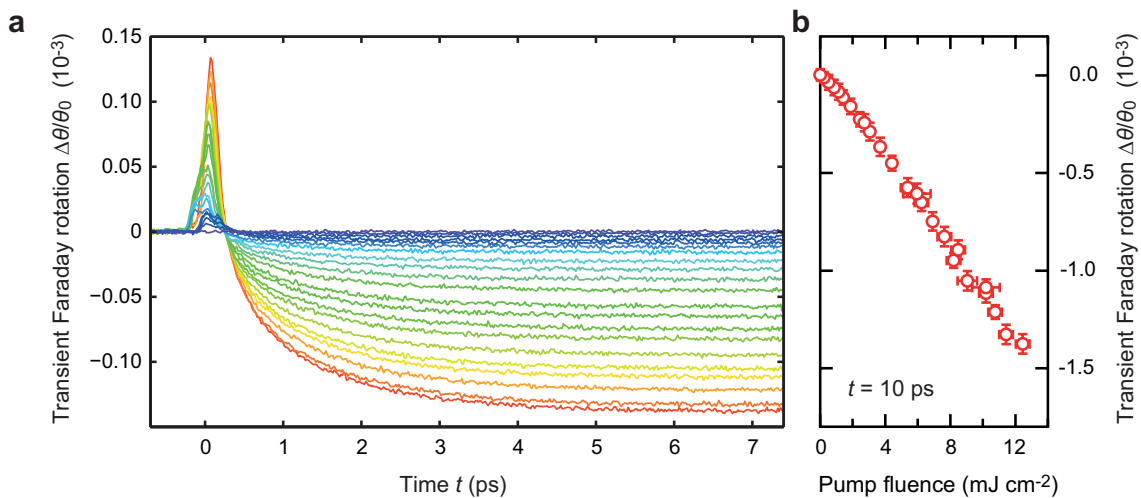


Figure 5.12.: Fluence dependence. **a**, Pump induced transient Faraday rotation for different pump fluences (rising from blue to red from 0 to $\sim 12 \text{ mJ cm}^{-2}$). **b**, Corresponding transient Faraday rotation $\Delta\theta/\theta_0$ at $t \approx 10$ ps versus pump fluence.

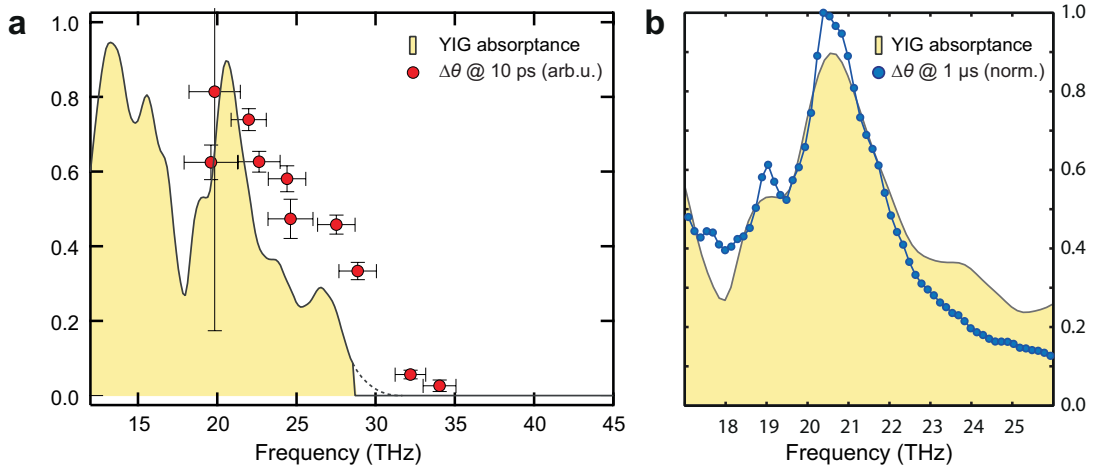


Figure 5.13.: Pump frequency dependence. **a**, Pump induced Faraday signal $\Delta\theta$ at 10 ps after excitation depending on the central frequency of the broadband pump pulse follows the YIG absorption spectrum. **b**, Complementary experiment by using the FHI FEL as a pump source and a cw-laser diode for probing. The high tunability of this narrowband THz source enables to resolve the phonon resonance behavior of the pump induced state at 1 μ s with high accuracy.

In order to get more narrow band, but still intense, excitation pulses in the same frequency regime, a similar series of experiments was performed using the FHI free electron laser (FEL)⁶. Its macro pulse repetition rate of 20 Hz allows to monitor the accumulated Faraday signal of all micro pulses (1 GHz) after each macro pulse. This corresponds to the accumulated magnetization signal after 1 μ s. The comfortable tuning and the narrow bandwidth of < 0.1 THz (FWHM) enables a massively improved frequency resolution in figure 5.13 a. Strikingly, also here the pump induced Faraday signal $\Delta\theta(t = 1\mu\text{s})$ follows the high frequency phonon absorption.

In conclusion, it can be generally pointed out, that the ultrafast faraday signal is caused by the linear absorption of likely all three double degenerate IR-active Γ -phonons above 16 THz (see phonon DOS in figure 5.4).

5.5.6 Comparison of BiGa:YIG and pure YIG

All pump-probe results shown in this section so far, were observed in BiGa:YIG samples. Hence, the question arises, if the Bi and Ga substitution plays a role in the mechanism for ultrafast phonon-driven magnetization dynamics compared to pure YIG. Therefore, analogous experimental series were conducted in pure YIG. This is very challenging due to the lower Verdet constant of pure YIG (see figure 5.7), which decreases the probe sensitivity by more than one order of magnitude [Han83, Mit87]. Nevertheless, with high accuracy and good statistics, the phonon pump-induced effect in pure YIG on all three relevant time scales could be found and analyzed

Figure 5.14 shows the transient Faraday rotation of both YIG and BiGa:YIG. Remarkably,

⁶Details on the general operation of FELs and properties of the FHI FEL can be found in: [Sal13] and [Sch15], respectively

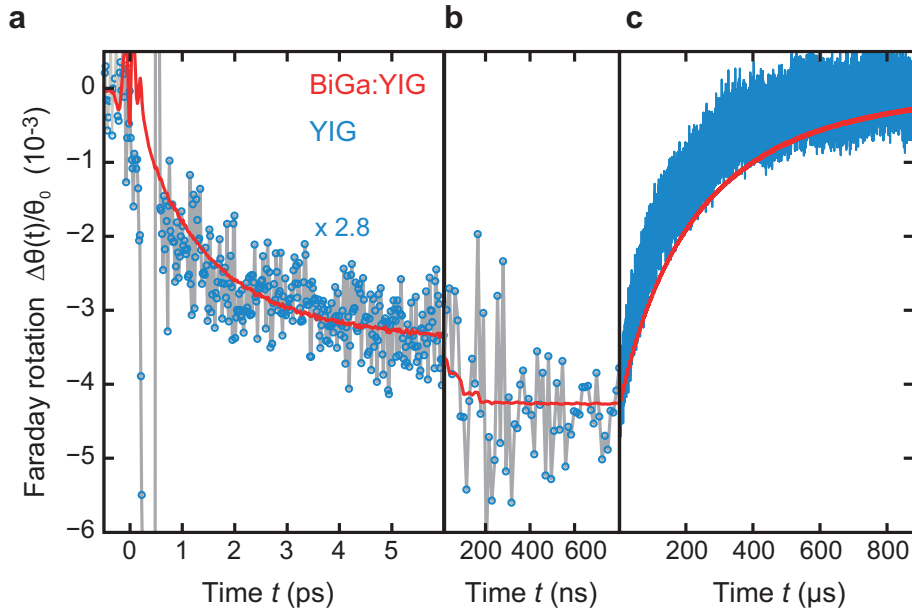


Figure 5.14.: Comparison of YIG and BiGa:YIG dynamics over all involved time scales. **a,b,** Despite the very different magneto-optic coupling constants (visible in the signal to noise ratio), pure YIG (blue dots) and BiGa:YIG (red line) show the same phonon-induced dynamics of the Faraday rotation up to 1 μ s. **c,** Slightly different decay times are found for the heat transport to the substrate. This difference is in good agreement with thermal conductivity simulations taking into account the different substrates of both samples.

although the two materials have very different Verdet constants, they exhibit an almost identical relative change $\Delta\theta/\theta_0$ in the Faraday rotation over multiple time scales. The 2.8 times larger transient relative Faraday signal of BiGa:YIG can be explained by two effects. First, BiGa:YIG's lower Curie temperature results in a 5 times larger slope $\partial\theta_0/\partial T_0$ of the equilibrium magnetization curve $\theta_0(T_0)$ at room temperature (see inset figure 5.8). Second, for the specific pump spectrum used, the BiGa:YIG sample absorbs only 56% of the power that is absorbed by the pure YIG sample.

The third, so far undiscussed time scale up to nearly 1 ms, accounts for the relaxation of the pump-induced Faraday signal due to the heat transport to the substrate. The slightly different relaxation time scales on the order of 100s μ s (5.14 c) are due to the different substrate of the BiGa:YIG and YIG sample. As the BiGa:YIG sample is glued on a diamond substrate, the thermal conductivity to the substrate is different to the pure YIG-sample grown on GGG. These time scales of the heat flow could be also verified using a Comsol-simulation.

Remarkably, these findings have several implications. First, the Bi ions do not introduce any resonances, that are responsible for the ultrafast Faraday signal. Second, the enhancement magneto-optic activity of BiGa:YIG versus pure YIG is thought to arise from increased spin-orbit coupling (SOC). Thus, the observed similar timescales of BiGa:YIG and YIG, indicate that SOC is very unlikely as a candidate for the microscopic ultrafast coupling mechanism between phonons and spins (discussed in detail in section 5.6.1). Finally, looking back at equation 5.5, it can be again excluded that the pump-induced signal

is caused by a temporal modulation in the magneto-optic coupling constants Δa_m as they are significantly different for pure YIG and BiGa:YIG. Consequently, this confirms again that the pump-probe signal is a measure of true spin dynamics.

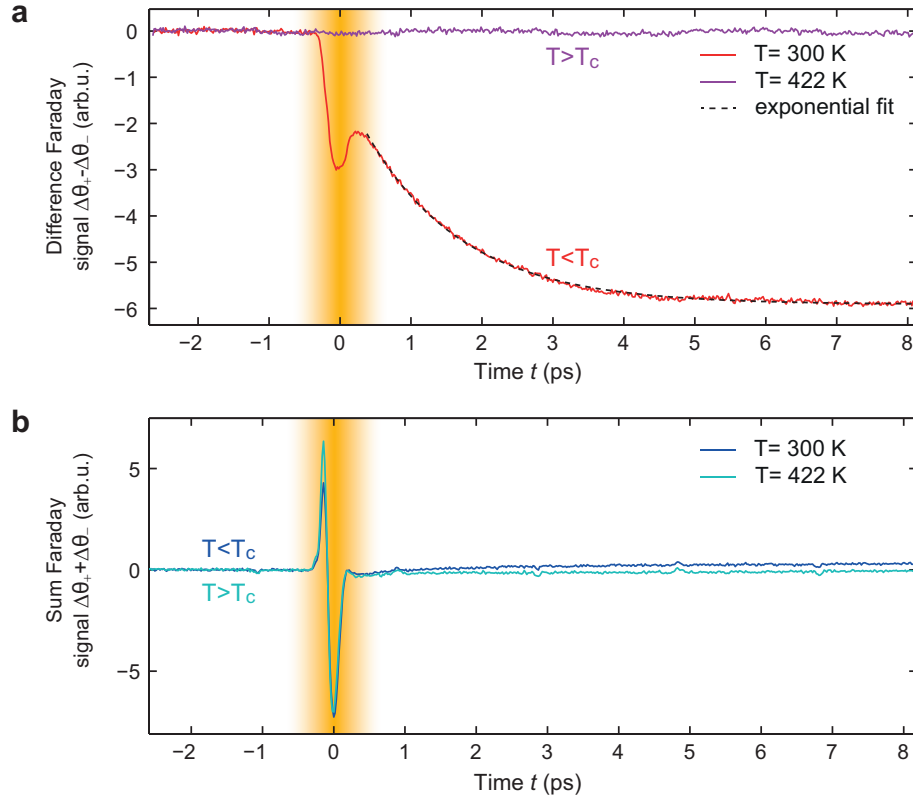


Figure 5.15.: Difference- and sum Faraday signal above and below T_C . **a**, The difference Faraday signal $\Delta\theta \propto \Delta\theta_+ - \Delta\theta_-$ completely vanishes above the critical temperature T_C , clearly demonstrating that it is sensitive only to changes in the magnetic order. **b**, The sum Faraday signal $\Delta\theta_+ + \Delta\theta_-$ as like expected independent of the magnetic order. The identical sum Faraday signal during the pump-probe overlap (indicated by the orange area) for above and below T_C confirms the non-magnetic origin of the spikes in the pump-probe signals around $t \approx 0$.

5.5.7 Temperature dependence

As it has been confirmed by the previous results, the THz pump-induced Faraday signal $\Delta\theta$ in YIG and BiGa:YIG can be interpreted as an ultrafast change in the magnetization state of both magnetic sublattices as soon as the pump and probe pulse do not temporally overlap anymore ($t > \tau_p$). Therefore the 1 ps-decay signal should vanish above the critical temperature T_C , because the unordered paramagnetic state ($T > T_C$) cannot be disturbed further.

This expectation is confirmed in the Faraday signal displayed in figure 5.15 a: The long-lived pump probe signal completely vanishes for $T > T_C$ as seen from the purple curve. A second interesting result can be obtained by calculation the sum Faraday signal $\Delta\theta_+ + \Delta\theta_-$ for the same pump-probe traces. Figure 5.15 b unveils the instantaneous signal during the temporal pump-probe overlap (indicated by orange shaded area). This signal contribution

remains unaffected by the phase transition, consistent with its non-magnetic origin.

To characterize the long-lived (~ 100 ns) transient state seen in our experimental data (e.g in figure 5.11), the sample temperature is increased stepwise from 300 K up to 420 K. For each temperature, the equilibrium Faraday rotation $\theta_0 = \theta(-2$ ps) is measured, as well as its pump-induced change $\Delta\theta$ at ultrashort ($t = 10$ ps, figure 5.14 a) and long time delays ($t = 1$ μ s, figure 5.14 b) after pumping. The resulting θ_0 versus T_0 has a shape similar to known static magnetization curves (figure 5.16 a) [Che93a, Han06b] whose slope $\partial\theta_0/\partial T_0$ steepens with rising T_0 until the transition into the paramagnetic phase occurs at the Curie temperature $T_C = 398$ K. In contrast, the pump-induced magnetization change at $t = 1$ μ s (blue squares, figure 5.16 b) increases with T_0 and reaches a maximum right below T_C , reminiscent of the derivative of the equilibrium magnetization curve (black line, figure 5.16 b). Indeed, $\Delta\theta(1$ μ s) versus T_0 follows closely the temperature dependence of $(\partial\theta_0/\partial T_0)\Delta T$. Here, $\Delta T = 0.39$ K is the increase in equilibrium temperature as calcula-

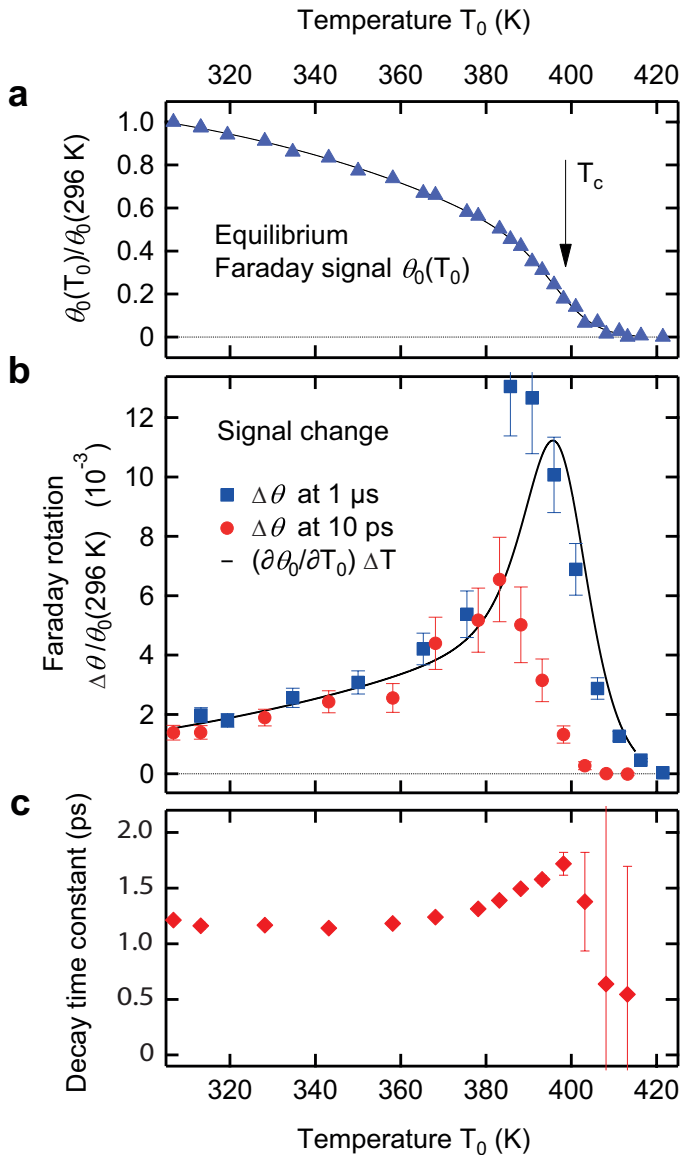


Figure 5.16: Ultrafast spin-lattice equilibration. **a**, Equilibrium Faraday rotation θ_0 vs ambient temperature T_0 along with a fit to an analytical function (see section 5.4.2). **b**, Pump-induced change $\Delta\theta/\theta_0$ at $t = 10$ ps (red dots) and 1 μ s (blue squares) after pump arrival. The black curve is the Faraday-rotation change expected from the temperature increase ΔT induced by the pump pulse. $\partial\theta_0/\partial T_0$ is calculated from panel a (thin solid line), and $\Delta T = 0.39$ K is calculated from the absorbed pump energy and the heat capacity of the excited volume. **c**, Temperature dependence of the decay constant extracted from mono-exponential fits of $\Delta\theta/\theta_0$ for every temperature.

ted from the energy density deposited by a $1\ \mu\text{J}$ incident pump pulse energy⁷. The good agreement of both curves shows that at about $1\ \mu\text{s}$ after pumping, the BiGa:YIG film is in thermodynamic equilibrium characterized by temperature $T_0 + \Delta T$.

Remarkably, figure 5.16 b also shows that the magnetization changes at $10\ \text{ps}$ and $1\ \mu\text{s}$ are approximately equal up to $T_0 = 380\ \text{K}$, right before the Curie point. The observation of virtually equal magnetization quenching at $10\ \text{ps}$ and $1\ \mu\text{s}$ is striking and indicates that lattice and spins have almost reached the magnetization-quenched equilibrium state already $10\ \text{ps}$ after sample excitation.

On the other hand, for temperatures $T_0 > 380\ \text{K}$, $\Delta\theta(10\ \text{ps})$ deviates from the thermal equilibrium case (black line in figure 5.16 b). This earlier break down of $\Delta\theta(10\ \text{ps})$ even before T_C will be reproduced by the microscopic model in section 5.7.5.

5.6 Interpretation and microscopic mechanisms

The novel results of this study raise the question of the underlying microscopic lattice-spin coupling mechanism. To develop a suitable model, the main findings will be briefly recapitulated here.

The results of section 5.5.2, showing transient Faraday rotation and ellipticity with identical dynamics for $t \geq 400\ \text{fs}$, indicate a magnetic order related origin of the phonon pump induced signal. Further, the isotropic transmission change $\Delta T_r/T_{r,0}$ is much smaller than the transient Faraday signals and shows a completely different temporal behavior. Together with the finding of only one single time constant for the ultrafast dynamics, this leads to the conclusion that variations of the magneto-optic coupling constants $\Delta a_m(t)$ can be neglected for $t \geq 400\ \text{fs}$ ($\Delta a_m(t) = 0$ for magnetic sublattice $m = a, d$). Therefore, we conclude that true spin dynamics are observed.

Moreover, section 5.5.5 unveiled a clear phonon resonance behavior. Accompanied with a linear fluence dependence (section 5.5.4), this leads to the final conclusion of purely phonon induced change of the magnetic order, which happens on a surprisingly fast timescale on the order of $1\ \text{ps}$. The subsequent, 5 orders of magnitude slower dynamic ($\sim 100\ \text{ns}$, see section 5.5.3) agrees with magnon lifetimes times in YIG extracted from FMR linewidth studies [Spe62, Vit85, Hun10]. The slow relaxation of the pump induced Faraday signal ($\sim 100\ \mu\text{s}$) can be directly explained by the heat diffusion to the substrate.

Nevertheless, the main question remains: what is the microscopic mechanism responsible for the ultrafast coupling ($\sim 1\ \text{ps}$) between the excited lattice and magnetic order?

5.6.1 Possible microscopic couplings

The measured signal is given by (see section 5.3.3 and 5.5.2):

$$\Delta\theta(t) = a_d\Delta M_d(t) + a_a\Delta M_a(t) \quad (5.7)$$

⁷The total absorption was calculated by taking into account: incident THz pump pulse energy and its measured spectrum, absorption spectrum of the sample, phonon heat capacity [Hof06], THz-pulse spot size, THz penetration depth and sample thickness

Equation 5.7, therefore suggests to focus on mechanisms that are capable of changing sublattice magnetizations M_d and M_a . According to the Ehrenfest theorem and the YIG spin Hamiltonian (see equation 3.22), the rate of change of each sublattice magnetization M_m is given by [Nol13]:

$$\frac{\partial}{\partial t} \langle \mathbf{M}_m \rangle = \frac{i}{\hbar} \langle [H, \mathbf{M}_m] \rangle = g\mu_B \sum \langle \mathbf{S}_{mj} \times \mathbf{B}_{mj} \rangle. \quad (5.8)$$

Here

$$\mathbf{B}_{mj} = \mathbf{B}_{\text{ext}} + \mathbf{B}_{\text{SOC}} + \mathbf{B}_{\text{SSMD}} + \mathbf{B}_{\text{XC}} \quad (5.9)$$

is the operator of an effective magnetic field encountered by spin j in sublattice $m = a, d$. It includes the different possible contributions from the microscopic spin interactions that were discussed in section 3.3. Briefly, \mathbf{B}_{ext} is an external magnetic field, \mathbf{B}_{SOC} is the spin-orbit field, \mathbf{B}_{SSMD} is the spin-spin magnetic dipole field and \mathbf{B}_{XC} is the effective field caused by exchange interaction.

To change the sublattice magnetization, meaning that $\frac{\partial}{\partial t} \langle \mathbf{M}_m \rangle \neq 0$, the pump pulse must modulate \mathbf{B}_{mj} . Thus, to identify couplings mechanism that are potentially strong enough to explain the observed 1 ps dynamics, we estimate the upper limit to the rate of change $\frac{\partial}{\partial t} \langle \mathbf{M}_m \rangle$ for each of the fields contributing to \mathbf{B}_{mj} (equation 5.9), by assuming a very conservative 100 % change of \mathbf{B}_{mj} .

The comparison of the different contributions to \mathbf{B}_{mj} is approached in two steps. First, an effective field B_{eff} is calculated by the interaction Hamiltonian H_{int} in the classical limit [Nol09]:

$$B_{\text{eff}} = -\frac{1}{\gamma} \frac{\partial H_{\text{int}}}{\partial S} \quad (5.10)$$

Then the precession frequency of a single spin ($S = 5/2 \hbar$) in this effective field is given by

$$\omega_0 \leq \gamma B_{\text{eff}} S / \hbar \quad (5.11)$$

Accordingly, ω_0 provides an upper limit to the inverse time constant of the \mathbf{M}_m dynamics, that is $1/\tau = \omega_0/(2\pi)$. In the following, these time constants for the different effective fields of B_{eff} are estimated.

Zeeman coupling

The only time-varying external field, is the magnetic field of the THz pump pulse. For a peak electric field of about 10 MV/cm, the pump pulse exhibits a magnetic field of $B_{\text{THz}} \approx 3.3$ T. Thus, the Zeeman coupling of the THz magnetic field is strong enough to account for a coupling time of 4 ps. However, this coupling mechanism has to be dismissed due to other reasons. First, Zeeman coupling should strongly depend on angle between \mathbf{M} and \mathbf{B}_{THz} , but no indications for such an angle dependence was observed in the experiment. Further, the pump pulse has to contain frequencies resonant to a magnon mode, but around 20 THz only antiferromagnon-resonances, which would increase the overall magnetization are found (see figure 5.5). Last but not least, there are no indications for coherent oscillatory contributions in the measured Faraday signals. Accordingly, Zeeman coupling has to be dismissed as microscopic coupling mechanism for the observed (sublattice-) mag-

netization dynamics.

Spin-Orbit coupling (SOC) and spin-spin magnetic dipole (SSMD) coupling

Both effects, SOC and SSMD coupling, can be summarized by an effective anisotropy field \mathbf{B}_A in the Hamiltonian [Nol09]. The pump induced anisotropy field ΔB_A was measured directly in very similar doped Bi:YIG samples by Hansteen and coworkers via coherent magnetization precession triggered by a visible laser pulse [Han06b, Han06a]. Their static hysteresis measurements indicated a total magnetic anisotropy field of about 5 mT corresponding to $\tau \geq 7$ ns. The VIS-pump induced anisotropy field was only a fraction of this value ($\Delta B_A \leq 0.15$ mT), corresponding to a coupling time $\tau \geq 95$ ns.

Due to this slow coupling times on the order of ns, SOC and SSMD coupling have to be also dismissed as potential microscopic coupling mechanism for the found 1 ps dynamic.

Exchange coupling

The exchange field can be directly calculated, using the Heisenberg Hamiltonian H_{XC} :

$$B_{XC,i} = -\frac{1}{\gamma} \frac{\partial H_{XC}}{\partial S_j} \leq \frac{1}{\gamma} \sum_i J_{ij} S_i \approx \frac{2}{\gamma} J_{ad} S_a = 2.6 \cdot 10^3 \text{ T}, \quad (5.12)$$

where the highest exchange constant (inter-lattice) $J_{ad} = 9.60 \cdot 10^{-21}$ J [Bar16, Che93a] and only the opposite sublattice next neighbor was used. This corresponds to a very rapid coupling time of $\tau \geq 5.5$ fs. This is also only lower limit estimate, but nevertheless exchange coupling is in opposite to the other mechanism strong enough to explain a ps coupling time between lattice and spins.

Note, that intra-lattice exchange coupling (J_{aa} and J_{dd}) have been omitted in this estimate, because they are much weaker [Che93a] and act only on one sublattice each. Therefore, they leave both M_a and M_d constant.

Result

The previous considerations lead to the conclusion, that in YIG only exchange coupling is strong enough to manipulate spins on ps time scale. Note, however, the exchange interaction Hamiltonian conserves the total spin (section 3.3.3). Therefore, no change in total magnetization M is possible, meaning that

$$\Delta M_a + \Delta M_d = 0 \quad (5.13)$$

has to be fulfilled.

Nevertheless, we are able to observe even such an effect, since the magneto-optic coupling constants $a_d \neq a_a$ in equation are not equal [Han84] (see equation 5.7). Hence, a weighted sublattice magnetization average is measured by $\Delta\theta$.

The here proposed scenario of exchange mediated microscopic coupling is consistent with the mono-exponential nature of the initial ultrafast dynamics of $\Delta\theta(t)$, meaning that $|\Delta M_a| = |\Delta M_d|$. Since exchange-mediated energy transfer between the lattice and spins is allowed, but under the constraint that angular momentum transfer is forbidden, angular momentum can only be exchanged between the two magnetic sublattices (meaning that: $\Delta M_a = -\Delta M_d$). This scenario is discussed in more detail in the following section 5.6.2 and will be theoretically modelled in section 5.7

5.6.2 Scenario: phonon-modulated exchange interaction

First, the question arises how the THz pump pulse can modulate the effective exchange field

$$B_{XC} \propto \sum_j J_{ij} S_j \quad (5.14)$$

Since direct coupling of the external field of the pump pulse to the spins S_j is not relevant (see section 5.6.1), the THz pump pulse can only change the effective exchange field by modulation of the exchange constant J_{ij} . Also this is only possible indirectly via modulating phonons or electron orbits. As the electron orbital degrees of freedom are inaccessible by the THz pump pulse, the pump pulse couples exclusively to phonons, as shown in section 5.5.5. Therefore, the modulation of the interaction constant ΔJ_{ij} must be caused by the change of one or more lattice coordinate u (see figure 5.17 a). To lowest (linear) order, this modulation can be written as:

$$\Delta J_{ad} = \frac{\partial J_{ad}}{\partial u} u. \quad (5.15)$$

As aforementioned, only J_{ad} is relevant since J_{aa} and J_{dd} leaves M_a and M_d constant. As the change of magnetic order mediated by ΔJ_{ij} has to fulfill the constraint $\Delta M_a = -\Delta M_d$, it is an angular momentum transfer from one magnetic sublattice to the other (see figure 5.17 b). Accordingly, the magnetization in both sublattices is reduced, but the net magnetization $M = M_d + M_a$ stays constant.

In other words: this is energy transfer from the lattice into the spin system, however, under the boundary condition of constant total spin angular momentum. This situation is very interesting and could be termed as "*constrained heating of a ferrimagnetic spin system*".

5.7 Microscopic model: phonon induced modulation of exchange coupling

5.7.1 Model assumptions

To model ultrafast spin-lattice interaction by phonon-induced modulation of exchange constants, the following three assumptions are made:

1. Phonons and spin subsystems are thermalized throughout the dynamics. Thus, the THz pump pulse acts to increase the lattice temperature. This assumption is reasonable as the lifetime of the excited Γ -phonons is on the order of 400 fs (known from absorption linewidth analysis including Lorenz oscillator fits of data shown in figure 5.9 a). Therefore the phonon lifetime is significantly shorter than the 1 ps time constant of the spin dynamics. Further, the isotropic transmission change ΔT_r shows only a step like change within the pump pulse duration (see figure 5.10 b). Hence, if we assume that the isotropic transmission change ΔT_r is sensitive to the thermalization of the lattice, figure 5.10 b indicates that the lattice has largely thermalized for $t > 400$ fs.
2. Spin-phonon coupling is mediated by $\Delta J_{ad} = J'_{ad}u$ (see equation 5.15), where u is the deflection of the super-exchange-mediating oxygen ion between adjacent Fe-a and Fe-d ions, as depicted in figure 5.17 a. This assumption is justified, because J_{ad} predominantly involves the a-Fe and d-Fe ions and the O ion in between. In addition, the iron atom is 3.5 times heavier than the oxygen atom. The initially excited phonon bands around 20 THz also correspond mostly to oxygen motions, according to the ab-initio calculations of the phonon density of states by P. Maldonado (see figure 5.4 c). Most obviously, the oxygen motion is expected to modulate inter-lattice superexchange most strongly.
3. The oxygen motion $u(t)$ can be described by white noise corresponding to a lattice temperature T_{lat} . This assumption is reasonable, because the oxygen ion motion participates in many lattice vibrations (see also figure 5.4 c) and therefore $u(t)$ is a

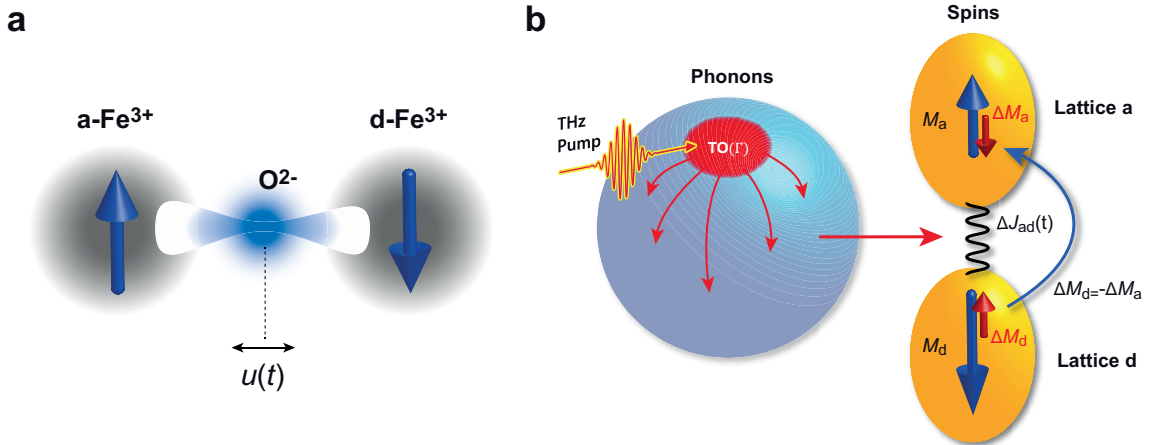


Figure 5.17.: Phonon-modulated exchange interaction. **a**, Superexchange between magnetic a-sublattice and d-sublattice is mediated by an oxygen ion with spatial coordinate $u(t)$. According to the element resolved phonon DOS (see figure 5.4) and due to the lighter atomic mass compared to Fe, the O ion is expected to move upon excitation of the high frequency TO Γ -phonons. Thereupon the exchange integral and thus the exchange constant J_{ij} is modulated. **b**, Total spin conserving sublattice demagnetization. The excited Γ phonons thermalize within 400 fs. Afterwards, the excited phonon bath leads to a modulation of the exchange constant ΔJ_{ad} , which triggers a sublattice demagnetization $\Delta M_a = \Delta M_d$ and therefore conserves the total spin angular momentum.

superposition of many harmonic oscillations.

The aim of the model is to calculate rate of change of dM_m/dt when lattice temperature is increased from T_0 to $T_0 + \Delta T$. For the implementation, we employ an existing, highly successful approach to spin dynamics, namely large-scale atomistic spin dynamics simulations [Now05, Atx09, Eva14, Etz15].

5.7.2 Stochastic exchange via atomistic spin model simulations

In the following, the technical details of the atomistic spin model simulations, implemented and performed by J. Barker⁸, are briefly introduced. For a detailed technical background please see [Bar16, Bar13, Mae16b].

1. The spins are treated as classical observables, meaning that $\langle \mathbf{S}_j \times \mathbf{B}_{\text{eff}} \rangle$ can be written $\langle \mathbf{S}_j \rangle \times \langle \mathbf{B}_{\text{eff}} \rangle$. Thereupon, a classical equation of motion can be set up for each spin.
2. The effective magnetic field B_{mj} has two stochastic components $\xi_i(t)$ and $\Delta B_{\text{XC}}(t)$, which arise from coupling of the spins to all other non-spin-degrees of freedom (termed as *bath*):
 - a) $\xi_i(t)$ transfers spin angular momentum and energy between the spin system and a bath having temperature T_0 . According to the fluctuation-dissipation theorem [Nol10b], in equilibrium, the fluctuations $\xi_i(t)$ are balanced by a friction force, namely a Gilbert term in the atomistic LLG [Bar16]. In this way, the spin system is driven into an equilibrium state at temperature T_0 . The time scale of this relaxation process is set by the Gilbert parameter α (see LLG equation 3.23). [Bar16, Bar13]
 - b) According to our model assumptions (see above), we need to add another stochastic component $\Delta B_{\text{XC}} \propto \sum_j \Delta J_{ij} S_j$ that describes the action of the phonon-modulated J_{ij} . This field is distinctly different from $\xi_i(t)$ as it causes energy transfer into the spin system, but leaves the total spin angular momentum unchanged. Since the temperature T_0 is already accounted for by $\xi_i(t)$, the ΔJ_{ij} scales with the temperature increase $\Delta T = T_{\text{lat}} - T_0$ induced by the pump pulse. By making use of the equipartition theorem [Nol10b], we write

$$m\Omega^2 \langle u^2 \rangle \propto k_B \Delta T (t = 0), \quad (5.16)$$

where Ω (≈ 20 THz) is the mean frequency of the coordinate u . Note that ΔB_{XC} is not balanced by an appropriate friction force. Thus, spin-angular-momentum-conserving energy transfer to the lattice is not accounted for. Therefore, our simulation is only meaningful directly after the pump has established the temperature difference $\Delta T(t = 0)$, since it neglects the subsequent decrease of ΔT .

⁸Institute for Materials Research, Tohoku University, Sendai 980-8577, Japan

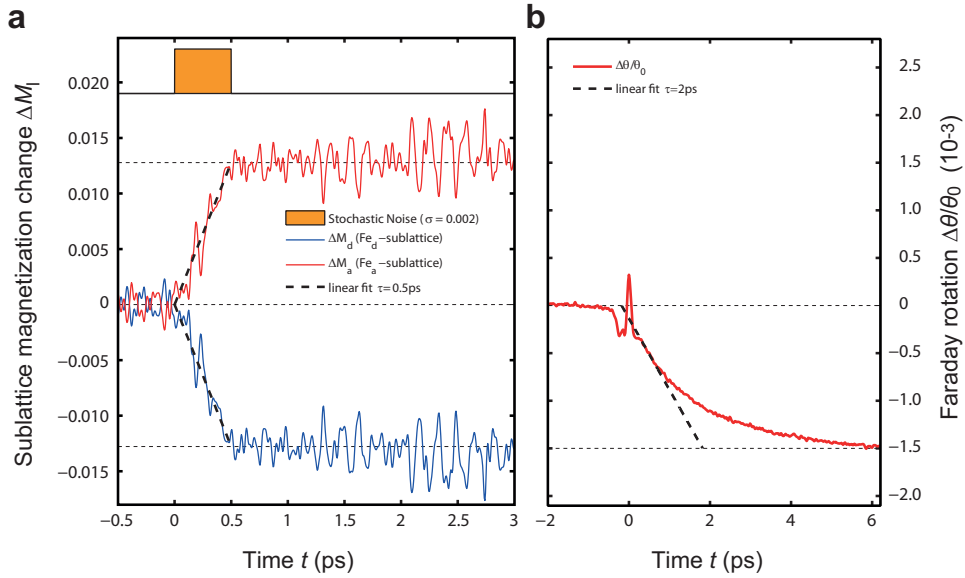


Figure 5.18.: Comparison: simulation and experiment. **a**, Atomistic spin model simulation with an additional noise stimulus (orange box) in the exchange constant J_{ad} leading to a sublattice demagnetization. Taking into account the number of iron spins in each sublattice (ratio 3:2) results in an equal amount of demagnetization. **b**, Comparison to the experimentally observed Faraday signal. Within the initial step, before a counterbalancing energy flow can set in, $\Delta\theta/\theta_0$ can be linearized and thus shows similar change rates as the simulation.

Despite this limitation, the simulation delivers the rate of change $\partial M_m/\partial t$ for a lattice-spin temperature difference $\Delta T(t=0)$ found directly after the pump pulse heated the lattice.

3. The fluctuations $\Delta J_{ij}(t)$ are assumed to be isotropic and centered about the zero temperature exchange value J_{ij} .
4. The fluctuations are uncorrelated in time (white noise) and space⁹, which is a reasonable assumption for a thermalized lattice. Thus, they are distributed normally about the mean:

$$\langle \Delta J_{ij}(t), \Delta J_{ij}(t') \rangle = 2\sigma |J_{ij}| \delta(t - t'), \quad (5.17)$$

with a width that equals a fraction σ of the exchange value $|J_{ij}|$. Fluctuations are included on all exchange parameters, J_{ad} , J_{aa} and J_{dd} . This means the lower exchange energies have smaller fluctuations, which is reasonable because their corresponding spins are separated by a further distance.

5.7.3 Simulation results

The simulations yield the sublattice magnetization (spin z -component) per atomic spin m_{FeD} and m_{FeA} , normalized to their $T_0 = 0\text{K}$ values. Multiplying with the corresponding ratio of Fe atoms ($N_d = 3, N_a = 2$) leads to the sublattice magnetization M_m .

⁹Nevertheless, one exchange parameter couples two spins j and i by $J_{ij} = J_{ji}$, thus the noise $\Delta J_{ij} = \Delta J_{ji}$ is correlated for these two spins.

The temporal evolution of M_m for a noise stimulus of $\sigma = 2 \cdot 10^{-3}$ is shown in figure 5.18 a. Astonishingly, the simulation result shows indeed a sublattice demagnetization ΔM_m as long as the stochastic noise ΔJ_{ad} is switched on (500 fs in the simulations, indicated by orange area). Moreover, ΔM_d and ΔM_a show opposite sign and clearly obey the constraint $\Delta M_d = -\Delta M_a$. Thus the total spin is conserved, as expected for exchange interaction. This result directly confirms the considerations in section 5.6.2.

Notably, the sublattice magnetization decreases linear in time since the simulations do not account for backflow of energy from spins to phonons via the exchange channel. As detailed above, spin damping is only introduced by Gilbert damping, which is in the case of YIG very slow. Therefore, the relaxation of M_m to their initial values happens on a ns-time scale (also reproduced by the simulations).

Furthermore, the stochastic exchange model delivers the sublattice demagnetization rate

$$\dot{M}_m = \frac{dM_m}{dt} = \frac{\Delta M_m}{\Delta t_{\text{perturb}}}, \quad (5.18)$$

which corresponds to the initial dynamics seen in the experiment (see figure 5.18 b). Accordingly, the simulated rate \dot{M}_m , can be compared with the experimentally observed rate, given by the linearization of the exponential decay for short times in figure 5.18 b. The ultrafast time scale agrees with the experiment for a stochastic noise term of $\sigma \approx 0.5 \cdot 10^{-3}$. The estimate in section 5.7.4 will show that this order of magnitude of the noise parameter σ is reasonable.

As an additional cross check, we varied J_{aa} , J_{dd} and J_{ad} in separate simulations. The resulting temporal evolution of the z -component of the magnetization per iron ion for sublattice d and sublattice is displayed in figure 5.19 b and 5.19 c, respectively. The results are consistent with the expectation that only J_{ad} leads to sublattice demagnetization, whereas J_{aa} and J_{dd} only trigger intra-sublattice angular momentum transfer leading to no change in M_z .

Finally, the sublattice demagnetization dependence on the perturbation strength σ was investigated. Figure 5.19 a clearly shows that the sublattice demagnetization rate grows linearly with the phonon noise strength σ . This finding implies that ΔM_l is proportional to the increase in phonon temperature ΔT as

$$\Delta M_m \propto \Delta J_{ad} \propto \langle u^2 \rangle^{\frac{1}{2}} \propto \Delta T (t = 0), \quad (5.19)$$

which is in agreement with the linear fluence dependence in the experimental findings (see figure 5.12).

Overall, the results of the simulations support the phonon-modulated-exchange scenario (section 5.6.2) and are in good agreement with the experimental findings (section 5.5).

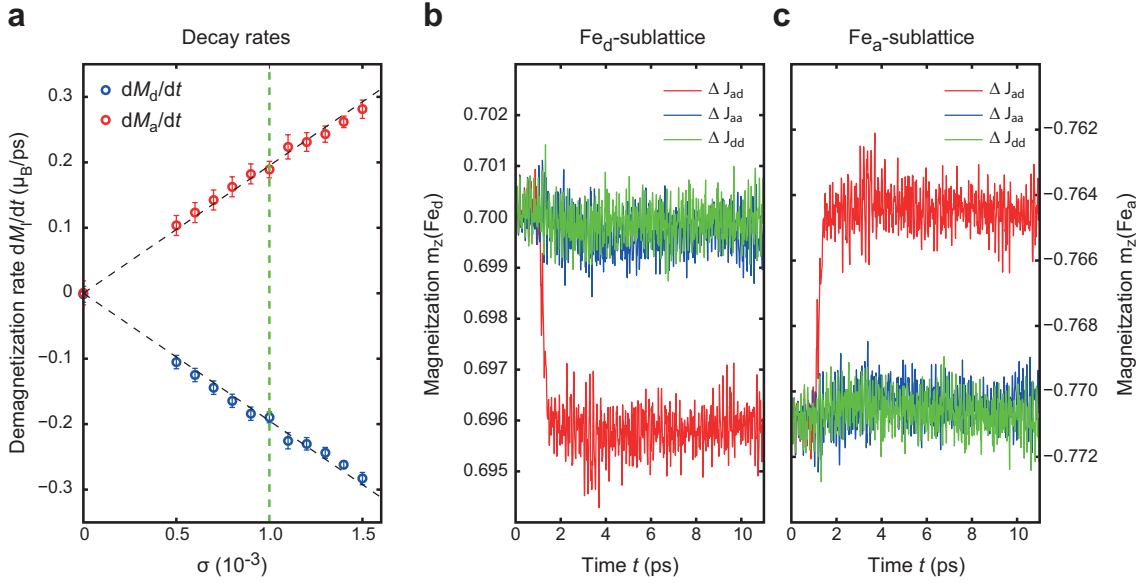


Figure 5.19.: Simulation results: sublattice resolved demagnetization. **a**, Sublattice demagnetization rate depending on the noise strength σ leading to $\Delta J = 2\sigma J_0$. **b**, Temporal evolution of the magnetization per iron atom of the d-sublattice (normalized to zero temperature value). Only a modulation of the superexchange constant J_{ad} leads to a demagnetization. **c**, similar to **b**, only for the a-sublattice.

5.7.4 Extraction of dJ_{ad}/du

The quantitative comparison between the experimental findings and the simulations enable an estimate of how strong the superexchange parameter J_{ad} is modulated by deflection of the oxygen ion. Let us consider from now on $J = J_{ad}$ and $J' = \partial J_{ad}/\partial u$. With the following relations, a direct comparison of the demagnetization rates $\dot{m} = dm/dt$ of theory and experiment becomes possible. From the simulations we obtain

$$\dot{m}_{\text{th}} = -a\Delta J, \quad (5.20)$$

whereas the experiment delivers

$$\dot{m}_{\text{exp}} = -b\Delta T. \quad (5.21)$$

Equating $\dot{m}_{\text{th}} = \dot{m}_{\text{exp}}$ leads to

$$\frac{\partial J}{\partial T} = \frac{\partial J}{\partial u} \cdot \frac{\partial u}{\partial T} \approx \frac{\Delta J}{\Delta T} = \frac{a}{b} \quad (5.22)$$

and therefore provides the estimate:

$$J' = \frac{\partial J}{\partial u} = \frac{\partial J}{\partial T} \cdot \frac{\partial T}{\partial u} = \frac{a/b}{\partial u/\partial T}. \quad (5.23)$$

All parameters on the right hand side can be extracted from experiment or simulations:

- a is given by the stochastic simulation results in figure 5.19 a. The slope of $|dm_m/dt|$ per variation σ (with $\Delta J = 2\sigma J_0$) leads to $a = \frac{-\dot{m}_m}{2J_0\sigma}$

- b can be extracted as follows: the rate \dot{m}_{exp} is experimentally determined by linearization of single-exponential decay $e^{-t/\tau} - 1$ to $-t/\tau$ with $\tau \approx 2$ ps around $t = 0$ (see broken line in figure 5.18 b). The experimentally observed linear fluence dependence (see figure 5.12) leads together with the phonon heat capacity ($\rho = 570 \text{ Jkg}^{-1}\text{K}^{-1}$ [Hof06]) and spectral absorption profile (see figure 5.9 a) to $\Delta T = 0.39 \frac{\text{K}}{\mu\text{J}} \cdot W_{p,\text{THz}}$ (where $W_{p,\text{THz}}$ is the incident THz pulse energy).
- $c = \frac{\partial u}{\partial T}$ can be estimated by linearization of the equipartition theorem (equation 5.16):

$$\Delta u(\Delta T) = \sqrt{\frac{k_B}{4m\Omega_0^2 T_0}} \cdot \Delta T = c \cdot \Delta T. \quad (5.24)$$

Plugging a , b and c into equation 5.23 yields the result:

$$J' = \frac{\partial J}{\partial u} = \frac{b}{ac} \approx 5J_0 \text{ \AA}^{-1} \quad (5.25)$$

This order of magnitude seems very reasonable as J changes by 100% when the oxygen atom moves by 5% of Fe-O bond length parameter ($d_{\text{Fe-O}} \approx 1.73 \text{ \AA}$ [Che93a, Gil80]). This is also in a good agreement with literature as the superexchange parameter is $J \propto t^4$, where t is the transfer matrix element linking the two iron d-wavefunctions with the oxygen p-wavefunction [Nol09]. Therefrom we can calculate $\partial t/\partial u \approx 1.25t_0 \text{ \AA}^{-1}$, meaning that the transfer integral changes by 100% when the oxygen moves by approximately 1/2 of the oxygen-iron distance $d_{\text{Fe-O}}$. This order of magnitude also seems not unrealistic. Therefore, the very reasonable resulting value of J' is a further important confirmation of our microscopic model of phonon modulated exchange interaction and is a very interesting finding by itself.

5.7.5 Temperature dependence

So far, simulation and experiment deliver dM_m/dt for a given ΔT . Equal rates dM_m/dt were obtained by setting $\partial J_{ad}/\partial u$, the change of the exchange constant J_{ad} upon elongation of the oxygen ion, to a realistic value. Now, $\partial J_{ad}/\partial u$ shall be kept fix ($\sigma = 0.002$) in order to study the dependence of simulated and measured dM_m/dt as a function of the equilibrium temperature T_0 . In the simulation, dM_m/dt obtained from the slope of $M_m(t)$ (see figure 5.18), whereas the demagnetization rate in the experiment is given by $\Delta\theta(10\text{ps})/\tau(T_0)$. Here $\tau(T_0)$ is determined by a single exponential fit to $\Delta\theta(t)$ for each temperature T_0 in the temperature dependent measurements (see figure 5.16 c).

The results are displayed in figure 5.20 a, which shows the equilibrium change dM_0^*/dT_0 as obtained from experiment (see black line in figure 5.16) and equilibrium simulations. For a better comparison, the unequal magneto-optic coupling constants $a_d = 1.5a_a$ [Han84] (see section 5.3.3) were multiplied to the simulated values $M_{0,m}$ (indicated by the asterisk in M^*). As seen in figure 5.20 a, the equilibrium data of simulation and experiment (both full lines) are in good agreement.

Figure 5.20 b shows the temperature dependent pump-induced change rate of the sum magnetization dM^*/dt in experiment and simulation. Again, here M^* is the weighted

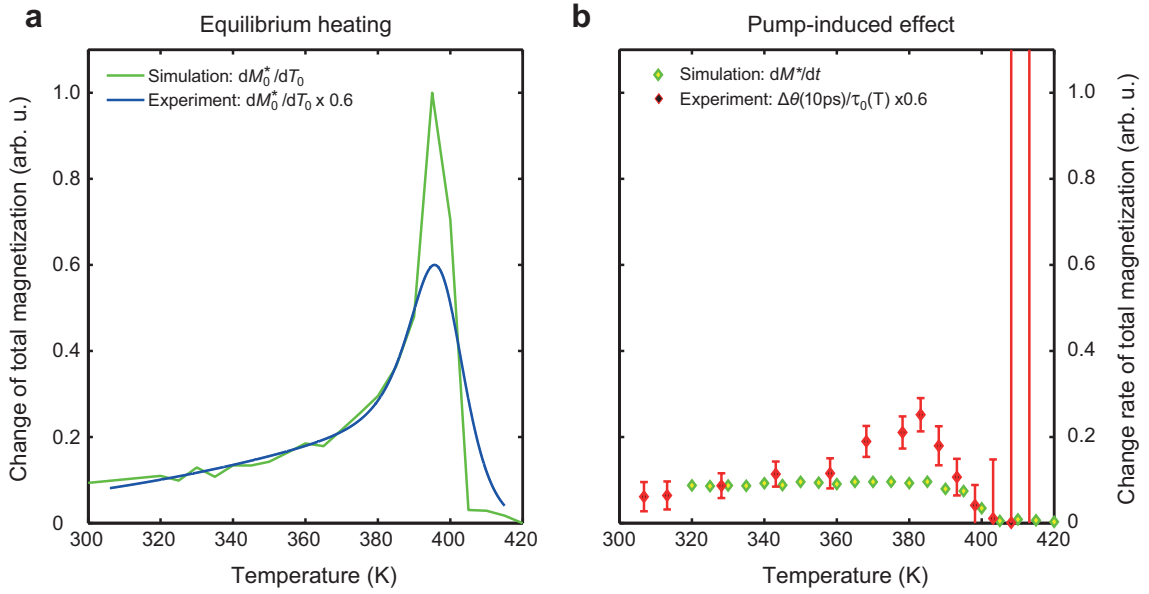


Figure 5.20.: Temperature dependence: simulation and experiment. **a**, Thermal equilibrium value of the (Verdet-constant weighted) total magnetization change $dM_0^*/dT_0 = d[M_{0,a} + 1.5M_{0,d}]/dT_0$. Experiment (blue line) and simulation (green line) show a good agreement. **b**, Pump induced change rates of the experiment $\Delta\theta(10\text{ps})/\tau_0(T_0)$ (red symbols) and the simulation dM^*/dt (green symbols). Both show a less pronounced maximum and an earlier break down compared to the equilibrium change in **a**. Here also the different Verdet constants are taken into account in the simulation.

sum over both sublattices taking into account the Verdet constant ratio 1:1.5. The temperature dependence of the simulated change rate of M^* and the change rate of the Faraday signal $\Delta\theta$ agree qualitatively. Especially the experimentally observed earlier breakdown of $\Delta\theta(10\text{ps})/\tau_0(T_0)$ compared to the equilibrium heating (figure 5.20 a) is reproduced by the simulation dM^*/dt . Quantitatively, the major difference is the experimentally observed, pronounced maximum of $\Delta\theta(10\text{ps})/\tau_0(T_0)$ which is not found by the model simulations. This discrepancy might be due to the fact that applying a constant stochastic noise over 500 fs does not necessarily imply that the spin system temperature is increased by the same amount ΔT , independent of the equilibrium temperature T_0 . In contrast, in the experiment, the pump pulse deposits approximately the same energy for all equilibrium temperatures T_0 .

5.7.6 Summary

All experimental observations and theory simulations are consistent with the following scenario (see figure 5.17 b): The THz-pump pulse excites the 3 double degenerate TO Γ -phonons above 16 THz, which thermalize significantly faster than 1 ps, resulting in a phonon bath with temperature $T_0 + \Delta T$. This leads to an increased oscillation amplitude of the superexchange-mediating oxygen ion, thereby causing increased fluctuations in the exchange integral J_{ad} (see figure 5.17 a). Via these modulations of the exchange parameter, energy is transferred from the lattice to the spin system, whereas angular mo-

momentum transfer to the spin system is forbidden due to the nature of exchange coupling. The energy increase of the spin system results in a transient state of the magnetic order, which is reached by angular momentum transfer from the d-sublattice to the a- lattice, corresponding to $\Delta M_d = -\Delta M_a$. After a much longer time scale of ~ 100 ns, the angular momentum equilibration between lattice and spin sets in, which is mediated by the much weaker spin-lattice couplings, for example SOC or SSMD. This corresponds to the experimentally observed second demagnetization step with an exponential decay time of $\tau_2 = 90$ ns (see section 5.5.3).

5.7.7 Elementary processes in exchange-induced reduction of magnetic order

This study deals with excited lattice and spin subsystems. Generally, the lowest-lying excited states of these subsystems are described by elementary excitations, that is, phonons for the lattice and magnons in terms of the spin system. Since the spin dynamics simulations used above are based on the full dynamics of each single spin and since the lattice was mainly described by a single degree of freedom u , it was not necessary to describe the solid's state by magnons and phonons. However, due to the importance of the concept of quasi-particles, we formulate the spin-lattice interaction through phonon-modulated exchange coupling in the phonon and magnon language.

For this purpose, we consider the YIG Heisenberg Hamiltonian for 2-sublattice ferrimagnet (see section 2.3.4):

$$H_{\text{XC}} = - \sum_n \left(\sum_{i=1}^8 \sum_{j=1}^8 J_{ij} \mathbf{S}_i \cdot \mathbf{S}_j + 2 \sum_{i=1}^8 \sum_{\alpha=9}^{20} J_{i\alpha} \mathbf{S}_i \cdot \mathbf{S}_\alpha + \sum_{\beta=9}^{20} \sum_{\alpha=9}^{20} J_{\alpha\beta} \mathbf{S}_\alpha \cdot \mathbf{S}_\beta \right). \quad (5.26)$$

Here, the indices α, β and i, j account for the Fe atoms in the a- and d-sublattice, respectively, whereas n runs over the number of all unit cells N . The starting point is a Taylor expansion of the inter-sublattice exchange parameters $J_{ij} = J_{ij} + \Delta u_{ij} \partial J_{ij} / \partial u$, leading to a Hamiltonian $H_{\text{XC}} = H_{\text{XC}}^0 + H_{\text{XC}}^1$. Afterwards, the perturbation Hamiltonian H_{XC}^1 including the classical ion displacement Δu is described by magnon/phonon annihilation and creation operators a and b , respectively (Holstein-Primakoff transformation). Omitting the detailed derivation by P. Maldonado [Mae16b], the perturbation Hamiltonian can be written in terms of phonons and magnons as

$$\begin{aligned} H_{\text{XC}}^1 = & \sum_{Q,K} \left(\sum_{l,m} F_{QK}(m,l) a_K^\dagger(m) a_{k-Q}(l) b_Q \right. \\ & + \sum_{\alpha\beta} G_{QK}(\alpha,\beta) a_{Q-K}^\dagger(\alpha) a_{-K}(\beta) b_Q \\ & \left. + \sum_{l,\alpha} L_{QK}(l,\alpha) a_Q^\dagger(l) a_{Q-K}^\dagger(\alpha) b_Q \right), \end{aligned} \quad (5.27)$$

where terms including phonon creation operators are omitted. In equation 5.27, the first two terms describe a processes in which a phonon and a magnon are annihilated and magnon is created. Importantly, the last term describes an annihilation of a phonon and a creation of two magnons. As a reminder, there are magnon bands of two types: ferromagnetic magnons (FM) and antiferromagnetic magnons (AFM) corresponding to spinwaves in the d- and a-sublattice, respectively. In the case of the last term in equation 5.27, the two created magnons are associated with different sublattices, one of them being AFM-type the other one FM-type. Therefore, they increase and decrease the total magnetization, respectively. This corresponds to a process, in which energy, wavevector and angular momentum are conserved, but the sublattice magnetization are reduced by $|\Delta M_m|$. In conclusion, to leading order, our consideration delivers the elementary magnon-phonon interaction processes of the phonon modulated exchange scenario. These processes can be summarized in the quasi particle language by

$$1 \text{ phonon} \rightarrow 1 \text{ antiferromagnon in a-sublattice (10 -20 THz)} \\ + 1 \text{ ferromagnon d-sublattice (0-10 THz)}.$$

5.8 Conclusion and outlook

In contrast to most ultrafast magnetic order studies in the last two decades [Bea96, Koo10, Kir10, Foe11b, Esc13, Big13], this work isolates an important part of the complex cascaded processes: energy and angular momentum transfer from the excited lattice to the spin system (see figure 5.21). This highly direct approach to measure spin-lattice coupling of a magnetic insulator provides the suitable tool for novel *lattice pump/spin probe* studies over 12 orders of magnitude in time, namely from fs to ms. Accordingly, this study reveals two extremely different time scales of phonon-magnon coupling in the model ferrimagnet Yttrium Iron Garnet (YIG).

On the first time scale, a surprisingly ultrafast energy transfer from the excited lattice to the spin system is proceeding. This process is mediated by the phonon-modulated exchange coupling between spin-sublattices (total angular momentum stays constant). Such ultrafast change of magnetic order on the time scale of 1-2 ps has never been observed in insulators. The second timescale of ~ 100 ns is 5 orders of magnitude slower than this initial energy transfer. Here, the angular momentum equilibrates between lattice and spin system, in agreement with known magnon lifetimes in YIG, measured by a number of FMR linewidth studies [Spe62, Vit85, Hun10]. Thus it can be concluded that the phonon-magnon equilibration time strongly depends on the observable (energy or angular momentum). This important result may explain the large range of phonon-magnon equilibration times that is debated in recent studies [Xia10, Sch13].

Remarkably, the ultrafast change of the magnetic order survives from about 10 ps up to 100 ns, which provides a new and interesting quasi-equilibrium state, in which the spin system is hot, but under the constraint of constant total spin angular momentum. This can be seen as a build-up of *spin pressure*, which is finally released once SOC and other microscopic spin-dissipative coupling mechanisms set in.

Further, by comparison to atomic spin dynamics simulations yields an estimate of the

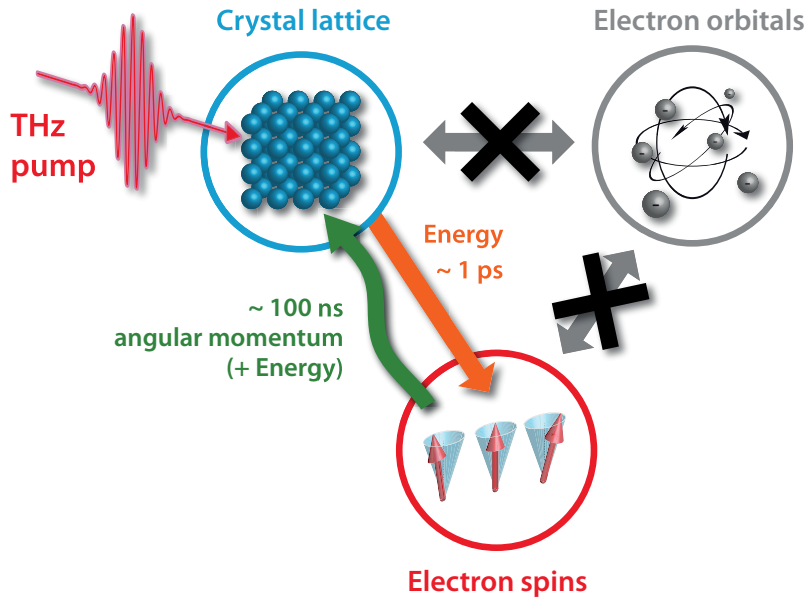


Figure 5.21.: Concluding picture. The results indicate that energy and angular momentum are exchanged between the lattice and spins on distinctively different time scales. High frequency excitations of the crystal lattice lead to modulations of the exchange coupling, causing a sublattice demagnetization on the timescale 1 ps. The resulting spin pressure is released on the timescale of 100 ns by angular momentum transfer to the lattice via weaker coupling mechanisms, such as SOC.

exchange modulation per oxygen ion movement $dJ_{ad}/du \approx 5\text{\AA}^{-1}$.

Our results have several important implications for contemporary research fields. The possibility of ultrafast manipulation of the magnetic order solely through exchange interaction is of considerable interest for all applications where the total spin S_{tot} has to be conserved. This in particular valid for the large material class of antiferromagnets ($S_{\text{tot}} = 0$), which are attracting a strongly increasing attention concerning spintronic applications [Shi10]. Antiferromagnetic spintronics is capable of manipulating and transporting of magnetic order in a zero net magnetic moment material. Accordingly, this could lead to magnetic storage devices, that are invisible to common readout techniques and offer high processing speed at the same time [Jun16].

Another exciting field is the spin Seebeck effect (SSE), where a temperature gradient imposed on the crystal lattice gives rise to spin transport along the gradient [Ada13, Jaw10, Wu16]. This effect gained much attention because of the high application potential concerning thermoelectric devices, which enable the recycling of waste heat from other processes and offer concepts for energy efficient information processing [Uch08]. In previous works, the build-up of a spin current triggered by SSE has been measured by a modulation of a thermal gradient up to 4 GHz [Kra15, Ros14]. That is significantly more rapid than the 100 ns time scale of angular momentum equilibration observed here. Therefore, the results of this chapter indicate that the SSE is triggered by a constraint spin heating process, that proceeds on the ps time scale. This would open up the new field of THz SSE spin currents. As a last example, spin angular momentum exchange between spin-sublattices has been

suggested to be crucial step in ultrafast reversal of the magnetization of ferrimagnetic alloys [Boe10, Rad11, Ber14]. Our experimental study isolates this essential mechanism and could lead to a better understanding of the interplay of the different sublattices during laser induced magnetization switching.

Further research routes are within direct reach. A THz double pump experiment (2D-THz-spectroscopy), could unveil the role of the 3 initially excited TO phonon modes and help to distinguish their contribution [Kue09, Mae11, Jun12]. Moreover, taking the next step in complexity, by exciting additionally electrons with a visible pump pulse in the constraint state ($10\text{ ps} < t < 100\text{ ns}$) can clarify the function of hot electrons as an angular momentum reservoir. Such experiments provide an appealing scenario to compare the capability of the lattice and hot charge carriers as sources or reservoirs for angular momentum.

Investigation of other magnetically ordered material classes such as multiferroics [VA07, Che07] or ferrimagnetic alloys [Boe10, Rad11, Ber14] with the method developed within this thesis is expected to lead to novel insights.

6 Terahertz two-photon absorption generates a coherent phonon

Stimulated Raman scattering is a fundamental light-matter interaction in which two incident optical waves induce a force oscillating at the difference of the light frequencies. This frequency down-conversion scheme has enabled numerous important applications, including coherent control of elementary modes like phonons and magnons by femtosecond laser pulses. In this work, the so far neglected up-conversion counterpart of this process is presented for the first time: sum-frequency stimulated Raman scattering. Based on this novel scheme, coherent control of an optical lattice vibration of diamond by two intense terahertz fields whose sum frequency equals the phonon frequency of 40 THz is achieved. Remarkably, the carrier-envelope phase of the driving pulse is directly imprinted on the lattice vibration. Sum-frequency stimulated Raman scattering selectively deposits energy in any Raman-active mode and opens up a novel pathway to their phase-sensitive coherent control. New prospects in vibrational and magnon spectroscopy, lattice trajectory control and laser machining emerge.

This chapter is based on the publication **Terahertz sum-frequency excitation of a Raman-active phonon** by Mährlein et al. (2016) [[Mae16a](#)].

6.1 Motivation

Gaining control over elementary motions of electrons, spins and ions in solids has been a longstanding goal and is of major interest from a fundamental as well as an applied viewpoint. Examples include steering of chemical reactions along a desired path [[LaR15](#)], switching of spins in magnetically ordered materials [[Kub14](#), [Kim05](#)] and charge transport in photovoltaic devices [[Cun08](#), [Jin14](#)]. Many efficient and selective control strategies take advantage of resonances and natural modes of the material. For instance, coherent lattice vibrations (phonons) have enabled new pathways to permanent material modification [[Kli11](#)], ultrafast insulator to metal transitions [[Kim12b](#), [Liu12](#), [Rin07](#), [Wal13](#)], magnetization control [[Kim12a](#), [Tem12](#)] and even light memories [[Eng13](#), [Fis16](#)]. In addition, phonons are considered model systems for magnons, plasmons and other bosonic excitations.

In the theory chapter on light matter interaction (section [3.2](#)), the coupling of electromagnetic radiation to phonons has been discussed. In the electric dipole approximation, two generic coupling types were identified: A direct coupling via the dipole moment associated with the phonon mode (section [3.2.1](#)) or an indirect coupling mediated through Raman coupling (section [3.2.2](#)).

The mechanism for ultrafast spin-lattice coupling revealed in the experiments of chapter [5](#), shows the enormous potential of THz excitations. One important reason is that THz

lattice excitation is a powerful tool to study and control mechanisms in condensed matter, while leaving electronic excitations in their orbital ground state (see figure 6.1 a). Unfortunately, not all phonon modes are accessible by direct coupling. This is particularly the case for centro-symmetric materials, where the mutual exclusion principle is valid and thus some phonon modes are solely Raman active [Hol04]. Accordingly, there is large interest to find a new coupling mechanism that marries the benefits of conventional impulsive Raman excitation and low energy resonant excitation.

After the discovery of the Raman effect by Raman and Krishnan in liquids [Ram28] and by Landsberg and Mandelstam in solids [Lan28] in 1928, we look back at nearly a century of Raman studies in which diamond is one of the most extensively studied solids [Kri]. Already in 1956, C.V. Raman summarized these studies in a work with the title 'The Diamond' [Ram56]. Since then, lots of Raman-scattering hallmark experiments with monochromatic lasers were performed, most of them focusing on the F_{2g} -Mode [Sol70].

The first impulsive stimulated Raman scattering (ISRS, see section 3.2.2) excitation of coherent lattice dynamics was observed by De Silvestri et. al. by means of periodic modulation of a transient grating in α -perylene crystals in 1985 [DS85]. The coherent phonon amplitude imprinted on the reflectivity was shortly later reported for Bi and Sb [Che90], and for GaAs [Cho90]. The similar technique in transmission geometry could be demonstrated in the high temperature superconductor YBCO in the same year [Chw90]. Only two years later in 1992, Zeiger et. al proposed an alternative excitation scheme: In their DECP model, the excitation shifts the electronic potential energy surface and therefore leads to a sudden shift of the equilibrium coordinate [Zij06] (see section 3.2.2). The DECP mechanism explains the generation of coherent phonons and their initial phase for a number of materials, where electronic absorptions play a role [Che91].

The 40 THz (F_{2g}) phonon mode in Diamond could finally be driven, when ultrashort laser pulses were established research tools. The impulsive Raman excitation and its time domain detection of this coherent phonon could be shown by K. Ishioka and coworkers in 2006 [Ish06].

Since these pioneering works, coherent phonon spectroscopy got established as a powerful tool to investigate all sorts of Γ -point (wavevector $q = 0$) phonons. Nevertheless, one remaining research question is still open: Is it possible to use low frequency radiation in the THz range to drive infrared inactive coherent phonons without changing the electron orbital degree of freedom in materials with a particularly small electric energy gap? Is there another kind of Raman effect that was so far overlooked?

6.1.1 New nonlinear excitation scheme

Following up on the question, if there is a mechanism to drive coherent phonons, that has been neglected so far, it is useful to stay in the framework of Raman processes where the driving force on a given phonon mode is $F \propto (E(t))^2$ in transparent materials (see section 3.2.2). In analogy to second order non-linear optics (section 3.1.3), where the polarization is $P \propto (E(t))^2$ and the electric field of the driving laser pulse is a linear superposition

of all frequency components $E(\omega_i)$, the beating of two frequency components $E(\omega_1)$ and $E(\omega_2)$ therefore leads to components of the force (see also figure 6.1 b)

$$F \propto (E(t))^2 \propto e^{-i(\omega_1 - \omega_2)t} + \text{c.c.} \quad (6.1)$$

Yet as in section 3.1.3, $(E(t))^2$ produces also force components oscillating with the sum frequency:

$$F \propto (E(t))^2 \propto e^{-i(\omega_1 + \omega_2)t} + \text{c.c.} \quad (6.2)$$

So far, these sum frequencies were neglected, because previous coherent-phonon studies were based on excitation pulses in the visible or NIR spectral range. Thus, the force oscillates much too fast for the fundamental excitations (phonons, magnons, excitations, plasmons) to follow. Therefore the sum frequency force is too far off their natural eigenfrequencies in this case.

In contrast, the strong-field THz source developed within this work enables nonlinear light-matter interactions at very low (THz) frequencies, thereby approaching the resonances from 'below' the first ground state excitation (see figure 6.1 c). Accordingly, strong THz fields should provide the possibility to observe a Raman process that is driven by the sum frequency beating for the first time instead of the conventional difference frequency beating.

For such first studies, the drosophila of Raman studies, the C-C bond vibration in diamond (F_{2g} -mode), exhibits an ideal test ground due to its high eigenfrequency, strong Raman interaction [Mil13] and its very weak damping even at room temperature [Ish06].

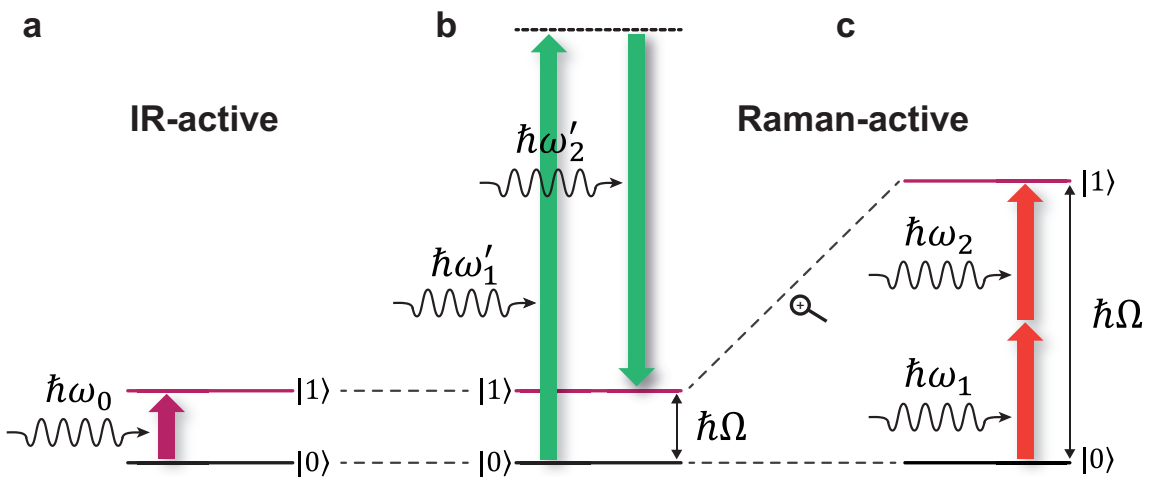


Figure 6.1.: Fundamental excitation schemes. **a**, Direct excitation: pump-field frequency ω_0 is resonant with the infrared-active phonon mode. **b**, Conventional stimulated Raman scattering (SRS): the difference frequency of two driving field components ($\omega'_1 - \omega'_2$) is resonant with a Raman-active phonon mode Ω . **c**, Novel sum-frequency SRS: the sum frequency of two incident THz electric fields ($\omega_1 + \omega_2$) is resonant with a Raman-active phonon mode.

6.2 Diamond material properties

The diamond lattice consists of the lowest mass element (carbon) that can form a covalently bonded crystal. The high symmetry and high purity (isotopic content 98.9% ^{12}C) together with one of the strongest covalent bonds leads to extreme material properties. These are not only useful for mechanical applications or jewelry, but also for optical technologies like light sources, sensors or manipulators [Zai01, Pal85].

Optical applications are favored by an extremely broad and featureless transmittance (nearly 80% for visible radiation) for wavelength below the bandgap ($\lambda > 225$ nm). Only between 2.6 μm and 6.2 μm the lattice absorption leads to a reduced transmission. [Mil13]. In pure, defect-free diamond, this infrared lattice absorption can only be caused by multi-phonon absorption, as monatomic crystals with inversion symmetry exhibit no phonons with an associated dipole moment. In a simple picture, the absorption of a single photon by a multi-phonon resonance (e.g. 2 phonon absorption) can be seen as a phonon that induces a net charge region and a second phonon that produces a dipole moment while oscillating through the gradient of this net charge [Lax55].

The high transmittance in the visible range is a consequence of the large indirect electronic bandgap of 5.50 eV [Mad04] (see figure 6.2 a). Therefore, there are no free charge carriers at room temperature, leading to a very long coherent phonon lifetime due to low scattering rates with charge carriers.

To get as close as possible to a defect-free crystal, in this work we use a sample of highest-purity single-crystal diamond (Type IIa). Compared to other types, it contains only negligible nitrogen (Type Ia and Ib) and negligible boron impurities (Type IIb) [Mil13].

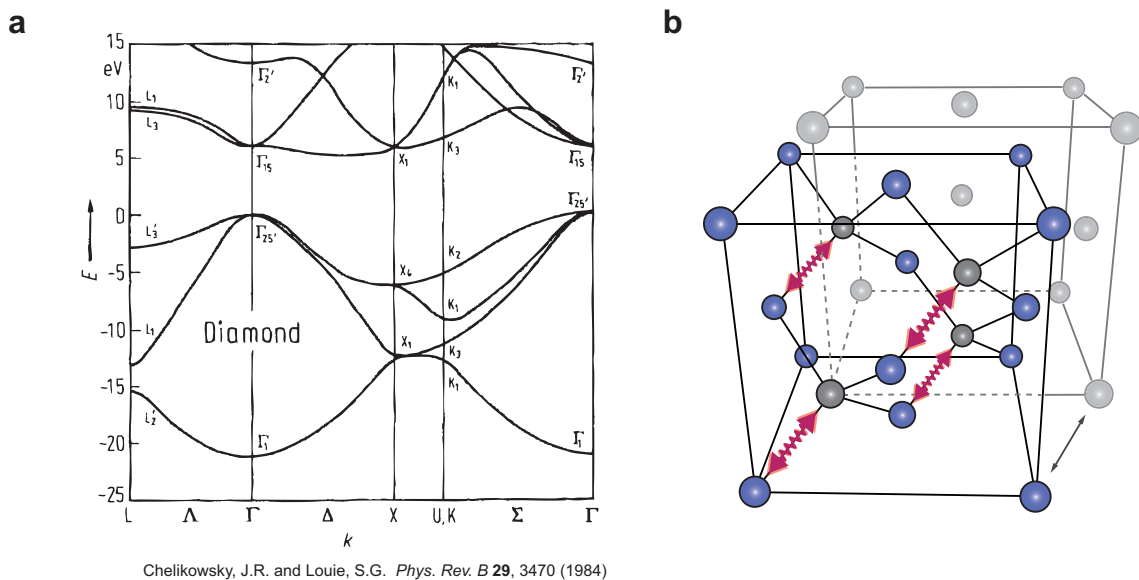


Figure 6.2.: Diamond Properties. **a**, Electronic band structure: Large indirect bandgap (5.50 eV) from $\Gamma_{25'}$ to the minimum of the Δ conduction band [Che84]. **b**, Diamond unit cell consisting of two interpenetrating fcc-lattices (blue and black spheres): The high frequency F_{2g} phonon mode shifts the two lattices against each other (red arrows).

6.2.1 Unit cell and phonon band structure

As shown in figure 6.2 b, the diamond lattice consists solely of two covalently bond carbon atoms per primitive unit cell [Sol70]. Each carbon atom is surrounded by four nearest neighbors, which form an equilateral tetrahedron. Obviously, the lattice consists of two interpenetrating face-centered cubic (fcc) Bravais lattices with a lattice parameter of 3.567 Å [Mad04]. The point group of diamond is hexoctahedral (O_h^7 in Schoenflies notation or space group $Fd\bar{3}m$) [Yu05].

Due to the low atomic mass of carbon and stiff covalent ion bonds, diamond inherits its uniquely rigid material properties and one of the highest known phonon frequencies. The full phonon dispersion is shown in figure 6.3, where the Brillouin center TO-phonon corresponds to the C-C-bond vibration, that moves the two fcc lattices against each other. This oscillation direction is indicated by the springs and arrows in figure 6.2 b. This Raman active F_{2g} TO-mode is triply degenerate at a resonance frequency of 39.9 THz ($1332.5 \pm 0.05 \text{ cm}^{-1}$ at 300 K) [Sol70].

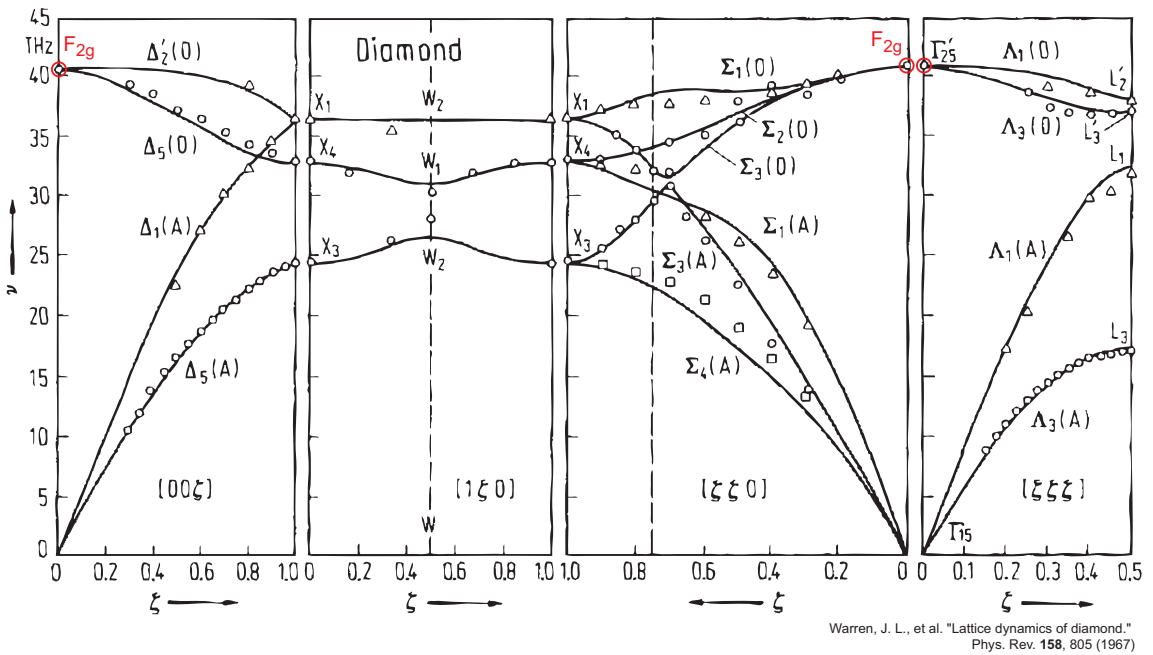


Figure 6.3.: Full phonon bandstructure of Diamond: The dispersion relation of the vibrational normal modes along the high symmetry directions are calculated by a shell-model at 296° K [War67]. The experimental data (black circles and squares) was determined by inelastic neutron scattering [War65, War67]. The red circles indicate the triply degenerate F_{2g} mode, that is investigated in this thesis.

6.2.2 Raman tensor

The large deformation potential combined with high density and small mass, ensures a high Raman scattering efficiency compared to other crystals. As discussed in the theory

section 3.2.2, the Raman scattering efficiency S is determined by:

$$S \propto \sum_j |\hat{\mathbf{e}}_s R_j \hat{\mathbf{e}}_i|^2, \quad (6.3)$$

with the polarization $\hat{\mathbf{e}}_i$ of the incident electric field, the polarization of the scattered Stokes polarization $\hat{\mathbf{e}}_s$ and the Raman tensors $R_j \propto \frac{\partial \chi_{kl}}{\partial Q_j}$ with degree of degeneracy j . Making use of the $F_{2g}(\equiv \Gamma^{(25+)})$ symmetry of the zone-center optical phonon leads to the (Raman-)tensors [Sol70]:

$$R_1 = d \begin{pmatrix} 0 & 0 & 0 \\ 0 & 0 & 1 \\ 0 & 1 & 0 \end{pmatrix}, \quad R_2 = d \begin{pmatrix} 0 & 0 & 1 \\ 0 & 0 & 0 \\ 1 & 0 & 0 \end{pmatrix}, \quad R_3 = d \begin{pmatrix} 1 & 0 & 0 \\ 0 & -1 & 0 \\ 0 & 0 & 0 \end{pmatrix} \quad (6.4)$$

Here $d = d\alpha/dQ$ is the change in polarizability α upon movement along the normal coordinate Q , associated with the F_{2g} -mode. Transforming from the coordinates of the cubic axes ($x = [100]$, $y = [010]$, $z = [001]$) above, to the common crystal orientation ($x' = [110]$, $y' = [\bar{1}\bar{1}0]$, $z' = [001]$), which was also used in the present experiments, leads to [Sol70]:

$$R_1 = \frac{d}{\sqrt{2}} \begin{pmatrix} 0 & 0 & 1 \\ 0 & 0 & 1 \\ 1 & 1 & 0 \end{pmatrix}, \quad R_2 = \frac{d}{\sqrt{2}} \begin{pmatrix} 0 & 0 & 1 \\ 0 & 0 & -1 \\ 1 & -1 & 0 \end{pmatrix}, \quad R_3 = d \begin{pmatrix} 1 & 0 & 0 \\ 0 & -1 & 0 \\ 0 & 0 & 0 \end{pmatrix} \quad (6.5)$$

The transformation is simply realized by a rotation about 45° around the z -axis. The value of $|d|$ has been measured to be about $4.4 \pm 0.310^{-16} \text{ cm}^2$ at a wavelength of 514.5 nm [Gri75, Mil13].

6.3 Experimental details

6.3.1 Experimental setup

The experimental scheme, shown in figure 6.4, mainly consists of a collinear THz-pump VIS-probing setup combined with a balanced detection scheme. The inherently phase stable THz pump pulses are generated by the table top high field source that was introduced in detail in section 4.2. The necessary regenerative Ti:sapphire laser amplifier (repetition rate, 1 kHz; pulse energy, 18 mJ; pulse duration, 35 fs) that feeds the dual OPA (section 4.1.3) is described particularly in section 4.1.

The p-polarized THz pump pulse (center frequency, 15 – 40 THz; pulse energy, 3 – 20 μJ ; pulse duration, ~ 200 fs) propagates collimated through a silicon beam combiner ($>2000 \Omega$ resistivity, double side polished, 400 μm thickness) with an angle of incidence (AOI) close to Brewster angle (74°) to minimize losses [CH05]. Afterwards it is focused by an off axis parabolic mirror (PM) with an effective focal length of 2 inch (parental focal length 1 inch). Thereupon, a THz-pump focus diameters of 150 μm can be reached easily.

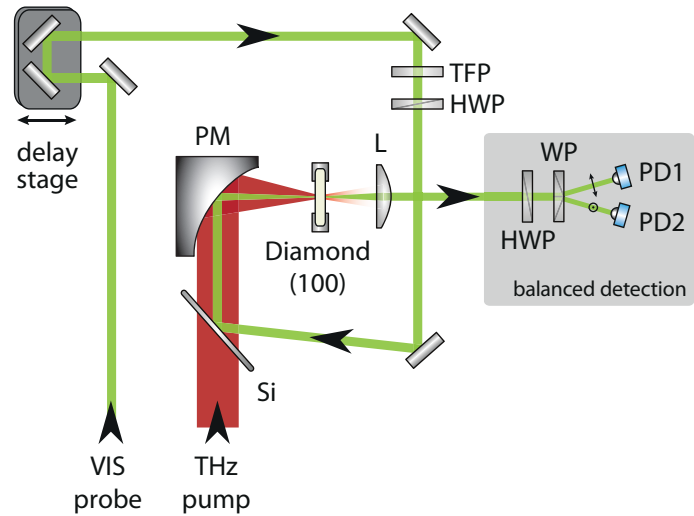
A synchronized 8 fs pulse (repetition rate, 80 MHz; center wavelength 750 nm; pulse energy,

1 nJ) from the MHz oscillator (see section 4.1.1) traverses the sample at a variable delay since sample excitation and probes its transient birefringence Δn_{ai} , thereby providing the full phase-resolved phonon dynamics. The probe pulse is mostly reflected by a thin silicon beam combiner (Si). Thus it can be overlapped with the THz beam collinearly and focused by the same gold off axis parabolic mirror (PM). The 750 nm beam is focused to diameter of 80 μm or smaller to ensure a lateral homogeneously excited probing spot. The initial polarization can be arbitrarily chosen by a thinfilm polarizer (TFP) and a broadband half-wave plate (HWP).

The transient polarization state of the probe pulse is measured with a balanced detection scheme after the transmission through the excited sample. The anisotropic change of the refractive index Δn_{ai} is precisely detected in the same way as in electrooptic sampling (EOS) described in section 4.3.1. The pump-probe delay is altered in fast scan mode by a motorized precision delay stage (Newport GTS 150) with a step size of 1 fs between two adjacent pump pulses. The following data acquisition procedure has been explained in section 4.3.3 (see 'Ultrashort time scales').

In this chapter, all experiments were performed at room temperature and under ambient conditions.

Figure 6.4: Experimental setup. The VIS probe pulse (750 nm, 8 fs, 1 nJ) from the seed oscillator is collinearly overlapped with the THz pump pulse (200 fs, 3 – 20 μJ) by a thin silicon wafer (Si, 400 μm). Both beams are focused onto the sample by the same parabolic Au-mirror (PM). Afterwards, the transient polarization state of the recollimated probe beam is measured by a balanced detection. A thin-film polarizer (TFP) combined with a half-wave plate (HWP) defines the initial probe beam polarization. The pump-probe delay is introduced by a high precision motorized delay stage.



6.3.2 Sample properties and experimental geometries

The sample used for nearly all shown data was a synthetic single crystal diamond (thickness, 200 μm) from the company Sumitomo Electric Hardmetal Corporation. The high purity type IIa chemical vapor deposition (CVD) diamond was oriented to expose the (100) surface. The results could be also reproduced in a less pure diamond window with likely more nitrogen and boron vacancies (see figure 6.11).

The pump and probe beams are collinearly incident normal to the (100) surface. The angle between pump and probe beam polarization is kept fix at $\approx 90^\circ$. Therefore, the probe beam is s-polarized. Further, the sample is mounted on a motorized rotation stage with rotation axis along the propagation direction, meaning normal to the diamond surface.

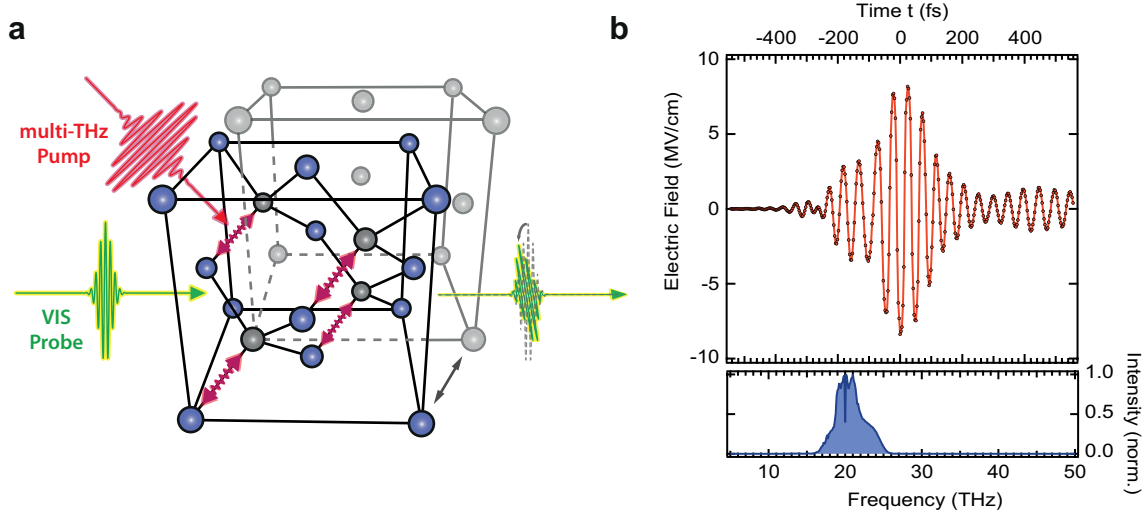


Figure 6.5.: Experimental scheme. **a**, Pump-probe scheme: The coherent lattice mode is excited by a strong-field THz-pulse (red pulse). After a certain delay time t , a probe pulse (green) experiences a specific birefringence depending on the current lattice distortion (red arrows), leading to a change in the polarization of the probe pulse. **b**, The THz pump field measured by EOS and corresponding Fourier spectrum: Full information of amplitude and phase is needed for the simulation in section 6.5.3.

The azimuthal angle of the sample was optimized for maximum coherent phonon signal, meaning that the driving field was parallel to the diamond's $x' = [110]$ -direction.

6.3.3 CEP-modulation technique

A major advantage of the high-field THz generation via OPA-based DFG is not only the inherent CEP stability and the intense fields, but also the ability to select an arbitrary CEP for the resulting THz pulses. This is done by precisely setting the temporal overlap of the two NIR generation pulses. If one of the two pulses is slightly delayed with respect to the envelope maximum of the other pulse, this is identical to an overall time shift

$$\mathbf{E}_B(t + \tau) = \sum_i \hat{\mathbf{E}}_i e^{-i\omega_i(t+\tau)} + c.c. \quad (6.6)$$

Therefore, it corresponds to a slightly different phase shift $\varphi_i = \omega_i\tau$ for every frequency component ω_i . As the simulation data of figure 6.6 show, during the DFG process this leads to a shift of the THz-CEP [Sel08a].

As complication, temporal drifts between the two OPAs may occur due to thermal fluctuations and convection air streams. Therefore, a reliable reference measurement for the CEP is crucially needed for CEP-dependent studies. For this purpose, an new scheme was developed which relies on the synchronized periodic modulation of the CEP rather than a fixed CEP. The faster this modulation takes place the less unwanted drift is possible. Obviously, the fastest modulation possible is the toggling of the CEP after every kHz-shot. That means that the delay between the two NIR generation pulses has to be modulated

with a frequency of 500 Hz synchronized to the 1 kHz repetition rate of the amplified laser system.

This is implemented by applying a triggered 500 Hz sine voltage to a piezo driven precision delay stage (PI Flexure Linear Stage). Accordingly, it is possible to toggle the CEP between a reference CEP $\Delta\phi_0$ and an arbitrary fixed CEP $\Delta\phi_k$ between adjacent laser shots (see figure 6.6 b). This also leads to the possibility to record two pump-probe traces within one pump-probe scan. Data from a single pump-probe scan with toggled CEPs after every laser shot can be seen in figure 6.7.

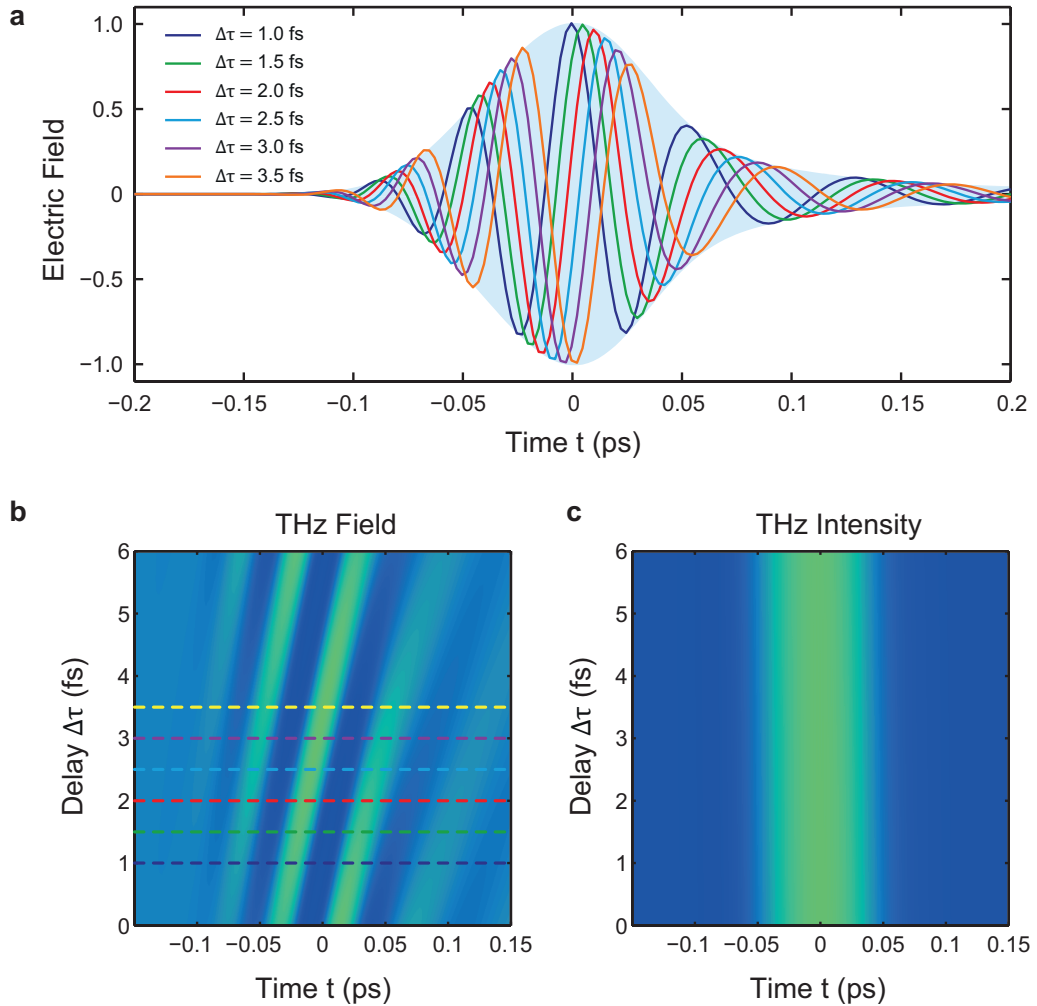


Figure 6.6.: CEP-modulation in the THz generation process (simulation). The simulation models a DFG process of two NIR pulses in a GaSe-crystal (thickness 200 μm , type II phase matching, AOI $\theta = 34^\circ$) with parameters similar to the experimental conditions (section 4.2.3) [Sei13]. **a**, Resulting THz fields for different delay times $\Delta\tau$ between the two mixing NIR pulses: These THz waveforms are cuts through the 2D simulation $E(t, \Delta\tau)$ shown in panel **b**. Noticeably, the time delay $\Delta\tau$ shifts only the CEP, but leaves the envelope, shown in panel **c**, unaffected.

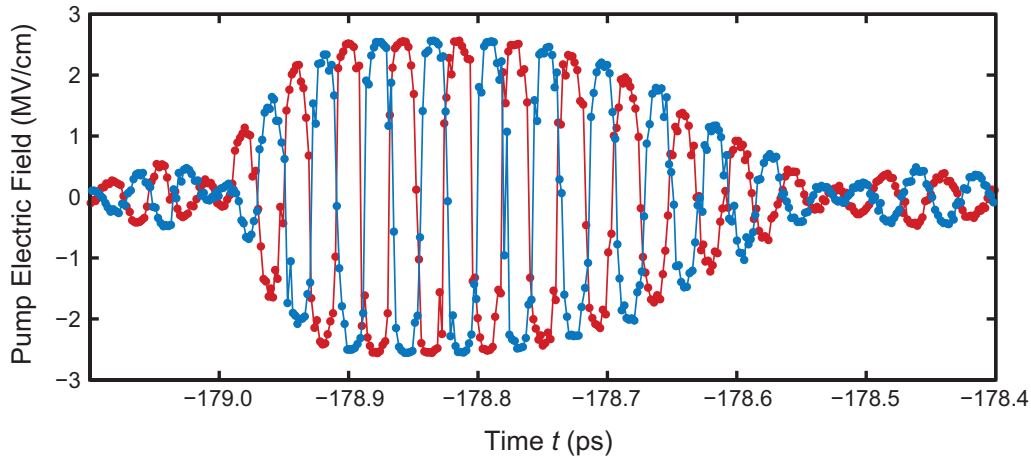


Figure 6.7.: Single run EOS scan with CEP-toggling. These experimental data demonstrate that the toggling of the CEP between two adjacent THz-shots synchronized to the repetition rate yields two CEP-shifted THz waveforms within one EOS-delay scan. Every data point is single shot data without any averaging. The increased pulse duration compared to the simulation (figure 6.6) is due to the thicker generation crystal (1 mm GaSe).

6.4 Experimental results

6.4.1 Excitation frequency dependence

In order to study the dynamic lattice response upon broadband THz excitation, we make use of the high tunability and short pulses of the strong field THz table top source. Therefore, first the THz-pump induced transient birefringence dependent on pump-probe delay and dependent on the broadband pump spectrum is investigated. The resulting overview over these studies is given in figure 6.8. Here, the measurements for three distinctive spectral excitation regimes together with the corresponding transient anisotropic transmission signals $S(t)$ are shown. The center frequency of the pump pulse was tuned successively to match the following cases: The center frequency of the pump pulse ω_0 corresponds to the resonant case ($\omega_0 = \Omega$) or to the non-resonant case below the fundamental excitation frequency ($\omega_0 = (3/4)\Omega$ and $\omega_0 = (1/2)\Omega$).

In the first case, when the pump center frequency is resonant with the target mode (figure 6.8 a), the pump-probe signal consists solely of a peak around $t = 0$ whose shape approximately follows the intensity envelope of the pump pulse (figure 6.8 b). This transient optical anisotropy $S(t)$ arises from the instantaneous nonresonant response of the diamond electrons to the THz field. Apart from this Kerr effect [Hof09], however, no oscillatory feature that would be indicative of a coherent lattice vibration can be observed. When the pump center frequency is reduced from $\omega_0 = \Omega$ to $\omega_0 = (3/4)\Omega$ (figure 6.8 c), very similar dynamics are found (figure 6.8 d).

However, a strikingly different response is obtained when the pump spectrum is centered at half the phonon frequency (figure 6.8 e): after the pump pulse has left the diamond sample, the transient birefringence is dominated by an oscillatory component (figure 6.8 f). Indeed, the Fourier spectrum of $S(t)$ exhibits a sharp peak located at 40 THz (figure 6.8 e). Please

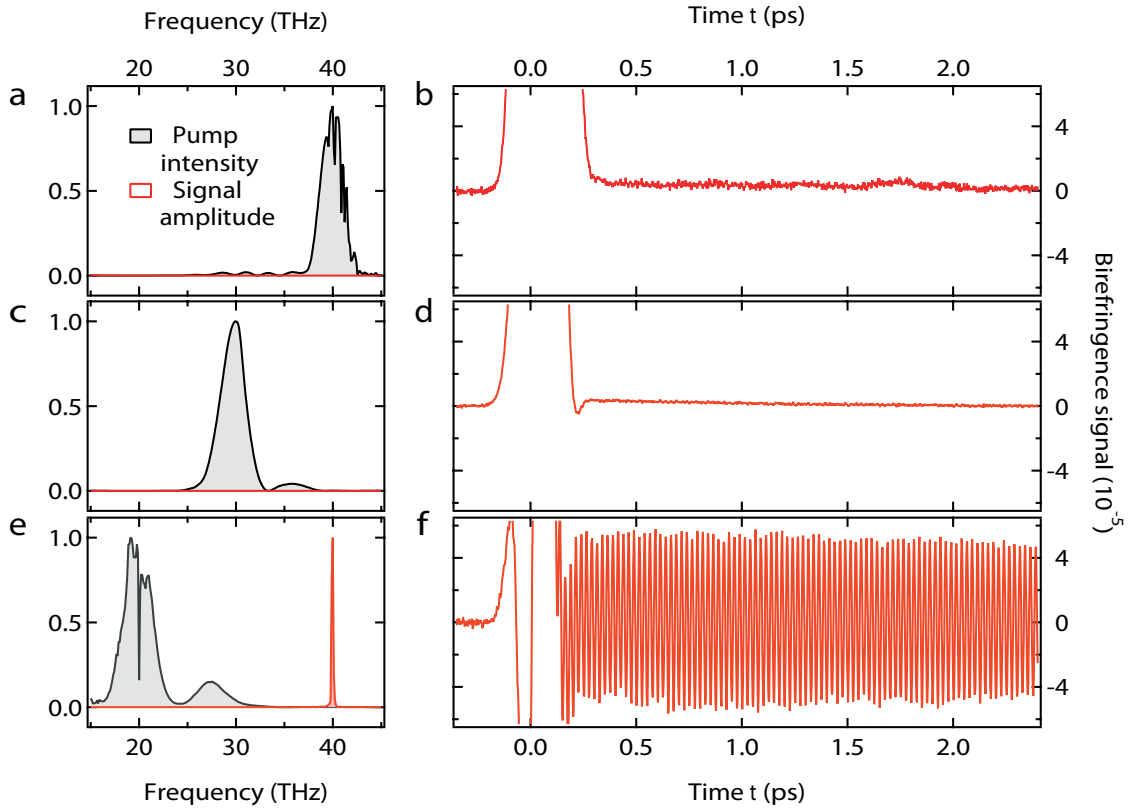


Figure 6.8.: Sum-frequency Raman driven coherent phonons. **a**, Spectrum of a pump pulse centered at the F_{2g} -phonon frequency Ω . **b**, Resulting pump probe signal, showing no signature of lattice vibrations. The peak around $t = 0$ is due to the instantaneous electronic response to the pump pulse. Panels **c**, **d** and **e**, **f** are as with **a**, **b**, but for a pump center frequency of $\omega_0 = (3/4)\Omega$ and $\Omega/2$, respectively. In panel **f**, a strong long-lived oscillation reveals coherent-phonon excitation with the expected frequency. All birefringence signals are normalized to an incident pump-pulse energy of $1 \mu\text{J}$.

note, that the narrow dip in the pump spectrum at exactly 20 THz is not related to the phonon absorption, because the spectrum shown here belongs to the incident pump pulse. The sharp feature is the fingerprint of the resonant absorption of the CO_2 bending mode in air, while working under ambient conditions [Per82, Mar32, May10].

In order to pinpoint the oscillation frequency Ω and the damping rate Γ more accurately, a time domain fit for $t > 200$ fs is performed. According to the harmonic oscillator model in section 3.2, the oscillatory component of the induced optical birefringence caused by the coherent lattice motion should follow the solution

$$Q(t) = A_0 e^{-\Gamma t} \sin(\Omega t + \delta), \quad (6.7)$$

when the pump pulse has left the sample. By fitting the initial amplitude A_0 , damping constant Γ , resonance frequency Ω and phase shift δ , a striking agreement with the $S(t)$ is revealed. The fit (blue line) is shown in figure 6.9 together with a zoomed in inset, which demonstrates the superior quality of the measured signal $S(t)$ (red line). It delivers

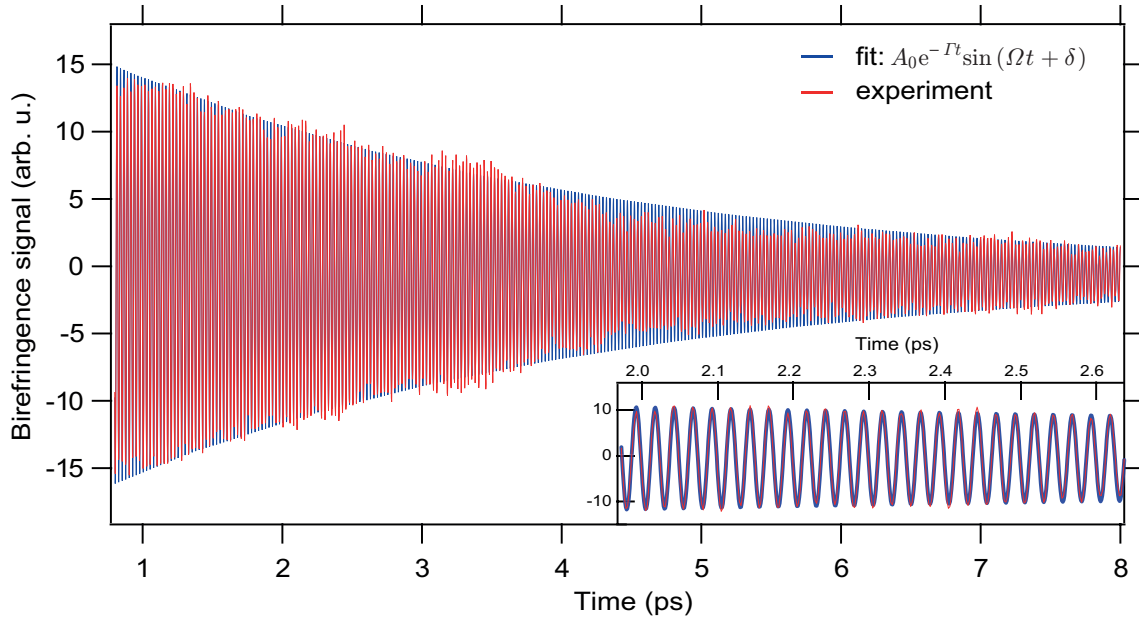


Figure 6.9.: Time domain fit. Transient birefringence signal excited at half resonance ($\omega_0 = \Omega/2$) fitted with a single damped harmonic oscillator solution ($Q(t) = A_0 \exp(-\Gamma t) \cdot \sin(\Omega t + \delta)$) for $t > 200$ fs. The inset is a zoom along the time axis that magnifies the fit quality.

a center frequency of $\Omega/2\pi = 39.95$ THz and a single exponential damping constant of $\Gamma = 0.283$ ps $^{-1}$. These values agree excellently with those inferred from stimulated Raman pumping by Ishioka et al. [Ish06] of the very same crystal using optical pump pulses with a center wavelength of 400 nm. Moreover, also the values from spontaneous Raman scattering [Sol70] coincide well (see table below). Therefore, the oscillatory pump-probe signal of figure 6.8 f is a clear hallmark of diamond's F_{2g} Brillouin center phonon.

	Solin et al.	Ishioka et al.	Maehrlein et al.
Method	spontaneous Raman scattering	difference frequency ISRS	sum frequency ISRS
Central frequency	39.95 ± 0.015 THz	39.84 THz	39.95 ± 0.01 THz
Damping constant	0.311 ps $^{-1}$	0.145 ps $^{-1}$	0.283 ps $^{-1}$
Reference	[Sol70]	[Ish06]	[Mae16a]

The slight deviation of $S(t)$ from the single exponential damping envelope can be caused by two effects. First, due to the long scanning time in order to gain 1 fs resolution in a long time window, the pump intensity might fluctuate within one pump-probe delay scan. This leads to slight changes in the oscillation amplitude for different pump-probe delay times. Secondly, due to ringing of CO $_2$ oscillations in the pump field (see figure 6.5 b), there is still a small driving field left, even after one picosecond. Therefore, a driving force has to be included in the equation of motion for $Q(t)$. This is accurately modeled in section 6.5.2.

Figure 6.10: Instantaneous electronic response. This figure shows the full magnitude of the birefringence signals of the main figure 6.8 b (blue), d (green) and f (red). For the blue and the green curve the signal roughly follows the envelope of the pump pulse and therefore is purely Kerr-type, whereas for the phonon excitation case (red curve), the instantaneous signal exhibits higher order nonlinearities.

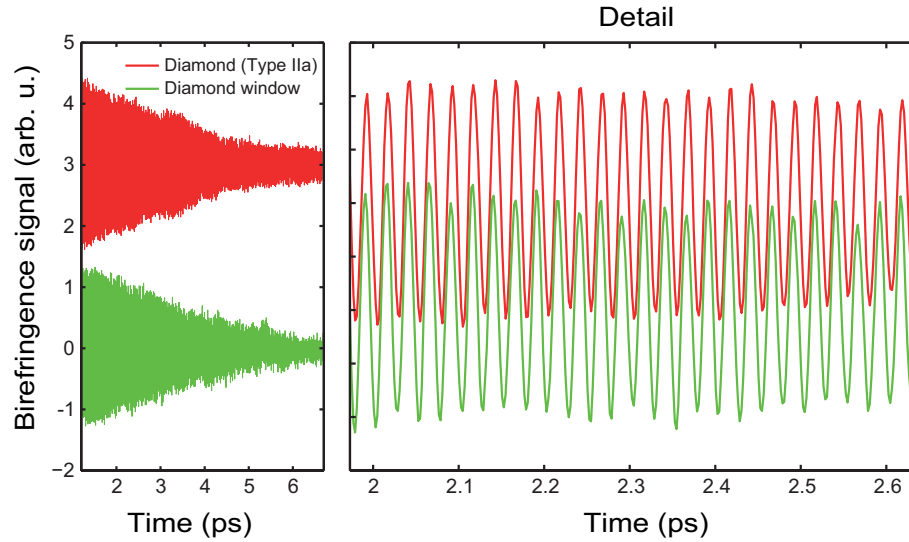
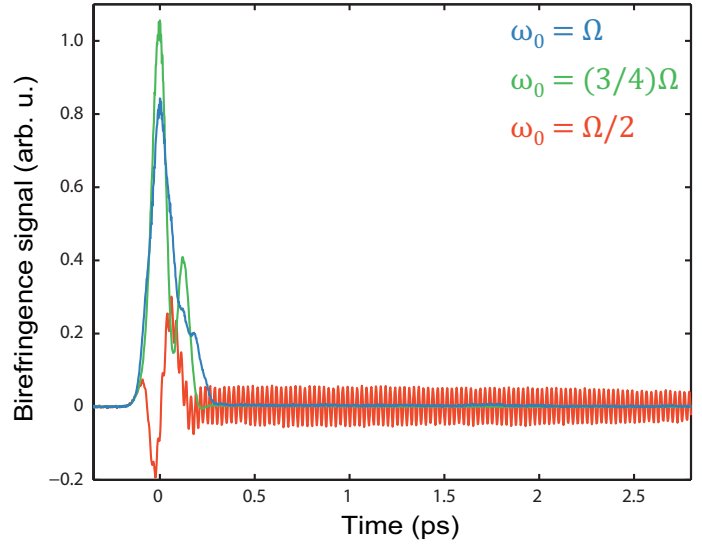


Figure 6.11.: Comparison between two different diamond samples. The red curve was measured in the high purity (Type IIa) diamond sample, that was used for all shown experiments within this work. The green curve was retrieved from a less pure sample (CVD diamond window). Except for the slightly larger damping rate Γ for the later sample, both phonon dynamics look very similar, demonstrating the reproducibility among different samples.

Figure 6.10 shows the Kerr-type contribution during the temporal pump-probe overlap ($-200 \text{ fs} \lesssim t \lesssim 300 \text{ fs}$) in detail. In the two cases for $\omega_0 = \Omega$ and $\omega_0 = (3/4)\Omega$, this instantaneous contribution corresponds roughly to the envelope of the driving pulse. In contrast, in the case of $\omega_0 = \Omega/2$, a more complex interplay between instantaneous contribution and coherent phonon signal governs the signal. The interplay between these two effects and their contribution to the anisotropic refractive index Δn_{eo} change will be included as well in the model in section 6.5.2.

The excitation at half of the resonance ($\omega_0 = \Omega/2$) was also repeated in a less pure chemical CVD diamond window material. Even in this sample, the excitation of the coherent F_{2g}

phonon could be clearly observed. Qualitatively, there is no significant difference between the transient birefringence signals induced by the 40 THz phonon in both samples (see figure 6.11). Only the slightly increased damping rate of $\Gamma = 0.345 \text{ ps}^{-1}$ is an indication for an larger amount of impurities in the CVD diamond window. The fitted central frequency of $\Omega_0/(2\pi) = 39.92$ is nearly identical to the high quality Type IIa sample.

In conclusion, these results demonstrate for the first time an excitation of a coherent phonon mode with a driving field below its fundamental resonance frequency like proposed in figure 6.1. The next section will show that, this novel excitation mechanism obeys the characteristics of a stimulated Raman excitation.

6.4.2 Fluence dependence

The phonon amplitude excited by the new mechanism SF-SRS that was proposed in section 6.1.1 should scale with the square of the driving electric field $E(t)$. This is obvious from the harmonic oscillator model in equation 3.15. Therefore, to prove the character of a Raman excitation, the phonon amplitude has to obey the symmetries of the Raman tensor $\partial\chi^{(1)}/\partial Q$ and has to scale with $(E(t))^2$.

In order to measure the fluence dependence, a pair of free-standing gold wire-grid polarizers (InfraSpecs) are inserted into the THz beam to control the THz intensity with a spectrally flat attenuation [Cos77]. The second polarizer is kept strictly at p-polarization, whereas the first one was rotated to change the incident power onto the diamond sample. The results are shown in figure 6.12. Here, the Fourier transform of the THz-pump induced optical anisotropy $S(t)$ exhibits again a sharp frequency component at 40 THz. For lower fluences this fingerprint of the F_{2g} -mode shrinks and then nearly vanishes. The phonon amplitude A_0 is extracted by fitting equation 6.7 to $S(t)$ in the time domain for all fluences. As the linear absorption spectrum is spectrally featureless around 20 THz [Mil13], it can

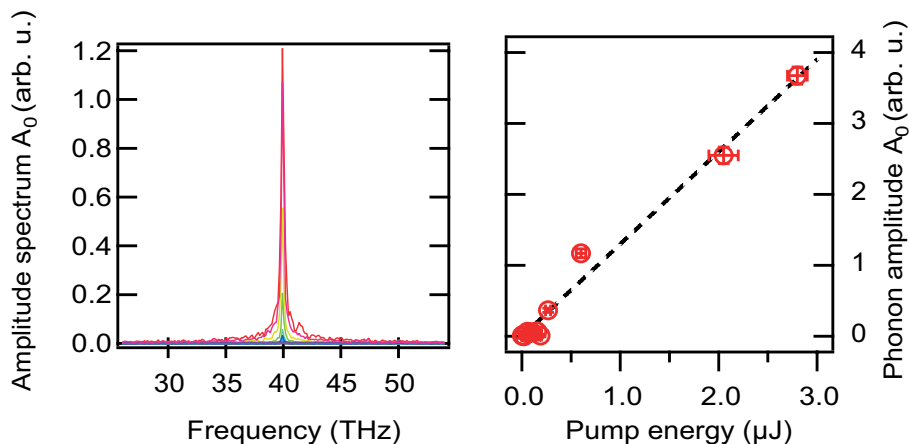


Figure 6.12.: Fluence dependence of the phonon amplitude. **a**, Fourier transform of the oscillatory components in the birefringence signals for different fluences. **b**, Initial phonon amplitude A_0 extracted from the time domain fits according to equation 6.7. Vertical errorbars correspond only to the fitting error, systematic errors due to temporal drifts might be larger.

be assumed that the absorbed intensity is proportional to the incident intensity. The dependence of the coherent phonon amplitude A_0 on the incident pump energy is shown in figure 6.12 b. This fluence dependence (excitation focus diameter was kept constant) clearly indicates that the excited phonon amplitude A_0 is linear to the absorbed energy, meaning that it scales with the square of the driving field $E(t)$. The same fluence dependence is obtained by integrating the Fourier spectrum $\tilde{S}(\omega)$ in figure 6.12 a from 38 to 42 THz. Additionally also the peak value of $\tilde{S}(\omega)$ shows a linear dependence on the incident pump fluence.

In conclusion, these results fulfill the requirement of a first order Raman process and prove that the assumption of a harmonic oscillator model driven by $(E(t))^2$ was justified [Sol70].

6.4.3 Symmetry properties

Finally, it is left to prove that the novel excitation mechanism inherits the symmetry properties from the Raman tensors for the excited Brillouin center mode (F_{2g}) given in equations 6.4. In previous ISRS studies, the coherent phonon amplitude was found to be maximum, if the polarization of the excitation field \hat{e}_p is parallel to the [110]-axis [Ish06]. Due to the twofold symmetry of the Raman tensors (equation 6.4), the excitation should show a $\cos 2\theta$ dependence for the angle θ between pump field polarization \hat{e}_p and [110]-crystal axis. Thanks to the orientation of the crystallographic axes, θ can be conveniently changed by azimuthal rotation of the diamond sample. The azimuthal angle is equal to θ , when the polarization of the pump field \hat{e}_p is fixed.

In analogy to the conventional ISRS excitation in diamond, the expected symmetry is investigated by rotating the sample by $\theta = 45^\circ$. Figure 6.13 shows that the oscillatory signal nearly completely vanishes for $\theta = 45^\circ$, whereas for $\theta = 0^\circ$ a maximum phonon amplitude is observed.

This leads to the final conclusion that the mechanism responsible for experimental results in this chapter is a novel type of Raman excitation because it scales quadratically with the field amplitude E and is proportional to the Raman tensor $\partial\chi^{(1)}/\partial Q$. In the following section, this sum frequency stimulated Raman excitation of a coherent phonon will be modeled as a damped harmonic oscillator with an external driving force.

6.5 Model

6.5.1 Equation of motion

Starting with a little reminder, it is useful to recapitulate the brief derivation of light-matter interaction concerning coherent phonons that was introduced in section 3.2. There, the harmonic approximation (section 2.2.1) was applied, which justifies that all phonon modes can be described as uncoupled (damped) harmonic oscillators, after the transformation to normal coordinates $Q_r(q, t)$ [Nol05]. In that case, $Q_r(q, t)$ can be interpreted as classical

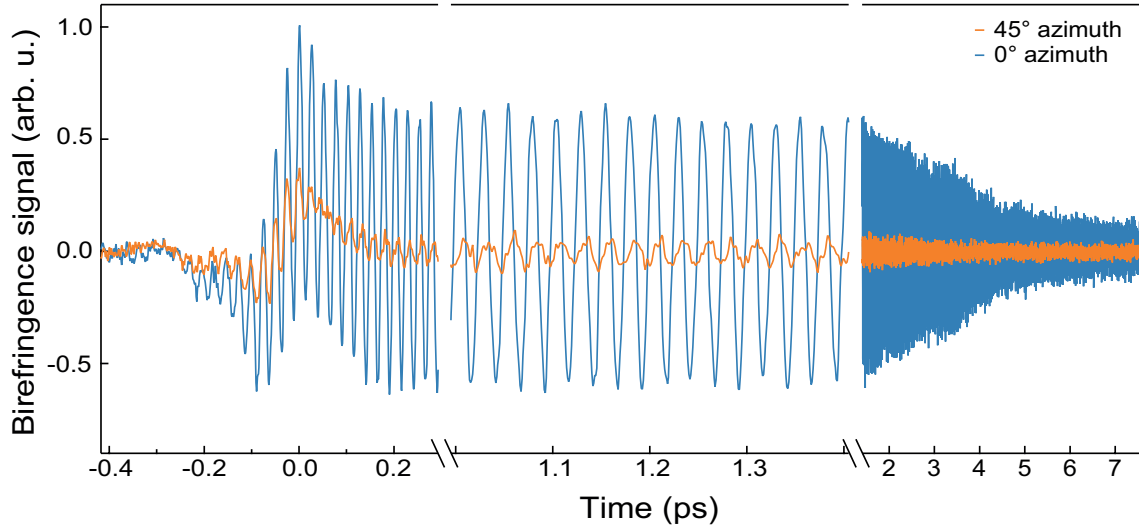


Figure 6.13.: Confirmation of the Raman tensor symmetry properties. The figure shows the two different birefringence signals on 3 different time scales. The maximum oscillatory signal is obtained, when $\mathbf{E}_{\text{THz}} \parallel [110]$ -crystal axis (blue line). An azimuthal rotation of 45° minimizes the signal (orange line), which confirms the Raman symmetry also observed in traditional SRS studies [Ish06].

amplitude of the r th phonon branch with wavevector q . The further introduction of light-matter interaction in the electric dipole approximation [She84] by utilizing the classical scalar Lagrangian formalism, lead to the equation of motion (see section 3.2):

$$\frac{\partial^2 Q(t)}{\partial t^2} + 2\gamma \frac{\partial Q(t)}{\partial t} + \omega_r^2 Q(t) = \frac{1}{m^*} \left(\frac{\partial P(Q, 0)}{\partial Q} E(t) + \epsilon_0 \frac{\partial \chi^{(1)}}{\partial Q} (E(t))^2 \right) \quad (6.8)$$

Here again the implicit assumption was made, that the material is excited far away from electronic resonances (transparent medium). Hence the response of the material can be assumed to be instantaneous without any memory function. Like mentioned before, in a centrosymmetric crystal like diamond the Raman active F_{2g} - mode cannot be infrared-active (mutual exclusion principle). Accordingly $\partial P(Q, 0)/\partial Q$ vanishes and the only driving force $F(t)$ is proportional to $(E(t))^2$.

Note that electrooptic sampling (section 4.3.1) provides the full information in amplitude and phase of the driving field $E(t)$ (see figure 6.5 b). Thus, the driving force $F(t)$ can be directly determined in time domain and then transformed to $\tilde{F}(\omega) \propto \text{FT}[(E(t))^2]$ in order to obtain the solution for the equation of motion 6.8 in frequency domain:

$$Q(\omega) \propto \frac{\text{FT}[(E(t))^2]}{\Omega^2 - \omega^2 - i\Gamma\omega} \quad (6.9)$$

However, the phonon amplitude $Q(t)$ is not measured directly in the experiment. More accurately, the anisotropic change in the refractive index $\Delta n_{eo}(t)$ is measured. Therefore, we need to model the measured signal $S(t)$, as will be done in the next section.

6.5.2 Modelling of the pump-probe signal

In addition to coherent phonons, the instantaneous non-resonant electronic response may also lead to changes in birefringence. Hence, a contribution proportional to $(E(t))^2$, a so called THz Kerr effect [Hof09], has to be added to the transient anisotropic refractive index change

$$\Delta n_{eo}(t) \propto Q(t) + CE^2(t) \quad (6.10)$$

where C is a phenomenological constant.

Additional complexity arises from the velocity mismatch of the ultrashort pump and probe pulse while propagating through the 200 μm thick diamond sample. One can easily imagine that such high frequency phonon oscillations could be thereupon "washed out". Therefore, to simulate the measured signal $S(t)$, the convolution with a transfer function must be included. The signal $S(t)$ is actually the phase difference $\frac{\lambda_{\text{probe}}}{2\pi} \Delta\phi(t)$ between two perpendicular polarization components of the probe pulse, which changes due to transient birefringence caused by the phonon oscillations (this can be described as a Raman effect as well [Dek00]). This phase difference is a convolution of the instantaneous refractive index change $\Delta n_{eo}(x=0, t)$ with a rectangular function of temporal width βd , where d is the sample thickness and β the inverse velocity mismatch [Saj15]. The velocity mismatch β used here is the mismatch between the phase velocity $v_p = c/n(\omega_0)$ of the 20 THz pump field and the group velocity $v_g = \partial\omega_{0,\text{probe}}/\partial k(\omega_{0,\text{probe}})$ of the probing pulse in the diamond sample. Accordingly, $S(t)$ can be written as:

$$\begin{aligned} S(t) = \frac{\lambda_{\text{probe}}}{2\pi} \Delta\varphi(t) &= \int_0^d \Delta n_{eo}(0, t + \beta z) \, dz \\ &= \left(\Delta n_{eo}(z=0, t) * \text{rect}(\beta d) \right) (t), \end{aligned} \quad (6.11)$$

for collinear propagating pump and probe pulses along z -direction. In frequency domain, this convolution with the rectangular window function transforms to a simple multiplication with a sinc-function:

$$\begin{aligned} \tilde{S}(\omega) &= \Delta \tilde{n}_{eo}(\omega) \cdot \frac{d\beta}{2} \text{sinc}\left(\omega \frac{d\beta}{2}\right) \\ &= \text{FT}[A(Q(t) + CE^2(t))] \cdot \frac{d\beta}{2} \text{sinc}\left(\omega \frac{d\beta}{2}\right) \end{aligned} \quad (6.12)$$

In the last step, equation 6.9 and equation 6.10 were plugged in. In this final equation 6.12, A and C are the only fitting parameters. All other parameters are known (Ω and Γ in $Q(t)$ are obtained from a time domain fit, $E(t)$ is directly measured via EOS, the equilibrium refractive index $n(\omega)$ is taken from [Mil13, Pet23]).

6.5.3 Results

According to equation 6.12, the anisotropy signal $\tilde{S}(\omega)$ is calculated in the frequency domain and then compared in the time domain with the measurements from section 6.4.

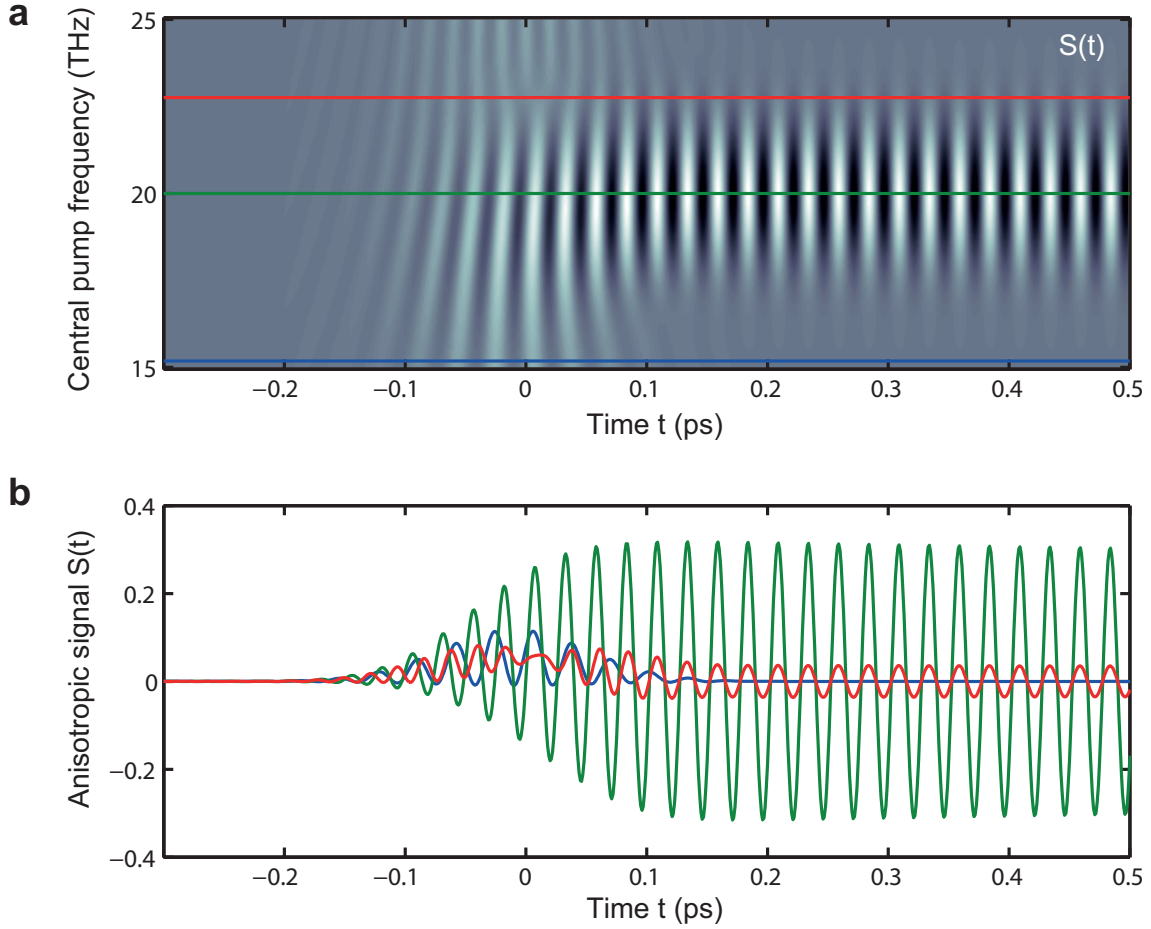


Figure 6.14.: Model results. **a**, Simulated birefringence signal $S(t, \omega_0)$ (equation 6.12) for various THz pump central frequencies ω_0 and **b**, corresponding constant pump frequency cuts: The THz-Kerr effect $\propto CE^2(t)$ dominates the signal during the pump probe overlap ($t \approx 0$) for all pump central frequencies ω_0 (e.g. blue line), whereas the long lived oscillation $\propto Q(t)$ only exist for pump central frequencies around half the phonon resonance $\Omega/2 = 20$ THz (green line). THz Kerr effect, coherent phonon amplitude and propagation effects (walk off) can lead to more complex signals (e.g. red line).

To first test the model, a two dimensional simulation was performed. Here, the anisotropy signals $S_j(t)$ depending on simulated THz pump fields $E_j(t)$ with different central frequencies $\omega_{0,j}$ is calculated. The envelope of the pump pulses including their peak amplitudes, as well as their pulse durations (FWHM = 200 fs) were kept constant.

The results are shown in figure 6.14. A clear resonance behavior around $\omega_0/(2\pi) = 20$ THz appears, which results in long-lived oscillations that indicate the coherent phonon excitation (see also corresponding constant frequency cut, green line in figure 6.14 a, b). This resonance is broadened around 20 THz (e.g. red line) due to the finite bandwidth of the pump pulse $E(\omega)$ leading to a number possible frequency pairs $\omega_1 + \omega_2 = \Omega$. Far off the resonance, e.g. for a central frequency of 15 THz (blue line), solely the instantaneous electronic response $\propto (E(t))^2$ dominates the signal. This is especially obvious because

the signal is present only around $t = 0$ when the pump and the probe beam copropagate through the sample.

For central pump frequency regions, where the interplay of all three effects (coherent phonon, Kerr effect and propagation walk off) governs the transient anisotropy of the sample, more complex signals $S(t)$ can arise. For example, this is the case for a central pump frequency of 22 THz (red line).

We are now ready to use our model to reproduce the measured data. Here, the data from figure 6.13 for 0° azimuthal angle is taken exemplarily. The electric field in figure 6.5 b is the measured driving field for this trace and is therefore plugged as $E(t)$ in our model. The phonon resonance frequency Ω and damping constant Γ are determined by an independent fit (displayed in figure 6.9). The scaling factors A and C in equation 6.12 are fit parameters, accordingly leading to the simulation results in figure 6.15. Obviously, the zoomed region in the middle of the figure, shows an excellent agreement, between simulation (grey line) and experiment (blue line). Additionally, the decay for $t > 2$ ps is also followed very well by the model. Even the more complex dynamics during the pump-probe overlap ($-300 \text{ fs} < t < 200 \text{ fs}$) are well reproduced by the model. The deviation between model and experimental data, can be explained by a slight drift in the THz field shape (e.g. CEP or chirp) between the reference EOS measurement of $E(t)$ and the actual transient birefringence measurement $S(t)$ in the diamond sample.

We conclude, that despite the simplicity of the classical harmonic oscillator assumption, the model developed within this section is suitable to explain coherent phonons driven by a THz field with $F(t) \propto (E(t))^2$ at half of the resonance frequency Ω and their impact on the anisotropy pump-probe signal $S(t)$.

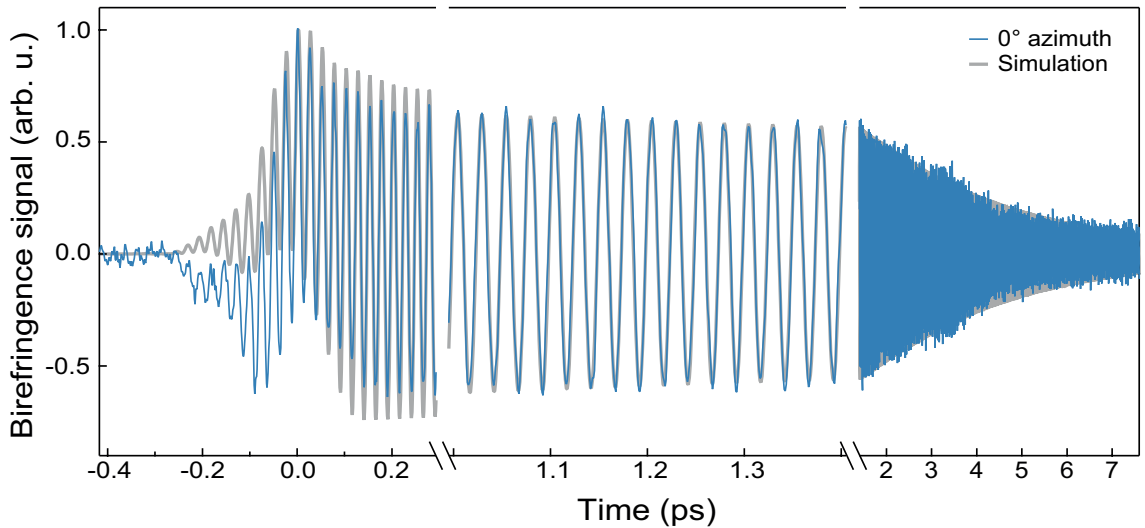


Figure 6.15.: Comparison of measurement and simulation. The blue trace is the measured signal at azimuthal angle $\theta = 0$). The grey curve is the simulation based on the model signal $S(t)$ (equation 6.12) with input parameters: electric pump field $E(t)$ from figure 6.5 b and phonon resonance frequency Ω and damping parameter Γ both derived from a time domain fit (figure 6.9).

6.6 Coherent phonon phase control

6.6.1 Concept

As shown in the previous sections, sum-frequency stimulated Raman scattering (SF SRS) is a novel tool to drive IR-inactive coherent phonons with strong THz or MIR pulsed laser sources. Compared to the traditional difference frequency SRS, it offers two major advantages.

First, SF SRS allows for a non-resonant excitation of coherent phonons, without providing excess energy that could lead to parasitic electronic excitations, which can be already intuitively seen in figure 6.1, by comparing the incident photon energies $\hbar\omega_i$ to the resonance energy $\hbar\Omega$. This could be a key benefit for some important applications that will be discussed in the conclusion section 6.7 of this chapter.

A further sophisticated advantage of the novel SF SRS mechanism, is the coherent phase control that is dictated by the inherent phase properties (i.e. CEP) of the excitation pulse. In order to understand this advantage, it is important to note that sum- and difference-frequency SRS exhibit a very different behavior with respect to the CEP of the pump pulse. Let us assume a driving pulse containing frequency pairs ω_1 and ω_2 with initial CEP φ_0 :

$$E(t) = (A_1 e^{-i\omega_1 t} + A_2 e^{-i\omega_2 t}) e^{-i\varphi_0} + c.c. \quad (6.13)$$

As the driving force oscillates with

$$(E(t))^2 \propto e^{-i(\omega_1 \mp \omega_2)t + (\varphi_0 \mp \varphi_0)}, \quad (6.14)$$

a CEP change by $\Delta\varphi$ therefore shifts the phase of the phonon oscillation by $\Delta\varphi - \Delta\varphi = 0$ in the difference-frequency case, but by $\Delta\varphi + \Delta\varphi = 2\Delta\varphi$ in the sum-frequency process. Thereupon, conventional (difference-frequency) Raman excitation is independent of the CEP, whereas its sum-frequency counterpart undergoes a shift of twice the CEP. Consequently, sum-frequency SRS should enable direct coherent phonon-phase control, by imprinting the light field's CEP onto the phonon motion.

6.6.2 Experimental confirmation

In order to demonstrate the ability of phonon phase control via THz CEP, a series of CEP-dependent SF SRS measurements is conducted. They are performed by making use of the CEP-modulation technique introduced in section 6.3.3. After the CEP-modulation $\Delta\varphi$ is set, a reference EOS measurement is taken, which includes the reference pulse $E_0(t)$ and the CEP-shifted pulse $E_j(t)$ shifted by $\Delta\varphi_j$ within the same pump-probe delay scan. This is shown for 5 distinctive CEP-modulations ($0, \pi/4, \pi/2, 3\pi/4$ and π) in figure 6.16 in the left hand panel. The broken lines correspond to the reference fields $E_0(t)$ in each measurement.

Thereafter, an anisotropy pump-probe measurement in the diamond sample is performed

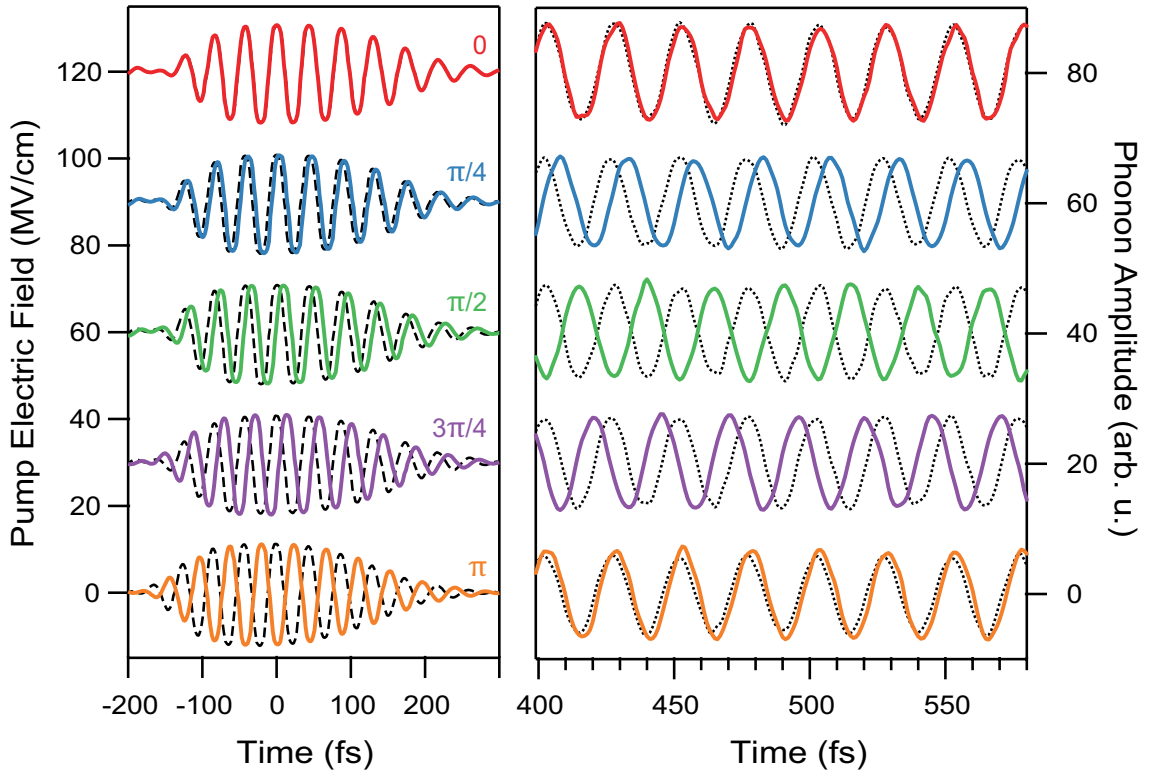


Figure 6.16.: Experimental result: phonon phase control via THz pump CEP. **a**, Measured transient electric field of the THz pump pulse for different settings of its CEP. For comparison, the $\Delta\varphi = 0$ reference transient is shown as broken line for each pump pulse. **b**, Corresponding coherent phonon signals measured after excitation by the pump fields of panel **a**. Clearly, the CEP-modulated pump pulses induce phonon phase shifts by $2\Delta\varphi_j$ (full lines) with respect to the coherent phonon launched by the reference pulse (dotted lines).

with the very same CEP-modulations and data acquisition. This leads to two separated pump-probe traces within the same scan, corresponding to a THz excitation with field $E_0(t)$ and $E_j(t)$, respectively. A detailed view on the resulting coherent phonon signal is shown on the right hand side in figure 6.16 for each $E_j(t)$.

Apparently, the phonon phase shifts always by $2\Delta\varphi_j$, while the arrival time of the pump pulse envelope remains always constant. This is most obvious in the case of $\Delta\varphi_3 = \pi/2$, when the phonon oscillation is found to undergo a π phase shift (green line). Also for a CEP shift of $\Delta\varphi_5 = \pi$, the phonon oscillation clearly is shifted by 2π .

These clear findings confirm the previous expectation, that CEP changes of the pump pulse result in a twice as large phase shift of the resulting lattice motion, thereby enabling a new pathway to phase control of coherent lattice vibrations and other fundamental modes of condensed matter.

6.7 Conclusion and outlook

In conclusion, within the work of this thesis, a novel mechanism for launching coherent lattice vibrations has been found and demonstrated: Sum-frequency stimulated Raman

scattering (SF SRS). This approach provides coherent control of all Raman-active modes such as magnons and plasmons that have so far been inaccessible by THz or mid-infrared radiation. Simultaneously, parasitic electronic excitation, which occurs when optical laser pulses are used, is greatly reduced. As an additional benefit, the CEP of the pump pulse is directly transferred into the phase of the phonon motion.

Besides the unambiguous demonstration of SF SRS for the well-known model F_{2g} mode in diamond, further scientific cases are directly within reach.

As similar C-C bonds are also found amongst other carbon based materials, it could be for example very interesting to study the role of coherent phonons in carbon nano tubes (CNTs) [San09, San13]. Especially the further investigation of already observed nonlinear coherent phonon dynamics in single-walled CNTs could be of high interest [Gam06].

Further, even sticking to the same F_{2g} mode in diamond could lead to interesting fundamental questions: Nowadays, the most promising progress in the development of quantum computing can be found among the research of quantum coherence of nitrogen vacancy (NV) centers in diamond [Chi06, Dut07]. In this scheme, logical operations between quantum bits of information, so called qubits, are represented by specific transitions of electronic or nuclear spin states in single NV-centers [Chi13]. As the lifetime of these qubits is mainly limited by spin-lattice coupling, SF SRS could be used to influence the qubit state. By controlling the phase of this dynamic lattice potential maybe a sort of feedback loop or at least a coherent disturbance between several qubits could be investigated.

Going further into the direction of quantum computing at room temperature, England and coworkers demonstrated a phononic light storage device based on a Raman sequence [Koz00, Nun07] exciting the very same F_{2g} mode in diamond [Eng13, Fis16]. There, in the write process, simply speaking, signal photons are annihilated in a Stokes process, creating an excited phonon state (= memory state). During the phonon lifetime, a subsequent read pulse leads to an anti-Stokes transition, which results in the emission of signal photons. With the benefits of SF SRS, additionally the CEP can be stored in the phonon mode and later read out by a Raman process, like demonstrated in section 6.6. Therefore, storing the CEP of a THz pulse in a coherent phonon mode may pave the way toward phonon-based quantum processing at room temperature.

Last but not least, by using superconducting diamond [Eki04] the role of coherent phonons and their phase in the superconducting state could be investigated by applying the novel SF SRS technique. Using conventional difference frequency SRS would immediately destroy the superconducting condensate due to the excessive photon energy.

In general, due to the low photon energies required, sum-frequency SRS provides a unique tool to steer chemical reactions or phase transitions in the electronic ground state, solely driven by Raman-active lattice vibrations. The extension to THz pulse sequences will enable independent phase and amplitude control of the lattice trajectory along multiple normal coordinates, which is challenging with optical pulses accompanied by electronic excitations [Kat13]. Sum-frequency SRS may therefore reveal novel routes to phase transitions [Kim12b, Rin07] or other phonon-mediated effects.

For industrial applications, it shall be mentioned that sum-frequency excitation of the phonon mode is intimately related to two-photon absorption, which is has so far not yet been

observed for a vibrational mode. Such selective energy deposition may enable machining of transparent materials by intense mid-infrared lasers [Wit13, Pow93].

Nevertheless, the most important and straightforward application in the scientific background is the extension of contemporary spectroscopic techniques: highly sensitive vibrational spectroscopies, such as action spectroscopy [Oom06] and Raman-force microscopy [Raj11], can be extended to infrared-forbidden yet Raman-active modes.

In conclusion, the novel light-matter coupling mechanism SF SRS that was found within the work of this thesis extends vibrational spectroscopy methods to infrared-forbidden modes, enables phase-sensitive studies of phonon-mediated phenomena and paves the way for full lattice trajectory control.

7 Summary

The results of this thesis demonstrate that phonons provide an important degree of freedom to control matter on fundamental time scales in a non-invasive way. A major reason is that lattice excitations are not spectators in many solid state phenomena, but can be used to dynamically steer fundamental effects, such as change of magnetic order. As demonstrated here in the case of magnetic order, high-frequency lattice excitations can lead to novel transient, quasi-equilibrium states that have not been accessible up to now (chapter 5). More generally, specific phonon excitation provides a versatile method to study isolated coupling processes instead of complex cascaded processes following electronic excitation of hot carriers.

Up to now, phonon excitation by THz or mid-IR pulses was only implemented by initial interaction with infrared-active phonons [Rin07, Fau11, Kim12b, Liu12], whereas non-infrared active yet Raman active modes remained inaccessible. In this thesis, a complementary light matter coupling scheme was established, which can be seen as the THz-counterpart of conventional impulsive stimulated Raman scattering [DS85, Cho90, Ish06, Rif07] (chapter 6).

In order to gain new fundamental insights, techniques and tools have to be developed and combined, that push the limits of state-of-the-art experiments. Therefore, one essential milestone of this thesis is a novel THz pump/visible probe setup, that combines three major developments (chapter 4). Most importantly, a table top high field THz-source was designed and implemented, that can compete with state of the art free electron laser sources in terms of peak electric fields [Gre16, Sch15, Tav11]. Nonlinear difference frequency mixing of two spectrally shifted NIR pulses yields inherent phase stable THz field transients with electric peak fields exceeding 50 MV/cm [Sel08a]. A collinear phase matching scheme in Gallium selenide allows for a convenient tunability, bridging a frequency region from 10 THz up to 60 THz and thereby covering most of the known high frequency phonon modes. In a pump-probe scheme, transient sample properties are monitored via electrooptic and magneto-optic observables by a synchronized 8 fs probe pulse. The sub-femtosecond time resolution is complemented by a novel data acquisition (DAQ) method, which allows us to cover a pump-probe delay range over 12 orders of magnitude, from the femtosecond to the millisecond time scale. This DAQ technique was crucial for the discovery of the slow magnetization dynamics in YIG. Further, a carrier envelope phase (CEP)-modulation scheme that is synchronized to the laser amplifier repetition rate was developed. It not only allows for setting an arbitrary CEP, but also enables a simultaneous recording of a given CEP reference measurement, monitored in the same pump-probe trace. This gives rise to drift free CEP-dependent measurements, that were necessary to observe phase shifts of the 40 THz phonon mode in diamond.

The introduced cutting-edge experimental setup was used to excite high-frequency TO phonon modes of the textbook ferrimagnetic insulator Yttrium Iron Garnet (YIG) and probes the resulting dynamics of the magnetic order from fs to μ s. The obtained results

demonstrate for the first time the possibility of ultrafast manipulation of the magnetic order by solely modulating the superexchange coupling of the two spin sublattices. Two distinctively different time scales for phonon-magnon equilibration times are revealed. First, a surprisingly rapid change of magnetic order for an insulator on the timescale of 1 ps is identified as ultrafast sublattice demagnetization. It is exclusively mediated by phonon-induced fluctuations of the exchange coupling and thus constrained by spin angular momentum conservation. The observed constrained quasi-equilibrium state persists over nanoseconds. Second, on a time scale of 100 ns, spin angular momentum is transferred from the spins to the lattice, resulting in spin-lattice equilibrium in terms of both heat and angular momentum. The latter time scale agrees with typical magnon lifetime, obtained from a number of FMR linewidth studies [Spe62, Vit85, Hun10]. The disentanglement of energy and angular momentum flow is one of the main achievements of this study.

These findings are supported by a microscopic model that assumes that the exchange constant (quantifying the antiferromagnetic coupling of the two magnetic sublattices) is modulated by the thermal motion of the superexchange-mediating oxygen ion, which fluctuates in space due to the heating of the lattice. This model, complemented with atomistic spin dynamics simulations by J. Barker, yields a numerical estimate for the modulation strength per oxygen elongation.

This study paves the way to further phonon-driven experiments and has important implications for other research fields, including spin-conserving switching in antiferromagnetic spintronics [Shi10, Jun16], and the extension of the spin Seebeck effect to the THz range, aiming for faster energy efficient thermoelectric devices [Uch08, Ada13, Ros14]. Finally, the observation of ultrafast sublattice demagnetization can also lead to a better understanding of the angular momentum transfer between different sublattices during laser induced magnetization switching in ferrimagnetic alloys [Boe10, Rad11, Ber14].

The investigation of ultrafast lattice-spin coupling relies initially on the efficient coupling of THz pulses to the electric dipole of IR-active phonons. However, phonon modes with a vanishing electric dipole moment were previously inaccessible by THz or mid-IR radiation. In this thesis, a novel light matter interaction scheme is explored, that leads to coherent phonon excitation via non-resonant two-photon absorption of intense THz fields. In this second-order nonlinear process, the sum frequency of two field components of the same THz pulse drives the coherent lattice motion. This mechanism can be conveniently described in the framework of stimulated Raman excitation (SRS) [Mer97, Gri08] and is therefore termed sum-frequency stimulated Raman scattering (SF SRS) in this thesis.

We demonstrate this THz sum frequency excitation by coherent control of a prototype Raman active mode, namely the highest frequency (F_2g -) mode in diamond. Our novel excitation scheme offers two additional important benefits. First, SF SRS avoids parasitic electronic excitation because no excessive photon energy is incident on the sample [Cho90, Rif07]. Second, compared to conventional SRS, sum frequency SRS provides the possibility of full control of the phonon phase dictated by the THz pump pulse CEP. A simple phenomenological model based on a harmonic oscillator reproduces all these findings in terms of a Raman process.

The demonstration of this universal mechanism opens new venues for vibrational spectroscopy, such as action spectroscopy [Oom06], or might be also applicable to other innovative methods like Raman-force microscopy [Raj11]. Combining SF SRS with THz pump-pulse sequences may enable full lattice trajectory control, which is challenging with optical pulses accompanied by electronic excitations [Kat13]. Therefore, specifically tailored routes to phase transitions [Rin07, Fau11, Kim12b, Liu12] or steering of chemical reaction [LaR15] come into reach. Recently, the F_{2g} mode in diamond was found to operate as light storage for quantum computing at room temperature [Eng13, Fis16]. SF SRS adds the benefit of additionally storing the light pulse's CEP. Finally, our findings could also have technological implications enabling the laser machining of transparent materials by intense mid-IR lasers [Wit13, Pow93].

In summary, this thesis highlights the large potential of THz lattice excitations for steering ultrafast phenomena in solids.

A Appendix

A.1 Harmonic approximation for antiferromagnets

Strictly speaking, in order to consider phonons in magnetic materials that consist of antiferromagnetic coupled magnetic sublattices, these different species of spins have to be considered in a harmonic approximation approach. This harmonic approximation for an antiferromagnet is briefly derived within this section. The case of a ferrimagnet is similar in the derivation, but one step higher in complexity.

An antiferromagnetic spin order can be described by two ferromagnetic sublattices, which are coupled antiferromagnetically. For the assumption that every atom of sublattice A has only sublattice B nearest neighbors and the restriction to only the exchange coupling $J_1 < 0$ to the nearest neighbor, we get following Heisenberg Hamiltonian [Nol09]:

$$H = - \sum_{i,j}^{n,n} J_{ij} \mathbf{S}_i \cdot \mathbf{S}_j - gJ \frac{\mu_B}{\hbar} (B_0 + B_A) \sum_i^A S_i^z - gJ \frac{\mu_B}{\hbar} (B_0 - B_A) \sum_i^B S_i^z, \quad (\text{A.1})$$

with anisotropy field B_A and external field B_0 assumed to be along the z -axis (= easy axis). To go along the same direction like in section 2.3.6, a Holstein-Primakoff transformation has to be performed for sublattice A ($a_{\mathbf{q}}, a_{\mathbf{q}}^\dagger$) and sublattice B ($b_{\mathbf{q}}, b_{\mathbf{q}}^\dagger$). Further in the framework of harmonic approximation only terms which are bilinear in wavevector \mathbf{q} are considered (e.g. $a_{\mathbf{q}}, b_{\mathbf{q}}, J(\mathbf{q}), \delta_{\mathbf{q},\mathbf{q}'}$). This finally leads to the Hamiltonian:

$$H = E_a + b_A \sum_{\mathbf{q}} a_{\mathbf{q}}^\dagger a_{\mathbf{q}} + b_B \sum_{\mathbf{q}} b_{\mathbf{q}}^\dagger b_{\mathbf{q}} + \sum_{\mathbf{q}} c(\mathbf{q}) \left(a_{\mathbf{q}} b_{\mathbf{q}} + a_{\mathbf{q}}^\dagger b_{\mathbf{q}}^\dagger \right), \quad (\text{A.2})$$

with

$$E_a = -NgJ\mu_B S B_A + NzJ_1 \hbar^2 S^2 \quad (\text{A.3})$$

$$c(\mathbf{q}) = -2J(\mathbf{q}) \hbar^2 S \quad (\text{A.4})$$

$$b_{A/B} = -2zJ_1 \hbar^2 S \pm gJ\mu_B (B_0 \pm B_A). \quad (\text{A.5})$$

But this raises a big problem: The Hamiltonian in equation A.2 is not diagonal in $a_{\mathbf{q}}$ and $b_{\mathbf{q}}$'s. After a further transformation with the following ansatz for new operators

$$\alpha_{\mathbf{q}} = c_1 a_{\mathbf{q}} + c_2 b_{\mathbf{q}}^\dagger \quad (\text{A.6})$$

$$\beta_{\mathbf{q}} = d_1 a_{\mathbf{q}}^\dagger + d_2 b_{\mathbf{q}}, \quad (\text{A.7})$$

that fulfill again the boson commutation relations, finally the Heisenberg Hamiltonian for an antiferromagnet can be written [Nol09]:

$$\tilde{H} = \tilde{E}_a(B_0) + \sum_{\mathbf{q}} \hbar\omega_\alpha(\mathbf{q}) \alpha_{\mathbf{q}}^\dagger \alpha_{\mathbf{q}} + \sum_{\mathbf{q}} \hbar\omega_\beta(\mathbf{q}) \beta_{\mathbf{q}}^\dagger \beta_{\mathbf{q}}, \quad (\text{A.8})$$

where the following abbreviations was used:

$$\hbar\omega_{\alpha/\beta}(\mathbf{q}) = \frac{1}{2} \left[\pm b_A \mp b_B + \sqrt{(b_A + b_B)^2 - 4c^2(\mathbf{q})} \right]. \quad (\text{A.9})$$

Substituting b_A and b_B back from equation A.5, leads to the excitation energies in anti-ferromagnet [Nol09]:

$$\hbar\omega_{\pm}(\mathbf{q}) = \sqrt{4S^2\hbar^4 (J_0^2 - J^2(\mathbf{q})) + g_J\mu_B B_A (g_J\mu_B B_A - 4SJ_0\hbar^2)} \pm g_J\mu_B B_0. \quad (\text{A.10})$$

In conclusion it can be seen that the energy spectrum of an antiferromagnet is distinctively different to ferromagnets. The antiferromagnet exhibits two spin wave branches, ω_+ and ω_- , which are degenerate in the absence of an external field ($B_0 = 0$). Additionally for $\mathbf{q} = 0$ and for $B_0 = 0$, the minimum spin wave energy leads to an energy gap E_g in the spin wave spectrum:

$$E_g = \sqrt{g_J\mu_B B_A (g_J\mu_B B_A - 4SJ_0\hbar^2)} \quad (\text{A.11})$$

For small wavevectors $q = |\mathbf{q}|$, the spinwave dispersion is linear with q for an antiferromagnet and quadratic in the ferromagnetic case.

For a ferrimagnet the derivation above becomes significantly more complicated as the two sublattices have a different magnitude in magnetization ($|M_A| \neq |M_B|$) in the Heisenberg ground state.

A.2 Electron-phonon coupling

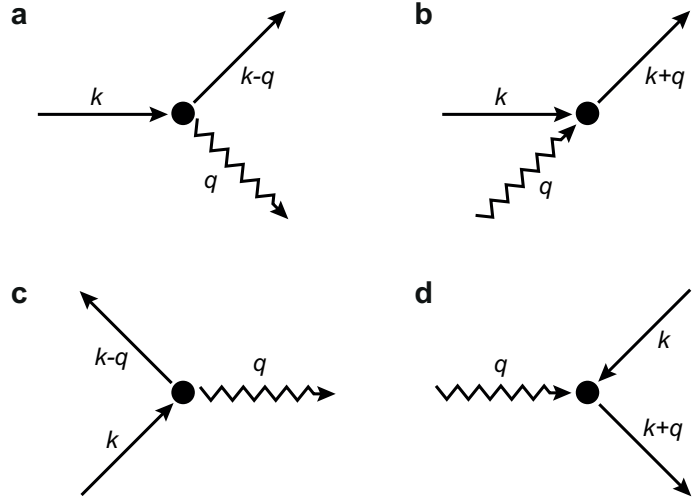
As mentioned in the introduction of section 2.2, the degrees of freedom of the core ions and the valence electrons were assumed to be independent. The contribution of the static ion lattice to the valence electron states is already contained in the electronic band structure of a solid. The derivation of the electronic band structure can be found in standard solid state text books like [Yu05, Nol05, Ash05]. Its theoretical description, only plays a minor role for the understanding of the research presented within this work.

Thus the electron-lattice interaction Hamiltonian $H_{e-\text{lat}}$ is only governed by the variations of the ion positions around their equilibrium lattice sites. Consequently the electron-lattice interaction can be comprehensively described by the interactions of electrons and holes with phonons. This description in terms of quasi particles makes the possible interaction processes tangible, as graphically summarized in figure A.1. All four possible processes emit or absorb a phonon with energy $\hbar\omega_r(\mathbf{q})$ by elastic scattering with an electron (figure A.1 a-b), or creation or annihilation of an electron-hole pair (figure A.1 c-d).

Under the assumption that the ions move rigidly and do not deform within the interaction with the electrons the following electron-phonon interaction Hamiltonian can be derived [Nol05]:

$$H_{\text{ep}} = \sum_{\mathbf{k}\sigma} \sum_{\mathbf{q}\mathbf{K}} \sum_i T_{\mathbf{k},\mathbf{q},\mathbf{K}}^{(i)} \left(b_{\mathbf{q}r} + b_{\mathbf{q}r}^\dagger \right) a_{\mathbf{k}+\mathbf{q}+\mathbf{K}\sigma}^\dagger a_{\mathbf{k}\sigma}, \quad (\text{A.12})$$

Figure A.1: Electron-phonon scattering processes. **a**, Phonon emission (zigzag arrow) by an electron (straight arrow). **b**, Phonon absorption by an electron. **c**, phonon creation via electron-hole recombination and **d**, electron-hole pair creation by annihilation of a phonon [Nol05].



where $T_{\mathbf{k},\mathbf{q},\mathbf{K}}^{(i)}$ is the electron-phonon coupling matrix element and is derived in detail in [Nol05]. Here the index $i = (r, s)$ is again a combined index that runs over all phonon branches r and all atoms in the Bravais lattice base s . The operators $a_{\mathbf{k}\sigma}$ and $a_{\mathbf{k}+\mathbf{q}+\mathbf{K}\sigma}^\dagger$ annihilates an electron with wave vector \mathbf{k} and spin state σ and creates an electron with vector $\mathbf{k} + \mathbf{q} + \mathbf{K}$ and with the same spin state, respectively. The additional reciprocal lattice vector \mathbf{K} is due to the periodicity of the phonon momentum $\hbar(\mathbf{q} + \mathbf{K})$. If $\mathbf{K} \neq 0$, the scattering process is called Umklapp-process [Yu05]. It can be seen as scattering out of the first Brillouin zone, which is equivalent to back folding by the reciprocal lattice vector \mathbf{K} .

From equation A.12 it is obvious that the change of electron momentum by $\Delta\mathbf{k} = +\mathbf{q}(+\mathbf{K})$ requires an emission of a phonon with wave vector $-\mathbf{q}$ or an absorption of a phonon with wave vector $+\mathbf{q}$. Thus momentum and energy conservation are not violated. All processes depicted in figure A.1, can be expressed obviously by combinations of creation and annihilation operators of electron states and phonons in equation A.12.

A.3 Description of light propagation

A.3.1 Maxwell and material equations

In the (semi-)classical picture (see section 3.1.1), the interaction of light with matter is fully described by the material equations and the macroscopic Maxwell equations [Ash05]:

$$\begin{aligned} \nabla \cdot \mathbf{D} &= \rho & \nabla \times \mathbf{E} &= -\frac{\partial \mathbf{B}}{\partial t} \\ \nabla \cdot \mathbf{B} &= 0 & \nabla \times \mathbf{H} &= \frac{\partial \mathbf{D}}{\partial t} + \mathbf{j} \end{aligned} \quad (\text{A.13})$$

where the current density \mathbf{j} and the charge density ρ are the source terms for the magnetic fields (\mathbf{H}, \mathbf{B}) and electric fields (\mathbf{E}, \mathbf{D}), respectively. The material equations are summarized as:

$$\mathbf{D} = \epsilon_0 \mathbf{E} + \mathbf{P} \quad \mathbf{B} = \mu_0 \mathbf{H} + \mathbf{M} \quad (\text{A.14})$$

Here \mathbf{P} is the electric polarization field and \mathbf{M} is the magnetization field. The permittivity ϵ_0 and permeability μ_0 of free space are universal constants, which have to be present for expressing the fields in SI-units.

A.3.2 Wave equation of optics

For the theoretic description of light propagation, the assumption of media with no free charges $\rho = 0$ or currents ($j = 0$) shall be kept. In addition, the restriction to nonmagnetic media ($\mathbf{M} = 0$) is made. Starting from the Maxwell-equations A.13 and material equations A.14, these assumptions directly lead to the most general form of wave equation in nonlinear optics:

$$\nabla \times \nabla \times \mathbf{E} + \frac{1}{c^2} \frac{\partial^2}{\partial t^2} \mathbf{E} = -\frac{1}{\epsilon_0 c^2} \frac{\partial^2}{\partial t^2} \mathbf{P} \quad (\text{A.15})$$

The first part of the identity $\nabla \times \nabla \times \mathbf{E} = \nabla(\nabla \cdot \mathbf{E}) - \nabla^2 \mathbf{E}$ can be neglected by making use of the slowly varying amplitude approximation [Boy08]. The approximation is justified, when the fractional change of the amplitude in a distance on the order of the wavelength is much smaller than unity [Boy08]. This leads to the commonly used inhomogeneous wave equation for the electric field:

$$\nabla^2 \mathbf{E} - \frac{1}{c^2} \frac{\partial^2}{\partial t^2} \mathbf{E} = \frac{1}{\epsilon_0 c^2} \frac{\partial^2}{\partial t^2} \mathbf{P} \quad (\text{A.16})$$

From this wave equation it can be clearly seen, that the polarization \mathbf{P} acts as the source term for new components of the electromagnetic wave.

A.3.3 Phase matching

In a simple picture, phase matching is fulfilled, when generated waves at different points in the crystal are able to interfere constructively along the propagation pathway of the initial generation pulse. Generally the dispersion of the material prevents this from happening. Phase matching is required because nonlinear process (DFG shall be exemplary considered here as need in section 4.2.2 and 4.2.3) not only has to fulfill energy conservation ($\hbar\omega_2 = \hbar\omega_3 - \hbar\omega_1$), but also wave vector conservation. Therefore the wavevector mismatch

$$\Delta kz = (\mathbf{k}_3 - \mathbf{k}_1 - \mathbf{k}_2) \cdot \mathbf{r} \quad (\text{A.17})$$

has to be minimized in order reach significant gain of ω_2 photons along an arbitrary direction \hat{z} . The intensity I_i conversion can be quantitatively calculated by the Manley-Rowe relations:

$$\frac{d}{dz} \left(\frac{I_1}{\omega_1} \right) = \frac{d}{dz} \left(\frac{I_2}{\omega_2} \right) = -\frac{d}{dz} \left(\frac{I_3}{\omega_3} \right) \quad (\text{A.18})$$

Consequently the total intensity, measured in photons per area per time, is a conserved quantity. For a lossless optical medium the Manley-Rowe relations lead to the following

coupled amplitude equations in the case of DFG [Boy08]:

$$\frac{dA_1}{dz} = \frac{2i\omega_1^2 d_{\text{eff}}}{k_1 c^2} A_3 A_2^* e^{i\Delta k z} \quad (\text{A.19})$$

$$\frac{dA_2}{dz} = \frac{2i\omega_2^2 d_{\text{eff}}}{k_2 c^2} A_3 A_1^* e^{i\Delta k z} \quad (\text{A.20})$$

where d_{eff} is the effective nonlinearity from $\chi^{(2)}$, taking the polarization and geometric properties into account. Additionally, an intense (pump) field A_3 is assumed with negligible depletion ($dA_3/dz = 0$). Obviously, the perfect phase matching between all three waves is given for $\Delta k = 0$. If this is not the case the generated amplitude A_2 after a crystal thickness L is proportional to the integration along z [Boy08]:

$$A_2 \propto \int_0^L e^{i\Delta k z} dz = \frac{e^{i\Delta k L} - 1}{i\Delta k}. \quad (\text{A.21})$$

As the intensity (time-averaged Poynting vector) scales with the squared modulus of the amplitude $|A_2|^2$, the phase mismatch factor is usually given as a sinc function:

$$\left| \frac{e^{i\Delta k L} - 1}{i\Delta k} \right|^2 = L^2 \text{sinc}^2(\Delta k L/2). \quad (\text{A.22})$$

The inherent birefringent properties of typical nonlinear generation crystals can be harnessed to optimize the phase-matching conditions and to compensate for dispersion. [Dmi96]. This is typically employed for table-top high field THz-generation via DFG and is explained in detail in section 4.2.3. When birefringence cannot be utilized, sometimes a quasi-phase-matching is possible. For quasi-phase matching a ferroelectric material is stacked periodically in layers with alternating orientations of its crystalline axis along the z -direction. The alternating inversion of the crystalline axis leads to an alternating sign of d_{eff} and thus prevents the amplitude A_2 to decrease after the coherent buildup length $L_c = 2/\Delta k$ [Boy08]. One prominent example for quasi-phase-matching is periodically poled lithium niobate (PPLN) [Mye95].

Bibliography

- [Ada13] H. Adachi, K.-i. Uchida, E. Saitoh, & S. Maekawa. *Theory of the spin Seebeck effect*. Rep. Prog. Phys. **76**, 3, (2013) 036501.
- [Agr13] M. Agrawal, V. I. Vasyuchka, A. A. Serga, A. D. Karenowska, G. A. Melkov, & B. Hillebrands. *Direct Measurement of Magnon Temperature: New Insight into Magnon-Phonon Coupling in Magnetic Insulators*. Phys. Rev. Lett. **111**, 10, (2013) 107204.
- [And64] E. E. Anderson. *Molecular Field Model and the Magnetization of YIG*. Phys. Rev. **134**, 6A, (1964) A1581.
- [And76] B. Andlauer, J. Schneider, & W. Wettling. *Optical and magneto-optical properties of YIG and FeBO₃* **10**, 3, (1976) 189.
- [Ant04] V. Antonov, B. Harmon, & A. Yaresko. *Electronic structure and magneto-optical properties of solids*. Kluwer Academic Publishers, 2004.
- [Arm04] A. Armitage, S. R. Andrews, J. A. Cluff, P. G. Huggard, E. H. Linfield, & D. A. Ritchie. *Ultrafast optical excitation of coherent two-dimensional plasmons*. Phys. Rev. B **69**, 12, (2004) 125309.
- [Ash05] N. W. Ashcroft & N. D. Mermin. *Solid state physics (holt, rinehart and winston, new york, 1976)*. 2005.
- [Atx09] U. Atxitia, O. Chubykalo-Fesenko, R. W. Chantrell, U. Nowak, & A. Rebei. *Ultrafast Spin Dynamics: The Effect of Colored Noise*. Phys. Rev. Lett. **102**, 5, (2009) 057203.
- [Atx14] U. Atxitia, J. Barker, R. W. Chantrell, & O. Chubykalo-Fesenko. *Controlling the polarity of the transient ferromagneticlike state in ferrimagnets*. Phys. Rev. B **89**, 22, (2014) 224421.
- [Bac97] S. Backus, C. G. Durfee, G. Mourou, H. C. Kapteyn, & M. M. Murnane. *0.2-TW laser system at 1 kHz*. Opt. Lett. **22**, 16, (1997) 1256.
- [Bac98] S. Backus, C. G. Durfee, M. M. Murnane, & H. C. Kapteyn. *High power ultrafast lasers*. Review of Scientific Instruments **69**, 3, (1998) 1207.
- [Bad10] S. D. Bader & S. S. P. Parkin. *Spintronics*. Annu. Rev. Condens. Matter Phys. **1**, 1, (2010) 71.

- [Bak98] H. J. Bakker, G. C. Cho, H. Kurz, Q. Wu, & X.-C. Zhang. *Distortion of terahertz pulses in electro-optic sampling*. J. Opt. Soc. Am. B **15**, 6, (1998) 1795.
- [Bar07] A. F. Bartelt, A. Comin, J. Feng, J. R. Nasiatka, T. Eimüller, B. Ludescher, G. Schütz, H. A. Padmore, A. T. Young, & A. Scholl. *Element-specific spin and orbital momentum dynamics of Fe/Gd multilayers*. Applied Physics Letters **90**, 16, (2007) 162503.
- [Bar13] J. Barker. *Atomistic Models of Magnetic Systems with Combined Ferromagnetic and Antiferromagnetic Order*. Dissertation, The University of York, Department of Physics (2013).
- [Bar16] J. Barker & G. E. W. Bauer. *Thermal spin dynamics of yttrium iron garnet*. ArXiv e-print:1607.03263 .
- [Bat10] M. Battiato, K. Carva, & P. M. Oppeneer. *Superdiffusive Spin Transport as a Mechanism of Ultrafast Demagnetization*. Phys. Rev. Lett. **105**, 2, (2010) 027203.
- [Bau12] G. E. W. Bauer, E. Saitoh, & B. J. van Wees. *Spin caloritronics*. Nat Mater **11**, 5, (2012) 391.
- [Bea96] E. Beaurepaire, J.-C. Merle, A. Daunois, & J.-Y. Bigot. *Ultrafast Spin Dynamics in Ferromagnetic Nickel*. Phys. Rev. Lett. **76**, 22, (1996) 4250.
- [Bec97] H. Becquerel. *The Faraday and Zeeman Effects*. Comptes Rendus **125**, (1897) 679.
- [Bec10] M. Beck, H. Schäfer, G. Klatt, J. Demsar, S. Winnerl, M. Helm, & T. Dekorsy. *Impulsive terahertz radiation with high electric fields from an amplifier-driven large-area photoconductive antenna*. Opt. Express **18**, 9, (2010) 9251.
- [Ben12] K.-H. Bennemann & J. B. Ketterson. *The Physics of Superconductors: Vol. I. Conventional and High-Tc Superconductors*. Springer Science & Business Media, 2012.
- [Ber14] N. Berggaard, V. López-Flores, V. Halté, M. Hehn, C. Stamm, N. Pontius, E. Beaurepaire, & C. Boeglin. *Ultrafast angular momentum transfer in multislattice ferrimagnets*. Nat Commun **5**.
- [Bha74] S. M. Bhagat & P. Lubitz. *Temperature variation of ferromagnetic relaxation in the 3d transition metals*. Phys. Rev. B **10**, 1, (1974) 179.
- [Big09] J.-Y. Bigot, M. Vomir, & E. Beaurepaire. *Coherent ultrafast magnetism induced by femtosecond laser pulses*. Nat Phys **5**, 7, (2009) 515.

-
- [Big13] J.-Y. Bigot & M. Vomir. *Ultrafast magnetization dynamics of nanostructures*. Ann. Phys. **525**, 1-2, (2013) 2.
- [Blo30] F. Bloch. *Zur Theorie des Ferromagnetismus*. Zeitschrift für Physik **61**, 3, (1930) 206.
- [Boe10] C. Boeglin, E. Beaurepaire, V. Halte, V. Lopez-Flores, C. Stamm, N. Pontius, H. A. Durr, & J.-Y. Bigot. *Distinguishing the ultrafast dynamics of spin and orbital moments in solids*. Nature **465**, 7297, (2010) 458.
- [Bos62] I. M. Boswarva, R. E. Howard, & A. B. Lidiard. *Faraday Effect in Semiconductors*. Proc R Soc Lond A Math Phys Sci **269**, 1336, (1962) 125.
- [Boy08] R. W. Boyd. *Nonlinear Optics*. Academic Press, 2008, 3. Aufl.
- [Car02] G. L. Carr, M. C. Martin, W. R. McKinney, K. Jordan, G. R. Neil, & G. P. Williams. *High-power terahertz radiation from relativistic electrons*. Nature **420**, 6912, (2002) 153.
- [Car08] E. Carpene, E. Mancini, C. Dallera, M. Brenna, E. Puppini, & S. De Silvestri. *Dynamics of electron-magnon interaction and ultrafast demagnetization in thin iron films*. Phys. Rev. B **78**, 17, (2008) 174422.
- [Car11a] R. A. Carlton. *Pharmaceutical microscopy*. Springer Science & Business Media, 2011 7 – 64.
- [Car11b] K. Carva, M. Battiato, & P. M. Oppeneer. *Is the controversy over femtosecond magneto-optics really solved?* Nat Phys **7**, 9, (2011) 665.
- [CH05] D. Chandler-Horowitz & P. M. Amirtharaj. *High-accuracy, midinfrared ($450\text{cm}^{-1} < \omega < 4000\text{cm}^{-1}$) refractive index values of silicon*. Journal of Applied Physics **97**, 12, (2005) 123526.
- [Cha07] C. Chappert, A. Fert, & F. N. Van Dau. *The emergence of spin electronics in data storage*. Nat Mater **6**, 11, (2007) 813.
- [Cha12] S. Chatrchyan, V. Khachatryan, A. M. Sirunyan, A. Tumasyan, W. Adam, E. Aguilo, T. Bergauer, M. Dragicevic, J. Erö, C. Fabjan, M. Friedl, R. Frühwirth, V. M. Ghete, J. Hammer, M. Hoch, N. Hörmann, J. Hrubec, M. Jeitler, W. Kiesenhofer, V. Knünz, M. Krammer, I. Krätschmer, D. Liko, W. Majerotto, I. Mikulec, M. Pernicka, B. Rahbaran, C. Rohringer, H. Rohringer, R. Schoefbeck, J. Strauss, F. Szoncsó, A. Taurok, W. Waltenberger, G. Walzel, E. Widl, C.-E. Wulz, V. Chekhovsky, I. Emelianchik, A. Litomin, V. Makarenko, V. Mosolov, N. Shumeiko, A. Solin, R. Stefanovitch, J. Suarez Gonzalez, A. Fedorov, M. Korzhik, O. Missevitch, R. Zuyeuski, M. Bansal, S. Bansal, W. Beaumont, T. Cornelis, E. A. De Wolf, D. Druzhkin, X. Janssen, S. Luyckx, L. Mucibello,

S. Ochesanu, B. Roland, R. Rougny, M. Selvaggi, Z. Staykova, H. Van Haevermaet, P. Van Mechelen, N. Van Remortel, A. Van Spilbeeck, F. Blekman, S. Blyweert, J. D'Hondt, O. Devroede, R. Gonzalez Suarez, R. Goorens, A. Kalogeropoulos, M. Maes, A. Olbrechts, S. Tavernier, W. Van Doninck, L. Van Lancker, P. Van Mulders, G. P. Van Onsem, I. Villella, B. Clerbaux, G. De Lentdecker, V. Dero, J. P. Dewulf, A. P. R. Gay, T. Hreus, A. Léonard, P. E. Marage, A. Mohammadi, T. Reis, S. Rugovac, L. Thomas, C. Vander Velde, P. Vanlaer, J. Wang, J. Wickens, V. Adler, K. Beernaert, A. Cimmino, S. Costantini, G. Garcia, M. Grunewald, B. Klein, J. Lellouch, A. Marinov, J. McCartin, A. A. Ocampo Rios, D. Ryckbosch, N. Strobbe, F. Thyssen, M. Tytgat, S. Walsh, E. Yazgan, N. Zaganidis, S. Basegmez, G. Bruno, R. Castello, L. Ceard, J. De Favereau De Jeneret, C. Delaere, P. Demin, T. du Pree, D. Favart, L. Forthomme, A. Giammanco, G. Grégoire, J. Hollar, V. Lemaitre, J. Liao, O. Militaru, C. Nuttens, D. Pagano, A. Pin, K. Piotrkowski, N. Schul, J. M. Vizán Garcia, N. Beliy, T. Caebergs, E. Daubie, G. H. Hammad, G. A. Alves, L. Brito, M. Correa Martin Junior, T. Martins, M. E. Pol, M. H. G. Souza, W. L. Aldá Júnior, W. Carvalho, A. Custodio, E. M. Da Costa, D. De Jesus Damiao, C. De Oliveira Martins, S. Fonseca De Souza, D. Matos Figueiredo, L. Mundim, H. Nogima, V. Oguri, W. L. Prado Da Silva, A. Santoro, A. Sznajder, A. Vilela Pereira, T. S. Anjos, C. A. Bernardes, F. A. Dias, T. R. Fernandez Perez Tomei, E. M. Gregores, R. L. Iope, C. Lagana, S. M. Lietti, F. Marinho, P. G. Mercadante, S. F. Novaes, S. S. Padula, L. Dimitrov, V. Genchev, P. Iaydjiev, S. Piperov, M. Rodozov, S. Stoykova, G. Sultanov, V. Tcholakov, R. Trayanov, I. Vankov, M. Vutova, C. Roumenin, D. Uzunova, R. Zahariev, A. Dimitrov, R. Hadjiiska, V. Kozhuharov, L. Litov, B. Pavlov, P. Petkov, J. G. Bian, G. M. Chen, H. S. Chen, K. L. He, C. H. Jiang, W. G. Li, D. Liang, S. Liang, X. Meng, G. Sun, H. S. Sun, J. Tao, J. Wang, X. Wang, Z. Wang, H. Xiao, M. Xu, M. Yang, J. Zang, X. Zhang, Z. Zhang, Z. Zhang, W. R. Zhao, Z. Zhu, C. Asawatangtrakuldee, Y. Ban, J. Cai, S. Guo, Y. Guo, W. Li, H. T. Liu, S. Liu, Y. Mao, S. J. Qian, H. Teng, D. Wang, Y. L. Ye, L. Zhang, B. Zhu, W. Zou, C. Avila, J. P. Gomez, B. Gomez Moreno, A. F. Osorio Oliveros, J. C. Sanabria, N. Godinovic, D. Lelas, R. Plestina, D. Polic, I. Puljak, Z. Antunovic, M. Kovac, V. Brigljevic, S. Duric, K. Kadija, J. Luetic, S. Morovic, A. Attikis, M. Galanti, G. Mavromanolakis, J. Mousa, C. Nicolaou, F. Ptochos, P. A. Razis, M. Finger, M. Finger Jr., A. Aly, Y. Assran, A. Awad, S. Elgammal, A. Ellithi Kamel, S. Khalil, M. A. Mahmoud, A. Mahrous, A. Radi, A. Hektor, M. Kadastik, K. Kannike, M. Müntel, M. Raidal, L. Rebane, A. Strumia, A. Tiko, P. Eerola, G. Fedi, M. Voutilainen, E. Anttila, J. Härkönen, A. Heikkinen, V. Karimäki, H. M. Katajisto, R. Kinnunen, M. J. Kortelainen, M. Kotamäki, T. Lampén, K. Lassila-Perini, S. Lehti, T. Lindén, P. Luukka, T. Mäenpää, T. Peltola, E. Tuominen, J. Tuominiemi, E. Tuovinen, D. Ungaro, T. P. Vanhala, L. Wendland, K. Banzuzi, A. Karjalainen, A. Korpela, T. Tuuva, M. Anfreville, M. Besancon, S. Choudhury, M. Dejardin, D. Denegri, B. Fabbro, J. L. Faure, F. Ferri, S. Ganjour, F. X. Gentit, A. Givernaud, P. Gras, G. Hamel de Monchenault, P. Jarry, F. Kircher, M. C. Lemaire, E. Locci, J. Malcles, I. Mandjavidze,

- A. Nayak, J. P. Pansart, J. Rander, J. M. Reymond, A. Rosowsky, I. Shreyber, M. Titov, P. Verrecchia, J. Badier, S. Baffioni, F. Beaudette, E. Becheva, L. Benhabib, L. Bianchini, M. Bluj, C. Broutin, P. Busson, M. Cerutti, D. Chamont, C. Charlot, N. Daci, T. Dahms, M. Dalchenko, L. Dobrzynski, Y. Geerebaert, R. Granier de Cassagnac, M. Haguenaue, P. Hennion, G. Milleret, P. Miné, C. Mironov, I. N. Naranjo, M. Nguyen, C. Ochando, P. Paganini, T. Roman-teau, D. Sabes, R. Salerno, A. Sartirana, Y. Sirois, C. Thiebaut, C. Veelken, A. Zabi, J.-L. Agram, J. Andrea, A. Besson, D. Bloch, D. Bodin, J.-M. Brom, M. Cardaci, E. C. Chabert, C. Collard, E. Conte, F. Drouhin, C. Ferro, J.-C. Fontaine, D. Gelé, U. Goerlach, C. Goetzmann, L. Gross, D. Huss, P. Juillot, E. Kieffer, A.-C. Le Bihan, J. Pansanel, Y. Patois. *Observation of a new boson at a mass of 125 GeV with the CMS experiment at the LHC*. Physics Letters B **716**, 1, (2012) 30.
- [Che84] J. R. Chelikowsky & S. G. Louie. *First-principles linear combination of atomic orbitals method for the cohesive and structural properties of solids: Application to diamond*. Phys. Rev. B **29**, 6, (1984) 3470.
- [Che90] T. K. Cheng, S. D. Brorson, A. S. Kazeroonian, J. S. Moodera, G. Dresselhaus, M. S. Dresselhaus, & E. P. Ippen. *Impulsive excitation of coherent phonons observed in reflection in bismuth and antimony*. Applied Physics Letters **57**, 10, (1990) 1004.
- [Che91] T. K. Cheng, J. Vidal, H. J. Zeiger, G. Dresselhaus, M. S. Dresselhaus, & E. P. Ippen. *Mechanism for displacive excitation of coherent phonons in Sb, Bi, Te, and Ti₂O₃*. Applied Physics Letters **59**, 16, (1991) 1923.
- [Che93a] V. Cherepanov, I. Kolokolov, & V. L'vov. *The saga of YIG: Spectra, thermodynamics, interaction and relaxation of magnons in a complex magnet*. Phys. Rep. **229**, 3, (1993) 81.
- [Che93b] V. Cherepanov, I. Kolokolov, & V. L'vov. *The saga of YIG: spectra, thermodynamics, interaction and relaxation of magnons in a complex magnet* .
- [Che07] S.-W. Cheong & M. Mostovoy. *Multiferroics: a magnetic twist for ferroelectricity*. Nat Mater **6**, 1, (2007) 13.
- [Che10] L. Chen, M. Zhang, & Z. Zhang. *Dispersion compensation devices* .
- [Chi89] S. L. Chin. *Fundamentals of laser optoelectronics*, Bd. 1. World scientific, 1989.
- [Chi06] L. Childress, M. V. Gurudev Dutt, J. M. Taylor, A. S. Zibrov, F. Jelezko, J. Wrachtrup, P. R. Hemmer, & M. D. Lukin. *Coherent Dynamics of Coupled Electron and Nuclear Spin Qubits in Diamond*. Science **314**, 5797, (2006) 281.

- [Chi13] L. Childress & R. Hanson. *Diamond NV centers for quantum computing and quantum networks*. MRS Bulletin **38**, 02, (2013) 134.
- [Cho90] G. C. Cho, W. Kütt, & H. Kurz. *Subpicosecond time-resolved coherent-phonon oscillations in GaAs*. Phys. Rev. Lett. **65**, 6, (1990) 764.
- [Chu15] A. V. Chumak, V. I. Vasyuchka, A. A. Serga, & B. Hillebrands. *Magnon spintronics*. Nat Phys **11**, 6, (2015) 453.
- [Chw90] J. M. Chwalek, C. Uher, J. F. Whitaker, G. A. Mourou, J. Agostinelli, & M. Levental. *Femtosecond optical absorption studies of nonequilibrium electronic processes in high T_c superconductors*. Applied Physics Letters **57**, 16, (1990) 1696.
- [Coc91] J. F. Cochran, J. M. Rudd, W. B. Muir, G. Trayling, & B. Heinrich. *Temperature dependence of the Landau–Lifshitz damping parameter for iron*. Journal of Applied Physics **70**, 10, (1991) 6545.
- [Cos77] A. E. Costley, K. H. Hursey, G. F. Neill, & J. M. Ward. *Free-standing fine-wire grids: Their manufacture, performance, and use at millimeter and submillimeter wavelengths*. J. Opt. Soc. Am. **67**, 7, (1977) 979.
- [Cou07] A. Couairon & A. Mysyrowicz. *Femtosecond filamentation in transparent media*. Physics Reports **441**, 2-4, (2007) 47.
- [Cun03] S. T. Cundiff & J. Ye. *Colloquium : Femtosecond optical frequency combs*. Rev. Mod. Phys. **75**, 1, (2003) 325.
- [Cun08] P. D. Cunningham & L. M. Hayden. *Carrier Dynamics Resulting from Above and Below Gap Excitation of P3HT and P3HT/PCBM Investigated by Optical-Pump Terahertz-Probe Spectroscopy*. J. Phys. Chem. C **112**, 21, (2008) 7928.
- [dA11] J. A. del Alamo. *Nanometre-scale electronics with III-V compound semiconductors*. Nature **479**, 7373, (2011) 317.
- [Dan07] A. Dantan, J. Laurat, A. Ourjoumtsev, R. Tualle-Brouri, & P. Grangier. *Femtosecond Ti:sapphire cryogenic amplifier with high gain and MHz repetition rate*. Opt. Express **15**, 14, (2007) 8864.
- [Dar67] M. I. Darby. *Tables of the Brillouin function and of the related function for the spontaneous magnetization*. British Journal of Applied Physics **18**, 10, (1967) 1415.
- [Deb15] M. Deb, M. Vomir, J.-L. Rehspringer, & J.-Y. Bigot. *Ultrafast optical control of magnetization dynamics in polycrystalline bismuth doped iron garnet thin films*. Appl. Phys. Lett. **107**, 25, (2015) 252404.

-
- [Dek95] T. Dekorsy, H. Auer, C. Waschke, H. J. Bakker, H. G. Roskos, H. Kurz, V. Wagner, & P. Grosse. *Emission of Submillimeter Electromagnetic Waves by Coherent Phonons*. Phys. Rev. Lett. **74**, 5, (1995) 738.
- [Dek00] T. Dekorsy, G. C. Cho, & H. Kurz. *Coherent phonons in condensed media*. In M. Cardona & G. Güntherodt (Hg.), *Topics in Applied Physics*, Bd. 76. Springer Berlin Heidelberg, 2000 169–209–.
- [Dem08] W. Demtröder. *Laser Spectroscopy 2*. Springer, 2008, 4. Aufl.
- [Dem13] W. Demtröder. *Laser spectroscopy: basic concepts and instrumentation*. Springer Science & Business Media, 2013.
- [Dex07] S. L. Dexheimer. *Terahertz spectroscopy: principles and applications*. CRC press, 2007.
- [Die06] J.-C. Diels & W. Rudolph. *Ultrashort laser pulse phenomena*. Academic press, 2006.
- [Dil58] J. F. Dillon. *Optical Properties of Several Ferrimagnetic Garnets*. Journal of Applied Physics **29**, 3, (1958) 539.
- [Dio09] G. F. Dionne. *Magnetic oxides*, Bd. 14. Springer, 2009.
- [Dir81] P. A. M. Dirac. *The principles of quantum mechanics*. Nr. 27. Oxford university press, 1981.
- [Dmi96] V. G. Dmitriev, G. G. Gurzadyan, & D. N. Nikogosyan. *Handbook of Nonlinear Optical Crystals*. Springer, Berlin, 1996.
- [Don63] B. Donovan & T. Medcalf. *The inclusion of multiple reflections in the formulation of the Faraday effect in semiconductors*. Physics Letters **7**, 5, (1963) 304.
- [Dre05] A. Dreyhaupt, S. Winnerl, T. Dekorsy, & M. Helm. *High-intensity terahertz radiation from a microstructured large-area photoconductor*. Applied Physics Letters **86**, 12, (2005) 121114.
- [DS85] S. De Silvestri, J. Fujimoto, E. Ippen, E. B. Gamble, L. R. Williams, & K. A. Nelson. *Femtosecond time-resolved measurements of optic phonon dephasing by impulsive stimulated raman scattering in α -perylene crystal from 20 to 300 K*. Chemical Physics Letters **116**, 2, (1985) 146.
- [Dut07] M. V. G. Dutt, L. Childress, L. Jiang, E. Togan, J. Maze, F. Jelezko, A. S. Zibrov, P. R. Hemmer, & M. D. Lukin. *Quantum Register Based on Individual*

- Electronic and Nuclear Spin Qubits in Diamond.* Science **316**, 5829, (2007) 1312.
- [Ebe96] H. Ebert. *Magneto-optical effects in transition metal systems.* Reports on Progress in Physics **59**, 12, (1996) 1665.
- [Ega07] T. Egami. *Essential role of the lattice in the mechanism of high temperature superconductivity.* In *High TC Superconductors and Related Transition Metal Oxides.* Springer, 2007 103–129.
- [Ein05] A. Einstein. *Über einen die Erzeugung und Verwandlung des Lichtes betreffenden heuristischen Gesichtspunkt.* Ann. Phys. **322**, 6, (1905) 132.
- [Eki04] E. A. Ekimov, V. A. Sidorov, E. D. Bauer, N. N. Mel'nik, N. J. Curro, J. D. Thompson, & S. M. Stishov. *Superconductivity in diamond.* Nature **428**, 6982, (2004) 542.
- [Eng13] D. G. England, P. J. Bustard, J. Nunn, R. Lausten, & B. J. Sussman. *From Photons to Phonons and Back: A THz Optical Memory in Diamond.* Phys. Rev. Lett. **111**, 24, (2013) 243601.
- [Eno75] R. D. Enoch. *Magnetic domain studies on yttrium iron garnet using an infrared image converter.* Contemporary Physics **16**, 6, (1975) 561.
- [Esc13] A. Eschenlohr, M. Battiato, P. Maldonado, N. Pontius, T. Kachel, K. Holldack, R. Mitzner, A. Föhlisch, P. M. Oppeneer, & C. Stamm. *Ultrafast spin transport as key to femtosecond demagnetization.* Nat Mater **12**, 4, (2013) 332.
- [Esc14] A. Eschenlohr, M. Battiato, P. Maldonado, N. Pontius, T. Kachel, K. Holldack, R. Mitzner, A. Föhlisch, P. M. Oppeneer, & C. Stamm. *Reply to 'Optical excitation of thin magnetic layers in multilayer structures'.* Nat Mater **13**, 2, (2014) 102.
- [Etz15] C. Etz, L. Bergqvist, A. Bergman, A. Taroni, & O. Eriksson. *Atomistic spin dynamics and surface magnons.* Journal of Physics: Condensed Matter **27**, 24, (2015) 243202.
- [Eva14] R. F. L. Evans, W. J. Fan, P. Chureemart, T. A. Ostler, M. O. A. Ellis, & R. W. Chantrell. *Atomistic spin model simulations of magnetic nanomaterials.* Journal of Physics: Condensed Matter **26**, 10, (2014) 103202.
- [Fü11] J. A. Fülöp, L. Pálfalvi, M. C. Hoffmann, & J. Hebling. *Towards generation of mJ-level ultrashort THz pulses by optical rectification.* Opt. Express **19**, 16, (2011) 15090.
- [Fau11] D. Fausti, R. Tobey, N. Dean, S. Kaiser, A. Dienst, M. Hoffmann, S. Pyon,

- T. Takayama, H. Takagi, & A. Cavalleri. *Light-Induced Superconductivity in a Stripe-Ordered Cuprate*. *Science* **331**, 6014, (2011) 189.
- [Fed10] J. Federici & L. Moeller. *Review of terahertz and subterahertz wireless communications*. *Journal of Applied Physics* **107**, 11, (2010) 111101.
- [Fer94] N. C. Fernelius. *Properties of gallium selenide single crystal*. *Progress in Crystal Growth and Characterization of Materials* **28**, 4, (1994) 275.
- [Fer02] M. E. Fermann, A. Galvanauskas, & G. Sucha. *Ultrafast lasers: Technology and applications*, Bd. 80. CRC Press, 2002.
- [Fey49] R. P. Feynman. *Space-Time Approach to Quantum Electrodynamics*. *Phys. Rev.* **76**, 6, (1949) 769.
- [Fis16] K. A. G. Fisher, D. G. England, J.-P. W. MacLean, P. J. Bustard, K. J. Resch, & B. J. Sussman. *Frequency and bandwidth conversion of single photons in a room-temperature diamond quantum memory*. *Nat Commun* **7**, (2016) .
- [Foe11a] M. Foerst, C. Manzoni, S. Kaiser, Y. Tomioka, Y. Tokura, R. Merlin, & A. Cavalleri. *Nonlinear phononics as an ultrafast route to lattice control*. *Nat Phys* **7**, 11, (2011) 854.
- [Foe11b] M. Foerst, R. I. Tobey, S. Wall, H. Bromberger, V. Khanna, A. L. Cavalieri, Y.-D. Chuang, W. S. Lee, R. Moore, W. F. Schlotter, J. J. Turner, O. Krupin, M. Trigo, H. Zheng, J. F. Mitchell, S. S. Dhesi, J. P. Hill, & A. Cavalleri. *Driving magnetic order in a manganite by ultrafast lattice excitation*. *Phys. Rev. B* **84**, 24, (2011) 241104.
- [Fra61] P. A. Franken, A. E. Hill, C. W. Peters, & G. Weinreich. *Generation of Optical Harmonics*. *Phys. Rev. Lett.* **7**, 4, (1961) 118.
- [Fra12] K. J. Franke & J. I. Pascual. *Effects of electron-vibration coupling in transport through single molecules*. *Journal of Physics: Condensed Matter* **24**, 39, (2012) 394002.
- [Fri15] B. Frietsch, J. Bowlan, R. Carley, M. Teichmann, S. Wienholdt, D. Hinzke, U. Nowak, K. Carva, P. M. Oppeneer, & M. Weinelt. *Disparate ultrafast dynamics of itinerant and localized magnetic moments in gadolinium metal*. *Nat Commun* **6**, (2015) .
- [Gal83] G. Gale & A. Laubereau. *Direct measurement of picosecond and sub-picosecond phonon lifetimes in α -quartz*. *Opt. Commun.* **44**, 4, (1983) 273.
- [Gam06] A. Gambetta, C. Manzoni, E. Menna, M. Meneghetti, G. Cerullo, G. Lanzani, S. Tretiak, A. Piryatinski, A. Saxena, R. L. Martin, & A. R. Bishop. *Real-*

- time observation of nonlinear coherent phonon dynamics in single-walled carbon nanotubes.* Nat Phys **2**, 8, (2006) 515.
- [Gar96] G. A. Garrett, T. F. Albrecht, J. F. Whitaker, & R. Merlin. *Coherent THz Phonons Driven by Light Pulses and the Sb Problem: What is the Mechanism?* Phys. Rev. Lett. **77**, 17, (1996) 3661.
- [Geb55] T. H. Geballe & G. W. Hull. *Seebeck Effect in Silicon.* Phys. Rev. **98**, 4, (1955) 940.
- [GG10] C. F. Gilbert Grynberg, Alain Aspect. *Introduction to Quantum Optics: From the Semi-classical Approach to Quantized Light.* Cambridge University Press, 2010.
- [Gil80] M. A. Gilleo. *Ferromagnetic materials*, Bd. 2. North-Holland, Amsterdam, 1980
- [Gra16] A. X. Gray, M. C. Hoffmann, J. Jeong, N. P. Aetukuri, D. Zhu, H. Y. Hwang, N. C. Brandt, H. Wen, A. J. Sternbach, S. Bonetti, A. H. Reid, R. Kukreja, C. Graves, T. Wang, P. Granitzka, Z. Chen, D. J. Higley, T. Chase, E. Jal, E. Abreu, M. K. Liu, T.-C. Weng, D. Sokaras, D. Nordlund, M. Chollet, H. Lemke, J. Glowia, M. Trigo, Y. Zhu, H. Ohldag, J. W. Freeland, M. G. Samant, J. Berakdar, R. D. Averitt, K. A. Nelson, S. S. P. Parkin, & H. A. Dürr. *Ultrafast THz Field Control of Electronic and Structural Interactions in Vanadium Dioxide.* ArXiv e-prints .
- [Gre16] B. Green, S. Kovalev, V. Asgekar, G. Geloni, U. Lehnert, T. Golz, M. Kuntzsch, C. Bauer, J. Hauser, J. Voigtlaender, B. Wustmann, I. Koesterke, M. Schwarz, M. Freitag, A. Arnold, J. Teichert, M. Justus, W. Seidel, C. Ilgner, N. Awari, D. Nicoletti, S. Kaiser, Y. Laplace, S. Rajasekaran, L. Zhang, S. Winnerl, H. Schneider, G. Schay, I. Lorincz, A. A. Rauscher, I. Radu, S. Maehrlein, T. H. Kim, J. S. Lee, T. Kampfrath, S. Wall, J. Heberle, A. Malnasi-Csizmadia, A. Steiger, A. S. Müller, M. Helm, U. Schramm, T. Cowan, P. Michel, A. Cavalleri, A. S. Fisher, N. Stojanovic, & M. Gensch. *High-Field High-Repetition-Rate Sources for the Coherent THz Control of Matter.* Scientific Reports **6**, (2016) 22256.
- [Gri75] M. H. Grimsditch & A. K. Ramdas. *Brillouin scattering in diamond.* Phys. Rev. B **11**, 8, (1975) 3139.
- [Gri08] V. N. Gridnev. *Phenomenological theory for coherent magnon generation through impulsive stimulated Raman scattering.* Phys. Rev. B **77**, 9, (2008) 094426.
- [Gui02] L. Guidoni, E. Beaurepaire, & J.-Y. Bigot. *Magneto-optics in the Ultrafast*

-
- Regime: Thermalization of Spin Populations in Ferromagnetic Films.* Phys. Rev. Lett. **89**, 1, (2002) 017401.
- [Gur96] A. G. Gurevich & G. A. Melkov. *Magnetization oscillations and waves.* CRC press, 1996.
- [Hae06] T. W. Haensch. *Passion for Precision (Nobel Lecture)13.* ChemPhysChem **7**, 6, (2006) 1170.
- [Han81] P. Hansen, H. Heitmann, & K. Witter. *Temperature dependence of the Faraday rotation of lead- and bismuth-substituted gadolinium iron garnet films at 633 nm.* Phys. Rev. B **23**, 11, (1981) 6085.
- [Han83] P. Hansen, K. Witter, & W. Tolksdorf. *Magnetic and magneto-optic properties of lead- and bismuth-substituted yttrium iron garnet films.* Phys. Rev. B **27**, 11, (1983) 6608.
- [Han84] P. Hansen & J.-P. Krumme. *Special Issue on Magnetic Garnet Films Magnetic and magneto-optical properties of garnet films.* Thin Solid Films **114**, 1, (1984) 69.
- [Han06a] F. Hansteen. *Ultrafast optical control of magnetization in ferrimagnetic garnets.* Dissertation, Radboud University, Nijmegen (2006).
- [Han06b] F. Hansteen, A. Kimel, A. Kirilyuk, & T. Rasing. *Nonthermal ultrafast optical control of the magnetization in garnet films.* Phys. Rev. B **73**, 1, (2006) 014421.
- [Has02] M. Hase, M. Kitajima, S.-i. Nakashima, & K. Mizoguchi. *Dynamics of Coherent Anharmonic Phonons in Bismuth Using High Density Photoexcitation.* Phys. Rev. Lett. **88**, 6, (2002) 067401.
- [Hau04] H. Haug & S. W. Koch. *Quantum theory of the optical and electronic properties of semiconductors*, Bd. 5. World Scientific, 2004.
- [Hau11] C. P. Hauri, C. Ruchert, C. Vicario, & F. Ardana. *Strong-field single-cycle THz pulses generated in an organic crystal.* Applied Physics Letters **99**, 16, (2011) 161116.
- [Heb02] J. Hebling, G. Almasi, I. Kozma, & J. Kuhl. *Velocity matching by pulse front tilting for large area THz-pulse generation.* Opt. Express **10**, 21, (2002) 1161.
- [Heb08] J. Hebling, K.-L. Yeh, M. C. Hoffmann, B. Bartal, & K. A. Nelson. *Generation of high-power terahertz pulses by tilted-pulse-front excitation and their application possibilities.* J. Opt. Soc. Am. B **25**, 7, (2008) B6.

- [Hei25] W. Heisenberg. *Über quantentheoretische Umdeutung kinematischer und mechanischer Beziehungen*. Zeitschrift für Physik **33**, 1, (1925) 879.
- [Hei27] W. Heitler & F. London. *Wechselwirkung neutraler Atome und homöopolare Bindung nach der Quantenmechanik*. Zeitschrift für Physik **44**, 6, (1927) 455.
- [Hes90] D. Hestenes. *The zitterbewegung interpretation of quantum mechanics*. Foundations of Physics **20**, 10, (1990) 1213.
- [Hil11] D. Hillerkuss, R. Schmogrow, T. Schellinger, M. Jordan, M. Winter, G. Huber, T. Vallaitis, R. Bonk, P. Kleinow, F. Frey, M. Roeger, S. Koenig, A. Ludwig, A. Marculescu, J. Li, M. Hoh, M. Dreschmann, J. Meyer, S. Ben Ezra, N. Narkiss, B. Nebendahl, F. Parmigiani, P. Petropoulos, B. Resan, A. Oehler, K. Weingarten, T. Ellermeyer, J. Lutz, M. Moeller, M. Huebner, J. Becker, C. Koos, W. Freude, & J. Leuthold. *26 Tbit s⁻¹ line-rate super-channel transmission utilizing all-optical fast Fourier transform processing*. Nat Photon **5**, 6, (2011) 364.
- [Hir11] H. Hirori, A. Doi, F. Blanchard, & K. Tanaka. *Single-cycle terahertz pulses with amplitudes exceeding 1 MV/cm generated by optical rectification in LiNbO₃*. Appl. Phys. Lett. **98**, 9, (2011) 091106.
- [Hof92] A. M. Hofmeister & K. R. Campbell. *Infrared spectroscopy of yttrium aluminum, yttrium gallium, and yttrium iron garnets*. J. Appl. Phys. **72**, 2, (1992) 638.
- [Hof06] A. M. Hofmeister. *Thermal diffusivity of garnets at high temperature* **33**, 1, (2006) 45.
- [Hof09] M. C. Hoffmann, N. C. Brandt, H. Y. Hwang, K.-L. Yeh, & K. A. Nelson. *Terahertz Kerr effect*. Appl. Phys. Lett. **95**, 23, (2009) 231105.
- [Hoh97] J. Hohlfeld, E. Matthias, R. Knorren, & K. H. Bennemann. *Nonequilibrium Magnetization Dynamics of Nickel*. Phys. Rev. Lett. **78**, 25, (1997) 4861.
- [Hol40] T. Holstein & H. Primakoff. *Field Dependence of the Intrinsic Domain Magnetization of a Ferromagnet*. Phys. Rev. **58**, 12, (1940) 1098.
- [Hol00] R. Holzwarth, T. Udem, T. W. Hänsch, J. C. Knight, W. J. Wadsworth, & P. S. J. Russell. *Optical Frequency Synthesizer for Precision Spectroscopy*. Phys. Rev. Lett. **85**, 11, (2000) 2264.
- [Hol04] J. M. Hollas. *Modern spectroscopy*. John Wiley & Sons, 2004.
- [Hub00] R. Huber, A. Brodschelm, F. Tauser, & A. Leitenstorfer. *Generation and field-resolved detection of femtosecond electromagnetic pulses tunable up to 41 THz*. Appl. Phys. Lett. **76**, 22, (2000) 3191.

- [Hub14] T. Huber, S. O. Mariager, A. Ferrer, H. Schäfer, J. Johnson, S. Grübel, A. Lübecke, L. Huber, T. Kubacka, C. Dornes, C. Laulhe, S. Ravy, G. Ingold, P. Beaud, J. Demsar, & S. Johnson. *Coherent Structural Dynamics of a Prototypical Charge-Density-Wave-to-Metal Transition*. Phys. Rev. Lett. **113**, 2, (2014) 026401.
- [Hub15] T. Huber, M. Ranke, A. Ferrer, L. Huber, & S. L. Johnson. *Coherent phonon spectroscopy of non-fully symmetric modes using resonant terahertz excitation*. Applied Physics Letters **107**, 9, (2015) 091107.
- [Hue98] W. Huebner & G. P. Zhang. *Ultrafast spin dynamics in nickel*. Phys. Rev. B **58**, 10, (1998) R5920.
- [Hun10] D. S. Hung, Y. P. Fu, S. F. Lee, Y. D. Yao, & F. B. A. Ahad. *Relaxation behaviors of the bismuth-substituted yttrium iron garnet in the microwave range*. J. Appl. Phys. **107**, 9, (2010) 09A503.
- [Ish06] K. Ishioka, M. Hase, M. Kitajima, & H. Petek. *Coherent optical phonons in diamond*. Appl. Phys. Lett. **89**, 23, (2006) 231916.
- [Jaw10] C. M. Jaworski, J. Yang, S. Mack, D. D. Awschalom, J. P. Heremans, & R. C. Myers. *Observation of the spin-Seebeck effect in a ferromagnetic semiconductor*. Nat Mater **9**, 11, (2010) 898.
- [Jin14] Z. Jin, D. Gehrig, C. Dyer-Smith, E. J. Heilweil, F. Laquai, M. Bonn, & D. Turchinovich. *Ultrafast Terahertz Photoconductivity of Photovoltaic Polymer-Fullerene Blends: A Comparative Study Correlated with Photovoltaic Device Performance*. J. Phys. Chem. Lett. **5**, 21, (2014) 3662.
- [Jun10] F. Junginger, A. Sell, O. Schubert, B. Mayer, D. Brida, M. Marangoni, G. Cerullo, A. Leitenstorfer, & R. Huber. *Single-cycle multiterahertz transients with peak fields above 10 MV/cm*. Opt. Lett. **35**, 15, (2010) 2645.
- [Jun12] F. Junginger, B. Mayer, C. Schmidt, O. Schubert, S. Maehrlein, A. Leitenstorfer, R. Huber, & A. Pashkin. *Nonperturbative Interband Response of a Bulk InSb Semiconductor Driven Off Resonantly by Terahertz Electromagnetic Few-Cycle Pulses*. Phys. Rev. Lett. **109**, 14, (2012) 147403.
- [Jun16] T. Jungwirth, X. Marti, P. Wadley, & J. Wunderlich. *Antiferromagnetic spintronics*. Nat Nano **11**, 3, (2016) 231.
- [Kab91] A. Kabychenkov. *Magnetic phase transitions in a light wave*. JETP **73**, 2, (1991) 672.
- [Kal07] A. M. Kalashnikova, A. V. Kimel, R. V. Pisarev, V. N. Gridnev, A. Kirilyuk, & T. Rasing. *Impulsive Generation of Coherent Magnons by Linearly Polarized*

- Light in the Easy-Plane Antiferromagnet FeBO₃*. Phys. Rev. Lett. **99**, 16, (2007) 167205.
- [Kal08] A. M. Kalashnikova, A. V. Kimel, R. V. Pisarev, V. N. Gridnev, P. A. Usachev, A. Kirilyuk, & T. Rasing. *Impulsive excitation of coherent magnons and phonons by subpicosecond laser pulses in the weak ferromagnet FeBO₃*. Phys. Rev. B **78**, 10, (2008) 104301.
- [Kam02] T. Kampfrath, R. G. Ulbrich, F. Leuenberger, M. Münzenberg, B. Sass, & W. Felsch. *Ultrafast magneto-optical response of iron thin films*. Phys. Rev. B **65**, 10, (2002) 104429.
- [Kam06] T. Kampfrath. *Charge-Carrier Dynamics in Solids and Gases Observed by Time-Resolved Terahertz Spectroscopy*. Dissertation, Freien Universität Berlin (2006).
- [Kam07] T. Kampfrath, J. Notzold, & M. Wolf. *Sampling of broadband terahertz pulses with thick electro-optic crystals*. Appl. Phys. Lett. **90**, 23, (2007) 231113.
- [Kam11] T. Kampfrath, A. Sell, G. Klatt, A. Pashkin, S. Maehrlein, T. Dekorsy, M. Wolf, M. Fiebig, A. Leitenstorfer, & R. Huber. *Coherent terahertz control of antiferromagnetic spin waves*. Nat. Photon. **5**, 1, (2011) 31.
- [Kas61] T. Kasuya & R. C. LeCraw. *Relaxation Mechanisms in Ferromagnetic Resonance*. Phys. Rev. Lett. **6**, 5, (1961) 223.
- [Kat13] H. Katsuki, J. C. Delagnes, K. Hosaka, K. Ishioka, H. Chiba, E. S. Zijlstra, M. E. Garcia, H. Takahashi, K. Watanabe, M. Kitajima, Y. Matsumoto, K. G. Nakamura, & K. Ohmori. *All-optical control and visualization of ultrafast two-dimensional atomic motions in a single crystal of bismuth*. Nat Commun **4**.
- [Kim02] A. V. Kimel, R. V. Pisarev, J. Hohlfeld, & T. Rasing. *Ultrafast Quenching of the Antiferromagnetic Order in FeBO₃: Direct Optical Probing of the Phonon-Magnon Coupling*. Phys. Rev. Lett. **89**, 28, (2002) 287401.
- [Kim05] A. V. Kimel, A. Kirilyuk, P. A. Usachev, R. V. Pisarev, A. M. Balbashov, & T. Rasing. *Ultrafast non-thermal control of magnetization by instantaneous photomagnetic pulses*. Nature **435**, 7042, (2005) 655.
- [Kim07] A. V. Kimel, A. Kirilyuk, F. Hansteen, R. V. Pisarev, & T. Rasing. *Nonthermal optical control of magnetism and ultrafast laser-induced spin dynamics in solids*. Journal of Physics: Condensed Matter **19**, 4, (2007) 043201.
- [Kim12a] J.-W. Kim, M. Vomir, & J.-Y. Bigot. *Ultrafast Magnetoacoustics in Nickel Films*. Phys. Rev. Lett. **109**, 16, (2012) 166601.

-
- [Kim12b] K. W. Kim, A. Pashkin, H. Schäfer, M. Beyer, M. Porer, T. Wolf, C. Bernhard, J. Demsar, R. Huber, & A. Leitenstorfer. *Ultrafast transient generation of spin-density-wave order in the normal state of BaFe₂As₂ driven by coherent lattice vibrations*. Nat Mater **11**, 6, (2012) 497.
- [Kir10] A. Kirilyuk, A. V. Kimel, & T. Rasing. *Ultrafast optical manipulation of magnetic order*. Rev. Mod. Phys. **82**, 3, (2010) 2731.
- [Kir13] A. Kirilyuk, A. V. Kimel, & T. Rasing. *Laser-induced magnetization dynamics and reversal in ferrimagnetic alloys*. Reports on Progress in Physics **76**, 2, (2013) 026501.
- [Kit66] C. Kittel. *Introduction to solid state*. John Wiley & Sons, 1966.
- [Kle66] W. H. Kleiner. *Space-Time Symmetry of Transport Coefficients*. Phys. Rev. **142**, 2, (1966) 318.
- [Kli11] C. Klieber, E. Peronne, K. Katayama, J. Choi, M. Yamaguchi, T. Pezeril, & K. A. Nelson. *Narrow-band acoustic attenuation measurements in vitreous silica at frequencies between 20 and 400 GHz*. Applied Physics Letters **98**, 21, (2011) 211908.
- [Koo00] B. Koopmans, M. van Kampen, J. T. Kohlhepp, & W. J. M. de Jonge. *Ultrafast Magneto-Optics in Nickel: Magnetism or Optics?* Phys. Rev. Lett. **85**, 4, (2000) 844.
- [Koo03] B. Koopmans. *Spin Dynamics in Confined Magnetic Structures II*. Springer Berlin Heidelberg, Berlin, Heidelberg, 2003 256–323.
- [Koo05] B. Koopmans, J. J. M. Ruigrok, F. D. Longa, & W. J. M. de Jonge. *Unifying Ultrafast Magnetization Dynamics*. Phys. Rev. Lett. **95**, 26, (2005) 267207.
- [Koo10] B. Koopmans, G. Malinowski, F. Dalla Longa, D. Steiauf, M. Fahnle, T. Roth, M. Cinchetti, & M. Aeschlimann. *Explaining the paradoxical diversity of ultrafast laser-induced demagnetization*. Nat Mater **9**, 3, (2010) 259.
- [Koz00] A. E. Kozhekin, K. Mølmer, & E. Polzik. *Quantum memory for light*. Phys. Rev. A **62**, 3, (2000) 033809.
- [Kra15] F.-G. Kramer. *Time-Resolved Spin Seebeck Experiments*. Diplomarbeit, Technische Universität München (2015).
- [Kre96] G. Kresse & J. Furthmüller. *Efficiency of ab-initio total energy calculations for metals and semiconductors using a plane-wave basis set*. Computational Materials Science **6**, 1, (1996) 15.

- [Kri] R. S. Krishnan. *The scattering of light in diamond and its Raman spectrum*.
- [Ku13] S. A. Ku, C. M. Tu, W.-C. Chu, C. W. Luo, K. H. Wu, A. Yabushita, C. C. Chi, & T. Kobayashi. *Saturation of the free carrier absorption in ZnTe crystals*. *Opt. Express* **21**, 12, (2013) 13930.
- [Kub14] T. Kubacka, J. A. Johnson, M. C. Hoffmann, C. Vicario, S. de Jong, P. Beaud, S. Grübel, S.-W. Huang, L. Huber, L. Patthey, Y.-D. Chuang, J. J. Turner, G. L. Dakovski, W.-S. Lee, M. P. Minitti, W. Schlotter, R. G. Moore, C. P. Hauri, S. M. Koochpayeh, V. Scagnoli, G. Ingold, S. L. Johnson, & U. Staub. *Large-Amplitude Spin Dynamics Driven by a THz Pulse in Resonance with an Electromagnon*. *Science* 1242862.
- [Kue04] C. Kuebler, R. Huber, S. Tübel, & A. Leitenstorfer. *Ultrabroadband detection of multi-terahertz field transients with GaSe electro-optic sensors: Approaching the near infrared*. *Appl. Phys. Lett.* **85**, 16, (2004) 3360.
- [Kue05] C. Kuebler, R. Huber, & A. Leitenstorfer. *Ultrabroadband terahertz pulses: generation and field-resolved detection*. *Semiconductor Science and Technology* **20**, 7, (2005) S128.
- [Kue09] W. Kuehn, K. Reimann, M. Woerner, & T. Elsaesser. *Phase-resolved two-dimensional spectroscopy based on collinear n-wave mixing in the ultrafast time domain*. *J. Chem. Phys.* **130**, 16, (2009) 164503.
- [Kum67] N. Kumar & K. Sinha. *A new mechanism of magnon-phonon relaxation process in ferrimagnetic insulators*. *Physica* **36**, 4, (1967) 655.
- [Kur11] H. Kurebayashi, O. Dzyapko, V. E. Demidov, D. Fang, A. J. Ferguson, & S. O. Demokritov. *Controlled enhancement of spin-current emission by three-magnon splitting*. *Nat Mater* **10**, 9, (2011) 660.
- [Kuz94] A. V. Kuznetsov & C. J. Stanton. *Theory of Coherent Phonon Oscillations in Semiconductors*. *Phys. Rev. Lett.* **73**, 24, (1994) 3243.
- [Kuz95] A. V. Kuznetsov & C. J. Stanton. *Coherent phonon oscillations in GaAs*. *Phys. Rev. B* **51**, 12, (1995) 7555.
- [Lan28] G. Landsberg & L. Mandelstam. *Eine neue Erscheinung bei der Lichtzerstreuung in Krystallen*. *Naturwissenschaften* 557–558.
- [LaR15] J. L. LaRue, T. Katayama, A. Lindenberg, A. S. Fisher, H. Öström, A. Nilsson, & H. Ogasawara. *THz-Pulse-Induced Selective Catalytic CO Oxidation on Ru*. *Phys. Rev. Lett.* **115**, 3, (2015) 036103.

-
- [Lax55] M. Lax & E. Burstein. *Infrared Lattice Absorption in Ionic and Homopolar Crystals*. Phys. Rev. **97**, 1, (1955) 39.
- [Liu12] M. Liu, H. Y. Hwang, H. Tao, A. C. Strikwerda, K. Fan, G. R. Keiser, A. J. Sternbach, K. G. West, S. Kittiwatanakul, J. Lu, S. A. Wolf, F. G. Omenetto, X. Zhang, K. A. Nelson, & R. D. Averitt. *Terahertz-field-induced insulator-to-metal transition in vanadium dioxide metamaterial*. Nature **487**, 7407, (2012) 345.
- [Lou64] R. Loudon. *The Raman effect in crystals*. Advances in Physics **13**, (1964) 423.
- [Lou00] R. Loudon. *The quantum theory of light*. OUP, 2000, 3. Aufl.
- [Lu16] J. Lu, X. Li, H. Y. Hwang, B. K. Ofori-Okai, T. Kurihara, T. Suemoto, & K. A. Nelson. *Two-dimensional terahertz magnetic resonance spectroscopy of collective spin waves*. ArXiv e-prints .
- [Mad04] O. Madelung. *Semiconductors: data handbook*. Springer, 2004, 3. Aufl.
- [Mae11] S. F. Maehrlein. *Feldaufgelöste zweidimensionale Multi-Terahertz-Spektroskopie an Indiumantimonid und $\text{Bi}_2\text{Sr}_2\text{CaCu}_2\text{O}_8$* . Diplomarbeit, Universität Konstanz (2011).
- [Mae16a] S. Maehrlein, A. Paarmann, M. Wolf, & T. Kampfrath. *Terahertz sum-frequency excitation of a Raman-active phonon*. submitted to Phys. Rev. Lett. , arXiv:1703.02869.
- [Mae16b] S. F. Maehrlein, I. Radu, P. Maldonado, A. Paarmann, M. Gensch, A. M. Kalashnikova, R. V. Pisarev, M. Wolf, P. M. Oppeneer, J. Barker, & T. Kampfrath. *Ultrafast phonon driven magnetization dynamics*. in preparation .
- [Mai60] T. H. Maiman. *Stimulated Optical Radiation in Ruby*. Nature **187**, 4736, (1960) 493.
- [Mal16] P. Maldonado & P. Oppeneer. *in preparation*. tba .
- [Mar32] P. E. Martin & E. F. Barker. *The Infrared Absorption Spectrum of Carbon Dioxide*. Phys. Rev. **41**, 3, (1932) 291.
- [May10] B. Mayer. *Feldaufgelöstes Vier-Wellen-Mischen mit hochintensiven Multi-Terahertz-Impulsen*. Diplomarbeit, Universität Konstanz (2010).
- [May15] B. Mayer, C. Schmidt, A. Grupp, J. Bühler, J. Oelmann, R. E. Marvel, R. F. Haglund, T. Oka, D. Brida, A. Leitenstorfer, & A. Pashkin. *Tunneling breakdown of a strongly correlated insulating state in VO_2 induced by intense multiterahertz excitation*. Phys. Rev. B **91**, 23, (2015) 235113.

- [Mel11] A. Melnikov, I. Razdolski, T. O. Wehling, E. T. Papaioannou, V. Roddatis, P. Fumagalli, O. Aktsipetrov, A. I. Lichtenstein, & U. Bovensiepen. *Ultrafast Transport of Laser-Excited Spin-Polarized Carriers in Au/Fe/MgO(001)*. Phys. Rev. Lett. **107**, 7, (2011) 076601.
- [Mer97] R. Merlin. *Generating coherent THz phonons with light pulses*. Solid State Communications **102**, 2-3, (1997) 207.
- [Mil87] D. L. Mills. *Ionic contributions to the Raman tensor of insulators*. Phys. Rev. B **35**, 17, (1987) 9278.
- [Mil10] P. W. Milonni & J. H. Eberly. *Laser Physics*. John Wiley & Sons, Inc., 2010.
- [Mil13] R. P. Mildren. *Optical Engineering of Diamond*. Wiley-VCH Verlag GmbH & Co, 2013.
- [Mit87] T. B. Mitchell & P. E. Wigen. *The Faraday rotation of bismuth- and thulium-substituted yttrium iron garnet*. Journal of Applied Physics **61**, 8, (1987) 3259.
- [Muk99] S. Mukamel. *Principles of nonlinear optical spectroscopy*. Nr. 6. Oxford University Press on Demand, 1999.
- [Mye95] L. E. Myers, W. R. Bosenberg, G. D. Miller, R. C. Eckardt, M. M. Fejer, & R. L. Byer. *Quasi-phase-matched 1.064- μm -pumped optical parametric oscillator in bulk periodically poled LiNbO₃*. Opt. Lett. **20**, 1, (1995) 52.
- [Nie89] R. Nies & F. R. Kessler. *Coherent and Incoherent Magneto-optical Reflection and Transmission Effects of Multilayer Structures*. phys. stat. sol. (a) **111**, 2, (1989) 639.
- [Nol05] W. Nolting. *Grundkurs Theoretische Physik 7: Viel-Teilchen-Theorie*. Springer, 2005.
- [Nol09] W. Nolting & A. Ramakanth. *Quantum Theory of Magnetism*. Springer-Verlag Berlin Heidelberg, 2009.
- [Nol10a] W. Nolting. *Grundkurs Theoretische Physik 2: Analytische Mechanik*, Bd. 2. Springer Science & Business Media, 2010.
- [Nol10b] W. Nolting. *Grundkurs Theoretische Physik 6: Statistische Physik*, Bd. 6. Springer Science & Business Media, 2010, 5. Aufl.
- [Nol13] W. Nolting. *Grundkurs Theoretische Physik 5/1: Quantenmechanik – Grundlagen*, Bd. 5.1. Springer Science & Business Media, 2013, 8. Aufl.

-
- [Nol15] W. Nolting. *Grundkurs Theoretische Physik 5/2: Quantenmechanik – Methoden und Anwendungen*, Bd. 5.2. Springer Science & Business Media, 2015, 8. Aufl.
- [Now05] U. Nowak, O. N. Mryasov, R. Wieser, K. Gusliencko, & R. W. Chantrell. *Spin dynamics of magnetic nanoparticles: Beyond Brown's theory*. Phys. Rev. B **72**, 17, (2005) 172410.
- [Nun07] J. Nunn, I. A. Walmsley, M. G. Raymer, K. Surmacz, F. C. Waldermann, Z. Wang, & D. Jaksch. *Mapping broadband single-photon wave packets into an atomic memory*. Phys. Rev. A **75**, 1, (2007) 011401.
- [Oom06] J. Oomens, B. G. Sartakov, G. Meijer, & G. vonHelden. *Gas-phase infrared multiple photon dissociation spectroscopy of mass-selected molecular ions*. International Journal of Mass Spectrometry **254**, 1-2, (2006) 1.
- [Opp01] P. M. Oppeneer. *Magneto-optical Kerr spectra*. Handbook of Magnetic Materials **13**, (2001) 229.
- [Pal85] E. D. Palik. *Handbook of optical constants of solids*. Academic Press, Orlando, 1985.
- [Pap62] E. Pappalardo. *Crystal-field calculation for the three sites of yttrium iron garnet*. Il Nuovo Cimento (1955-1965) **26**, 4, (1962) 748.
- [Pas10] A. Pashkin, M. Porer, M. Beyer, K. W. Kim, A. Dubroka, C. Bernhard, X. Yao, Y. Dagan, R. Hackl, A. Erb, J. Demsar, R. Huber, & A. Leitenstorfer. *Femtosecond Response of Quasiparticles and Phonons in Superconducting $YBa_2Cu_3O_{7-\delta}$ Studied by Wideband Terahertz Spectroscopy*. Phys. Rev. Lett. **105**, 6, (2010) 067001.
- [Pas14] A. Pashkin & A. Leitenstorfer. *Particle physics in a superconductor*. Science **345**, 6201, (2014) 1121.
- [Ped90] F. L. Pedrotti & P. Bandettini. *Faraday rotation in the undergraduate advanced laboratory*. Am. J. Phys **58**, 6, (1990) 542.
- [Pel03] J. Pelzl, R. Meckenstock, D. Spoddig, F. Schreiber, J. Pflaum, & Z. Frait. *Spin-orbit-coupling effects on g -value and damping factor of the ferromagnetic resonance in Co and Fe films*. Journal of Physics: Condensed Matter **15**, 5, (2003) S451.
- [Per66] P. S. Pershan, J. P. Van der Ziel, & L. D. Malmstrom. *Theoretical discussion of the inverse Faraday effect, Raman scattering, and related phenomena*. Physical Review **143**, 2, (1966) 574.

- [Per82] W. B. Person & G. Zerbi. *Vibrational intensities in infrared and Raman spectroscopy*, Bd. 20. Elsevier Science Ltd, 1982.
- [Pet23] F. Peter. *Über Brechungsindizes und Absorptionskonstanten des Diamanten zwischen 644 und 226 m μ* . Zeitschrift für Physik **15**, 1, (1923) 358.
- [Pit61] L. P. Pitaevskii. *Electric forces in a transparent dispersive medium*. Sov. Phys. JETP **12**, 5, (1961) 1008.
- [Pow93] J. Powell. *CO₂ laser cutting*, Bd. 214. Cambridge Univ Press, 1993.
- [Rad11] I. Radu, K. Vahaplar, C. Stamm, T. Kachel, N. Pontius, H. A. Durr, T. A. Ostler, J. Barker, R. F. L. Evans, R. W. Chantrell, A. Tsukamoto, A. Itoh, A. Kirilyuk, T. Rasing, & A. V. Kimel. *Transient ferromagnetic-like state mediating ultrafast reversal of antiferromagnetically coupled spins*. Nature **472**, 7342, (2011) 205.
- [Raj11] I. Rajapaksa & H. Kumar Wickramasinghe. *Raman spectroscopy and microscopy based on mechanical force detection*. Applied Physics Letters **99**, 16, (2011) 161103.
- [Ral08] D. C. Ralph & M. D. Stiles. *Spin transfer torques*. Journal of Magnetism and Magnetic Materials **320**, 7, (2008) 1190.
- [Ram28] V. Raman, C. & S. Krishnan, K. *A New Type of Secondary Radiation* **121**, 3048, (1928) 501.
- [Ram56] C. V. Raman. *The diamond*. In *Proceedings of the Indian Academy of Sciences-Section A*, Bd. 44. Springer, 1956 99–110.
- [Rei03] K. Reimann, R. P. Smith, A. M. Weiner, T. Elsaesser, & M. Woerner. *Direct field-resolved detection of terahertz transients with amplitudes of megavolts per centimeter*. Opt. Lett. **28**, 6, (2003) 471.
- [Ric94] A. Rice, Y. Jin, X. F. Ma, X.-C. Zhang, D. Bliss, J. Larkin, & M. Alexander. *Terahertz optical rectification from <110> zinc-blende crystals*. Appl. Phys. Lett. **64**, 11, (1994) 1324.
- [Rif07] D. M. Riffe & A. J. Sabbah. *Coherent excitation of the optic phonon in Si: Transiently stimulated Raman scattering with a finite-lifetime electronic excitation*. Phys. Rev. B **76**, 8, (2007) 085207.
- [Rin07] M. Rini, R. Tobey, N. Dean, J. Itatani, Y. Tomioka, Y. Tokura, R. W. Schoenlein, & A. Cavalleri. *Control of the electronic phase of a manganite by mode-selective vibrational excitation*. Nature **449**, 7158, (2007) 72.

-
- [Ros14] N. Roschewsky, M. Schreier, A. Kamra, F. Schade, K. Ganzhorn, S. Meyer, H. Huebl, S. Geprägs, R. Gross, & S. T. Goennenwein. *Time resolved spin Seebeck effect experiments*. Appl. Phys. Lett. **104**, 20, (2014) 202410.
- [Rub12] A. Rubano, L. Braun, M. Wolf, & T. Kampfrath. *Mid-infrared time-domain ellipsometry: Application to Nb-doped SrTiO₃*. Applied Physics Letters **101**, 8, (2012) 081103.
- [Ruc12] C. Ruchert, C. Vicario, & C. P. Hauri. *Scaling submillimeter single-cycle transients toward megavolts per centimeter field strength via optical rectification in the organic crystal OH1*. Opt. Lett. **37**, 5, (2012) 899.
- [Rue14] A. Rueckriegel, P. Kopietz, D. A. Bozhko, A. A. Serga, & B. Hillebrands. *Magnetoelastic modes and lifetime of magnons in thin yttrium iron garnet films*. Phys. Rev. B **89**, 18, (2014) 184413.
- [Rul05] C. Rulliere. *Femtosecond laser pulses*. Springer, 2005.
- [Saj15] M. Sajadi, M. Wolf, & T. Kampfrath. *Terahertz-field-induced optical birefringence in common window and substrate materials*. Opt. Express **23**, 22, (2015) 28985.
- [Sal13] E. Saldin, E. V. Schneidmiller, & M. V. Yurkov. *The physics of free electron lasers*. Springer Science & Business Media, 2013.
- [San09] G. D. Sanders, C. J. Stanton, J.-H. Kim, K.-J. Yee, Y.-S. Lim, E. H. Házroz, L. G. Booshehri, J. Kono, & R. Saito. *Resonant coherent phonon spectroscopy of single-walled carbon nanotubes*. Phys. Rev. B **79**, 20, (2009) 205434.
- [San13] G. D. Sanders, A. R. T. Nugraha, K. Sato, J.-H. Kim, J. Kono, R. Saito, & C. J. Stanton. *Theory of coherent phonons in carbon nanotubes and graphene nanoribbons*. Journal of Physics: Condensed Matter **25**, 14, (2013) 144201.
- [Sat15] D. N. Sathyanarayana. *Vibrational spectroscopy: theory and applications*. New Age International, 2015.
- [Sbi11] R. Sbiaa, H. Meng, & S. N. Piramanayagam. *Materials with perpendicular magnetic anisotropy for magnetic random access memory*. Phys. Status Solidi RRL **5**, 12, (2011) 413.
- [Sch08] T. Schneider, A. A. Serga, B. Leven, B. Hillebrands, R. L. Stamps, & M. P. Kostylev. *Realization of spin-wave logic gates*. Applied Physics Letters **92**, 2, (2008) 022505.
- [Sch13] M. Schreier, A. Kamra, M. Weiler, X. Jiang, G. E. W. Bauer, R. Gross, & S. T. B. Goennenwein. *Magnon, phonon and electron temperature profiles and*

the spin Seebeck effect in magnetic insulator/normal metal hybrid structures [arXiv:1306.4292](#) [[cond-mat.mes-hall](#)].

- [Sch14] O. Schubert, M. Hohenleutner, F. Langer, B. Urbanek, C. Lange, U. Huttner, D. Golde, T. Meier, M. Kira, S. W. Koch, & R. Huber. *Sub-cycle control of terahertz high-harmonic generation by dynamical Bloch oscillations*. Nat Photon **advance online publication**, (2014) .
- [Sch15] W. Schöllkopf, S. Gewinner, H. Junkes, A. Paarmann, G. von Helden, H. Bluem, & A. M. M. Todd. *The new IR and THz FEL facility at the Fritz Haber Institute in Berlin*. Bd. 9512. 2015 95121L–95121L–13.
- [Sei13] T. Seifert. *Generation of Intense and Spectrally Narrow Terahertz Pulses*. Diplomarbeit, Freie Universität Berlin (2013).
- [Sei16] T. Seifert, S. Jaiswal, U. Martens, J. Hannegan, L. Braun, P. Maldonado, F. Freimuth, A. Kronenberg, J. Henrizi, I. Radu, E. Beaurepaire, Y. Mokrousov, P. M. Oppeneer, M. Jourdan, G. Jakob, D. Turchinovich, L. M. Hayden, M. Wolf, M. Münzenberg, M. Kläui, & T. Kampfrath. *Efficient metallic spintronic emitters of ultrabroadband terahertz radiation*. Nat Photon **10**, 7, (2016) 483.
- [Sel08a] A. Sell, A. Leitenstorfer, & R. Huber. *Phase-locked generation and field-resolved detection of widely tunable terahertz pulses with amplitudes exceeding 100 MV/cm*. Opt. Lett. **33**, 23, (2008) 2767.
- [Sel08b] A. Sell, R. Scheu, A. Leitenstorfer, & R. Huber. *Field-resolved detection of phase-locked infrared transients from a compact Er: fiber system tunable between 55 and 107 THz*. Appl. Phys. Lett. **93**, 25, (2008) 251107.
- [Ser10] A. A. Serga, A. V. Chumak, & B. Hillebrands. *YIG magnonics*. J. Phys. D: Appl. Phys. **43**, 26, (2010) 264002.
- [Sha15] M. Shalaby & C. P. Hauri. *Demonstration of a low-frequency three-dimensional terahertz bullet with extreme brightness*. Nat Commun **6**.
- [She84] Y. Shen. *The Principles of Nonlinear Optics*. Wiley-Interscience, 1984.
- [Shi10] A. B. Shick, S. Khmelevskiy, O. N. Mryasov, J. Wunderlich, & T. Jungwirth. *Spin-orbit coupling induced anisotropy effects in bimetallic antiferromagnets: A route towards antiferromagnetic spintronics*. Phys. Rev. B **81**, 21, (2010) 212409.
- [Smi89] F. W. Smith, H. Q. Le, V. Diadiuk, M. A. Hollis, A. R. Calawa, S. Gupta, M. Frankel, D. R. Dykaar, G. A. Mourou, & T. Y. Hsiang. *Picosecond GaAs-based photoconductive optoelectronic detectors*. Applied Physics Letters **54**, 10, (1989) 890.

-
- [Sol62] I. H. Solt. *Temperature Dependence of YIG Magnetization*. Journal of Applied Physics **33**, 3, (1962) 1189.
- [Sol70] S. A. Solin & A. K. Ramdas. *Raman Spectrum of Diamond*. Phys. Rev. B **1**, 4, (1970) 1687.
- [Spe62] E. G. Spencer & R. C. LeCraw. *Ferromagnetic relaxation in yttrium-iron garnet and the relation to applications*. Proceedings of the IEE - Part B: Electronic and Communication Engineering **109**, 21, (1962) 66.
- [Sta71] H. E. Stanley. *Introduction to phase transitions and critical phenomena*, Bd. 1 von *Monographs on Physics*. Oxford University Press, 1971, first edition Aufl.
- [Sta14] R. L. Stamps, S. Breitkreutz, J. Åkerman, A. V. Chumak, Y. Otani, G. E. Bauer, J.-U. Thiele, M. Bowen, S. A. Majetich, & M. Kläui. *The 2014 magnetism roadmap*. J. Phys. D: Appl. Phys. **47**, 33, (2014) 333001.
- [Ste02] T. E. Stevens, J. Kuhl, & R. Merlin. *Coherent phonon generation and the two stimulated Raman tensors*. Phys. Rev. B **65**, 14, (2002) 144304.
- [Sti02] M. D. Stiles & A. Zangwill. *Anatomy of spin-transfer torque*. Phys. Rev. B **66**, 1, (2002) 014407.
- [Sto07] J. Stoehr & H. Siegmann. *Magnetism: From Fundamentals to Nanoscale Dynamics*. Springer Berlin Heidelberg, 2007.
- [Sub14] A. Subedi, A. Cavalleri, & A. Georges. *Theory of nonlinear phononics for coherent light control of solids*. Phys. Rev. B **89**, 22, (2014) 220301.
- [Sug00] S. Sugai, S. Sugano, & N. Kojima. *Magneto-Optics*. Springer, Berlin,, 2000.
- [Tav11] F. Tavella, N. Stojanovic, G. Geloni, & M. Gensch. *Few-femtosecond timing at fourth-generation X-ray light sources*. Nat Photon **5**, 3, (2011) 162.
- [Tay11] A. J. Taylor & R. A. Kaindl. *Time-Domain and Ultrafast Terahertz Spectroscopy*. In *Optical Techniques for Solid-State Materials Characterization*. CRC Press, 2011 397–442.
- [Tem12] V. V. Temnov. *Ultrafast acousto-magneto-plasmonics*. Nat Photon **6**, 11, (2012) 728.
- [Tog09] A. Togo. *Phonopy* (2009).
- [Tok00] Y. Tokura. *Colossal Magnetoresistive Oxides*. Taylor & Francis, 2000.

- [Tre69] E. Treacy. *Optical pulse compression with diffraction gratings*. Quantum Electronics, IEEE Journal of **5**, 9, (1969) 454.
- [Uch08] K. Uchida, S. Takahashi, K. Harii, J. Ieda, W. Koshibae, K. Ando, S. Maekawa, & E. Saitoh. *Observation of the spin Seebeck effect*. Nature **455**, 7214, (2008) 778.
- [Uch14] K.-i. Uchida, T. Kikkawa, A. Miura, J. Shiomi, & E. Saitoh. *Quantitative Temperature Dependence of Longitudinal Spin Seebeck Effect at High Temperatures*. Phys. Rev. X **4**, 4, (2014) 041023.
- [Urb01] R. Urban, G. Woltersdorf, & B. Heinrich. *Gilbert Damping in Single and Multilayer Ultrathin Films: Role of Interfaces in Nonlocal Spin Dynamics*. Phys. Rev. Lett. **87**, 21, (2001) 217204.
- [VA07] R. Valdés Aguilar, A. B. Sushkov, C. L. Zhang, Y. J. Choi, S.-W. Cheong, & H. D. Drew. *Colossal magnon-phonon coupling in multiferroic $\text{Eu}_{0.75}\text{Y}_{0.25}\text{MnO}_3$* . Phys. Rev. B **76**, 6, (2007) 060404.
- [Vat92] A. Vaterlaus, T. Beutler, D. Guarisco, M. Lutz, & F. Meier. *Spin-lattice relaxation in ferromagnets studied by time-resolved spin-polarized photoemission*. Phys. Rev. B **46**, 9, (1992) 5280.
- [vdZ65] J. P. van der Ziel, P. S. Pershan, & L. D. Malmstrom. *Optically-Induced Magnetization Resulting from the Inverse Faraday Effect*. Phys. Rev. Lett. **15**, 5, (1965) 190.
- [Vic15] C. Vicario, M. Jazbinsek, A. V. Ovchinnikov, O. V. Chefonov, S. I. Ashitkov, M. B. Agranat, & C. P. Hauri. *High efficiency THz generation in DSTMS, DAST and OH1 pumped by Cr:forsterite laser*. Opt. Express **23**, 4, (2015) 4573.
- [Vid11] S. Vidal, J. Degert, M. Tondusson, J. Oberlé, & E. Freysz. *Impact of dispersion, free carriers, and two-photon absorption on the generation of intense terahertz pulses in ZnTe crystals*. Applied Physics Letters **98**, 19, (2011) 191103.
- [Vie75] T. K. Vien, J. L. Dormann, & H. Le gall. *Crystal Field Splitting in Octahedral and Tetrahedral Symmetry for Fe^{3+} Ions in $\text{Y}_3\text{Fe}_5\text{O}_{12}$* . phys. stat. sol. (b) **71**, 2, (1975) 731.
- [Vit85] C. Vittoria, P. Lubitz, P. Hansen, & W. Tolksdorf. *FMR linewidth measurements in bismuth-substituted YIG*. J. Appl. Phys. **57**, 8, (1985) 3699.
- [Vog14] K. Vogt, F. Y. Fradin, J. E. Pearson, T. Sebastian, S. D. Bader, B. Hillebrands, A. Hoffmann, & H. Schultheiss. *Realization of a spin-wave multiplexer*. Nat Commun **5**.

-
- [Wal13] S. Wall, L. Foglia, D. Wegkamp, K. Appavoo, J. Nag, R. F. Haglund, J. StÄhler, & M. Wolf. *Tracking the evolution of electronic and structural properties of VO₂ during the ultrafast photoinduced insulator-metal transition*. Phys. Rev. B **87**, 11, (2013) 115126.
- [Wan16] R. Wang, Y.-X. Shang, R. Wu, J.-B. Yang, & Y. Ji. *Evolution of Magnetic Domain Structure in a YIG Thin Film*. Chinese Physics Letters **33**, 4, (2016) 047502.
- [War65] J. L. Warren, R. G. Wenzel, & J. L. Yarnell. *Dispersion curves for phonons in diamond*. In *Inelastic Scattering of Neutrons. Vol. I. Proceedings of the Symposium on Inelastic Scattering of Neutrons*. 1965 .
- [War67] J. L. Warren, J. L. Yarnell, G. Dolling, & R. A. Cowley. *Lattice Dynamics of Diamond*. Phys. Rev. **158**, 3, (1967) 805.
- [Web77] W. Weber. *Adiabatic bond charge model for the phonons in diamond, Si, Ge, and α - Sn*. Phys. Rev. B **15**, 10, (1977) 4789.
- [Wil07] I. Wilke & S. Sengupta. *Nonlinear optical techniques for terahertz pulse generation and detection—optical rectification and electrooptic sampling*. In *Terahertz spectroscopy: principles and applications*, Bd. 131. CRC press, 2007 41.
- [Win81] G. Winkler. *Magnetic Garnets, Friedr. Vieweg & Sohn, Braunschweig* .
- [Win09] S. Winnerl, B. Zimmermann, F. Peter, H. Schneider, & M. Helm. *Terahertz Bessel-Gauss beams of radial and azimuthal polarization from microstructured photoconductive antennas*. Opt. Express **17**, 3, (2009) 1571.
- [Wit13] W. J. Witteman. *The CO₂ laser*, Bd. 53. Springer, 2013.
- [Wol01] S. A. Wolf, D. D. Awschalom, R. A. Buhrman, J. M. Daughton, S. von Molnár, M. L. Roukes, A. Y. Chtchelkanova, & D. M. Treger. *Spintronics: A Spin-Based Electronics Vision for the Future*. Science **294**, 5546, (2001) 1488.
- [Wu96] Q. Wu & X.-C. Zhang. *Ultrafast electro-optic field sensors*. Applied Physics Letters **68**, 12, (1996) 1604.
- [Wu16] S. M. Wu, W. Zhang, K. C. Amit, P. Borisov, J. E. Pearson, J. S. Jiang, D. Lederman, A. Hoffmann, & A. Bhattacharya. *Antiferromagnetic Spin Seebeck Effect*. Phys. Rev. Lett. **116**, 9, (2016) 097204.
- [Xia10] J. Xiao, G. E. W. Bauer, K.-c. Uchida, E. Saitoh, & S. Maekawa. *Theory of magnon-driven spin Seebeck effect*. Phys. Rev. B **81**, 21, (2010) 214418.
- [Yar85] A. Yariv. *Optical Electronics*. Holt, Rinehart and Winston, 1985, 3. Aufl.

- [Ye05] J. Ye. *Femtosecond optical frequency comb: principle, operation and applications*. Springer Science & Business Media, 2005.
- [Yu05] P. Y. Yu & M. Cardona. *Fundamentals of semiconductors*. Springer, 2005, 3. Aufl.
- [Zai01] A. M. Zaitsev. *Optical Properties of Diamonds*. In *A Data Handbook*. Springer-Verlag Berlin, 2001 502.
- [Zak90] J. Zak, E. R. Moog, C. Liu, & S. D. Bader. *Fundamental magneto-optics*. Journal of Applied Physics **68**, 8, (1990) 4203.
- [Zei92] H. J. Zeiger, J. Vidal, T. K. Cheng, E. P. Ippen, G. Dresselhaus, & M. S. Dresselhaus. *Theory for displacive excitation of coherent phonons*. Phys. Rev. B **45**, 2, (1992) 768.
- [Zij06] E. S. Zijlstra, L. L. Tatarinova, & M. E. Garcia. *Laser-induced phonon-phonon interactions in bismuth*. Phys. Rev. B **74**, 22, (2006) 220301.

List of Publications

Publications within this thesis

S. Maehrlein, I. Radu, P. Maldonado, A. Paarmann, M. Gensch, A. M. Kalashnikova, R. V. Pisarev, M. Wolf, P. M. Oppeneer, J. Barker, and T. Kampfrath. *Ultrafast phonon driven magnetization dynamics*, in preperation, (2016)

S. Maehrlein, A. Paarmann, M. Wolf, and T. Kampfrath. *Terahertz sum-frequency excitation of a Raman-active phonon*, submitted to Phys. Rev. Lett., preprint arXiv:1703.02869, (2016)

B. Green, S. Kovalev, V. Asgekar, G. Geloni, U. Lehnert, T. Golz, M. Kuntzsch, C. Bauer, J. Hauser, J. Voigtlaender, B. Wustmann, I. Koesterke, M. Schwarz, M. Freitag, A. Arnold, J. Teichert, M. Justus, W. Seidel, C. Ilgner, N. Awari, D. Nicoletti, S. Kaiser, Y. Laplace, S. Rajasekaran, L. Zhang, S. Winnerl, H. Schneider, G. Schay, I. Lorincz, A. A. Rauscher, I. Radu, S. Maehrlein, T. H. Kim, J. S. Lee, T. Kampfrath, S. Wall, J. Heberle, A. Malnasi-Csizmadia, A. Steiger, A. S. Mueller, M. Helm, U. Schramm, T. Cowan, P. Michel, A. Cavalleri, A. S. Fisher, N. Stojanovic, and M. Gensch. *High-Field High-Repetition-Rate Sources for the Coherent THz Control of Matter*, Scientific Reports **6**, (2016), 22256

T. Kampfrath, M. Battiato, P. Maldonado, G. Eilers, J. Notzold, S. Maehrlein, V. Zbarsky, F. Freimuth, Y. Mokrousov, S. Blugel, M. Wolf, I. Radu, P.M. Oppeneer, and M. Müntzenberg. *Terahertz spin current pulses controlled by magnetic heterostructures*, Nature Nanotechnology **8**, (2013), 256

Publications concerning other topics

F. Junginger, B. Mayer, C. Schmidt, O. Schubert, S. Maehrlein, A. Leitenstorfer, R. Huber, and A. Pashkin. *Nonperturbative Interband Response of a Bulk InSb Semiconductor Driven Off Resonantly by Terahertz Electromagnetic Few-Cycle Pulses*, Physical Review Letters **109**, (2012), 147403

T. Kampfrath, A. Sell, G. Klatt, A. Pashkin, S. Maehrlein, T. Dekorsy, M. Wolf, M. Fiebig, A. Leitenstorfer, and R. Huber. *Coherent terahertz control of antiferromagnetic spin waves*, Nature Photonics **5**, (2011), 31

Academic curriculum vitae

Sebastian F. Mährlein
12059 Berlin

Der Lebenslauf ist in der Online-Version aus Gründen des Datenschutzes nicht enthalten.

Acknowledgments

I would like to thank everyone who took part in my scientific work and/or was part of my life during the recent wonderful years. Especially I would like to mention the following supportive people:

Definitely, the biggest thanks go to *Tobias Kampfrath*. He was a great supervisor and mentor who shared his physical knowledge and visions, and supported me without any compromise, day and night if necessary! I appreciate his ability to explain complex issues in a simple way, while keeping a broader scientific vision. Thank you for providing a most enjoyable working atmosphere in your THz group!

A big amount of thanks also goes to *Martin Wolf* for the possibility of doing my PhD at the FHI, where he always sets the right tone for cutting-edge science in a friendly and personal atmosphere. I appreciate his interest in my work during the last years and the chance of being the chairman of the Gordon Research Seminar 2016.

Additionally, I want to express my gratitude to *Katharina Franke* for taking over the second supervision in a friendly and uncomplicated manner.

Of course I appreciate the vast contributions by the two main collaborators to my main projects: A big thank you to *Ilie Radu* (MBI, Berlin), who initially kicked off the ultrafast magnetization studies, provided excellent samples and shared a number of beam time shifts at FLASH with me. Further, I really enjoyed the beam times and elaborate discussions with *Alexander Paarmann*. Alex, it's always refreshing to get your point of view on scientific and non-scientific problems.

Without the contributions from theoreticians the interpretation of the magnetization studies would have hardly been possible. Therefore, many thanks to *Pablo Maldonado* (U. Uppsala, Sweden), *Joseph Barker* (Tohoku U., Japan) and *Peter M. Oppeneer* (U. Uppsala, Sweden) for their constant theory support and a number of very educative video conferences.

Further, I would like to thank the collaborators *Michael Gensch* (HZDR, Dresden) and *Nikola Stojanovic* (DESY, Hamburg) for beam time support at FELBE and FLASH respectively and *Alexandra Kalashnikova* (Ioffe Institute, St. Petersburg, Russia), *Roman V. Pisarev* (Ioffe Institute, St. Petersburg, Russia) and *Kunie Ishioka* (NIMS, Tsukuba, Japan) for generously providing the samples studied in this work.

Honestly, I want to thank *Rupert Hubert* (University of Regensburg) and *Alfred Leitenstorfer* (University of Konstanz) for guiding my first scientific steps into the beautiful and adventurous world of ultrafast phenomena. In the same spirit, I want to take the opportunity to thank *Peter Müller* und *Werner Heckmann*, for feeding my curiosity in the early days.

Unspeakable thanks go to *Lukas Braun*! How crazy is this? Starting and submitting the thesis together on the same day. Thank you so much for the big piece of life that we shared. The race is on: Who will defend first?

Of course I also thank the THz crew *Julius, Tom, Mohsen* (+ *Yujin*) for the good, the bad and the ugly times in the lab. As well I have to thank my scottitalian office mates *Christele* and *Michestopher*. Thanks also to *Lutz, Melanie, Laura, Ralph, Harald, Kramer, Ilya, Daniel, Patrick* and all other PhDs/PostDocs/students that I forgot for spreading the friendly atmosphere. An honorary mention is given to the *Fabeck BBQ-society*.

Big thanks also to the administrative and technologic backbone of the FHI especially *Marcel Krenz, Reinhard Franke, Sven Kubala, Albrecht Ropers, Frank Quadt, Willi Krauss* und *Manuel Krüger*. Thanks also to the *E-lab* crew.

Thanks again to my former Konstanz Φ -*boys*, not only for building the common scientific basis, but also for the gravitational waves that are expected whenever we meet.

One big shout out for disturbing my work-work balance to the *Harries* and my ultimate team *Parkscheibe*: *Mens sana in corpore sano!*

Cheers to *Gauvain, Hannes* und *Michael* for still being a complete set of basis states after all those years.

Finally, I owe an infinite debt of gratitude to my *family*, especially to my *parents* for providing unlimited support and faith.

... and I am deeply grateful for having you, *Andrea*, as part of my life ... einfachso

Selbstständigkeitserklärung gemäss der Promotionsordnung

Sämtliche verwendeten Hilfsmittel, Hilfen und Quellen sind an der entsprechenden Stelle angegeben. Ich versichere, dass ich auf dieser Grundlage diese Arbeit selbstständig verfasst habe. Diese Arbeit wurde bisher weder in gleicher noch ähnlicher Form einer anderen Prüfungskommission vorgelegt oder veröffentlicht.

Berlin, den

Sebastian F. Mährlein